NANOSCALE CONFINEMENT EFFECTS ON POLY(ε-CAPROLACTONE) CRYSTALLIZATION AT THE AIR/WATER INTERFACE & SURFACTANT INTERACTIONS WITH PHOSPHOLIPID BILAYERS

Qiongdan Xie

A dissertation submitted to the faculty of the
Virginia Polytechnic Institute and the State University
in partial fulfillment of the requirement for the degree of

Doctor of Philosophy
in
Chemistry

Alan R. Esker, Chairman
Hervé Marand
Richard D. Gandour
John R. Morris
Harry C. Dorn

February 16, 2010
Blacksburg, Virginia

Keywords: Langmuir monolayers, Magnetic nanoparticles, Poly(ε-caprolactone), Crystallization, Diffusion limited growth, Nanoscale confinement, Phospholipid bilayer, Surfactants

NANOSCALE CONFINEMENT EFFECTS ON POLY(ε-CAPROLACTONE) CRYSTALLIZATION AT THE AIR/WATER INTERFACE & SURFACTANT INTERACTIONS WITH PHOSPHOLIPID BILAYERS

Qiongdan Xie

(Abstract)

Two-dimensional (2D) nanoscale confinement effects on poly(ε-caprolactone) (PCL) crystallization were probed through crystallization studies of PCL-b-poly(tert-butyl acrylate) (PCL-b-PtBA) copolymers, PCL with bulky tri-tert-butyl ester endgroups (PCL triesters), PCL with triacid end groups (PCL triacids), and magnetic nanoparticles stabilized by PCL triacid (PCL MNPs) at the air/water (A/W) interface. Thermodynamic analyses of surface pressure-area per monomer (Π−A) isotherms for the Langmuir films at the A/W interface showed that PCL-b-PtBA copolymers, PCL triheads and PCL MNPs all formed homogenous monolayers below the dynamic collapse pressure of PCL, Π_C ~11 mN•m^{-1}. For compression past the collapse point, the PCL monolayers underwent a phase transition to three-dimensional (3D) crystals and the nanoscale confinements impacted the PCL crystalline morphologies. Studies of PCL-b-PtBA copolymers revealed that the morphologies of the LB-films became smaller and transitioned to dendrites with defects, stripes and finally nano-scale cylindrical features as the block length of PtBA increased.

For the case of PCL triester, irregularly shaped crystals formed at the A/W interface and this was attributed to the accumulation of bulky tert-butyl ester groups around the crystal growth fronts. In contrast, regular, nearly round-shaped lamellar crystals were obtained for PCL triacids. These morphological differences between PCL triacids and PCL triesters were molar mass dependent and attributed to differences in dipole density and the submersion of carboxylic acid groups in the subphase. Nonetheless, enhanced uniformity for PCL triacid

crystals was not retained once the polymers were tethered to the spherical surface of a PCL MNP. Instead, the PCL MNPs exhibited small irregularly shaped crystals. This nano-scale confinement effect on the surface morphology at the A/W interface was also molar mass dependent. For the small molar mass PCL MNPs, two layers of collapsed nanoparticles were observed.

In a later chapter, studies of polyethylene glycol (PEG) surfactant adsorption onto phospholipid bilayers through quartz crystal microbalance with dissipation monitoring (QCM-D) measurements revealed a strong dependence of the adsorption and desorption kinetics on hydrophobic tail group structure. PEG surfactants with a single linear alkyl tail inserted and saturated the bilayer surface quickly and the surfactants had relatively fast desorption rates. In contrast, PEG lipids, including dioleoyl PEG lipids and cholesterol PEGs, demonstrated slower adsorption and desorption kinetics. The interactions of Pluronics and Nonoxynol surfactants with phospholipid bilayers were also studied. Pluronics showed no apparent affinity for the phospholipid bilayer, while the Nonoxynol surfactants damaged the lipid bilayers as PEG chain length decreased.

ACKNOWLEDGMENTS

I would like to thank my advisor, Prof. Alan R. Esker for his guidance and support. Alan is very strict mentor and I especially appreciate that he corrected my partially wrong view about science. I would like to thank my committee members: Prof. Hervé Marand, Prof. Richard D. Gandour, Prof. John R. Morris, and Prof. Harry C. Dorn. In particular, I am thankful to Prof. Richard D. Gandour and his former PhD student André A. Williams for the help in the initial stage of my projects. I would also like to thank John Boyle and Philip Huffstetler in Prof. Judy S. Riffle's group, Tomonori Saito in Prof. Timothy E. Long's group for the help in polymer syntheses. I thank Sha Yang for the help in DSC measurement. I thank Prof John R. Morris for letting me use the AFM for free. I thank Prof. Gordon T. Yee for being the substitute committee member in my thesis defense. I would also like to acknowledge the financial support of the Department of Chemistry at Virginia Tech in the form of teaching assistantship and in the form of tuition funds, and the National Science Foundation (NSF) in the form of research funds. I am also grateful to all my former and present group members: Sheila Gradwell, Jianjun Deng, Suolong Ni, Rituparna Paul, Bingbing Li, Woojin Lee, Ufuk Karabiyik, Wen Yin, Jae-Hyun Sim, Joshua Kittle, Zelin Lin, Yang Liu, Xiaosong Du, Chuanzi OuYang and Abdulaziz Kaya. An especial thank here is dedicated to my brilliant and hard-working undergraduates: Samantha Farris, Liz Huh, and Sarah Dyer, especially Liz Huh and Sarah Dyer. Their work contributes a big part to my thesis.

As always, I would like to thank my family for their unconditional love and support all over the years. They are the important reason I continued and finished my graduate school study.

TABLE OF CONTENTS

LIST OF FIGURES

Chapter 2

Chapter 3

Chapter 4

Chapter 5

Chapter 6

Chapter 7

List of Tables

Chapter 3

Chapter 4

Chapter 5

Chapter 6

Chapter 7

Chapter 1

Overview of Thesis

Confinement of semi-crystalline polymers with nanoscale geometries is an intriguing subject. Confinement affected the chain mobility, diffusion, material availability and consequently, the final morphologies of semi-crystalline polymers throughout the crystallization process. The semi-crystalline polymer of interest in this thesis is poly(ε-caprolactone) (PCL). PCL is a hydrophobic polyester with a bulk glass transition temperature of $T_g \sim -60$ ˚C and a melting point of $T_m \sim 50$ ˚C. Previous studies of PCL at the air/water (A/W) interface revealed that the two dimensional (2D) monolayer transformed into three dimensional (3D) lamellar crystals after the collapse of the monolayer.[1] This process was analogous to homogenous nucleation and growth. The subsequent report of PCL/poly(t-butyl acrylate) (PtBA) blends showed dendritic crystalline morphologies which were a result of diffusion limited crystal growth.[2] In order to further investigate how nanoscale confinement affected PCL crystallization, this thesis probed three mechanisms for altering nanoscale confinement within a monolayer at the A/W interface: (1) adding an amorphous amphiphilic PtBA block to PCL (PCL-b-PtBA); (2) adding a bulky headgroup to one end of the PCL chain, and (3) tethering PCL to the surface of a magnetic nanoparticle to create nano-spherical confinement. In a later chapter, synthetic methods were developed to make end functionalized poly(ethylene glycol)s (PEGs) and surfactant PEGs. Interactions of these surfactants with biomimetic phospholipid bilayers were also examined.

Chapter 2 provides "An Introduction and Review" related to this study, including phase transitions in Langmuir monolayers, thin film crystallization, block copolymer phase diagram, block copolymer thin film morphologies, and surfactants in aqueous solutions. Relevant background for techniques used for studying Langmuir and Langmuir-Blodgett (LB) films such as surface pressure-area per monomer (Π-A) isotherm studies, Brewster angle microscopy (BAM), and atomic force microscopy (AFM) along with quartz crystal microbalance with dissipation monitoring (QCM-D) for adsorption studies are also summarized in this chapter.

Chapter 3, “Materials and Experimental Methods,” contains a detailed description of the material synthesized for this project. In addition, preparations and experimental methods and procedures used in subsequent chapters are summarized in Chapter 3.

In Chapter 4, “Morphological Studies of Poly(ε-caprolactone)-b-Poly(tert-butyl acrylate) Block Copolymers at the Air/Water Interface”, PCL-b-PtBA block copolymers were studied by surface pressure-average area per monomer (Π−A) isotherms. Distinctive features of both amphiphilic polymers were observed in different regions of the Π-A isotherms. The crystallization pressure for the PCL block was lower than the collapse pressure for the PtBA block; therefore, PCL block crystallization was confined laterally by the coexisting amorphous PtBA monolayer. As expected, the crystal morphologies showed a strong dependence on the PtBA block length for a fixed PCL block length. LB-films prepared from monolayers at the A/W interface were studied by AFM and revealed a systematic transition in morphologies from reduced crystal sizes, to dendrites with defects, thin stripes, and finally to the nanoscale cylindrical domains. This system could also be viewed as a 2D block copolymer system where the microphase separation was induced by crystallization of the PCL block. A tentative explanation based on the size of the block in 2D was also provided in the chapter.

In Chapter 5, “Morphological Studies of Poly(ε-caprolactone) Stabilized Magnetic Nanoparticles at the Air/Water Interface,” one end of the linear PCL chains was attached to a nanoparticle surface by a tricarboxylic acid headgroup. The effect of confinement to a nanoscale spherical surface significantly hindered the growth of PCL crystals at the A/W interface. The sizes of the PCL nanoparticle crystals were dramatically smaller relative to crystals of PCL triacids grown under similar conditions. Further investigation of the headgroup effects for PCL crystallization used bulky amphiphilic triester headgroups, the synthetic precursor for the hydrophilic triacid endgroups. Bulky triester headgroups also hindered crystallization and led to small and multi-faceted lamellar crystals. In contrast, PCL with a hydrophilic triacid formed large and elliptical crystals at the A/W interface. The morphological differences between the PCL triacids and PCL triesters was attributed to the influence of line tension and the hindrance of the bulky ester groups.

In Chapter 6, "Quartz Crystal Microbalance with Dissipation Monitoring (QCM-D) Studies of Nonionic Polymeric Surfactant Adsorption onto Phospholipid Bilayers," the adsorption of poly(ethylene glycol) surfactants onto lipid bilayers was studied by QCM-D. The results revealed binding affinity was strongly dependent upon the hydrophobic tail group structure: a size-match for the tail group structure with the lipid tail groups was required for the incorporation of the hydrophobic tail groups into the phospholipid bilayer. Effects of tail group size on adsorption and desorption kinetics was also probed.

Chapter 7, "Conclusions and Suggestions for Future Work," provides the overall conclusions for this thesis and several suggestions for future work. Suggestions for future work were guided by preliminary results in four areas: (1) The crystallization of PCL within PCL/oleic acid MNP blends and PCL/oleic acid blend monolayers; (2) PCL crystallization within micro-phase separated monolayers of PCL-b-polystyrene (PCL-b-PS) at the A/W interface. (3) Preparation of tethered lipid bilayers on metal oxide surfaces via PEG surfactants; and (4) Interactions between water soluble polysaccharides modified with various fatty acids and phospholipid bilayers.

References:

(1) Li, B.; Wu, Y.; Liu, M.; Esker, A. R. *Langmuir* **2006**, *22*, 4902.

(2) Li, B.; Marand, H.; Esker, A. R. *J Polym Sci Part B: Polym Phys* **2007**, *45*, 3300.

Chapter 2

Introduction and Review

2.1. Introduction to Polymer Thin Films at Interfaces

Polymer thin films at interfaces continually attract interest for fundamental studies and industrial applications. In general, a better understanding of polymer phase behavior, properties, and morphologies that arose from reduced thickness and confined geometries confinements has enhanced the application of polymeric materials. For instance, block copolymers increased the compatibility of two im-miscible polymer phases by self-assembly at the interface of the two phases.[1] For biological applications, a layer of poly(ethylene glycol) effectively reduced non-specific protein binding and increased the circulation time of pegylated drugs.[2] Moreover, the periodic morphologies of block copolymer thin films as potential templates for the fabrication of new generation computer chips has attracted the attention of the semiconductor industry.[3] Consequently, a huge volume of literature with respect to polymer thin film research has developed, of which the effects of nanoscale factors such as nano-fillers on thin films has been an very active field.[4]

2.2. Monolayer Formation at the Air/Water Interface

Among all interfaces, the air/water (A/W) interface has been heavily investigated for a long time. Studies of the molecular interactions at the A/W interface have yielded a wealth of knowledge about various intra- or inter-molecular interactions, phase transitions, molecular orientations, conformations, etc. The earliest monolayer studies at the A/W interface dated back to the famous Clapham pond experiment by Benjamin Franklin in 1774.[5] Over the centuries, the development of the Langmuir trough[6] and Langmuir film balance,[7-8] allowed for qualitative studies of molecules at the A/W interface. These developments were quickly followed by the Langmuir-Blodgett (LB) technique which allowed films to be transferred onto solid substrates. Furthermore, the invention of more state-of-art characterization technique such as atomic force microscopy (AFM), fluorescence microscopy and Brewster angle microscopy (BAM) rejuvenated the research at the A/W interface. With these techniques, detailed information about surface morphologies was obtained. While early studies focused on small molecules, research on polymers at the A/W interface quickly caught up.

For small molecules, to form a monolayer, the molecules needed to have two distinct parts: a hydrophobic tail which inhibited dissolution of the molecules into the subphase and a hydrophilic head which anchored the molecules onto the A/W interface. The balance of these two opposing forces kept the molecules at the interface. The amphiphiles formed an isolated, essentially two-dimensional (2D) system. The monolayer film formed by amphiphiles was called a Langmuir monolayer. Many small molecules can form Langmuir monolayers on water, such as most fatty acids and phospholipids.

For amphiphilic polymers, hydrogen bonding with water molecules allowed the spreading of macromolecules at the A/W interface. However, the polymer cannot be too hydrophilic or dissolution will occur. Common amphiphilic polymers that formed monolayers at the A/W interface included polyesters such as poly(lactic acid) (PLA) and poly(ε-caprolactone) (PCL), polyethers such as high molar mass poly(ethylene oxide) (PEO), polyvinylesters such as poly(vinylacetate), silicones, comblike copolymers processing long alkyl side chains, amphiphilic block copolymers (AB, ABC, ABA, etc), polyacrylates such as poly(tert-butyl acrylate) (PtBA), polymethacrylates such as poly(tert-butyl methacrylate) (PtBMA) and poly(methyl methacrylate) (PMMA), etc.[9] The common feature for these polymers was the presence of oxygen atoms in the repeat unit, which formed hydrogen bonding with water molecules and stabilized the polymers at the interface. The thermodynamics and phase behavior of amphiphilic polymers at the A/W interface was used as a probe of phase changes of polymers in 2D spatially confined conditions. The A/W interface system offered a unique means for the manipulation of molecules in 2D.

2.2.1. Surface Tension and Surface Pressure. At an air/liquid interface, surface tension arose from unbalanced intermolecular forces. As shown in Figure 2.1 A, bulk molecules experienced balanced forces from neighboring molecules. For interfacial molecules, a net inward force pulled the interfacial molecules to the bulk molecules. When the bulk liquid was incompressible, this force minimized the surface area and was called surface tension. The surface tension was defined as the surface energy per unit area.

$$\gamma = \left(\frac{\partial F}{\partial A}\right)_{T,V,n_i} = \left(\frac{\partial G}{\partial A}\right)_{T,P,n_i} \tag{2-1}$$

where γ is the surface tension, F is the Helmholtz free energy, G is the Gibbs free energy and A is the surface area. Surface tension has units of force per unit length or energy per unit area. The two are equivalent, but the unit of energy per unit area termed surface energy, is applied to solids and liquids more frequently.

The Wilhelmy plate technique depicted in Figure 2.1B was developed and became a common technique for the measurement of liquid surface tensions and surface pressures. In the measurement, a wet thin plate of paper, glass, mica or platinum is dipped into the aqueous subphase. The balance of the different forces that acted on the wet plate yielded an equation for the surface tension:

$$\gamma = \frac{F_{obs} - W}{2(L+t)cos\theta} = \frac{F_{obs} - W}{2L} \tag{2-2}$$

where F_{obs} is the force observed for the plate contact with water, W is the gravitational force that acted on the wet plate, and L and t are the length and width of the plate, respectively, and θ is the contact angle of the subphase with the plate. For perfect wetting, $\theta \approx 0$, and a plate of negligible thickness therefore $2(L + t) \approx 2L$, the simplified expression is valid. In practice, the maximum reading of F_{obs} as the plate is pulled out of the water is used in the calculation so that the upward buoyant force is negligible.

The presence of surface active molecules at the A/W interface decreases the surface tension. The repulsive interaction of the surface active molecules at the interface is defined as surface pressure (Π). At equilibrium, Π is generally considered to be equal to the reduction of the pure liquid surface tension by the film:

$$\Pi = \gamma_0 - \gamma = \frac{F_{obs,0}-F_{obs}}{2(L+t)cos\theta} = \frac{F_{obs}-F_{obs}}{2L} \tag{2-3}$$

where $\gamma_0$is the surface tension for the pure A/W interface and γ is the surface tension of the film covered surface.

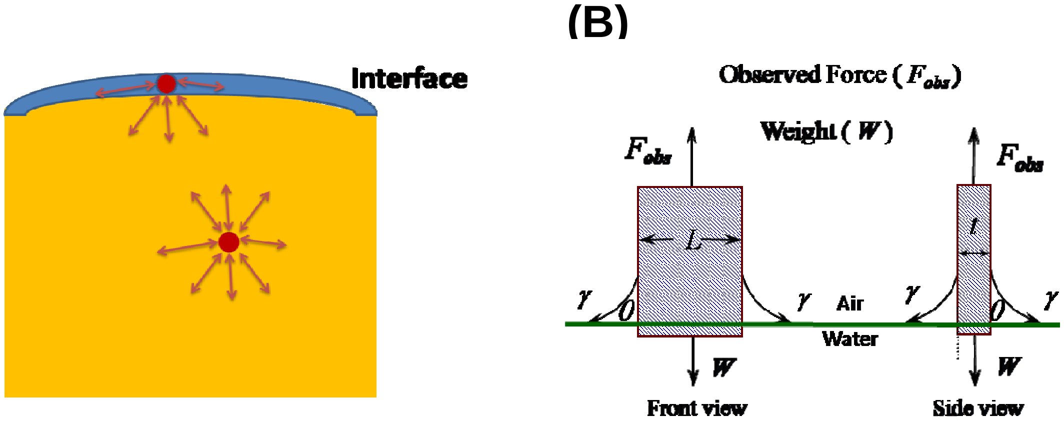

Figure 2.1. (A) Forces on liquid molecules in the bulk and at an interface. (B) A schematic depiction of Wilhelmy plate technique for surface pressure and surface tension measurements and the forces acting on the Wilhelmy plate.

2.2.2. Surface Pressure-Molecular Area (Π–A) Isotherms. Perhaps, the most important quantitative characterization of monolayers at the A/W interface is afforded by surface pressure-molecular area (Π-A) isotherms. For polymeric amphiphiles, area per repeat unit (monomer for short) has been more common.[10] The molecular area is measured and manipulated by a Langmuir trough as depicted in Figure 2.2. An average area (A) is simply defined as

$$Molecular\ Area\ (A) = \frac{Trough\ Area}{Number\ of\ Molecules} \tag{2-4}$$

For polymers, the denominator is the number of monomers. Langmuir troughs are normally made of polytetrafluoroethylene (PTFE), also known as Telfon^{TM}, because PTFE is hydrophobic and chemically inert.[11] A monolayer of amphiphiles is first spread at the A/W surface with the help of a highly volatile spreading solvent such as chloroform, hexane, dichloromethane, etc. Movable barriers then change the surface area occupied by the molecules and hence the surface concentration. Barriers are commonly made of hydrophilic Delrin^{TM}, or PTFE. The Langmuir tough is usually placed on a floating table for the minimization of vibrations and thermostated for the maintenance of constant temperature.

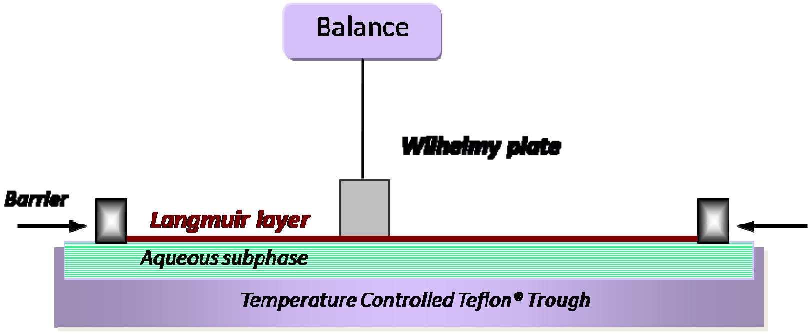

Figure 2.2. The instrumental setup for a Langmuir isotherm trough.

2.2.3. Phases in Langmuir Monolayers. Π-A isotherms for monolayers of insoluble amphiphiles at the A/W interface are analogs of pressure-volume (P-V) isotherms in 3D systems. Monolayers in 2D have exhibited phases that were similar to 3D gas, liquid, and solid in 3D. At low enough Π, the molecules were well separated and exhibited gas like properties, whereby a 2D analog of the ideal gas law can be applied.

$$\Pi A_t = nRT \tag{2-5}$$

where A_t is the total area occupied by the molecules, n is the number of moles, R is the gas constant, and T is the absolute temperature. Equation 2-5 is also expressed in terms of average molecular area:

$$\Pi A = k_B T \tag{2-6}$$

where k_B is Boltzmann's constant. Hence, the 2D compression factor (Z) is:

$$\mathrm{Z} = \frac{\Pi A}{k_B T} \tag{2-7}$$

Z > 1 at high Π reflected repulsive interactions from excluded area (analogous to excluded volume in 3D). For small molecules such as n-alkyl carboxylic acids, the transition from gas to solid phases is more complex than for a corresponding bulk phase. A Π-A isotherm for long alkyl tail carboxylic acids and the corresponding phases is depicted in Figure 2.3. In the gas phase (G), the molecules are well separated from each other and "lie down" at the interface. As the molecules start interacting, part of the molecules lift off the interface and the process corresponds to a gas to liquid transition (L/G). There are two broadly defined liquid phase LE (lipid expanded state) and LC (liquid condensation state). The LE phase is characterized by the highly disordered molecules. The LC phase is found to actually be several different phases.[12] In fact, at least, 4 different monolayer phase characterized by different crystallographic scattering had been found. Hence some researchers had called the LC phase a condensed phase with solid-like character because of the existence of long range order. Whether or not a LE, LC or both phases are present in an isotherm is material dependent. If a material formed a LE and LC phase at a given T, a LC/LE transition is observed. However, LC/LE transition pressures are generally very small or non-existent for most systems. Usually, only gas, liquid and solid phases have been observed in Π–A isotherms, for example, oleic acid only forms a LE phase because of the cis-unsaturation in the long alky chain. In LC phases, the molecules are more closely packed with the tail groups pointing toward the air.[13] In the solid phase (S), the molecules were tightly packed with the molecular axes oriented perpendicular to the interface. Further compression of the monolayer beyond the solid phase leads to the collapse of the monolayer into bilayers or multilayers.

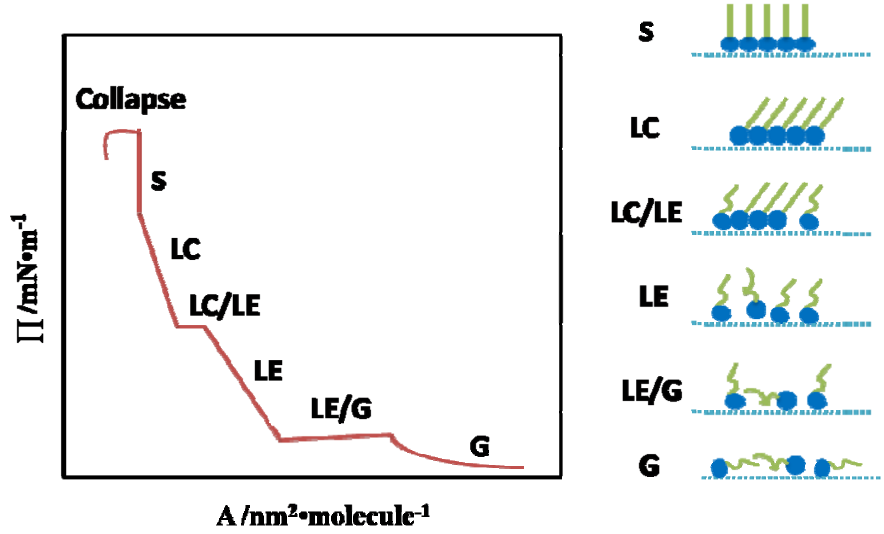

Figure 2.3. A schematic Π-A isotherm for a small amphiphilic molecule. Letters correspond to G (gas), LE (liquid expanded phase), LE/G (coexisting LE and G phases), LC (liquid condensed phase), LE/LC (coexisting LE and LC) and S (solid) phases. The conformations of the molecules in different phase are also depicted schematically.

As shown in Figure 2.3, the conformation and packing density of the molecules changed for different phases. Consequently, the compressibility of the monolayer is also phase dependent. The inverse of the compressibility of the monolayer, an analog to bulk modulus is defined as the 2D lateral modulus, ε_s , which is also called the static dilational elasticity. ε_s is deduced from Π-A isotherms via

$$\varepsilon_s = -A\left(\frac{\partial \Pi}{\partial A}\right)_T \tag{2-8}$$

The monolayer in a more ordered phase will has a higher ε_s. For amphiphilic polymers, the 2D phase diagrams were generally thought to be simpler. Normally, only the gas phase, one liquid phase, and a collapsed state are observed.[14] One notable exception is poly(L-lactic acid) (PLLA), which exhibited a molar mass dependent LE/LC phase coexistence. The LE/LC phase coexistence of the PLLA monolayer is not only observed in the Π−A compression isotherms, but circular LC domains were also observed by BAM because of the refractive index differences between the two phases.[15] Langmuir-Blodgett (LB) transferred films of PLLA prepared from the LC phase revealed a 10_3 helix formed over the entire single PLLA molecule. To date, PLLA has still been the only polymer shown to have complex monolayer phase behavior.

2.2.4. Crystallization in Monolayers at the A/W Interface: Small Molecules to Macromolecules. The crystallization of monolayers at the A/W interface has been observed in many systems from small molecules to large bio-molecules such as proteins. The non-equilibrium growth of condensed phases in Langmuir monolayers has been evaluated for a number of small amphiphilic molecules such as N-dodecylgluconamide,[16] dioctadecylamine (DODA), ethyl palmitate (EP), ethyl stearate (ES),[17]etc.

For natural polymers, protein crystallization within lipid monolayers at the A/W interface was demonstrated.[18] This technique allowed the preparation of protein crystals for X-ray crystallography.[19] For synthetic homopolymers, PCL was the first and at present only reported homopolymer which has clearly undergone crystallization at the A/W interface.[20-21] The monolayer started homogeneous nucleation and growth of crystals around A ~ 40 $Å^2$•monomer^{-1} and the monolayer collapse pressure of Π_C ~ 10-12 mN•m^{-1}. After the onset of the crystallization, a crystal growth plateau was observed in the compression Π-A isotherm. The collapsed monolayer formed ~ 8 nm thick lamellar crystals by a folding-up mechanism of the polymer chains with chain axes oriented perpendicular to the water surface. Upon expansion of the monomer area, the folded up chains melted and respread (dissolved) back to the A/W interface. BAM studies confirmed the disappearance of the PCL crystals. PCL provided a unique model for the study of transformations of 2D polymer chains in the monolayer to 3D conformations in the crystalline state. Subsequently, blends of PCL with medium molar mass polystyrene (PS)[22] and PCL with poly(tert-butyl acrylate) (PtBA)[23] at the A/W interface were reported. The mixed monolayers of PtBA/PCL showed dendritic crystalline morphologies.[23] The diffusion-limited morphologies included dense-branched morphologies, dendrites, and fractal structures that were similar to morphologies observed in a number of thin film crystallization studies.[24-28] The formation of the highly branched morphologies was attributed to the depletion of crystallizable material in the vicinity of the growth front in the ultra thin films when growth rates exceeded diffusion rates through the second phase. As a result, the PCL crystallization at the A/W interface shared similar features with polymer crystallization in thin films on solid substrates. PCL crystallization at the A/W interface provided a convenient framework for the study of polymer crystallization in 2D.

2.3. Polymer Adsorption onto Planar Surfaces from Dilute Solution

Polymer adsorption and desorption at the liquid/solid interface was a fundamental question for many polymer applications and biological processes. In general, the adsorbed chain conformations can be divided into two types as shown in Figure 2.4A and B: One was a flat-on conformation as a result of multiple binding sites with the interface. In this conformation, the adsorbed chains adopted a conformation with loops that extended into the liquid phase as depicted in Figure 2.4A,[29] the second conformation was one where the polymer chain adsorbed onto the surface at one end with the rest of the chain extended into the liquid phase as shown in Figure 2.4B. The reactivity difference for the end group with the substrate affected the adsorption and desorption kinetics. For instance, chemical bonding of the end groups with the surface resulted in irreversible adsorption.

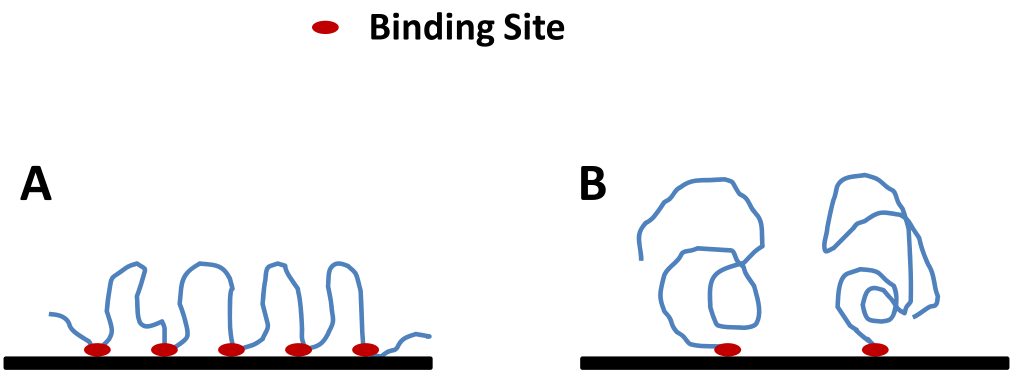

Figure 2.4. Polymer adsorption onto a surface through (A) multiple binding sites and (B) a single end group.

The adsorption and desorption kinetics for these two types of adsorption were different. For the adsorption of high molar mass macromolecules with multiple binding sites, desorption kinetics were typically too small to measure (time scales of hours). The activation energy to peel a chain off all of the binding sites at the same time was so great that the desorption was kinetically blocked. For adsorption, the process was divided into two stages in terms of time scale. In the first stage, the molecules diffused and adsorbed onto the initial surface in a fast step. This was followed by a second step, an aging step, where the adsorbed molecules rearranged (slow conformational change). Although the desorption was negligible, the replacement of the adsorbed polymers by another polymers has been a widely studied subject. The replacement time τ_{off} was the time required for the adsorbed chains to be replaced by another polymer which possessed a greater affinity for the surface. The conformational rearrangement stage in the adsorption process had a profound effect on τ_{off}. The longer the adsorbed layer aged, the greater the τ_{off}.[30] τ_{off} had an exponential relationship with the activation energy (ΔF):[31]

$$\tau_{off} \sim \exp\left(\frac{\Delta F}{k_B T}\right) \sim \exp(\alpha M) \tag{2-9}$$

The activation energy was proportional to the number of binding sites of one molecule which increased linearly with the molar mass (M). As a consequence, the displacement time had an exponential relationship with the molar mass, which was observed in several reported studies.[32-33]

At high temperature, the replacement of the adsorbed chains by other polymers was activation energy dependent. At low temperature, the activation energy (ΔF) no longer controlled the process and τ_{off} was governed by the diffusion flux R(t) of the molecules. The desorption rate at low temperature was given as:

$$\frac{d\Gamma(t)}{dt} = -\mathrm{R(t)}\Gamma(t) \tag{2-10}$$

where $\Gamma(t)$ is the time dependent surface excess, and $\mathrm{R(t)} = (\mathrm{D}/\pi \mathrm{t})^{0.5}$, where D is the diffusion coefficient. The integrated form of the desorption rate is

$$\frac{\Gamma_t}{\Gamma_0} \sim \beta \exp\left(-\frac{t}{\tau_{off}}\right) \tag{2-11}$$

where Γ_0 is the surface excess at t = 0. For adsorption, the integrated adsorption rate is

$$\frac{\Gamma_t}{\Gamma_\infty} \sim 1 - \beta \exp\left(-\frac{t}{\tau_{on}}\right) \tag{2-12}$$

where Γ_∞ is the surface excess at infinite time. For a diffusion controlled process led to $\beta = 0.5$ and for an activation energy controlled process $\beta = 1$.[34]

For reversible adsorption up to monolayers, the Langmuir isotherm is frequently employed. The Langmuir isotherm assumes that the adsorption is limited to a monolayer and is fully reversible, adsorption occurs at a finite number of binding sites, and all binding sites are equal. For the case of adsorption kinetics, the surface excess changes with time according to

$$\frac{d\Gamma}{dt} = k_{ads}C(\Gamma_{max} - \Gamma) - k_{off}\Gamma \tag{2-13}$$

where, k_{ads} is the adsorption rate constant (a function of the activation energy). Γ_{max} is the surface excess for a saturated monolayer, and k_{off} is the desorption rate constant (a measurement of the energy barrier for desorption). In order to obtain k_{ads} and k_{off}, two boundary conditions for the Langmuir isotherm are considered. At the beginning of the adsorption process, the rate of desorption is assumed to be equal to zero. Therefore, the adsorption rate equation becomes:

$$\frac{d\Gamma}{dt} = k_{ads}C(\Gamma_{max} - \Gamma) \tag{2-14}$$

with an integrated form of

$$\ln\frac{\Gamma_{max}}{\Gamma_{max}-\Gamma} = k_{ads}Ct \tag{2-15}$$

According to the Langmuir model, $\ln\frac{\Gamma_{max}}{\Gamma_{max}-\Gamma}$ increases linearly with t at the beginning of the adsorption process. The second boundary condition applies to the initial stage of desorption where the adsorption term is assumed to be zero, hence the kinetics become

$$\frac{d\Gamma}{dt} = -k_{off}\Gamma \tag{2-16}$$

With an integrated form of

$$\ln\frac{\Gamma}{\Gamma_{max}} = -k_{off}t \tag{2-17}$$

Like the integrated form of the adsorption rate, $\ln\frac{\Gamma}{\Gamma_{max}}$ has a linear relationship with time and the desorption constant k_{off} can be deduced from the slope. The adsorption constant k is calculated from the ratio of the adsorption constant to the desorption rate constant.

$$k = \frac{k_{ads}}{k_{off}} \tag{2-18}$$

This k is the same as the equilibrium constant in the classical Langmuir adsorption isotherm:

$$\Gamma = \frac{\Gamma_{\infty}\mathrm{k}\mathrm{C}}{1+kC} \tag{2-19}$$

where Γ_{∞} is the limiting surface concentration at infinite bulk concentration. The linearized form of the Langmuir adsorption isotherm is:

$$\frac{1}{\Gamma} = \frac{1}{\Gamma_{\infty}} + \frac{1}{\Gamma_{\infty}\mathrm{k}\mathrm{C}} \tag{2-20}$$

Therefore, plots of $\frac{1}{\Gamma}$ versus $\frac{1}{C}$ should be linear and Γ_∞ and k can be deduced from the intercept and slope for processes where the Langmuir model is appropriate.

2.4. Diffusive Processes

Diffusive processes are intimately coupled to adsorption/desorption kinetics. The diffusion constants for solutes in a solution are expressed as the rate of transfer, a flux, j, which is defined as the number of solute molecules that pass through a cross-sectional unit area per unit time. j is related to the concentration gradient (c) and diffusion coefficient (D) by Fick's law:[35]

$$j = -D\nabla c \tag{2-21}$$

The minus sign in Equation 2-21 accounts for the solute molecule movement from high concentration to low concentration regions. ∇c is the concentration gradient. Fick's law also yields the diffusion equation

$$\frac{dc}{dt} = -\nabla j = -D\nabla^2 c \tag{2-22}$$

Fick's law also shows that solutes with large diffusion coefficients and higher concentration gradients have greater fluxes.

2.5. Conformations of the Adsorbed Polymer Chains Tethered to a Surface at One End

Two fundamental questions for the adsorption of polymers at the liquid/solid interfaces are the size and conformation of the adsorbed chains. To answer these questions, it is necessary to start from the size of a single polymer random coil in dilute solution, which is closely related to the size of adsorbed polymers at the interface. Theoretical and experimental work have quantatively related the size of a random coil polymer to the nature (rigidity and charge) of the macromolecule, degree of polymerization, and solvent quality (good, poor and theta solvent). Some important theoretical results are surveyed here.

For an ideal freely jointed Gaussian chain, the root mean square end to end distance, the Flory radius (R_F), is related to the degree of polymerization (N) and the length of the monomer (b) as $R_F = bN^{1/2}$. For a real chain in a good solvent, the excluded volume is greater than an ideal chain. Therefore, the excluded volume need to be considered in the calculation for R_F. Flory expressed the free energy of a single polymer chain as a balance between the entropic contribution related to the size of the polymer and repulsions due to excluded volume. The free energy A_{ch} of a single chain is [36]

$$\frac{A_{ch}}{k_B T} \cong \frac{R^2}{Nb^2} + b^3 \frac{N^2}{R^3} \tag{2-23}$$

where the left-hand term on the right side of the equation is the entropic contribution and the right-hand term is the energy from the excluded volume interactions. k_B is the Boltzmann's constant and T is the absolute temperature. These two terms inversely depended on the length of the polymer chain (R). The R that minimizes the free energy is the Flory radius in 3D

$$R_F \cong bN^{3/5} \tag{2-24}$$

In a more general equation for a polymer chain in a good solvent

$${R_F}^{d+2} \cong bN^3 \tag{2-25}$$

where d is the dimension of the system. Accordingly, R_F for a 2D random coil in a good solvent is

$$R_F \cong bN^{3/4} \tag{2-26}$$

Flory's formula is considered to be exact for most applications. The equation for the size in 2D is used to calculate the size of amphiphilic polymers at the A/W interface which is a pseudo 2D system. For a 2D theta solvent, the polymer coils assumed an unperturbed random coil conformation and $R_F = bN^{1/2}$.

On the basis of the scaling approaches already discussed, random coils tethered to a planar surface at one end will adopt one of two conformations. The first is the unperturbed mushroom conformation at low graft density (Figure 2.5). This scenario corresponds to the case where R_F is much smaller than the separation between graft points (D). At low graft densities, each well-separated chain occupies roughly one half of a sphere with a radius comparable to the Flory radius for a coil, Eq. 2-24 for a good solvent.

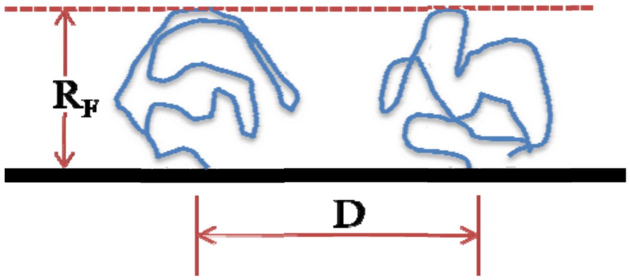

Figure 2.5. The mushroom conformation of a polymer chain tethered at one end with low grafting density in a good solvent.

In an overcrowded situation, $D < R_F$, the adsorbed polymer coils are forced to stretch and form a dense polymer brush as depicted in Figure 2.6. A grafted chain in a brush conformation can be subdivided into "blobs" of linear size D, each containing g_D monomers. Over small distances, the size of the blob (ξ) is equal to D, and obeys the equation for R_F:

$$D = \xi = b g_D{}^{3/5} \tag{2-27}$$

from which the brush thickness L is

$$\mathrm{L} = \mathrm{Nb}\sigma^{1/3} \tag{2-28}$$

where, σ is the graft density of the polymer chains. As seen in Eq. 2-28, L is proportional to the molar mass.

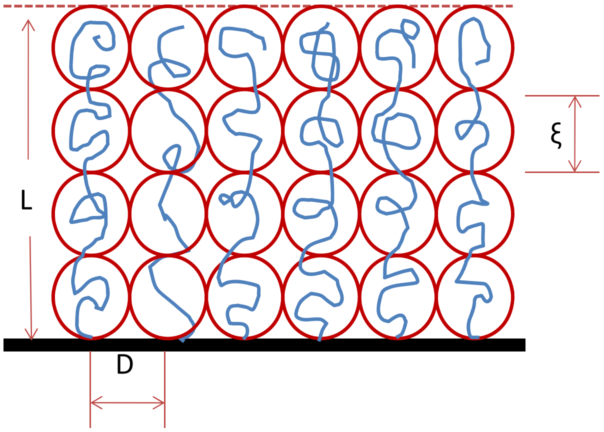

Figure 2.6. A schematic depiction of a strongly stretched grafted layer in a good solvent. The red circles indicate the "blobs" which act as hard spheres and fill space densely.

The closely packed polymers depicted in Figure 2.6, require repulsive lateral intermolecular forces. The elastic force comes from changes of the polymer conformation. If the whole chain is viewed as a spring, the spring constant is given by

$$K_{sp} = \frac{3k_BT}{{R_F}^2} = \frac{3k_BT}{Nb^2} \tag{2-29}$$

The elasticity of the polymer chain can also be viewed from the standpoint of entropy changes associated with changes in the end to end distance of the chain. The entropy of a Gaussian chain can be expressed as a function of the distance of the two ends at r and r'.

$$S = const. + k_B lnG = const. - \frac{3k_B}{Nb^2}(r - r')^2 \tag{2-30}$$

where G is the Gaussian distribution for the end-end distance. The Helmholtz free energy of the chain is:

$$A = const. + \frac{3k_BT}{2Nb^2}(r - r')^2 \tag{2-31}$$

Therefore the force which required for the alteration of the end to end distance (r-r') is:

$$F = \frac{dA}{dr} = \frac{3k_BT}{Nb^2}(r - r') \tag{2-32}$$

The entropy is the origin of the elasticity of a polymer chain. Hence, it is also called entropic elasticity. The entropic elasticity is attributed to rubber elasticity and steric repulsion for colloidal stabilization in solution. The other interesting question is the energy required for a constraint of a random coil polymer in a finite volume as depicted in Figure 2.7, which is similar to the situation when a polymer is confined in a dense brush conformation. The energy (A_{conf}) required to confine the chain is [36]

$$A_{conf} = TN\left(\frac{b}{D}\right)^{5/3} \tag{2-33}$$

This energy barrier act like a steric hindrance for monolayer adsorption of polymeric solutes. Therefore, the adsorption kinetics are different after the densely packed mushroom conformation is formed. Hence, further adsorption at surface concentrations greater than those that led to the mushroom regime are retarded by steric repulsion.[37]

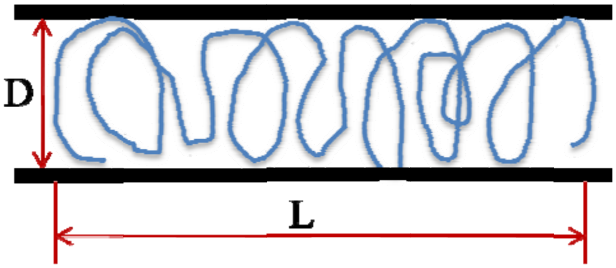

Figure 2.7. The confinement of a polymer chain in a square tube.

2.6. Polymer-Polymer Interactions: From Binary Mixtures to Block Copolymers

The classical lattice model of Flory and Huggins provides a framework for the thermodynamics of mixtures of amorphous polymer.[38] The model for the free energy of mixing(ΔF)for a binary blend consists of an ideal mixing entropy and a polymer-polymer interaction energy:

$$\frac{\Delta F}{k_B T} = \frac{\phi_1}{N_1} ln\phi_1 + \frac{1-\phi_1}{N_2} ln(1-\phi_1) + \phi_1(1-\phi_1)\chi_{12} \tag{2-34}$$

where $\phi_1$is the volume fraction of polymer 1, and N_1 and N_2 are degrees of polymerization for polymer 1 and 2, respectively. χ_{12} , the interaction parameter in Equation 2-34, is defined as

$$\chi_{12} = [\varepsilon_{12} - 1/2(\varepsilon_{11} + \varepsilon_{22})]/k_B T \tag{2-35}$$

where ε_{11}, ε_{22} and ε_{12} are the interaction energies between monomers from polymer 1, monomers from polymer 2, and a monomer from 1 with a monomer from polymer 2, respectively. The first two terms on the right-hand side of Eq. (2-34) are an approximation of the (ideal) combinatorial entropy, and the last term $(\phi_1(1-\phi_1)\chi_{12})$ represents the enthalpy of mixing. χ_{12} is the Flory-Higgins interaction parameter, which assumes that segment-segment interactions can be described entirely in terms of the energy of interaction between chemically different species and is independent of chain length differences between the polymers. The original mathematic form of χ_{12} in Eq. 2-35 captured the energetic penalty associated with breaking pure component segment-segment contacts (ε_{11} and ε_{22}) and forming cross contacts (ε_{12}) in the randomly mixed state. However, this equation is an over-simplification and omitted the excluded volume of the polymer chains which contribute to the entropic part of the χ_{12}. Hence, χ_{12} is found to be more accurately expressed as:[39]

$$\chi = A + B/T \tag{2-36}$$

Here, an excess entropy term (A) and enthalpy term (B) were introduced into the equation.

The phase separation of the two immiscible amorphous polymers results in macrophase separation. For a block copolymer, large length scale phase separation is prohibited by the connection of the two blocks. Consequently, the phase diagrams and phase separation morphologies for block copolymers are different from those of a binary mixture. The physics of microphase separation of block copolymer involve the competition between the interfacial tension between two domains, which normally increases the domain area, and the entropic penalty of stretching the polymers was to maintain a uniform segment density.

The competition sets the domain size and shape. Theoretical and experimental morphological studies agreed that the bulk morphologies of block copolymers are the result of the competition between the overall number of monomers per chain, the volume fraction of each block, and χ_{12}. The microphase separation in block copolymers exhibited an upper critical solution temperature (UCST). The theoretical phase diagrams for block copolymers was first derived by Leibler[40] and a universal phase diagram (Figure 2.8) was established by Matsen and Bates.[41] Such systems contained a single critical point at the symmetric block ϕ_1 = 0.5 which was predicted to scale as

$$(\mathrm{N}\chi_{12})_{\mathrm{c}} = 10.5 \tag{2-37}$$

where $N = N_1 + N_2$. Eq. (2-37) showed that for high molar mass block copolymers, microphase separated morphologies are readily obtained.

Leibler et al.[40] proposed that small angle X-ray and neutron scattering could be used to measure χ at the block copolymer order to disorder transition point. These measurements were later done by Bates and Hartney.[39] The results corrected the original Flory-Huggins χ_{12} expression with an additional entropic term (Eq. 2-36). The experimental results also showed that χ_{12} was dependent upon the composition and the theoretical phase diagram required correction for the polydispersity of the block polymer. Furthermore, the critical point for block copolymer was also shifted slightly from $\phi = 0.5$ due to Kuhn statistical segment length differences between the two blocks.[39]

The phase diagram in Figure 2.8 above was for block copolymers in 3D. In a 2D geometry, the theoretical work excluded intrinsically three-dimensional mesophases such as the cubic bcc and gyroid structures. Only stripes and spherical domains are predicted by self-consistent field theory for the morphologies of the block copolymer on the surface of sphere.[42] However, experimentally, it was difficult to prove the concepts for 2D block copolymer phase diagrams due to the lack of technique for manipulating molecules in 2D without interference from other factors. Interactions with substrates are always present. For instance, polymeric thin films dewet from solid substrates due to lower surface energy of the support substrate.[43] The only system that was close to a 2D system was the A/W interface. At the A/W interface, the amphiphilic polymers are confined to a quasi 2D geometry. However, the A/W was not an ideal solution as the polymer-water interactions will need to be considered in any analysis.

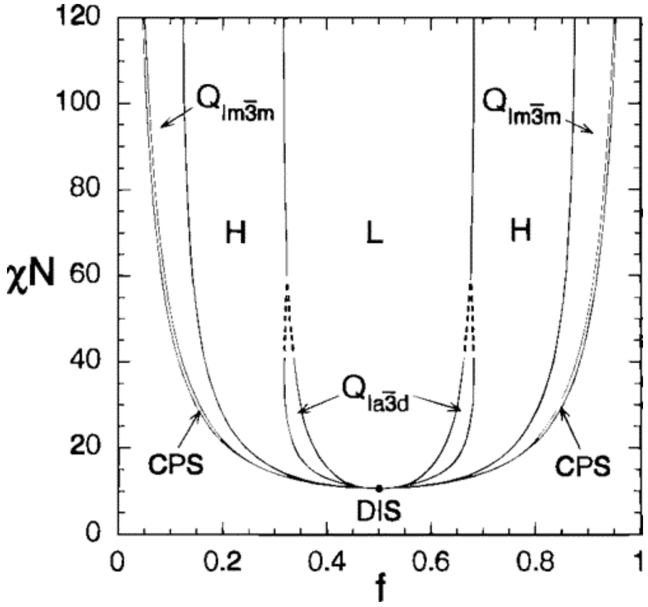

Figure 2.8. The universal phase diagram for block copolymers. Reproduced from Ref. 28 with permission. Copyright 1996, American Chemical Society. Phases are labeled as L (lamellar), H (hexagonal cylinders), $Q_{Ia\bar{3}d}$ (bicontinuous Ia$\bar{3}$d cubic), $Q_{Im\bar{3}m}$ (bcc spheres), CPS (close-packed spheres), and DIS (disordered). Dashed lines denote extrapolated phase boundaries, and the dot at a volume fraction of 0.5 denoted the mean-field critical point.

With the establishment of block copolymer theories, studies of block copolymer thin films quickly followed. The periodic morphologies formed by block copolymers provided a unique way to align and pattern materials of interest on a solid substrate. A recent review by Hamley[44] summarized the current and future perspectives for the research and application of block copolymer thin films. In general, there are three factors that affected the final morphologies of polymer thin films. First, the block copolymer phase diagram was still applicable to the thin films. In addition, the film thickness and polymer-substrate interactions also affected film morphologies. Many studies focused on symmetric block copolymer thin films. In bulk, symmetric diblock copolymers form lamellar microphases. In thin films, for a neutral substrate surface, one with no preferential interactions with either block, the lamellae oriented perpendicular to the substrate. If the surface had a preferential interaction with one block and the film was confined to the substrate, two possible surface morphologies can form depending on the thickness of the film. As illustrated in Figure 2.9 for asymmetric interfaces such as solid/air interface, one layer will preferentially wet the substrate and a uniform film requires a thickness of (n + 1/2)L_0. If the initial film thickness was not equal to (n + 1/2)L_0, islands or holes formed to conserve volume and achieve the (n + 1/2)L_0 for different domains.[45] If the block copolymers are placed in air or sandwiched between two identical substrates, the wetting was symmetric and the film thickness was quantized as nL_0 as shown in Figure 2.9B. The formation of islands at the surface of lamellar block copolymer films was studied using AFM.[46]

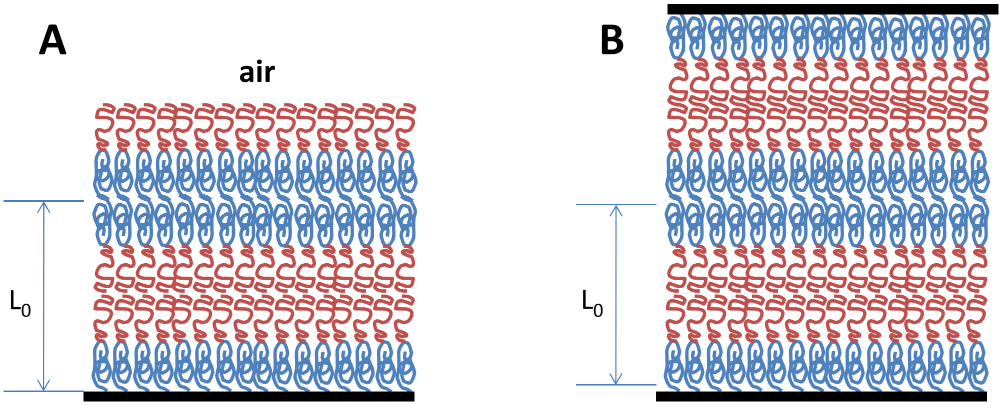

Figure 2.9. (A) Asymmetric wetting and (B) symmetric wetting of the interfaces by block copolymers.

The microphase separation of block copolymers can confine one block to well defined domains such as lamellae. This property was extensively employed for studies of confined crystallization. Results showed that the crystallization of one block did not disrupt the previously existing microphase separated structure.[44] The reported studies usually involved block copolymers where one block was semi-crystalline and the other was amorphous with a glass transition temperature (T_g) above the melting point (T_m) of the semi-crystalline block. The lamellar morphology confined the semi-crystalline block between the two amorphous layers to form a "sandwich" structure. The crystallization of the confined block in the middle layer can be considered as a 1D confined crystallization.[47]

2.7. Lipid Monolayers, Bilayers, and Tethered Lipid Bilayers

Studies of polymer adsorption onto a planer surface, such as interactions of macromolecules such as proteins, peptides or charged polymers with phospholipid bilayers and monolayers has gained increasing attention. Phospholipids are the principal components of the cell membranes (essentially a phospholipid bilayer with lesser amounts of proteins, cholesterol and other lipids) and serve as the main barrier for exchanges of materials between the cell and matrix. In Chapter 6, the interaction of nonionic polymeric surfactants with phospholipid bilayers will be presented. Some background knowledge including the discovery and the fabrication of phospholipid bilayers and morphologies of aggregated surfactants in aqueous phases will be discussed in this section.

2.7.1. Phospholipid Bilayers and Monolayers: An Introduction. The fluid mosaic model for biological membranes was first proposed by Singer-Nicolson in 1972.[48] A key feature of cell membranes was that the lipids remained in a fluid state, but are still highly ordered in the membrane plane. Lateral mobility of the phospholipids was on the order of 1 $\mu m^2 \bullet s^{-1}$; whereas, vertically, lipids crossing the membrane by a flip-flop mechanism occurred only once every few hours.[49] The lateral mobility of lipids in the cell membrane facilitated the movement of membrane proteins. The lipid bilayers are usually viewed as a 2D solvent for proteins. In nature, the slow kinetics associated with phospholipids flipping to the opposite side of the bilayer facilitates the establishment of asymmetric cell membrane compositions which can serve as cell signals for different functions such as cell apoptosis. Natural cell membranes were known to be composed of phospholipid bilayers with asymmetric phospholipid compositions.[50] For example, phosphatidylethanolamine (PE), phosphatidylserine (PS), and phosphatidylinositol (PI) existed overwhelmingly in the cytoplasmic leaflet, whereas phosphatidylcholine (PC) and cholesterol were found relatively equally between both leaflets.[51-52] Due to the lateral mobility of the lipids, phase separation of the cell membrane components was often observed under *in vitro* and *in vivo* conditions.[53] Two different domains were observed in the cell membrane: ordered (L_o) and disordered (L_d) lipid domains. A L_o domain (lipid rafts) was normally a cholesterol and sphingolipid-enriched microdomain within the cell membrane, which had a higher density compared to L_d domains. These L_o microdomains served as organizing centers for the assembly of signaling molecules, influenced membrane fluidity and membrane protein trafficking, and regulated neurotransmission and receptor trafficking.[54] Besides phospholipids and cholesterol, membrane proteins were another important component of the cell membranes. More than half of the known proteins interact with cell membranes. In fact, protein-membrane recognition has remained an important topic for protein research.

Phospholipid monolayers and bilayers prepared from a single phospholipid or mixtures with other cell membrane components such as cholesterol or proteins served as *in vitro* models for studies of cell membrane interactions with adsorbed molecules.[55-56] The ability to deposit lipid bilayers on solid surfaces which are suitable mimics of the cell membrane are important for fundamental research and practical applications. For instance, phospholipid bilayers were used for cell adhesion studies, drug pre-screening, and protein-membrane interactions.[57] These so-called substrate-supported membranes were mainly prepared by two methods: (1) monolayer transfer from Langmuir films[58-59] and (2) vesicle fusion.[60-62] The vesicle fusion method was usually preferred because it was simple and allowed the deposition of membranes with membrane spanning proteins. The formation of lipid bilayers required substrate surfaces with nanoscale smoothness and hydrophilicity. Silica, mica and glass surfaces met these requirements and are frequently used. If a hydrophobic surface was used as the substrate, vesicle fusion yielded a phospholipid monolayer.

2.7.2. Lipid Vesicle Fusion for the Preparation of Phospholipid Bilayers

As depicted in Figure 2.10, exposure of a hydrophilic surface to a lipid vesicle solution causes vesicle adsorption onto the surface. Rupture and subsequent lateral sliding of the phospholipid over the solid surface completes the process. The competition between adhesion energy (F_a)

$$F_a = -WA^* \tag{2-38}$$

where, W and A^* are the effective contact potential and the contact area respectively, and bending energy (F_b)

$$F_b = \left(\frac{k}{2}\right) \oint dA (C_1 + C_2 - C_0)^2 \tag{2-39}$$

where k is the bending rigidity of the membrane, C_1 and C_2 were the two principal curvatures, and C_0 is the spontaneous curvature determined whether the lipid vesicles ruptured and spread to form lipid bilayers or remained in the form of lipid vesicles. The integration in Equation 2-39 is performed over the surface area of the vesicle. F_a favors deformation of the adsorbed vesicle while F_b opposes shape changes. When the adhesion energy between the substrate with the vesicles dominated, planar bilayers resulted via the fusion of the vesicles.[63-64]

For the surfaces with a weak F_a such as TiO_2 and streptavidin, Ca^{2+} ions,[65] high concentration PEG water solution[66] or amphiphilic viral peptides[67] are employed as fusogens which rupture phospholipid vesicles. For charged solid substrates, vesicles of mixed phospholipids with different charged headgroups are also employed as they enhanced interactions with substrates. [65]

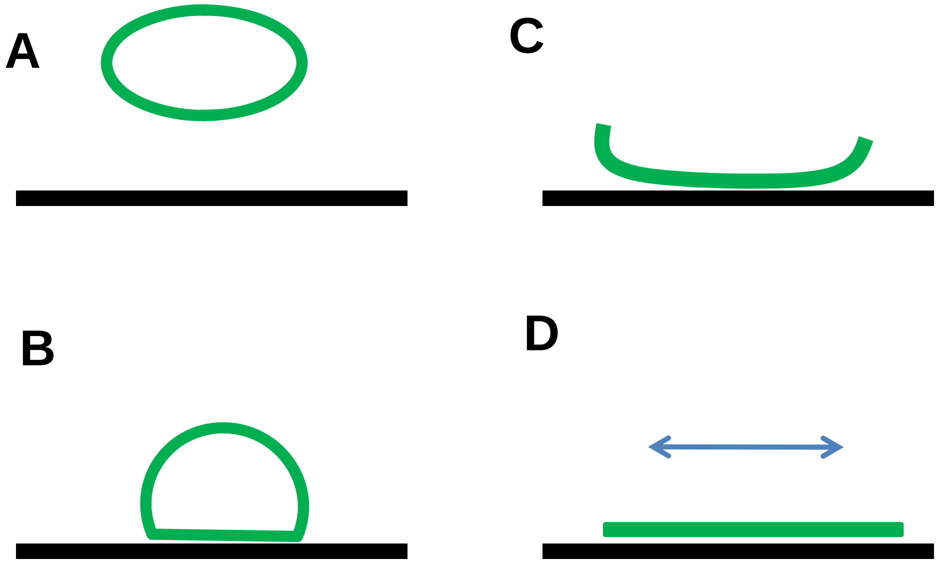

Figure 2.10. Schematic depiction of the formation of a supported membrane by the fusion of lipid vesicles from solution onto a solid surface. Vesicle fusion involves (A) approach, (B) adhesion, (C) rupture, and (D) lateral spreading of the vesicle to form the membrane.

The mechanism and kinetic studies of vesicle fusion were reported by Rädler and Sackmann.[57,68] In their study, the spreading of the phospholipid bilayer membranes and the conditions for the formation of continuous bilayers on rough glass surfaces, and smooth (mica) solids were studied by using reflection interference contrast microscopy. They showed that two fundamentally different spreading mechanisms were possible. The first was the sliding of a single bilayer onto a thin lubricating water film as depicted Figure 2.11A. In contrast, the second was the rolling of thin lobes of two juxtaposed bilayers as depicted in Figure 2.11 B. A general spreading law for velocity of a spreading bilayer on a solid surface was given as:

$$v(t) = (\beta / t)^{1/2} \tag{2-40}$$

where β is the kinetic spreading coefficient. For a perfectly smooth surface such as mica, the rolling velocity of lipid bilayers was given as

$$v_r(t) = \left(\frac{2W_A R_c}{\pi \eta_m d_m t} \right)^{1/2} \tag{2-41}$$

where W_A is the free energy per unit area, R_c is the radius of curvature of the inner monolayer, d_m denotes the bilayer thickness, and η_m is the viscosity of the water film. Theoretical models allowed one to understand the conditions of bilayer sliding or rolling motion. Surfaces that strongly dehydrated the membrane and presumably led to an ultrathin water boundary layer were wetted by a rolling mechanism. In contrast, surfaces that were very hydrophilic and did not dehydrate the membrane possessed a thin water layer between the membrane and the solid surface which allowed the membrane to spread by a sliding mechanism. The lipid bilayers were formed on glass slides through both mechanisms.[57,68]

Figure 2.11. Two different types of spreading of lipid layers onto a solid substrate. (A) A single bilayer formed by sliding with a nearly straight front on a surface. (B) Finger-like lobes of juxtaposed bilayers (rolling motion) on a solid surface.

2.7.3. Preparation of Polymer Cushioned Tethered Phospholipid Bilayers

For bilayers prepared by vesicle fusion, a lubricating water layer (10-20 Å) was present between the hydrophilic planar solid surface and the lipid bilayer. Although, this thin water layer provided fluidity to the lipid bilayer, it made the lipid bilayer less mechanically stable.[58-59] Therefore, the preparation of tethered planar bilayers on organic substrates was also interesting. Stelzle et al.[69] used charged self-assembled monolayer (SAM) surfaces which were oppositely charged relative to the phospholipid head groups that promoted bilayer formation and enhanced adhesion. Spinke et al.[70] on the other hand, used a polymeric SAM with phospholipid analogue side-chains to tether lipid bilayers onto the substrate surface. William et al.[71] reported the use of cholesterol functionalized SAMs to tether lipid bilayers. Cornell's group used an oligomer PEG layer to tether the bilayers which were incorporated with ion-channel switches.[72] However, incorporation of large integral membrane proteins required an aqueous space between the lipid bilayer and the substrate so that the proteins will not contact directly with the surface. As discussed in the Section 2.5, the thickness of the polymer in solution was mainly decided by the molar mass. By selecting a polymer with a desirable size, polymer cushioned phospholipid bilayers provided sufficient space between protein and substrate. Polymer–lipid composite bilayers opened a new perspective for the reconstitution of membrane-spanning proteins.[68,73] Tamm's research group reported a neat method for the preparation of polymer cushioned tethered lipid bilayers through the combination of LB-transfer and lipid vesicle fusion. In their method, a monolayer of lipid was first deposited onto PEG lipid cushions. Sequentially, another layer was fused onto the pre-formed monolayer by vesicle fusion. The PEG lipids had a lipid moiety which can insert into the lipid bilayer and tether the bilayer.[74]

2.7.4. Polymer Interactions with Phospholipid Bilayers. Polymeric surfactants have aroused interest for biomedical applications. Polyethylene oxide (PEO) has been used extensively in the biomedical and pharmaceutical arenas due to its aqueous and organic solubility, non-toxicity, and sheathing ability.[75-79] PEGylation of peptides and proteins has grown in interest as a mechanism for the enhancement of the therapeutic and biotechnological effects.[80] The conjugation of lipid molecules with PEGs (PEG lipids) increased the blood circulation times of therapeutic liposomes loaded with cancer drugs by the incorporation of the lipid moiety into the vesicle lipid membranes.[81-82] Besides the auxiliary functions for drug delivery, PEG surfactants had beneficial bio-functions. Pluronic surfactants, a central hydrophobic block of poly(propylene oxide) and two peripheral hydrophilic blocks of poly(ethylene oxide), not only inhibited the adsorption of proteins and bacterials;[83-89] but also inhibited drug efflux transporters, drug sequestration for cancer treatment [90,91]

A detailed understanding of the interactions between surfactants and lipid membranes has been deemed essential for improved application of polymeric surfactants. Due to the complexity of natural cell membranes, phospholipid bilayers are usually employable as model membranes for quantitative *in vitro* studies. Previous studies showed that charged polymers that were oppositely charged relative to the lipid head groups were destructive to the membrane.[98] A more recent result[92] showed that the addition of a hydrophobic moiety to a hydrophilic chain enhanced the interaction of the hydrophilic polymers with the phospholipid bilayers and the size of the hydrophobic tail played an important role.[93] However, reviews and summaries regarding the interactions and kinetics of surfactants with lipid bilayers were lacking.

2.8. Surfactant Aggregates in Aqueous Systems

In general, surfactants are composed of a hydrophilic head group and a hydrophobic tail group. For small molecules, the headgroup is usually charged. In very dilute conditions, below the critical aggregation concentration (CAC), the surfactant molecules exist as single isolated molecules. For concentrations in excess of the CAC, surfactants assemble to form different aggregates in which the non-polar tails are shielded from water by the polar head groups. The size and shape of the aggregates were correlated with the surfactant parameter, N_s.[94]

$$N_s = \frac{v}{la_0} \approx \frac{c_0}{a_0} \tag{2-42}$$

where v is the volume for the hydrophobic portion of the surfactants**;** l is the length of the hydrocarbon chains, a_0 is the effective area of the hydrophilic head groups, and c_0 is the cross-sectional area of the hydrophobic tail groups. Therefore, N_s is the area ratio of the hydrophobic group to the hydrophilic head group. Small N_s implies highly curved aggregates such as micelles. When the value of N_s is close to unity, planar bilayers usually form. One good example is the formation of planar bilayers by phospholipids. A simple relationship for the formation of spheres, cylinders and planar bilayers exists between the volume, area, and radius (thickness). The surfactant number indicates optimal aggregates are

Spherical micelles ($N_s = 0.33$)

Infinite cylinders ($N_s = 0.5$)

Planer bilayers ($N_s = 1$)

Inverted cylinders and micelles ($N_s > 1$)

For N_s between 0.33 and 0.5 or 0.5 and 1.0, highly, symmetrically shaped aggregates or phase separation can occur. The surfactant number only roughly predicted the shape of the aggregates. For $N_s \approx 1$, parts of the bilayers closed back on themselves and formed vesicles. The formation of liposomes by phospholipids in water is one example.

Amphiphilic block copolymers in water can also self-assemble into various ordered mesophases. Discher at al.[95] reported the formation of the large block copolymer vesicles (polymersomes) by the self-assembly of poly(ethylene oxide)-b-poly(ethylethylene) (EO_{40}-b-E_{37}) in aqueous conditions. Zhang et al.[96] reported that for highly asymmetric polystyrene-poly-(acrylic acid) block copolymers prepared in a low molar mass solvent system, four different morphologies of spheres, rods, lamellae, and vesicles were observed in aqueous solution depending on solution conditions. A more systematic study by Jain et al.[97] showed that as the PEO block length gradually increased, the aggregate morphologies changed from vesicles, to Y conjunction cylinders, cylinders and spheres. Compared to liposomes formed by phospholipids, the polymersomes were tougher and less permeable.

2.9. Experimental Techniques

In this section, the key experimental techniques that were used in this thesis are introduced.

2.9.1. Quartz Crystal Microbalance with Dissipation Monitoring (QCM-D). A quartz crystal microbalance (QCM) measures a mass per unit area by measuring the change in frequency of a quartz crystal resonator. A QCM can be used in vacuum, in gas phases and more recently in liquid environments. Frequency measurements are easily made to high precision and surface mass densities down to a level below 1 $\mu g \bullet cm^{-2}$ have been obtained. In addition to frequency, the dissipation can also be obtained and used to analyze viscoelastic properties of the adsorbed layer. The dissipation factor (D) is defined as[98-99]

$$D = \frac{E_d}{2\pi E_s} \tag{2-44}$$

where E_d is the energy dissipated during one oscillation, and E_s is the energy stored in the oscillating system. The dissipation is a parameter quantifying the energy damping potential of the system. After the discovery that the QCM can also operate in water, the over damping from the viscous layer and the liquid to the vibration of the quartz crystal become an obstacle to extract the exact mass of the adsorbed layer from QCM. Nonetheless, QCMs have evolved into a powerful technique for studies of aqueous systems.

2.9.2. Principles of QCM. A QCM utilizes the piezoelectric properties of quartz crystals. The ability of a material to generate an electric field or electric potential in response to applied mechanical stress and vice versa is piezoelectricity. The QCM consists of a thin piezoelectric plate with electrodes on both sides as depicted in Figure 2.12A. The application of alternating current to the quartz crystal induces oscillations of the plate and a standing shear wave can be generated with a properly cut crystal. Common equipment allows resolution down to 1 Hz on crystals with a fundamental resonant frequency in the 4 – 6 MHz range. When a quartz crystal is excited to oscillate at its fundamental resonant frequency, a small layer adds to the electrodes and induces a decrease in the resonant frequency change (Δf) which is linearly proportional to the mass (Δm) of the layer. If the added layer is rigid, evenly distributed, and much thinner than the crystal, Δf is linearly proportional to Δm as predicted by the Sauerbrey equation:[100]

$$\Delta m = -C\frac{\Delta f}{n} \tag{2-43}$$

where C = 17.7 ng•cm^{-2}•Hz^{-1}, a constant that is specific to the physical properties of the crystal materials .($\Delta f/n$) is the scaled frequency change, and n is the overtone number.

In vacuum and rigid film conditions, the scaled frequency changes ($\Delta f/n$) from different overtones overlap in accordance with the Sauerbrey equation. However, the dissipation (D) of energy over-damped the vibration of the crystal and Δf for different n differed because different overtones sense different depths of the surrounding liquid medium. The higher overtones had a higher energy, and consequently penetrated deeper into the liquid layer. Consequently, the Sauerbrey equation was invalid under these conditions. In fact, it was a major obstacle for the application of QCM in liquids. Therefore, a new method of measurement and processing of the signals obtained in liquid environment was required if correct masses and viscoelastic properties were to be obtained. By the mid 1980's, two methods arrived. One was the modification of the oscillator circuit, the other was a passive determination of the resonance frequency with a network analyzer.[101] The network analyzer measured the electrical impedance of the device as a function of frequency without resorting to amplification of the oscillation (Figure 2.12B).[102] The resonance frequency was fit with resonance curves. An alternative ring-down method for the network analyzer was also provided, in which, the driving power of a piezoelectric oscillator was switched periodically on and off and the decay of the voltage displacement was monitored with time (Figure 2.12C).[103] These two methods yielded the resonance bandwidth in addition to Δf. The latter method was the basis for the QCM-D technique. The shift in bandwidth was proportional to the amount of energy transferred from the crystal to the sample and liquid phase per unit time. The half-bandwidth at half-maximum (bandwidth, for short) (Γ) was used to quantify such processes. Qualitatively, dissipation values (D) were equal to the bandwidth over the frequency ($\mathrm{D} = \frac{2\Gamma}{f}$). Users of QCM-D, often display their results in terms of the frequency and dissipation.

2.9.3. Data Modeling. The generic results obtained from QCM-D were the frequency changes (Δf) and the dissipation value changes (ΔD) for different overtones (n). For small ΔD ($<\sim 5 \times 10^{-6}$), Eq. 2-43 was valid and analysis was simple. More generally, accurate mass and viscoelastic information about adsorbed layers required modeling. Most commercial QCM-D instruments now have software package that support Voigt-based viscoelastic modeling. However, even this modeling required the assumption of no-slip boundary conditions for the adsorbed layer.[104]

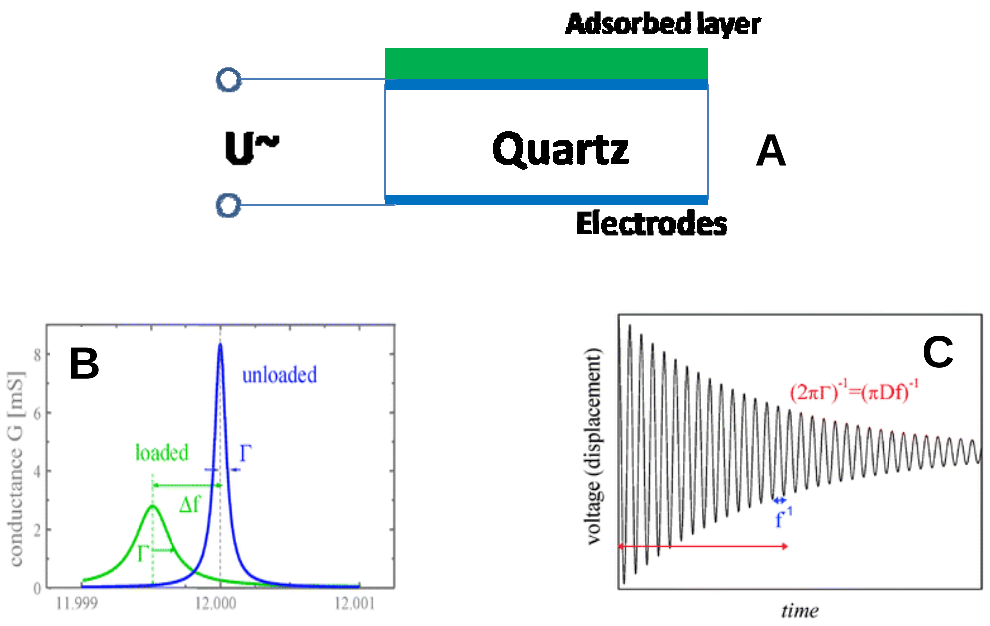

Figure 2.12. Key features of QCM: (A) the instrumental setup for a QCM sensor and (B) a QCM impedance analysis result. The central parameters of the measurement are the resonance frequency, *f*, and the bandwidth, 2*Γ*. (C) Ring-down yields the equivalent information for time-domain measurements. Images were reproduced from Ref. 110 with permission. Copyright 2008 RSC Publishing.

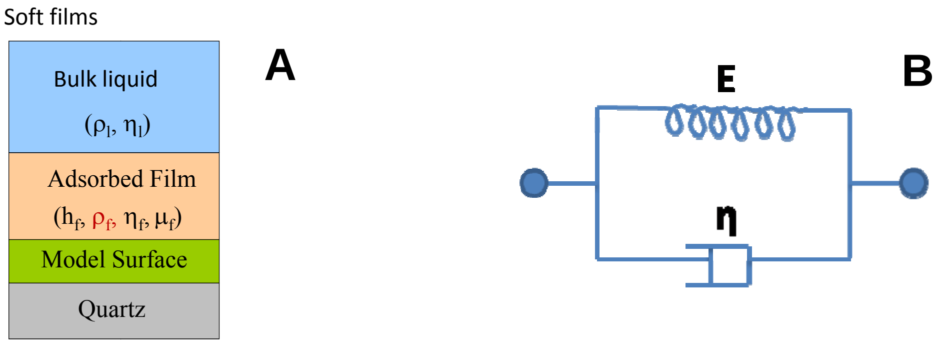

Figure 2.13. (A) Geometry of a QCM crystal surface covered by a model layer and a viscoelastic layer. (B) A schematic depiction of the equivalent electrical circuit for the Voigt model.

Under the assumption that a homogenous adsorbed layer of uniform thickness was surrounded by a semi-infinite Newtonian fluid under no-slip boundary conditions, the complex shear modulus (G) of the adsorbed layer is described as:

$$G = G^{'} + G" = \mu_i + i2\pi f\eta_f = \mu_i(1 + i2\pi f\tau_i) \tag{2-45}$$

where G' is the storage modulus, $G^{''}$is the loss modulus, μ_i is the elastic shear modulus, η_f is the shear viscosity, f is the oscillation frequency, and τ_i is the characteristic relaxation time of the film. The changes of frequency (Δ*f*) and dissipation (Δ*D*) for the surface in Figure 2.13 A are

$$\Delta f = Im(\frac{\beta}{2\pi l_q\rho_q}) \tag{2-46}$$

$$\Delta D = -R_e(\frac{\beta}{\pi f l_q\rho_q}) \tag{2-47}$$

where

$$\beta = \xi_1 \frac{2\pi f\eta_1 - i\mu_f}{2\pi f}\left(\frac{1-\alpha\exp(2\xi_1 h_1)}{1+\alpha\exp(2\xi_1 h_1)}\right) \tag{2-48}$$

$$\alpha = \frac{\left(\frac{\xi_1}{\xi_2}\right)\frac{2\pi f\eta_f - i\mu_f}{2\pi f\eta_f}+1}{\left(\frac{\xi_1}{\xi_2}\right)\frac{2\pi f\eta_f - i\mu_f}{2\pi f\eta_f}-1} \tag{2-49}$$

$$\xi_1 = \sqrt{-\frac{(2\pi f)^2\rho_f}{\mu_f + i2f\eta_f}} \tag{2-50}$$

$$\xi_2 = \sqrt{i\frac{2\pi f\rho_1}{\eta_1}} \tag{2-51}$$

and ρ_1 and h_f are the density and thickness of the adsorbed film, respectively. The software package of the QCM-D (Q-Sense Sweden) includes the Voigt model, Maxwell model, and other models. For the fully hydrated film, the Voigt model was usually used for modeling with the assumption that the adsorbed layer has a density equal to water and a viscosity equal to water at the designated temperature. For good modeling, the simulated curves overlap the experimental results.

2.9.4. Atomic Force Microscopy (AFM)

Atomic force microscopy (AFM), also known as scanning probe microscopy (SPM) was developed as a high-resolution imaging technique that can resolve features as small as atomic lattices.[105] The instrumental setup of AFM is depicted in Figure 2.14. Typical AFM instruments consist of a cantilever with a sharp tip (probe) at its end that actually scans the surface of the specimen. The cantilevers are typically silicon or silicon nitride with a tip radius of curvature on the order of nanometers. The surface forces that act on the AFM tip bend the cantilever according to Hooke's law. The forces arise from mechanical contact, van der Waals forces, capillary forces, chemical bonding, electrostatic forces, magnetic forces, etc. Deflection of the cantilever is measured by an optical approach. Laser light from a solid state diode is reflected from the back of the cantilever and collected by a photodetector comprised of two photodiodes. The signal from the photodiodes is collected by an amplifier and processed. The feedback controller also adjusts the piezoelectric tube (PZT) which is located beneath the sample, to adjust the sample-to-tip distance or to maintain a constant force between the tip and sample. The PZT moves the sample in the Z direction and maintains a constant force, while the X and Y directions are scanned. The resulting map of the area represents the topography of the sample.

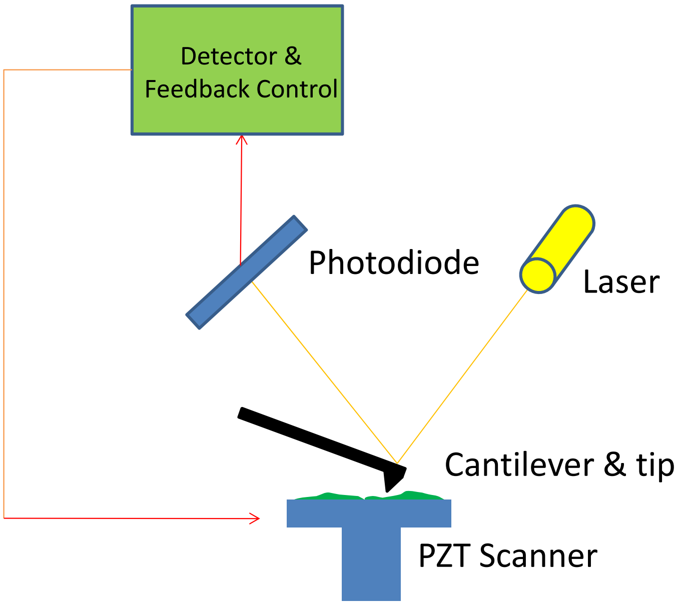

Figure 2.14. A schematic depiction of an AFM instrument.

In general, AFM has been done in contact mode, non-contact mode and tapping mode.[106] The three operational modes are depicted in Figure 2.15. In the contact mode (Figure 2.15 A), the tip directly contacts the sample surface through a thin adsorbed fluid layer during imaging. The contact mode operation takes place in ambient and liquid environments. The contact mode gives high resolution, however, sample damage for soft samples due to a strong tracking force can also occur. Therefore, it is usually used to measure tough and rough surfaces. In the non-contact mode (Figure 2.15B), the tip hovers ~5-10 nm over the sample surface and senses the van der Waals attractive forces between the tip and the surface. A large area can be imaged at a fast scan rate in this mode. However, the weak tip–sample interaction usually results in low resolution. In tapping mode AFM (Figure 2.15C), The cantilever is oscillated at or near its resonant frequency with a constant amplitude that ranges from ~20 to ~100 nm at ~50 to ~500 kHz. The tip briefly touches the surface and lifted off. The tip-sample interaction is kept constant by maintaining constant oscillation amplitude. The oscillation amplitude is used as a feedback signal to gain topographical information about the surface. Phase imaging is an extension of the tapping mode that provides information about material properties such as adhesion, viscoelasticity, and hardness. In phase imaging, the phase lag between the cantilever and the drive oscillation is monitored and this information produces a phase image of an x-y surface. AFM in tapping mode has been commonly used for the characterization of soft samples such as polymers as the contact mode may cause damage to soft polymeric materials and non-contact mode usually did not provide images with sufficient resolution.

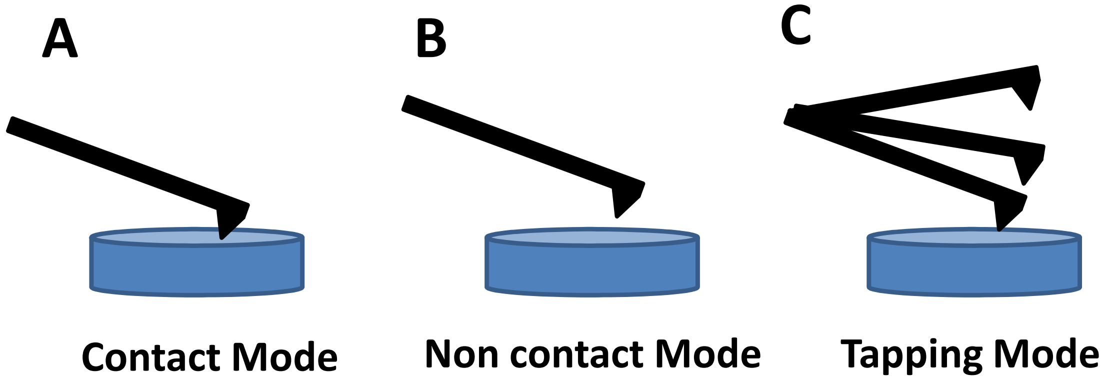

Figure 2.15. AFM operational modes: (A) contact mode (B) non-contact mode, and (C) tapping mode.

AFM instruments have measured forces from 3 pN to several nN with a dynamic range ≥ 10 μs.[107] Of all of the techniques used in single-molecule force spectroscopy, AFM has been the one that readily allowed the measurements of nN forces with pN precision.[108] This feature made AFM suitable for the investigation of chemical-binding forces, which were on the order of nN.[109,110] AFM can also be used for measurements of colloidal interactions with planar surfaces.[111,112-114] Other AFM instruments, ones which probed specific chemical and physical interactions, have also been developed. For instance, magnetic force microscopy (MFM) was used for the imaging of magnetic field gradients and the distribution of magnetic domains.[115-123]

2.9.5. Dynamic Light Scattering (DLS). Dynamic light scattering (DLS) has evolved as one of the standard techniques for size measurements of colloidal suspensions. The fundamentals of the measurement are based on the interference of the light scattered by the solutes in Brownian motion in solution. When light interacts with small particles (small compared to the wavelength of the light), the light scatters in all directions. If the light source is a monochromatic, coherent laser, time-dependent fluctuations of the scattering intensity are observed. Due to the constant and random motion of the solutes (Brownian motion), the re-emitted scattered light has a time dependent phase and undergoes either constructive or destructive interference. An autocorrelation function, a mathematical model, is used to extract information from the time dependent fluctuation of the scattering intensity. The scattering intensity autocorrelation function:

$$\langle I(t)I(t+\tau)\rangle = \lim_{T\to\infty}\frac{1}{T}\int_0^T I(t)I(t+\tau)dt \tag{2-52}$$

accounts for the average production of two scattering intensities $I(t)$ and $I(t+\tau)$ measured at two different times separated by the time interval τ over a long period of time T. The scattering intensity $I(t)$ fluctuates around an average value $\langle I\rangle$; therefore, it is convenient to write:

$$\langle I(t)\rangle = \langle I\rangle + \Delta I(t) \tag{2-53}$$

By the assumption of **Ergodicity**, the intensity autocorrelation function is given as

$$\frac{\langle I(t)I(t+\tau)\rangle}{\langle I\rangle^2} = 1 + \frac{\langle \Delta I(t)\Delta I(t+\tau)\rangle}{\langle I\rangle^2} = 1 + f g_2(\tau) \tag{2-54}$$

$$f = 1 + \frac{\langle \Delta I^2\rangle}{\langle I\rangle^2} \tag{2-55}$$

$$g_2(\tau) = \frac{\langle \Delta I(t)\Delta I(t+\tau)\rangle}{\langle \Delta I^2\rangle} \tag{2-56}$$

where f is the coherence factor which is a property of the instrument and $g_2(\tau)$ is the baseline-subtracted, normalized intensity autocorrelation function. $g_2(\tau)$ decays to 1 as τ

→ ∞. The electric-field autocorrelation function which is generated by the DLS instrument is defined as

$$g_1(\tau) = \frac{\langle E_s(t)E_s(t+\tau)\rangle}{\langle E_s(t)^2\rangle} \tag{2-57}$$

where, E_s is the electric field function for the light wave vector. The auto-correlation function $g_2(\tau)$ is related to $g_1(\tau)$ by

$$g_2(\tau) = |g_1(\tau)|^2 \tag{2-58}$$

The correlation functions are used for the determination of how long a given signal is correlated in terms of a correlation time τ. $g_1(\tau)$ is a first-order correlation function for the decay time and has an exponential relationship with decay time. For a monodisperse sample, it has a single exponential decay:

$$g_1(t) = e^{-\Gamma t} \tag{2-59}$$

where Γ is the decay rate, the inverse of τ. For a polydisperse sample, a cumulant expansion of the average decay rate equation is normally applied:[124-126]

$$g_1(t) = e^{A-\bar{\Gamma}t+\frac{\mu_2}{2}t^2-\frac{\mu_3}{6}t^3} \tag{2-60}$$

where A is a constant, $\bar{\Gamma}$ is the average decay rate, and $\mu_2$and μ_3 account for the decay rate distribution. The polydispersity is defined as

$$PDI = \frac{\mu_2}{\bar{\Gamma}^2} \tag{2-61}$$

The decay rate Γ is proportional to the square of the scattering wave vector (q):

$$\Gamma = D_m q^2 \tag{2-62}$$

where D_m is the mutual diffusion coefficient. The scattering wave vector, q, is defined as

$$q = \frac{4\pi n}{\lambda} sin\frac{\theta}{2} \tag{2-63}$$

where, n is the refractive index of the solvent, λ is the wavelength of the laser, and θ is the scattering angle. When PDI < 0.1, the sample is considered to be monodisperse.[127] The hydrodynamic radii are then deduced from the Stoke-Einstein relationship:

$$R_h = \frac{k_B T}{6\pi\eta_0 D_0} \tag{2-64}$$

where k_B is the Boltzmann's constant, T is the absolute temperature, and η_0 is the viscosity of the solvent. D_0 is the diffusion coefficient of the sphere. In a dilute solution, $D_m \approx D_0$.

CONTIN analyses have also frequently used and implemented in commercial DLS instruments. For a polydisperse sample, the measured $|g_1(t)|$ is the superposition of $\exp(-\Gamma\tau)$ terms with different values of Γ

$$|g_1(t)| = \int G(\Gamma)\exp(\Gamma\tau)\, d\Gamma = \int \Gamma G(\Gamma)\exp(\Gamma\tau)\, dln\Gamma \tag{2-65}$$

where $G(\Gamma)$ is the contribution of the each Γ and $\int G(\Gamma)d\Gamma = 1$. Since, the photodetector detects the light intensity, $G(\Gamma)$ is the scattering intensity distribution. As seen in Eq. 2-65, $|g_1(t)|$ is the Laplace transform of $G(\Gamma)$. Thus, a simple estimation of the size distribution is the inverse-Laplace transform of a graph of $\ln(|g_1(t)|)$ versus τ to yield the $\Gamma G(\Gamma)$ versus $ln\Gamma$ as shown in Figure 2.16.

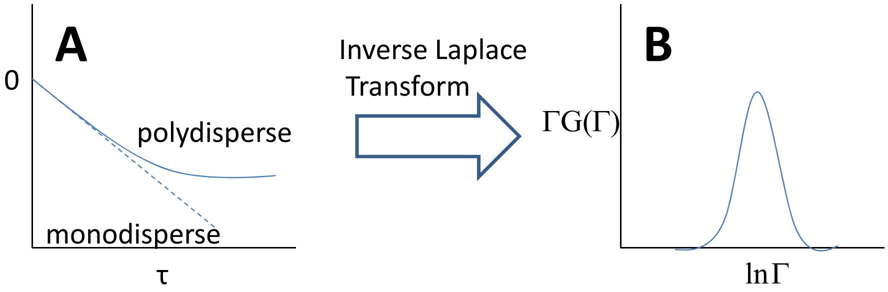

Figure 2.16. A schematic depiction of an inverse Laplace transformation of DLS data. (A) The polydispersity of the samples cause $\ln|g_1(\tau)|$ to deviate from a straight line. (B) The inverse Laplace transform of $\ln|g_1(\tau)|$ gives the intensity distribution as a function of $\ln\Gamma$. The graph was adapted from Ref. 133.

Generic DLS results are usually given as $\Gamma G(\Gamma)$ versus $ln\tau$ and can be converted to a plot of $\Gamma G(\Gamma)$ versus R_h or lnR_h as an intensity weighted size distribution. Compared to the cumulant method, CONTIN is handier; however, the results obtained from these two methods are consistent.

2.9.6. Brewster Angle Microscopy (BAM). Since 1990, Brewster angle microscopy (BAM) has frequently been combined with Langmuir or Langmuir-Blodgett studies for *in-situ* morphological characterization of Langmuir films.[128-129] As a non-invasive tool, BAM was used extensively in this thesis. Here, the key features of BAM are discussed.

2.9.6.1. Principle for BAM. When polarized light from an incident medium with lower refractive index (n_1) encounters an interface with a medium of a higher refractive index (n_2), the reflectivity (R) depends on the incident angle θ_i and the angle of polarization. If the electric field vector of the light lies in (or parallel to) the plane of incidence, it is called p-polarized light. Light which is polarized perpendicular to the plane of incidence is defined as s-polarized. According to Fresnel's law, the reflectivity of p-polarized (R_p) and s-polarized (R_s) light can be written as

$$R_p = \left(\frac{n_1 cos\theta_t - n_2 cos\theta_i}{n_1 cos\theta_t - n_2 cos\theta_i}\right)^2 = \frac{tan^2(\theta_i - \theta_t)}{tan^2(\theta_i + \theta_t)} \tag{2-66}$$

$$R_s = \left(\frac{n_1 cos\theta_i - n_2 cos\theta_t}{n_1 cos\theta_i - n_2 cos\theta_t}\right)^2 = \frac{sin^2(\theta_t - \theta_i)}{sin^2(\theta_i + \theta_t)} \tag{2-67}$$

where subscripts p and s represent p- and s-polarization, respectively, and θ_i and θ_t are the angle of incidence and refraction respectively. Meanwhile, Snell's law allows θ_t to be replaced by θ_i

$$n_t sin\theta_t = n_i sin\theta_i \tag{2-68}$$

Equations 2-66 to 2-68 allowed Figure 2.17 to be generated where R_p and R_s were plotted as a function of the incident angle.

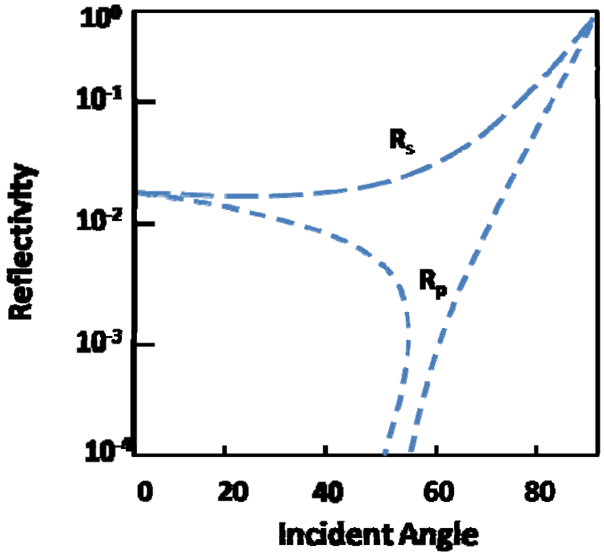

Figure 2.17. R_p and R_s as a function of incident angle.

As seen in Figure 2.17, a sharp decrease of R_p to a minimum is observed, when $\theta_i + \theta_t = 90°$. The incident angle at that minimum of R_p is defined as Brewster's angle θ_B. According to Snell's law,:

$$tan\theta_B = \frac{n_2}{n_1} \quad (2\text{-}69)$$

At θ_B, p-polarized light reflected form the interface is minimized. For water, $\theta_B = 53.1°$. The presence of a thin film at the A/W interface with a different n than water, cause an increase in reflected light intensity at θ_B for water. In principle, the refractive index (n(z)) is a function of position from the interface (z), however, an approximation of an isotropic average n is made. Drude derived the reflectivity of p-polarized light at Brewster's angle: [130]

$$R_p(\theta_B) = R_s(\theta_B)\overline{\rho_B}^2 \quad (2\text{-}70)$$

where $R_s(\theta_B)$ is the reflectivity for the s-polarized light at Brewster's angle and $\overline{\rho_B}$ is the ellipticity:[131]

$$\overline{\rho_B} = \frac{\pi}{\lambda}\frac{\sqrt{n_1^2+n_2^2}}{n_1^2-n_2^2}\int_{-\infty}^{+\infty}\frac{[n(z)^2-n_1^2][n(z)^2-n_2^2]}{n(z)^2}dz \quad (2\text{-}71)$$

where λ is the wavelength of the incident light. This treatment accounts for the fact that n(z) varies for different phases and different materials as well as thickness. The higher $\overline{\rho_B}$, the brighter the image.

The principle instrumental features of BAM are depicted in Figure 2.18. For the instrumental setup, the incident angle for p-polarized incident laser is set at Brewster's angle for water. A black plate is placed under the water at the point of reflection. The black plate reduces background signal from the refracted light that will otherwise scatter from the Teflon trough. In the absence of a film, essentially no p-polarized light is reflected from the interface and residual s-polarized is removed by the p-polarizer. Hence, the image captured by the CCD camera is black. When a film was present at the A/W interface, the refractive index and thickness of the film lead to a measurable intensity, which allows visualization of micron-scale changes in film morphology. [132-133] BAM studies of morphology have provided information about regarding molecular orientation, phase transitions and other aggregate formation such as the collapse of monolayers.[134]

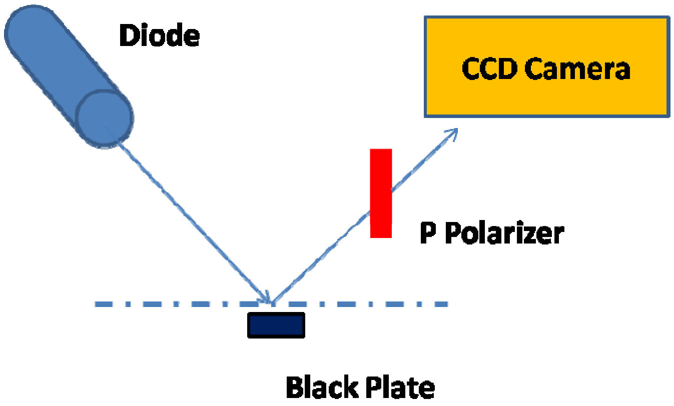

Figure 2.18. A schematic depiction of BAM. The BAM instrument used in this thesis consists of a p-polarized diode laser source, a p-polarizer, a CCD camera, and a black plate.

2.9.7. Langmuir-Blodgett (LB) and Langmuir-Schaefer (LS) Technology. Although, Π−A isotherms plus BAM provide a wealth of information regarding the sizes of molecules and intermolecular interactions, more detailed information still requires analysis techniques with greater resolution such as AFM or transmission electron microscopy (TEM). The Langmuir-Blodgett technology allows monolayer and/or multilayers to be transferred onto a solid substrate. The setup for the LB-transfer trough is similar to a traditional Langmuir trough except for a dipping well in the center of the trough that allows the vertical movement of solid substrates through the interface. A motor is attached to the LB-trough with a dipping head above the dipping well.[135] Sometimes, LB-troughs integrate BAM so that LB-transfer coincides with features of interest. There are three different types of LB-film deposition: X-, Y- and Z-type.[136] For molecules that undergo Y-type deposition, a hydrophobic solid substrate is lowered through the monolayer into the subphase so that one molecular layer adsorbs onto the substrate with its hydrophobic tails attached to the substrate. The substrate is then withdrawn from the subphase and picks up another layer with its hydrophilic heads attaching to the existing layer. Continuous up- or downstrokes allow multilayer films with head-to-head and tail-to-tail configurations to be formed at the constant Π and A. In order to maintain constant conditions during deposition, the surface pressure Π is kept constant by movable barriers and a feedback loop. The final configuration has the hydrophobic tails pointing toward air. If a hydrophilic substrate is used, the first layer is transferred as the substrate move up from the subphase with the hydrophilic head groups attached to the surface. In contrast, Z-type films only transfer on the upstrokes with a hydrophilic substrate, while X-type films only transfer on the downstrokes with hydrophobic substrates. A rotational dipper is needed for the X and Z type transfer. For X- and Z- type transfer, the LB-films ideally have the head to tail connections. However, X and Z type conformations are unstable and easily undergo structural rearrangement. The configurations of the multilayers of different modes are shown in Figure 2.19.

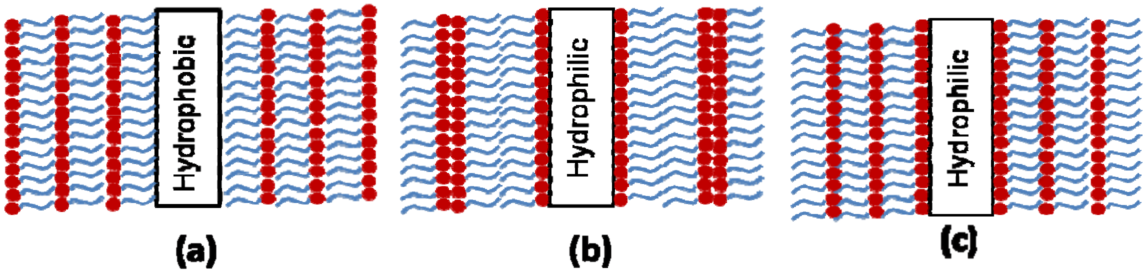

Figure 2.19. Structures of LB-multilayers: (a) X-, (b) Y-, and (c) Z-type.

One measure of the quality of LB-deposition is the transfer ratio [137]

$$\delta = \frac{A_L}{A_S} \tag{2-72}$$

which is the ratio of area of monolayer removed from the substrate of water (A_L) to the substrate area passed through the monolayer (A_S). A_L can be easily measured by maintaining a constant Π, while the area of substrate is measured prior to deposition. A transfer ratio close to unity indicates good LB-transfer in most cases and the orientation of molecules on solid substrates is expected to be similar to their orientation on the A/W interface. Deviation of the transfer ratio from unity suggests a poorly transferred film in most cases.

Another technique for the preparation of multilayers from the A/W interface, depicted in Figure 2.20, is known as the horizontal lifting method or Langmuir-Schaefer (LS) technique.[68] During LS-transfer, the hydrophobic substrate is placed parallel to the monolayer film. After contact, the hydrophobic substrate is lifted and separated from the water surface slowly. The process ideally transfers a monolayer onto the substrate. High-quality, X-type multilayers had been reported by the LS-technique; however, rearrangement is possible during the lifting process that leads to Y-type structures. As the ideal LS-films have the hydrophilic head groups pointing toward air; rearrangement of the LS-film with time is also possible. In practice, the LB-technique is a much gentler method compared to LS-transfer. Therefore, this thesis used the LB-technique for the transfer of the lamellar crystals onto solid substrates.

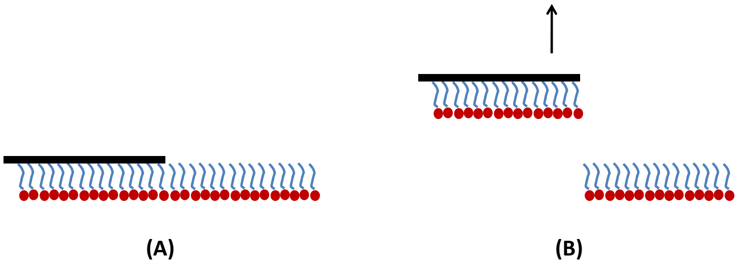

Figure 2.20. Deposition of LB-multilayers by the LS-technique. (A) Placement of a hydrophobic solid substrate onto the pre-formed monolayer. (B) Slow lifting of the substrate from the water surface.

2.10. Living Polymerization Techniques and Magnetic Nanoparticle Synthesis

The systems of interest in this thesis were PCL block copolymers and PCL magnetic nanoparticles (MNPs). The preparation of these materials employed two living polymerization techniques, ring opening polymerization and atom transfer radical polymerization (ATRP). The polymerization techniques and the method for the preparation of MNPs are reviewed here.

2.10.1. Ring Opening Polymerization of ε-Caprolactone (CL). The polymerization of CL was co-initiated by a primary amine or alcohol with tin(II) octoate ($Sn(Oct)_2$) which is the most commonly used initiator for the ring opening polymerization of cyclic esters.[138] The polymerization mechanism involves the insertion of the CL monomer into the tin-oxygen bond.[139] For initiation with a primary amine, the reaction of the primary $-NH_2$ with CL is preceded by a carboxylate-imide group exchange at the tin atom in $Sn(Oct)_2$, and is accompanied by a release of octanoic acid (OctH). The polymerization proceeds via CL monomer insertion at -Sn-NH- bond with formation of the $-Sn-O-(CH_2)_5C(O)-NH-$ species.

Finally, an exchange reaction with OctH results in -NH[C(O)(CH$_2$)$_5$]OH, or the polymerization continues with the insertion of the monomers into the Sn-O- bond.[140] A tertiary amine or alcohol can not initiate the polymerization because of the steric hindrance.

2.10.2. Atom Transfer Radical Polymerization (ATRP). In order to have stable polymerization kinetics with time and narrow molar mass distributions, the polymerization reaction needs to be initiated quickly with slow propagation. Traditional free radical polymerizations usually have very fast initiation and fast propagation. At the same time, termination through end to end coupling occurs near the end of the reaction and thus yields broad molar mass distributions. As shown in the Scheme 2.1, the ATRP method utilizes a transition metal ligand complex that deactivates the free radicals which form quickly during initiation of the reaction. The reactivation of the dormant species allows the polymer to grow again, only to be deactivated later. Such a process results in a polymer chain that grows slowly and steadily with a well-defined end group. The overall reaction rate is determined by a balance between the activation and deactivation rate constants, $K = \frac{k_{act}}{k_{deact}}$. The polymerization can tolerate traces of impurities and oxygen. It can even be carried out in aqueous solutions. By using ATRP, the design and fabrication of multifunction with controlled architectures can be achieved in an easier fashion relative to other living polymerization techniques which require very rigorous treatments for the monomer and polymerization conditions.

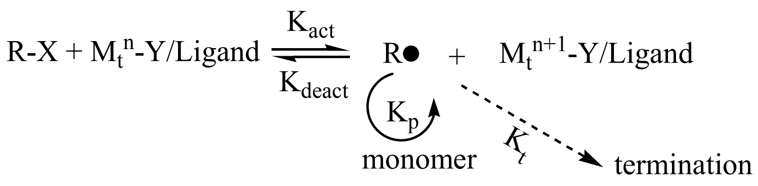

Scheme 2.1. The mechanism of ATRP adapted from Ref. 141.

Another recently developed free radical controlled polymerization is reversible addition–fragmentation chain transfer (RAFT). RAFT is a living radical polymerization, and uses thiocarbonylthio compounds, such as dithioesters, dithiocarbamates, trithiocarbonates, and xanthates for mediation of the polymerization via a reversible chain-transfer process. This technique allows access to polymers with low polydispersity indices and high degrees of functionality. Compared to RAFT, ATRP is easier to handle in a polymer physical laboratory and a good PDI can be achieved. In this thesis, the ATRP method was used for the preparation of PCL block copolymers. As shown in the Scheme 2.2, the PCL macro-initiator was prepared by ring opening polymerization of the CL monomer from a hydroxyl group of a bi-functional initiator. The second block was attached by ATRP.

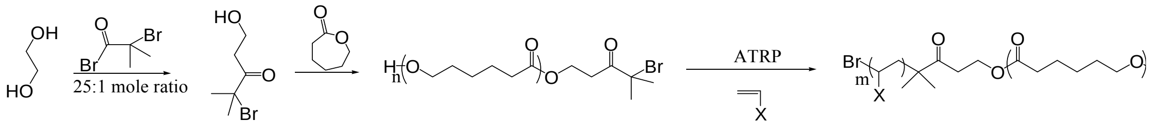

Scheme 2.2. The combination of CL ring opening polymerization and ATRP for the preparation of PCL block copolymers.

2.10.3. Preparation of Magnetic Particles with Uniform Sizes. Iron oxide magnetic nanoparticles (MNPs) have been prepared by two principle methods, aqueous co-precipitation and colloidal chemical synthesis. In the co-precipitation method, the MNPs are prepared by the aqueous co-precipitation of $FeCl_3$ and $FeCl_2$ under alkaline conditions. This method usually requires a size-selection procedure to decrease the particle size distribution. For this reason, the aqueous co-precipitation method has made relatively little progress toward small (< 20 nm) monodisperse nanoparticles. In contrast, the colloidal chemical synthesis method uses organic solution-phase decomposition of an iron precursor at high temperatures. It efficiently circumvents the broad distribution of MNPs produced by aqueous co-precipitation. These approaches involve either the rapid injection of reagents into hot surfactant solutions followed by aging at high temperature, or the mixing of reagents at a low temperature and slow heating under controlled conditions. Sun et al.[142] reported monodisperse Fe_3O_4 nanoparticles with controllable sizes that ranged from 3-20 nm by high temperature reactions of iron (III) acetylacetonate in the presence of dodecanediol, oleic acid, and oleylamine. Sun's group[143] later reported that the iron salt decomposed and formed iron oxide nanoparticles at high temperature, and the dodecanediol was unnecessary for the reduction of the iron salt. Consequently, the method was further simplified and became cheaper. By this method, the particle diameter can be tuned by variation of the reaction conditions. At the beginning of my thesis work, different sizes of magnetic nanoparticles were prepared according to Sun's method. The size of the nanoparticle can increase by using the synthesized particles as seeds for the growth of larger particles. As shown in Figure 2.21, the size of the MNPs can be controlled over the range of 5 to 20 nm with relatively narrow size distributions. The weight percentage for the oleic acid and oleylamine ligands decreased with increasing the nanoparticle diameters according to thermogravimetric analysis (TGA). Within this diameter range, the testing of magnetic properties showed that the Fe_3O_4 MNPs were super-paramagnetic at room temperature.

Various other reported methods for the preparation of monodisperse nanoparticles are reviewed below. The growth rates of the different crystal faces differ for different ligands. By using this property, anisotropic magnetic nanoparticles were achieved.[144-146] Two representative synthetic procedures are described here. In the first synthetic procedure, the rapid injection of organometallic reagents into hot surfactant solutions induced the simultaneous formation of multiple nuclei.[147] Alternatively, reducing agents were added to metal salt solutions at high temperature. In the second procedure, reagents were mixed at low temperature and the resulting reaction mixtures were slowly heated in a controlled manner that generated nuclei. Subsequently, particle growth occurs by the addition of reactive species. The growth of nanoparticles can be stopped by quenching the solution. Nanoparticles produced using these synthetic procedures often had particle size distributions with standard deviations of σ ~ 10%. The most frequently applied method that yielded narrow distributions involved the addition of a poor solvent to precipitate the larger particles.[148] Narrow particle size distributions were prepared through reverse micelles, which were water-in-oil droplets stabilized by a monolayer of surfactant. This approach was applied as nanoscale reactors for the synthesis of various nanoparticles.[149,150] The successes in synthesizing monodisperse MNPs triggered further research into the properties of MNPs. For examples, self-assembled two-dimensional or three-dimensional monodisperse MNPs formed super lattices (colloidal crystals) that attracted considerable interest as organized magnetic media. These systems are expected to achieve magnetic recording densities between 100 Gb/in.^{2} and 1 Tb/in.^{2}[151, 152-156] Monodisperse MNPs also provided interesting materials for potential biological applications. Jun et al.[157] showed that monodisperse MNPs can be used for cancer diagnosis by enhancing magnetic resonance (MRI) imaging signals.

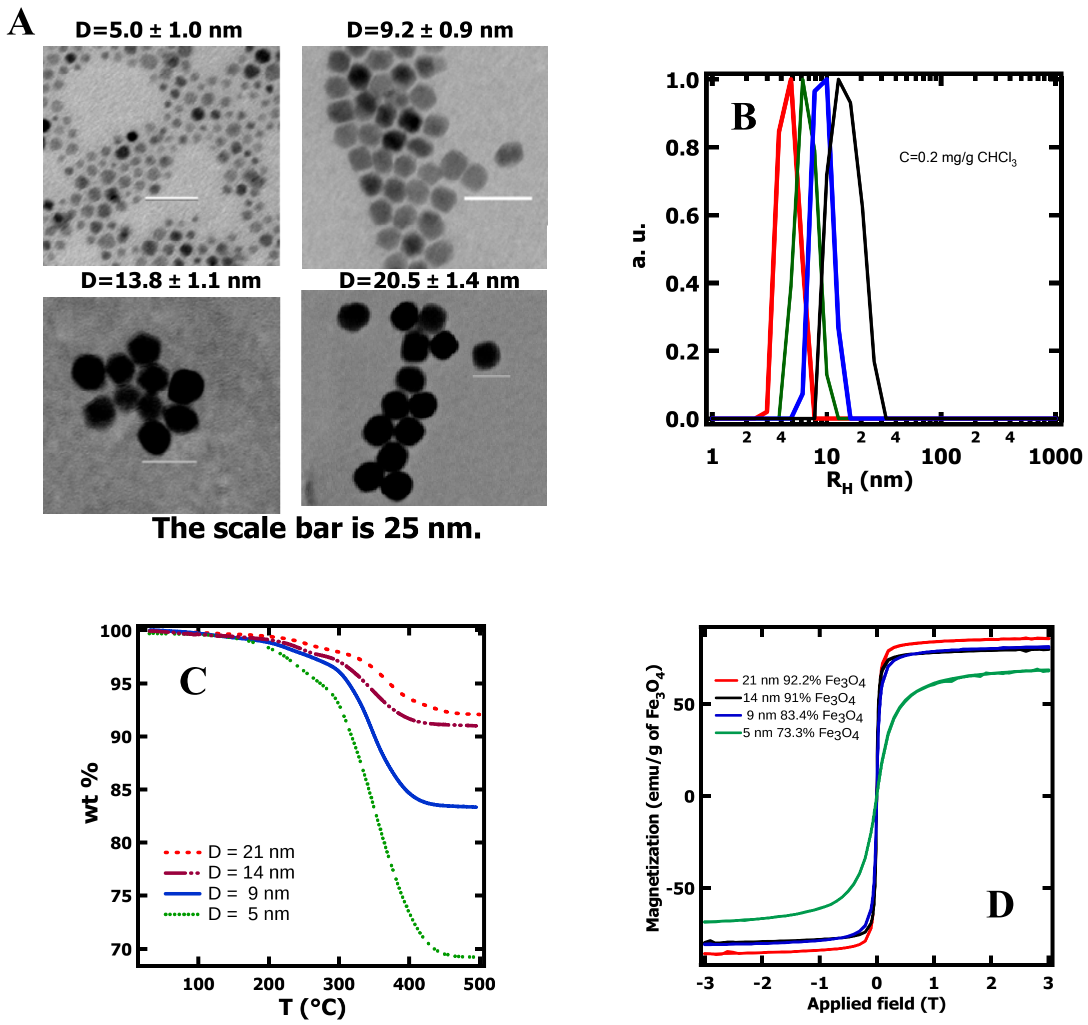

Figure 2.21. (A) TEM and (B) DLS characterization of MNPs prepared by colloidal chemical methods and (C) TGA and (D) magnetization tests for the synthesized MNPs at room temperature.

2.11. References

(1) Whitmore, M. D.; Nooland, J. *Macromolecules* **1985**, *18*, 2486.

(2) Harris, J. M.; Chess, R. B. *Nat. Rev. Drug Discovery* **2003**, *2*, 214.

(3) Segalman, R. A. *Mater Sci Eng R: Reports* **2005**, *48*, 191.

(4) Karabıyık, U. PhD, Virginia Tech, 2008.

(5) Franklin, B. *Phil. Trans.* **1774**, *64*, 445.

(6) Pockels, A. *Nature* **1891**, *43*, 437.

(7) Langmuir, I. *J. Am. Chem. Soc.* **1917**, *39*, 1848.

(8) Langmuir, I. *Trans. Faraday Soc.* **1920**, *15*, 62.

(9) Ni, S. L. PhD, Virginia Tech, 2006.

(10) Yee, C.; Kataby, G.; Ulman, A.; Prozorov, T.; White, H.; King, A.; Rafailovich, M.; Sokolov, J.; Gedanken, A. *Langmuir* **1999**, *15*, 7111.

(11) Fox, H. W.; Zisman, W. A. *Rev. Sci. Instrum.* **1948**, *19*, 274.

(12) Pershan, P. S. *Structure of Liquid Crystal Phase*; World Scientific: Singapore, 1998.

(13) Heimenz, P. C. *Principles of Colloidal and Surface Chemistry*; 2 nd ed.; New York, 1986.

(14) Esker, A. R., PhD, University of Wisconsin, 1996.

(15) Ni, S.; Lee, W.; Li, B.; Esker, A. R. *Langmuir* **2006**, *22*, 3672.

(16) Vollhardt, D.; Gutberlet, T.; Emrich, G.; Fuhrhop, J. H. *Langmuir* **1995**, *11*, 2661.

(17) Flores, A.; Corvera-Poiré, E.; Garza, C.; Castillo, R. *J. Phys. Chem. B* **2006**, *110*, 4824.

(18) Blankenburg, R.; Meller, P.; Ringsdorf, H.; Salesse, C. *Biochemistry* **1989**, *28*, 8214.

(19) Azadani, A. N.; Lopez, J. M.; Hirsa, A. H. *Langmuir* **2007**, *23*, 5227.

(20) Li, B.; Esker, A. R. *Langmuir* **2007**, *23*, 2546.

(21) Li, B.; Wu, Y.; Liu, M.; Esker, A. R. *Langmuir* **2006**, *22*, 4902.

(22) Li, B.; Esker, A. R. *Langmuir* **2007**, *33*, 574.

(23) Li, B.; Marand, H.; Esker, A. R. *J Polym Sci Part B: Polym Phys* **2007**, *45*, 3300.

(24) Mareau, V. H.; Prud'homme, R. E. *Macromolecules* **2002**, *35*, 5338.

(25) Mareau, V. H.; Prud'homme, R. E. *Macromolecules* **2003**, *36*, 675.

(26) Mareau, V. H.; Prud'homme, R. E. *Macromolecules* **2005**, *38*, 398.

(27) Mareau, V. H.; Prud'homme, R. E. *Polymer* **2005**, *46*, 7255.

(28) Reiter, G.; Sommer, J.-U. *Phys. Rev. Lett.* **1998**, *80*, 3771.

(29) Kaya, A.; Du, X.; Liu, Z.; Lu, J. W.; Morris, J. R.; Glasser, W. G.; Heinze, T.; Esker, A. R. *Biomacromolecules* **2009**, *10*, 2451.

(30) Frantz, P.; Granick, S. *Phys. Rev. Lett.* **1991**, *66*, 899.

(31) Johnson, H. E.; Granick, S. *Macromolecules* **1990**, *23*, 3367.

(32) Douglas, J. F. *Macromolecules* **1989**, *22*, 3707.

(33) Frantz, P.; Granick, S. *Phys. Rev. Lett.* **1990**, *66*, 899.

(34) Douglas, J. F.; Johnson, H. E.; Granick, S. *Science* **1993**, *262*, 2010.

(35) Brogioli, D.; Vailati, A. *Phys. Rev. E* **2001**, *63*, 12105.

(36) de Gennes, P. G. *Scaling Concepts in Polymer Physics*; Cornell University Press: Ithaca, N.Y., 1979.

(37) Huang, H.; Rankin, S. E.; Penn, L. S. *Langmuir* **2004**, *20*, 5770.

(38) Flory, P. J. *Principles of Polymer Chemistry*; Cornell Univ. Press, Ithaca, NY, 1971.

(39) Bates, F. S.; Hartney, M. A. *Macromolecules* **1985**, *18*, 2478.

(40) Leibler, L. *Macromolecules* **1980**, *13*, 1602.

(41) Matsen, M. W.; Bates, F. S. *Macromolecules* **1996**, *29*, 1091.

(42) Li, J. F.; Fan, J.; Zhang, H. D.; Qiu, F.; Tang, P.; Yanga, Y. L. *Eur. Phys. J. E* **2006**, *20*, 449.

(43) cois Drolet, F.; Fredrickson, G. H. *Phys. Rev. Lett.* **1999**, *83*, 4318.

(44) Hamley, I. W. *Progress in Polymer Science* **2009**, *34*, 1161.

(45) Ausserré, D.; Chatenay, D.; Coulon, G.; Collin, R. *J. Phys. Fr.* **1990**, *51*, 2571.

(46) Maaloum, M.; Ausserre, D.; Chatenay, D.; Coulon, G.; Gallot, Y. *Phys. Rev. Lett.* **1992**, *68*, 1575.

(47) Huang, P.; Zhu, L.; Guo, Y.; Ge, Q.; Jing, A. J.; Chen, W. Y.; Quirk, R. P.; Cheng, S. Z. D.; Thomas, E. L.; Lotz, B. B. S.; Carlos, H. A. A.; Sics, I. *Macromolecules* **2004**, *37*, 3689.

(48) Singer, S. J.; Nicolson, G. L. *Science* **1972**, *175*, 720.

(49) Saxton, M. J.; Jacobson, K. *Annu. Rev. Biophys. Biomol. Struct.* **1997**, *26*, 373.

(50) Kiessling, V., Crane, J. M., Tamm, L. K. *Biophys. J.* **2006**, *91*, 3313.

(51) Devaux, P. F. *Biochemistry* **1991**, *30*, 1163.

(52) Quinn, P. J. *Biochemistry* **2002**, *36*, 39.

(53) Fan, J.; Sammalkorpi, M.; Haataja, M. *Phys. Rev. Lett.* **2008**, *100*, 178102.

(54) Kai, S.; Ehehalt, R. *J. Clin. Invest.* **2002**, *110*, 597.

(55) Discher, D. E.; Eisenberg, A. *Science* **2002**, *297,* 967.

(56) Lipowsky, R.; Sackmann, E. *Structure and Dynamics of Membranes*; Elsevier, New York, 1995.

(57) Rädler, J.; Strey, H.; Sackmann, E. *Langmuir* **1995**, *11*, 4548.

(58) Merkel, R.; Sackmann, E. *J. Phys. Fr.* **1989**, *50*, 1535.

(59) Tamm, L. K.; McConnell, H. M. *Biophys. J.* **1985**, *47*, 105.

(60) Karb, E.; Frey, S.; Tamm, L. K. *Biochim. Biophys. Acta* **1992**, *1103*.

(61) Czaja, C.; Jekutsch, G.; Rothenhausler, B.; Gaub, H. E. *Biosensors*; VCH: Weinheim, New York, 1987.

(62) Bayerl, T. M.; Bloom, M. *Biophys. J.* **1990**, *58*, 357.

(63) Seifert, U.; Lipowsky, R. *Phys. Rev. A* **1990** *42*, 4768.

(64) Reviakine, I.; Brisson, A. *Langmuir* **2000**, *16*, 1806.

(65) Rossetti, F. F.; Bally, M.; Michel, R.; Textor, M.; Reviakine, I. *Langmuir* **2005**, *21*, 6443.

(66) Proux-Delrouyre, V.; Elie, C.; Laval, J.; Moiroux, J.; Bourdillon, C. *Langmuir* **2002**, *18*, 3263.

(67) Cho, N. J.; Cho, S. J.; Cheong, K. H.; Glenn, J. S.; Frank, C. W. *J. Am. Chem. Soc.* **2007**, *129*, 10050.

(68) Sackmann, E. *Science* **1996**, *271*, 43.

(69) Stelzle, M.; Weissmuller, G.; Sackmann, E. *J. Phys. Chem* **1993**, *97*, 2974.

(70) Spinke, J.; Yang, J.; Wolf, H.; Liley, M.; Ringsdorf, H.; Knoll, W. *Biophys. J.* **1992**, *63*, 1667.

(71) Williams, L. M.; Evans, S. D.; Flynn, T. M.; Marsh, A.; Knowles, P. F.; Bushby, R. J.; Boden, N. *Langmuir* **1997** *13,*, 751.

(72) Cornell, B. A.; Braach-Maksvytis, V. L. B.; King, L. G.; Osman, P. D. J.; Raguse, B.; Wieczorek, L.; Pace, R. J. *Nature* **1997**, *387*, 580.

(73) Elender, G.; Sackmann, E. *J. Phys. Fr.* **1994**, *4*, 455.

(74) Wagner, M. L.; Tamm, L. K. *Biophys. J.* **2000**, *79*, 1400.

(75) Harris, L. G., J.; Carmichael, A.; Riffle, J.; Harburn, J.; St. Pierre, T.; Saunders, M. *Chem. Mater.* **2003**, *15*, 1367.

(76) Holmberg, K. T., F.; Malmsten, M.; Brink, C. *Colloids Surf., A:* **1997**, *123-124*, 3168.

(77) Kingshott, P. Wei, J.; Bagge-Ravn, D.; Gadegaard, N.; Gram, L. *Langmuir* **2003**, *19*, 6912.

(78) Li, C.; Yu, D.; Yang, D.; Milas, L.; Hunter, N.; Kim, E.; Wallace, S. *Anticancer Drugs* **1996**, *7*, 642.

(79) Mai-ngam, K. *Colloids Surf., B* **2006**, *49*, 117.

(80) Veronese, F. M. *Biomaterials* **2001**, *22*, 417.

(81) Lasic, D.; Marin, F. J.; Gabizon, A.; Huang, S. K.; Papahadjopoulos, D. *Biochim.Biophys. Acta* **1991**, *1070*, 187.

(82) Papahadjopoulos, D.; Allen, T.; Gabizon, A.; Mayhew, E.; Matthay, K.; Huang, S.; Lee, K.; Woodle, M.; Lasic, D.; Redemann, C.; Martin, F. *Proc. Natl. Acad. Sci. USA* **1991**, *88*, 11460.

(83) Amiji, M.; Park, K. *Biomaterials* **1992**, *13*, 682.

(84) Bridgett, M. J.; Davies, M. C.; Denyer, S. P. *Biomaterials* **1992**, *13*, 411.

(85) Freij-Larsson, C.; Nylander, T.; Jannasch, P.; Wesslen, B. *Biomaterials* **1996**, *17*, 2199.

(86) Marsh, L. H.; Coke, M.; Dettmar, P. W.; Ewen, R. J.; Havler, M.; Nevell, T. G.; Smart, J. D.; Smith, J. R.; Tmimins, B.; Tsibouklis, J.; Alexander, C. *J. Biomed. Mater. Res., Part A* **2002**, *61*, 641.

(87) Nejadnik, M. R.; van der Mei, H. C.; Norde, W.; Busscher, H. J. *Biomaterials* **2008**, *29*, 4117.

(88) Norde, W.; Gage, D. *Langmuir* **2004**, *20*, 4162.

(89) Schroen, C. G. P. H.; Cohen Stuart, M. A.; van der Padt, A.; van der Voort Maarschalk, K.; van't Riet, K. *Langmuir* **1995**, *11*, 3068.

(90) Batrakova, E. V.; Kabanov, A. V. *J. Controlled Release* **2008**, *130*, 98.

(91) Sriadibhatla, S.; Yang, Z.; Gebhart, C.; Alakhov, V. Y.; Kabanov, A. *Molecular Therapy* **2006**, *13*, 804.

(92) Liu, G.; Fu, L.; Zhang, G. *J. Phys. Chem. B* **2009**, *113*, 3365.

(93) Firestone, M. A.; Seifert, S. *Biomacromolecules* **2005**, *6*, 2678.

(94) Evans, D. F.; Wennerström, H. *The Colloidal Domain Where Physcs,*

Chemistry, Biology, and Technology Meet; second ed.; Wiley-VCH, 1999.

(95) Discher, B. M.; Won, Y. Y.; Ege, D. S.; Lee, J. C. M.; Bates, F. S.; Discher, D. E.; Hammer, D. A. *Science* **1999**, *284*, 1143

(96) Zhang, L.; Eisenberg, A. *Science* **1995**, *268*, 1728.

(97) Jain, S.; Bates, F. S. *Science* **2003**, *300*, 460

(98) Rodahl, M.; Höök, F.; Krozer, A.; Kasemo, B.; Breszinsky, P. *Rev. Sci. Instrum.* **1995**, *66*.

(99) Voinova, M. V.; Rodahl, M.; Jonson, M.; Kasemo, B. *Phys. Scrip.* **1999**, *59*, 391.

(100) Sauerbrey, G. Z. *Phys. Rev. A* **1959**, *155*, 206.

(101) Arnau, A. S.; Jimenez, Y. *Rev. Sci. Instrum.* **2002**, *73*, 2724.

(102) Beck, R.; Pittermann, U.; Weil, K. G. *Ber. Bunsen-Ges. Phys. Chem.* **1988**, *92*, 1363.

(103) Rodahl, M.; Kasemo, B. *Rev. Sci. Instrum.* **1996**, *67*, 3238.

(104) Voinova, M. V.; Rodah, M.; Jonson, M.; Kasemo, B. *Phys. Scr.* **1999** *59*, 391.

(105) Braga, P. C.; Ricci, D. *Atomic force microscopy : biomedical methods and applications* Humana Press, 2004.

(106) Smith, R. L.; Rohrer, G. S. *In Scanning Probe Microscopy and Spectroscopy: Theory, Techniques, and Applications*; Wiley-VCH: New York, 2000.

(107) Beyer, M. K.; Schaumann, H. C. *Chem. Rev.* **2005**, *105*, 2921.

(108) Binnig, G.; Quate, C. F.; Gerber, C. *Phys. Rev. Lett.* **1986**, *56*, 930.

(109) Ross, M.; Steinem, C.; Galla, H. J.; Janshoff, A. *Langmuir* **2001** *17*, 2437.

(110) Albrecht, C.; Blank, K.; Lalic-Multhaler, M.; Hirler, S.; Mai, T.; Gilbert, I.; Schiffmann, S.; Bayer, T.; H. Clausen-Schaumann, H.; Gaub, H. E. *Science* **2003**, *301*, 367.

(111) Ducker, W. A.; Senden, T. J.; Pashley, R. M. *Nature* **1991** *353*, 239.

(112) Benmouna, F.; Johannsmann, D. *J. Phys.: Condens. Matter* **2003**, *15*, 3003.

(113) Liang, J.; Horton, J. H. *Langmuir* **2005,** *21*, 10608.

(114) Pasche, S.; Textor, M.; Meagher, L.; Spencer, N. D.; Griesser, H. J. *Langmuir* **2005**, *21*, 6508.

(115) Kisielewski, M.; Maziewski, A.; Zablotskii, V.; Polyakova, T.; Garcia, J. M.; Wawro, A.; Baczewski, L. T. *J. Appl. Phys.* **2003**, *93*, 6966.

(116) Landis, S.; Rodmacq, B.; Dieny, B.; Dal'Zotto, B.; Tedesco, S.; Heitzmann, M. *J. Magn. Magn. Mater.* **2001**, *226*, 1708.

(117) Lemke, H.; Lang, T.; Goddenhenrich, T.; Heiden, C. *J. Magn. Magn. Mater.* **1995**, *148*, 426.

(118) Swerts, J.; Temst, K.; van Bael, M. J.; Van Haesendonck, C.; Bruynseraede, Y. *Appl. Phys. Lett.* **2003**, *82*, 1239.

(119) Takahashi, H.; Ando, K.; Shirakawabe, Y. *Ultramicroscopy* **2002**, *91*, 63.

(120) Terris, B. D.; Folks, L.; Weller, D.; Baglin, J. E. E.; Kellock, A. J.; Rothuizen, H.; Vettiger, P. *Appl. Phys. Lett.* **1999**, *75*, 403.

(121) Tomlinson, S. L.; Farley, A. N. *J. of Appl. Phys.* **1997**, *81*, 5029.

(122) Wadas, A.; Moreland, J.; Rice, P.; Katti, R. R. *Appl. Phys. Lett.* **1994**, *64*, 1156.

(123) Wu, T. W.; Frommer, J. *J. Magn. Magn. Mater.* **2000**, *219*, 142.

(124) Kopel, D. *J. Phys. Chem.* **1972**, *57*, 4814.

(125) Chu, B. *Laser Light Scattering-Basic Principles and Practice*; 2nd ed.; Academic Press, Inc.: San Diego, 1991.

(126) Santos, N. C.; Castanho, A. R. B. *Biophys. J.* **1996**, *71*, 1641.

(127) Hassan, P. A. K., Kulshreshtha, S.K. *J. Colloid Interf. Sci.* **2006**, *300*, 744.

(128) Islam, M. N.; Kato, T. *Langmuir* **2005**, *21*, 10920.

(129) Overbeck, G. A.; Honig, D.; Mobius, D. *Langmuir* **1993**, *9*, 555.

(130) Drude, P. *Ann. Physik* **1891**, *279*, 126.

(131) Henon, S.; Meunier, J. *Rev. Sci. Instrum.* **1991**, *62*, 936.

(132) Rutnakornpituk, M.; Thmpson, M. S.; Harris, L. A.; Farmer, K. E.; Esker, A. R.; Riffle, J. S.; Connolly, J.; Pierre, T. G. S. *Polymer* **2002**, *43,* 2337.

(133) Honig, D.; Mobius, D. *J. Phys. Chem.* **1991**, *95*, 4590.

(134) Klopfer, K. J.; Vanderlick, T. K. *J. Colloid and Interface Sci.* **1996**, *182*, 220.

(135) Petty, M. C. *Langmuir-blodgett Films*; Cambridge University Press, 1996.

(136) Petty, M. C. *In Langmuir-Blodgett Films*; Roberts, G., Ed.; Plenum Press: New York, 1990.

(137) Langmuir, I. S., V. J.; Sobotka, H. *J. Am. Chem. Soc.* **1937**, *59*, 1751.

(138) Kowalski, A.; Duda, A.; Penczek, S. *Macromol. Rapid Commun.* **1998**, *19*, 567.

(139) Kowalski, A.; Libiszowski, J.; Biela, T.; Cypryk, M.; Duda, A.; Penczek, S. *Macromolecules* **2005**, *38*, 8170.

(140) Kowalski, A.; Duda, A.; Penczek, S. *Macromolecules* **2000**, *33*, 7359.

(141) Matyjaszewski, K.; Xia, J. *Chem. Rev.* **2001**, *101*, 2921.

(142) Sun, S.; Zeng, H. *J. Am. Chem. Soc.* **2002**, *124*, 8204.

(143) Xie, J.; Kohler, N.; Hou, Y.; Sun, S. *Adv. Mater.* **2007**, *19*, 3163.

(144) Puntes, V. F.; Krishnan, K. M.; Alivisatos, A. P. *Science* **2001**, *16*, 2115.

(145) Vargas, J. M.; Zysler, R. D. *Nanotechnology* **2005**, *16*, 1474.

(146) Zeng, H.; Rice, P. M.; Wang, S. X.; Sun, S. *J. Am. Chem. Soc.* **2004**, *126*,

11458.

(147) Murray, C. B.; Noms, D. J.; Bawendi, M. G. *J. Am. Chem. Soc.* **1993**, *115*, 8706.

(148) Hyeon, T. *Chem. Commun.* **2003**, *8*, 927.

(149) Pileni, M. P. *Langmuir* **1997**, *13*, 3266.

(150) Chen, J. P.; Sorensen, C. M.; Klabunde, K. J.; Hadjipanayis, G. C. *J. Appl. Phys.* **1994**, *76*, 6316.

(151) Sun, S.; Murray, C. B. *J. Appl. Phys.* **1999**, *85*, 4325.

(152) Condorelli, G. G.; Motta, A.; Fragal, I. L.; Giannazzo, F.; Raineri, V.; Caneschi, A.; Gatteschi, D. *Angew. Chem. Int. Ed.* **2004**, *43*, 4081.

(153) Fried, T.; Shemer, G.; Markovich, G. *Adv. Mater.* **2001**, *13*, 1158.

(154) Mendz, G. L.; Moore, W. J.; Kaplin, I. J.; Cornell, B. A.; Separovic, F.; Miller, D. J.; Brown, L. R. *Biochemistry* **1988**, *27*, 379.

(155) Naitabdi, A.; Bucher, J.; Gerbier, P.; Rabu, P.; Drillon, M. *Adv. Mater.* **2005**, *17*, 1612.

(156) Wang, Z. L.; Dai, Z.; Sun, S. *Adv. Mater.* **2000**, *12*, 1944.

(157) Jun, Y.; Huh, Y.; Choi, J.; Lee, J.; Song, H.; Kim, S.; Yoon, S.; Kim, K.; Shin, J.; Suh, J.; Cheon, J. *J. Am. Chem. Soc.* **2005** *127*, 5732.

Chapter 3

Materials and Experimental Methods

3.1. Preparation of Poly(ε-caprolactone) (PCL) Block Copolymers

3.1.1. Materials. 2-Bromoisobutyryl bromide (98%), anisole (anhydrous, 99.7%), copper (I) bromide (CuBr, 99%), ethylene glycol (99%) and stannous 2-ethylhexanoate ($Sn(Oct)_2$, 95%) were purchased from Aldrich and used as received. Tetrahydrofuran (THF) was distilled from sodium benzophenone ketyl and sodium metal under nitrogen prior to polymerization. ε-Caprolactone (CL, Acros, 99%) was dried over CaH_2 for 48 h and distilled prior to use. *tert*-Butyl acrylate, (tBA, Aldrich, 99%) and styrene (St, Aldrich, 99.5%) were passed through a basic Al_2O_3 column twice to remove inhibitors. N, N, N, N″, N″-pentamethyldiethylenetriamine (PMDETA, Aldrich, 99%) was used as received. 2, 2′-Bipyridyl (DPY, 99%, Aldrich) was recrystallized in ethanol at 4 °C prior to use.

The block copolymers were prepared according to Scheme 3.1.[1] The as-prepared block copolymers had the same poly(ε-caprolactone) (PCL) block and various block lengths of poly(tert-butyl acrylate) (PtBA).

3.1.2. Synthesis of the Bi-functional Initiator. The bi-functional initiator, 2-hydroxyethyl 2′-methyl-2′-bromopropionate (compound **1** in Scheme 3.1) was synthesized according the reported method.[2] 2-Bromoisobutyryl bromide (10 ml, 81 mmol) was added into a molar excess (25 times) of ethylene glycol (120 mL, 2.1 mol) dropwise and stirred for 10 h at 0 °C. The mixture was then dissolved in water and extracted with dichloromethane. The organic phase was washed with a saturated aqueous sodium bicarbonate solution, water and then dried with $MgSO_4$. The solvent was removed and the product (liquid) was further purified by vacuum distillation to yield 18.50 g of a colorless liquid product (78%). ^1H NMR (500 MHz,

$CDCl_3$), δ (ppm): 1.95 (s, 6H, -$C(CH_3)_2$), 2.17 (s, 1H, -OH), 3.87 (t, 2H, -CH_2OH), 4.31 (t, 2H, -$COOCH_2$-).

3.1.3. Synthesis of the HO-PCL-Br Macroinitiator (2). A 100 mL round-bottom flask was sealed by a rubber septum, flame dried and then charged with ultra pure N_2. CL (10 ml, 87.7 mmol), $Sn(Oct)_2$ (0.25 ml, 0.8 mmol), 2-hydroxyethyl 2′-methyl-2′-bromopropionate (0.167 g, 1 mmol), and anhydrous THF (20 mL) were transferred into the flask by canulla tubing or air-tight syringes under N_2. The solution was degassed through three freeze-thaw cycles and placed in an 80 °C temperature bath and reacted for 10 h. The reaction was stopped by precipitation of the mixture into cold hexanes. The precipitate was collected by filter paper, re-dissolved in THF and precipitated twice with methanol. The resulting white solid precipitate (2) was dried in vacuum for 12 h at room temperature to yield 7.0 g product.

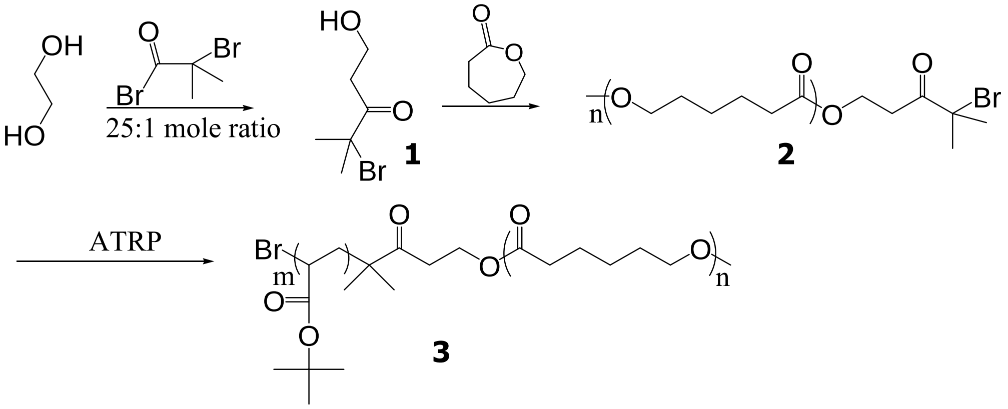

Scheme 3.1. Syntheses of PCL-b-PtBA copolymers. The scheme was adapted from Reference 1.

3.1.4. Synthesis of PCL-b-PtBA Block Copolymers (3). Block copolymers of PCL and PtBA (PCL-b-PtBA) were synthesized by atom transfer radical polymerization (ATRP). In an exemplary procedure, HO-PCL-Br macroinitiator (0.5 g, 0.067 mmol) was dissolved with 2 ml of anisole in a vial. The vial was then sealed with a rubber septum and degassed with 3 freeze-thaw cycles. A mixture of CuBr (10 mg, ~0.07 mmol), PMDETA (14 *μl*, ~0.07 mmol), and tBA (2.0 mL) was added to a Schlenk flask. The mixture was degassed with 3 freeze-thaw cycles and charged with N_2. The flask was then placed in the oil bath (T = 100 °C) equilibrated for 15 min, and a PCL macroinitiator in anisole solution was injected. The reaction continued for 24 hours and was stopped by exposure to air. The mixture was then diluted with THF and passed through a basic Al_2O_3 column to remove the copper complex. The product was isolated by precipitation into cold methanol and subsequently dried under reduced pressure. Different block lengths of PtBA were prepared by varying the amount of tBA monomer. The monomer conversion rate was ~80% for the reaction conditions for all the reactions.

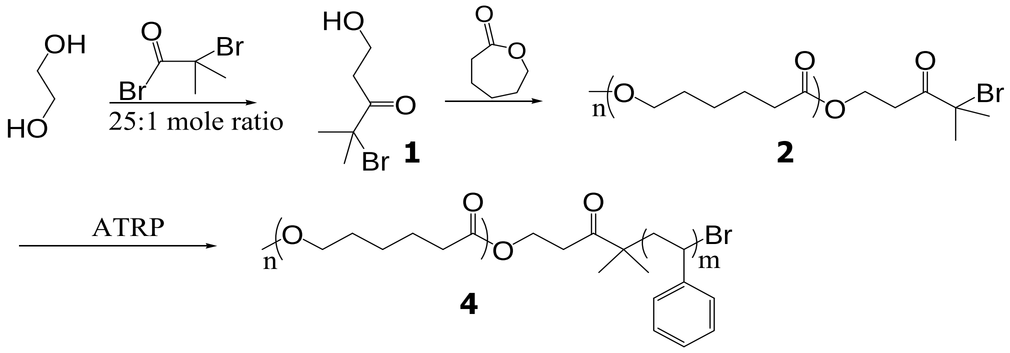

Scheme 3.2. Route for PCL-b-PS copolymer synthesis.

3.1.5. Synthesis of PCL-b-PS Copolymers (4). Block copolymers of PCL and polystyrene (PS) (PCL-b-PS) were prepared in a manner similar to the synthesis of PCL-b-PtBA in Section 3.1.4 with the same PCL macroiniator. In an exemplary synthesis, HO-PCL-Br macroinitiator (1.0 g, 0.13 mmol) was added to a vial and dissolved with 2 mL anisole. The vial was sealed by a rubber septum and degassed with three freeze-thaw cycles. A mixture of CuBr (20 mg, ~0.13 mmol), DPY (64 mg, ~0.40 mmol), St (1.0 mL) and anisole 1 mL was added to a Schlenk flask. The heterogeneous mixture was degassed with three freeze-thaw cycles and purged with N_2. The flask was then placed in the oil bath (T = 100 °C), equilibrated for 15 min, add a PCL macroinitiator in anisole solution was injected. The reaction was carried out for 10 h and stopped by exposure to air. The contents were then diluted with THF and passed through a column of basic alumina to remove the copper complex. The product was isolated by precipitation into cold methanol. The precipitate was filtered and dried under reduced pressure for 16 h and yielded 0.71 g copolymer.

3.1.6. Polymer Characterization. ^{1}H NMR spectra of the polymers were obtained on a JOEL 500 spectrometer operating at 500 MHz at ambient temperature. Deuterated chloroform (Cambridge Isotope Laboratories) was used as the solvent. One exemplary spectrum for an as-prepared PCL-b-PtBA copolymer and peak assignments is shown in Figure 3.1. The ratio of the degree of polymerization for the two blocks was obtained by a comparison of the integration of peak (d+b) and h. Gel permeation chromatography (GPC) was conducted with an Alliance Waters 2690 Separations Module with a Viscotek T60A dual viscosity detector and laser refractometer equipped with a Waters HR 0.5 + HR 2 + HR 3 + HR 4 styragel column set at 30 °C. Universal calibration yielded absolute molar masses. The results were presented in Chapter 4 (Table 4.1).

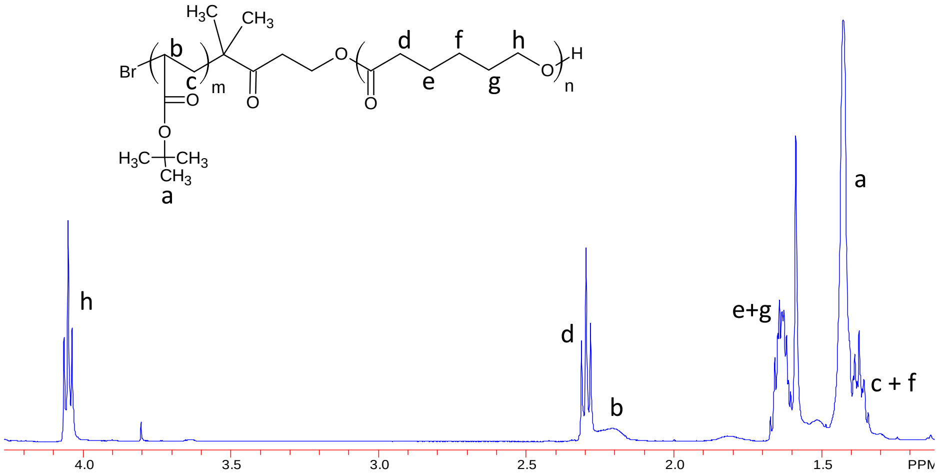

Figure 3.1. ^{1}H NMR analysis of a PCL-b-PtBA copolymer.

3.2. Preparation of PCL Triheads

3.2.1. Materials. Di-*tert*-butyl 4-amino-4-[2-(tert-butoxycarbonyl) ethyl] heptanedioate (aminotriester) was purchased from Frontier Scientific and used as received. 1,3-dicyclohexylcarbodiimide (DCC, Aldrich), 4-dimethylaminopyridine (DMAP, Aldrich), Z-6-aminohexanoic acid (Aldrich), tin(II) 2-ethylhexanoate ($Sn(Oct)_2$, Aldrich) and trifluoroacetic acid (TFA, Acros) were used as received. Tetrahydrofuran (HPLC, Fisher) was distilled from sodium metal with benzophenone under nitrogen prior to the polymerization. ε-Caprolactone (CL, Acros, 99%) was dried over calcium hydride for 48 h and distilled prior to use.

3.2.2. Synthesis of the Triester Amine Initiator (6). Due to the steric hindrance of the bulky tri-ester groups, the amine from the aminotriester failed to initiate the polymerization of ε-caprolactone. Therefore, the amine group was extended as shown in Scheme 3.3. In a typical reaction, 2 g aminotriester (4.8 mmol), 1.7 g Z-6-aminohexanoic acid (6.4 mmol), 1.6 g DCC (7.75 mmol), and DMAP (7.36 mmol) were mixed and stirred with a magnetic bar in 30 mL anhydrous dichloromethane for 7 days. The reaction product was eluted with ethyl acetate/hexanes (5/5, v/v) to yield 2.7 g white solid of compound **5** in Scheme 3.3 (83%). ^1H NMR (500 MHz, $CDCl_3$), δ (ppm): 1.34 (t, 2H, $-CH_2-$), 1.42 (s, 27H, $-C(CH_3)_3$), 1.51 (t, 2H, $-CH_2-$), 1.95 (t, 6H, $-CH_2-$), 2.10 (t, 2H, $-CH_2-$), 2.20 (t, 6H, $-CH_2-$), 3.20 (t, 2H, $-CH_2-$), 4.90 (s, 1H, -NH-), 5.08 (t, 2H, $-CH_2-$), 5.87 (s, 1H, -NH-), 7.31(m, 5H, $-(CH)_5-$). In a typical reaction for the removal of the benzyl protecting group, 2.5 g of compound **5** in Scheme 3.3 was dissolved in 15 mL methanol and then stirred with 0.5 g Pt/C (20 wt%) under H_2 (1 atm) at room temperature for 5 h. The catalyst was removed by filtration through Celite. The filtrate was concentrated by a rotary evaporator and eluted with chloroform/methanol/triethylamine (90:07:03, v/v/v) to yield 2.0 g light yellow solid of compound **6** (94%). ^1H NMR (500 MHz, $CDCl_3$), δ (ppm): 1.35 (t, 2H, $-CH_2-$), 1.42 (s, 27H,

-C(CH_3)$_3$), 1.45 (t, 2H, -CH_2-),1.96 (t, 6H, -CH_2-), 2.10 (t, 2H, -CH_2-), 2.20 (t, 6H, -CH_2-), 2.70 (t, 2H, -CH_2-), 5.86 (s, 1H, -NH-).

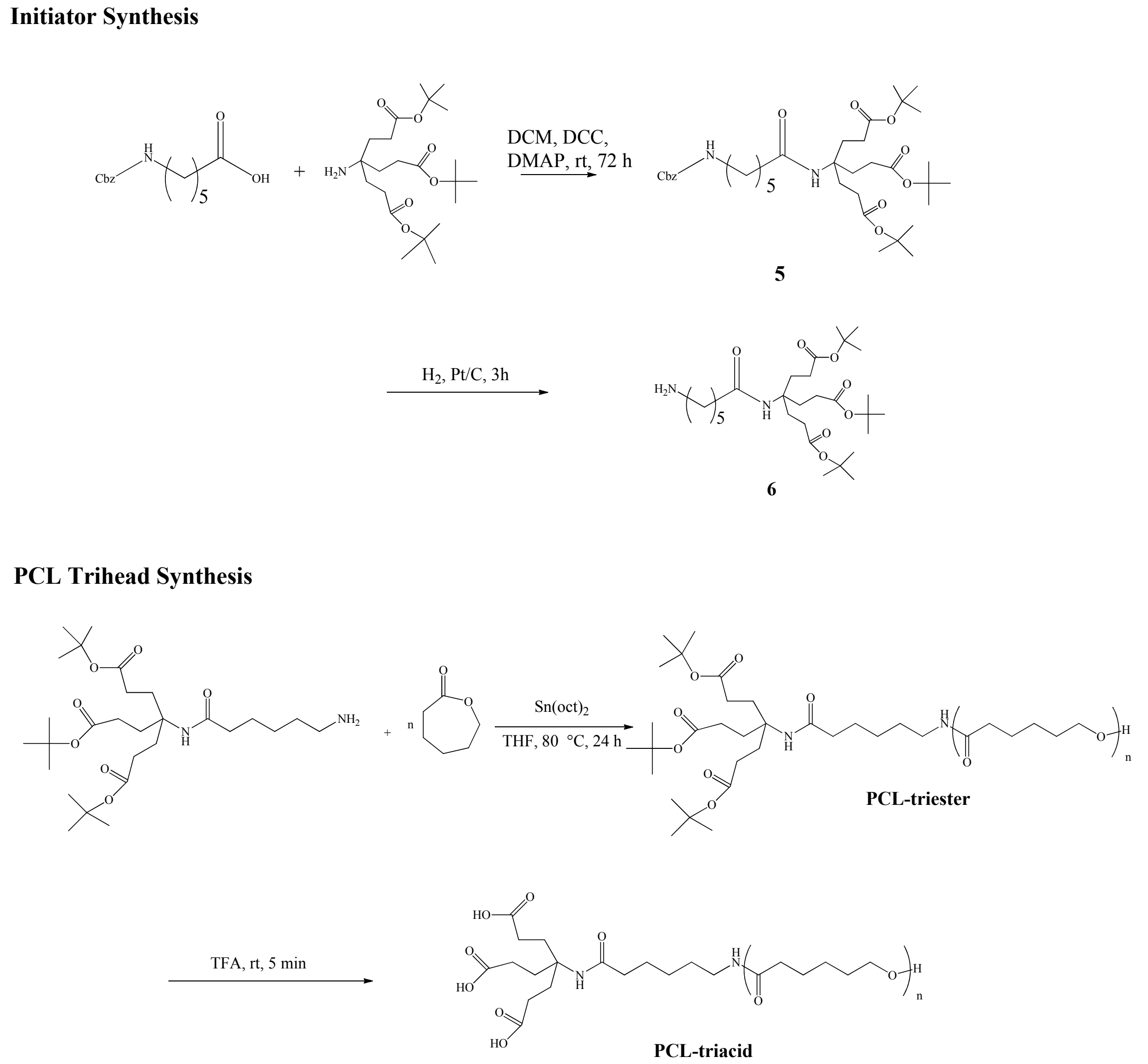
Initiator Synthesis

PCL Trihead Synthesis

Scheme 3.3. Routes to PCL Triheads.

3.2.3. Synthesis of PCL-Triesters. In an exemplary procedure, a 100 mL round-bottom flask was sealed by a rubber septum, flame dried and then charged with ultrapure N_2. CL (10 ml, 87.7 mmol), Sn(Oct)$_2$ (0.25 ml, 0.8 mmol), 0.167 g of compound **6** (1 mmol), and anhydrous THF (40 mL) were transferred into the flask by cannulla tubing or air-tight syringes under N_2. The solution mixture was degassed 3 times by a freeze-thaw procedure. The reaction continued at 80 ˚C for 24 h and was stopped by precipitation into cold hexanes. The precipitate was collected by filter paper, dissolved with THF and precipitated twice into methanol and dried in reduced pressure for 12 h at room temperature.

3.2.4. Hydrolysis of the PCL-Triester. The *t*-butyl groups of the PCL-triesters were removed by TFA. In an exemplary procedure, 0.5 g of the PCL-triester was dissolved in 5 mL TFA at room temperature and stirred for 5 min. The solution was precipitated into 50 mL methanol which was pre-equilibrated in a dry ice and isopropyl alcohol mixture temperature bath. The precipitate was collected and re-dissolved in 5 mL of THF, and reprecipitated twice more with methanol. 0.4 g of solid was obtained.

3.2.5. Polymer Characterization. ^{1}H NMR spectra of the polymers were obtained on a JOEL 500 spectrometer operating at 500 MHz at ambient temperature. Deuterated chloroform (Cambridge Isotope Laboratories) was used as the solvent. Two exemplary spectra for the as-synthesized triheads are shown in Figure 3.2. The NMR number average molar mass (M_n) was calculated from ^{1}H NMR results based on the ratio of the integration of the hydrogen signals from the methylene groups on the PCL repeat unit (h) to the proton signal from the initiator headgroup (c). Gel permeation chromatography (GPC) as described in Section 3.2.2 was used to obtain M_n and polydispersity indices (M_w/M_n) (Table 3.1).

Table 3.1. Molar Mass Characterization of PCL Triesters

Sample	**M_n (NMR) kg•mol^{-1}**	**M_n (GPC) kg•mol^{-1}**	M_w/M_n
3 k PCL Triester	2.3	2.8	1.18
6 k PCL Triester	6.3	6.1	1.09
9 k PCL Triester	13	8.7	1.37

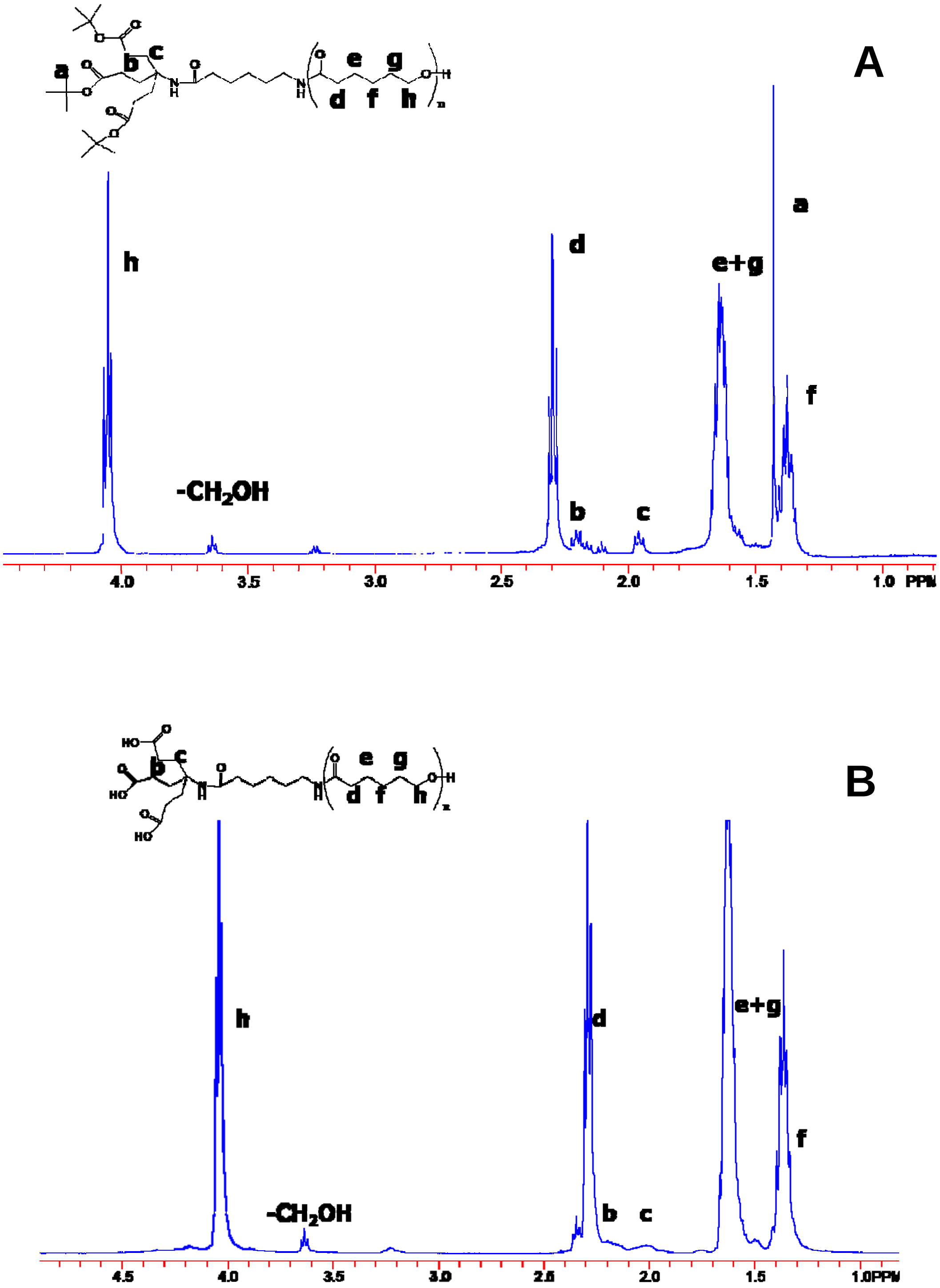

Figure 3.2. ^{1}H NMR spectra of (A) PCL triester and (B) PCL triacid.

3.3. PCL Magnetic Nanoparticles (PCL MNPs)

3.3.1. Magnetic Nanoparticle Synthesis. 9 nm monodisperse magnetite (Fe_3O_4), MNPs were synthesized according to a reported method.[3] $Fe(acac)_3$ (2 mmol), oleylamine (20 ml), and benzyl ether (20 ml) were mixed and stirred under N_2. The mixture was equilibrated at 100 ºC for 1 hour for the removal of moisture and then, under a nitrogen atmosphere, quickly heated to reflux (300 ºC) for another 2 hours. After the mixture was cooled, ethanol (40 mL) was added and a black precipitate was separated via a magnetic bar. The black product was dissolved in hexanes in the presence of oleic acid (0.05 ml). Centrifugation (2500 rpm, 20 min) was applied for the removal of any nondispersed residue. The product was then precipitated with acetone. The particles were redissolved into hexanes and precipitated with acetone twice more for the removal of ligand and dried under reduced pressure. 0.4 g oleic acid stabilized MNPs were obtained.

3.3.2. Ligand Exchange. PCL triacids were used for the exchange reaction with oleic acid on the nanoparticle surface by a ligand exchange method as shown in Figure 3.3. In an exemplary reaction, 15 mg of 9 nm MNPs were refluxed in 20 ml $CHCl_3$ with 0.15 g 6 k PCL triacid under N_2 for 24 hours. The solution was precipitated into hexanes and concentrated at the bottom of the container with a magnetic bar. The precipitate was re-dissolved in THF and dialyzed with a dialysis membrane (molecular weight cut-off (MWCO) = 50,000 $g \cdot mole^{-1}$) in acetone (100 mL, 5×) at room temperature for 4 days. The final solution was concentrated and dried under vacuum at room temperature. The compositions (wt% Fe_3O_4) of the MNPs were determined by a thermogravimetric analyzer (TGA, TA Instruments) at a temperature increment of 10 $°C \cdot min^{-1}$ under N_2.

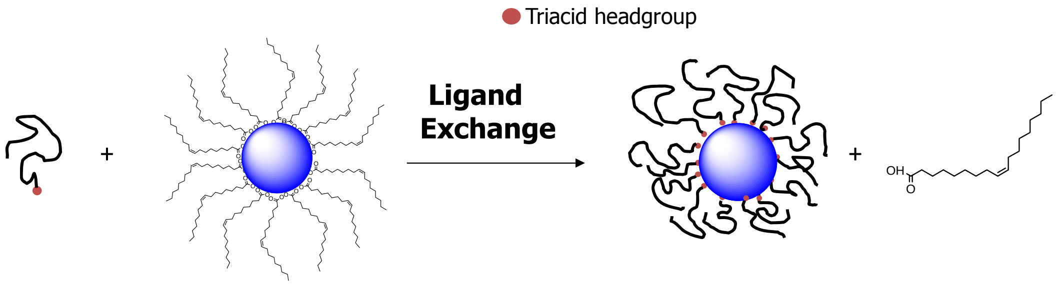

Figure 3.3. A depiction of the ligand exchange procedure for preparing PCL MNPs (not to scale).

3.4. Poly(ethylene glycol) (PEG) Surfactants

Monostearate PEG esters (n_{EO} = 10, 25, 40, and 45), monooleyl PEG ether (n_{EO} = 10) and PEG mono-4-nonylphenyl ethers (Nonoxynols, n_{EO} = 10, 15, 18, and 20) were obtained from TCI and used as received. Here, n_{EO} was the number of ethylene oxide repeat unit in the PEG chain. Brij58 ($HO\text{-}(CH_2CH_2O)_{20}C_{16}H_{33}$) and 2000 monomethyl PEG ether, designated as MPEG 2 k (k = kg•mol^{-1}), were obtained from Aldrich and used as received. 2.5 k cholesterol PEG, 6 k cholesterol PEG , and 6 k stearyl PEG were provided by Prof. Judy S. Riffle's group at Virginia Tech. PEG lipid surfactants: 1,2-dioleoyl-*sn*-glycero-3-phosphoethanolamine-N-[methoxy(polyethylene glycol)-3000] (ammonium salt, 18:1 PEG 3000 PE); 1,2-dioleoyl-*sn*-glycero-3-phosphoethanolamine-N-[methoxy(polyethylene glycol)-5000] (ammonium salt, 18:1 PEG 5000 PE); 1,2-distearoyl-sn-glycero-3-phosphoethanolamine-N-[methoxy(polyethylene glycol)-3000] (ammonium salt, 18:0 PEG 3000 PE); 1,2-distearoyl-sn-glycero-3-phosphoethanolamine-N-[methoxy(polyethylene glycol)-5000] (ammonium salt, 18:0 PEG5000 PE) purchased from Avanti Polar Lipid are denoted as 3 k dioleoyl PEG, 5 k dioleoyl PEG, 3 k distearoyl PEG and 5 k distearoyl PEG, respectively. PEG surfactant structures are shown in Figure 3.4. Pluronic block copolymers were received from BASF and used without further modification or purification. Their molar masses and compositions were summarized in Table 3.2.

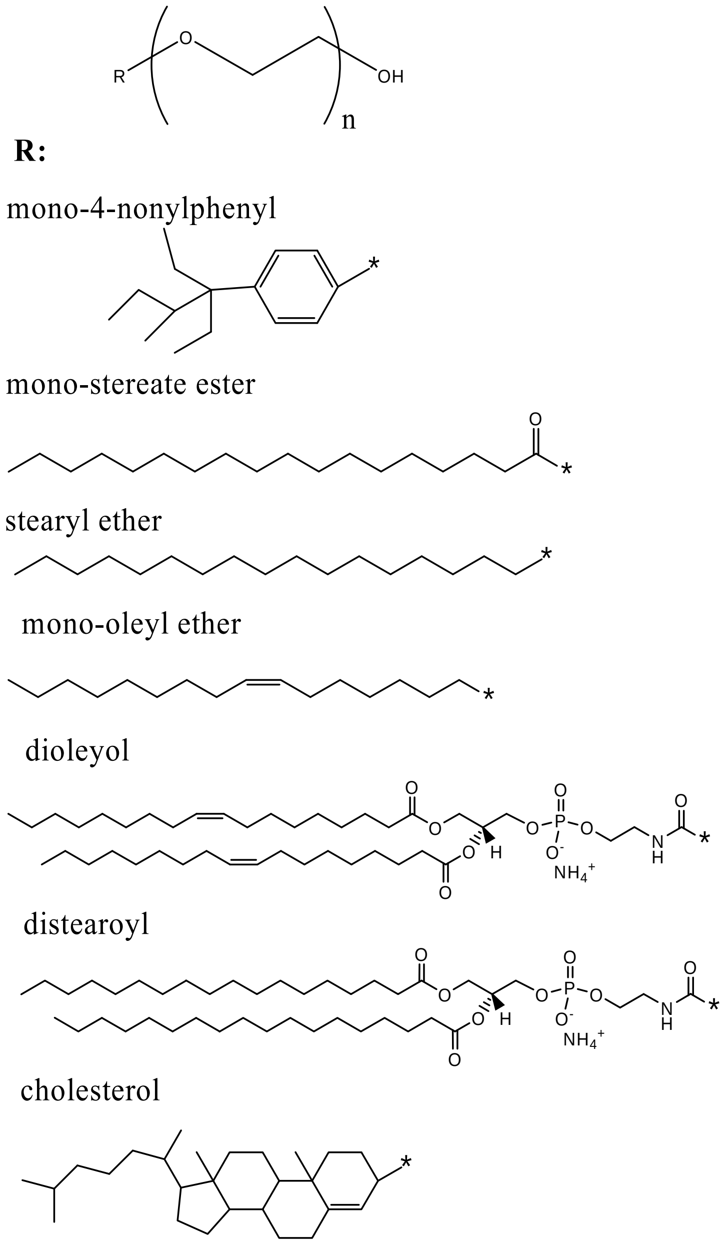

Figure 3.4. Various structures for PEG surfactants.

Table 3.2. Molar masses and compositions of Pluronic copolymers.

Pluronics	M_n[a] ($kg \cdot mol^{-1}$)	$(EO)_n(PO)_m(EO)_n$ n:m:n[a]	PPO[b] (mol %)
F-68	8.4	75:30:75	16.7
F-87	7.7	61:40:61	24.7
F-108	14.6	132:56:132	17.5
F-127	12.6	97:69:97	26.2
L-64	2.9	13:30:13	53.6
L-101	3.8	4:59:4	88.1
P-85	4.6	26:40:26	43.5
P-105	6.5	37:56:37	43.1

[a] The molar mass and the composition information were obtained from BASF.

[b] mol% PPO was calculated from the composition.

3.5. Phospholipids

1,2-di-(9Z-octadecenoyl)-*sn*-glycero-3-phosphocholine (DOPC), L-α-phosphatidylcholine (Egg PC), and 1,2-ditetradecanoyl-*sn*-glycero-3-phosphocholine (DMPC) were purchased from Avanti Polar Lipid and used as received.

3.6. Preparation of Phospholipid Vesicle Solutions

In order to prepare phospholipid bilayers, unilamellar phospholipid vesicle solutions were first prepared. In an exemplary procedure, ~10 mg of phospholipids was dissolved in 5 mL chloroform in a 100 mL round bottom flask, followed by the removal of chloroform by vacuum for ~ 1 hour. The flask was then filled with 30 mL of phosphate buffer saline (PBS buffer, [Na_2HPO_4] = 8.1 mM, [NaH_2PO_4] = 1.9 mM, [NaCl] = 100 mM, pH = 7.4) or ultrapure water, incubated in a 50 °C water bath and shaken periodically for 2 h. The mixture was homogenized with a probe sonicator and diluted to 0.1 mg•mL^{-1}.

3.7. Experimental Methods at the Air/Water Interface

3.7.1. Compression/Expansion Surface Pressure-Area per Monomer (Π−A) Isotherm Cycles. In the compression/expansion Π−A hysteresis experiments, the monolayer was compressed at a constant compression rate to a designated minimum trough area and was immediately expanded at the same barrier speed back to the initial maximum trough area. In a typical compression/expansion Π−A isotherm cycle study, the samples were dissolved in chloroform (HPLC grade, ~0.2 mg•g^{-1}) and were spread onto the surface of a standard Langmuir trough (Nima Technology Ltd. 601 BAM) filled with ultrapure water (Millipore, Milli-Q Gradient A-10, 18.2 MΩ•cm, < 5 ppb organic impurities) in a Plexiglas^{TM} box. Π was obtained by the Wilhelmy plate technique at a constant temperature of 22.5 °C. A completely wetted piece of filter paper was used as the Wilhelmy plate. The Langmuir trough and Plexiglas box were placed on a floating optical table that minimized vibrations.

3.7.2. Isobaric Area Relaxation Experiments. Isobaric (constant Π) area relaxation experiments were performed for monolayers in supersaturated states to explore diffusion limited crystalline morphologies of PCL-triheads. These experiments started after the monolayers were compressed to a desired target Π at a constant compression rate. Various target pressures in the supersaturated monolayer regime were chosen to study the effects of Π on the morphological evolution of PCL crystals during isobaric area relaxation experiments.

3.7.3. Brewster Angle Microscopy (BAM). Morphological features of the films were obtained at different stages of hysteresis experiments by BAM (MicroBAM3, NIMA Technologies). BAM micrographs were taken with a charge-coupled device (CCD) camera with a resolution ≤ 20 μm. The Langmuir trough, BAM, and Plexiglas box rested on a floating optical table to minimize vibrations. The BAM images presented in this thesis were cropped from the original 3.6 mm × 4.1 mm images.

3.8. Langmuir–Blodgett (LB) Film Deposition

3.8.1. Substrate Preparation. Silicon (100) wafers (Wafer World, Inc.) were cut into appropriately sized pieces and were boiled in a 1:1:5 (by volume) solution of ammonium hydroxide (28%): hydrogen peroxide (30%): ultrapure water for 1.5 h. After the substrates were rinsed with copious amounts of ultrapure water and dried under nitrogen, the silicon substrates were immersed in a 30:70 (by volume) solution of hydrogen peroxide (30%) :

concentrated sulfuric acid for ~ 1 h, rinsed with ultrapure water, and dried under nitrogen. The cleaned substrates were then hydrophobized by treatment with HF (J. T. Baker, 1:7 buffered etch oxide) and NH_4F (J. T. Baker, 40%) solutions, subsequently rinsed with copious water, and blown dry. Trimethylsilyl cellulose (TMSC) (degree of trimethylsilyl substitution = 2.7) was kindly provided by Prof. Thomas Heize's group at the University of Jena, Germany. Hydrophilic regenerated cellulose surfaces for LB-transfer of PCL crystals were prepared by spincoating 2.5 wt % TMSC in toluene solutions onto hydrophobized silicon surfaces at a spinning rate of 2000 rpm for ~ 60 s. The as-prepared surfaces were dried under reduced pressure at 70 °C for 24 h. The cellulose surfaces were regenerated upon exposure of the TMSC spincoated films to vapors of a 10 wt% HCl solution 3 min, and were then rinsed with water and blown dry with ultrapure N_2 gas. The hydrophilic regenerated cellulose layer was used to enhance interactions between the side of the PCL crystals in contact with water and the silicon surface. This process preserved the morphological features of crystals observed by BAM at the A/W interface. The features of interest were also transferred onto mica and silicon surfaces for AFM imaging.

3.8.2. LB-Transfer. For the transfer of a LB-film, the hydrophilic substrates were dipped from air into the subphase at 8 mm•min^{-1}. There was no trough area change during this process, an indication that no monolayer transferred onto the hydrophilic surface during the downstroke. The upstroke proceeded at a rate of 1 mm•min^{-1} at which time, a film was transferred onto the substrate.

3.9. Imaging of LB-Films

3.9.1. Optical Microscopy (OM). An optical microscope operating in reflection mode (Axiotech Vario 100 HD, Carl Zeiss) provided micron-scale resolution of monolayer features. The thin regenerated cellulose layer between the silicon substrate and the crystals enhanced the contrast, whereby the 7 to 8 nm thick crystals could be observed with visible light. The contrast mechanism was an interference effect that arose from differences in the optical path lengths between the cellulose layer and the cellulose layer plus PCL film for visible light reflected from the film/air and film/substrate interfaces.

3.9.2. Atomic Force Microscopy (AFM). For AFM, LB-films were transferred onto freshly cleaved mica surfaces. The LB-films were scanned in the tapping mode with a Nanoscope IIIa atomic force microscope (Digital Instruments, Inc., Santa Barbara, CA) by use of Veeco silicon probes (dimensions: T: 1.5-2.5 μm, L:115-135 μm, W: 25-35 μm). All the images were processed with a second-order flattening routine without further modification.

3.9.3. Transmission Electron Microscopy (TEM). TEM was performed using a JEOL 200CX transmission electron microscope operated at an accelerating voltage of 120 kV. The TEM samples were prepared by LB-transfer onto a carbon coated copper TEM grid (300 mesh, PSI). For PCL/oleic acid MNPs blends, the TEM copper grids (300 mesh, PSI) were coated with a thin layer of SiO_2.

3.10. Materials Characterization Techniques

3.10.1. Thermogravimetric Analysis (TGA). TGA analyses were performed with a TGA Q5000 Thermogravimetric Analyze (TA Instruments). The temperature ramped up to 500 °C with a heating rate of 10 °C•min^{-1}under nitrogen gas with a flow rate of 25 mL•min^{-1}.

3.10.2. Dynamic Light Scattering (DLS) Measurements. The hydrodynamic radii of the nanoparticles were measured with an ALV/CGS-3 Dynamic Light Scattering (DLS) Instrument (ALV-GmbH, Langen, Germany) at 25 °C. The autocorrelation functions for the particle chloroform solutions (~0.1 mg/g) were obtained at six different scattering angles ranging from 35˚ to 120˚. The data were analyzed with the cumulant method which yielded the diffusion coefficients; meanwhile, a CONTIN analysis yielded intensity average size distributions at 90˚.

3.10.3. Differential Scanning Calorimetry (DSC). Differential scanning calorimetry (DSC) measurements were performed using a DSC Q2000 Instrument (TA Instruments). A PEG phospholipid sample of ~ 2 mg was sealed in an aluminum sample pan, and the temperature of the sample was controlled in the DSC cell. Samples were kept under a nitrogen atmosphere. The heating rate was 5 ˚C • minute^{-1}, and the cooling rate was 20 ˚C • minute^{-1}. Two cycles with temperature ranges from - 60 to 100 ˚C were used.

3.11. Quartz Crystal Microbalance with Dissipation Monitoring (QCM-D) Studies of Biomimetic Phospholipid Bilayers

3.11.1. QCM-D Measurements. The adsorption of various surfactants onto phospholipid bilayers were investigated using QCM-D (Q-sense E4, Q-Sense AB), which monitors changes in both resonance frequency of the quartz crystal and dissipation of its energy as a function of time. Oscillations of the crystal for odd overtones (1 through 13) were simultaneously measured. Voigt-based viscoelastic modeling described in Chapter 2 provided estimates of film thickness, viscosity, and shear modulus.

3.11.2. Preparation of Phospholipid Bilayers on SiO_2 Crystal Surfaces. Biomimetic phospholipid bilayers were used as the model surfaces for the study of interactions between surfactants with phospholipid membrane components in Chapter 6. The fusion of phospholipid vesicles from the solutions in Section 3.6 onto SiO_2 QCM sensor surfaces was monitored *in situ*. SiO_2 coated quartz crystals were purchased from Q-Sense AB. Prior to their use, the crystals were first rinsed thoroughly with ultrapure water and sonicated in a 2 wt% sodium dodecyl sulfate SDS water solution for 10 min followed by UV ozone cleaning for 20 min. For DOPC and Egg PC, phospholipid bilayers were formed at 20 °C. For DMPC, the operational temperature was 25 °C, due to the fact that gel-liquid transition temperature of DMPC (23 °C) was slightly above room temperature. A 25 ± 1 Hz frequency shift and low dissipation values were the characteristics for the formation of a phospholipid bilayer.[4]

3.12. Reference:

(1) Jakubowski, W.; Matyjaszewski, K. *Macromol. Symp.* **2006**, *240*, 213.

(2) Wiltshire, J. T.; Qiao, G. G. *Macromolecules* **2006**, *39*, 9018.

(3) Xie, J. Xu, C.; Kohler, N.; Hou, Y.; Sun, S. *Adv. Mater.* **2007**, *19*, 3163.

(4) Richter, R. P.; Brisson, A. R. *Biophysical Journal* **2005**, *88*, 3422.

Chapter 4

Morphological Studies of Poly(ε-caprolactone)-b-Poly(tert-butyl acrylate) Block Copolymers at the Air/Water Interface

4.1. Abstract

Block copolymers of poly(ε-caprolactone)-b-poly(tert-butyl acrylate) (PCL-b-PtBA) were synthesized by *atom transfer radical polymerization* (ATRP) initiated from a linear poly(ε-caprolactone) (PCL) macro-initiator. The block copolymers had an identical PCL block number average molar mass (M_n = 7.5 kg•mol^{-1}) and various PtBA blocks. Thermodynamic analyses of surface pressure-area per monomer ($\Pi-A$) isotherms for the Langmuir films at the air/water (A/W) interface were consistent with block copolymers that formed homogenous monolayers below the dynamic collapse transition of the PCL blocks, $\Pi_C \sim 10.5$ mN•m^{-1}. For $\Pi > \Pi_C$, the crystallization of the PCL block at the A/W induced micro-phase separation. Brewster angle microscopy (BAM), optical microscopy (OM) and atomic force microscopy (AFM) studies on Langmuir and Langmuir-Blodgett films, respectively, revealed surface morphologies that depended upon the length of the PtBA blocks.

4.2. Introduction

Micro-phase separation of block copolymers can well-defined periodic polymer domains.[1] Furthermore, block copolymers have been employed to study polymer crystallization in confined geometries and numerous studies have focused upon thin film crystallization.[2-14] For example, micro-phase separation of polystyrene(PS)-b-poly(ethylene oxide) (PEO) diblocks led to one dimensional (1D) confinement of PEO phase between two PS layers in a "sandwich" structure and subsequently, 1D confinement effects for PEO crystallization were studied.[2,3] In traditional studies, polymer thin films were normally spincoated onto a solid substrate. For the block copolymer thin film morphologies, two other factors in addition to microphase separation controlled the resulting morphologies and the topographies, preferential wetting of the substrate and film thickness.[15] As a consequence of limitations imposed by film preparation methods on the control of these variables, the study of block copolymer crystallization from a two dimensional (2D) monolayer to a three dimensional (3D) crystal on a solid substrate was not feasible.

Systems that approach 2D systems are Langmuir monolayers at the air/water (A/W) interface. The A/W interface provides an ultra smooth interface for thermodynamic studies of monolayers. The water subphase can serve as a heat "reservoir" that maintains isothermal conditions. Li et al.[16-17] first reported the crystallization of linear PCL at the A/W interface. The PCL monolayer underwent a 2D monolayer to 3D lamellar crystal transition by a homogenous nucleation and growth mechanism. The unique behavior of PCL monolayers at the A/W interface enabled studies of polymer crystallization under 2D confinement. Following Li's initial discoveries, several studies about confinement effects on PCL crystalline morphologies at the A/W interface were reported. Dendritic growth of PCL crystals was observed for PCL and poly(tert-butyl acrylate) PtBA mixed monolayers that arose from diffusion limited control of crystallization.[18] The confinement effects on PCL crystallization at the A/W interface that arose from tethering a PCL block to a PEO block have also been reported.[19-20] In these systems, the PEO block went into the subphase prior to crystallization of the PCL block. Nonetheless, Studies of how in-plane confinements by an amphiphilic block or hydrophobic block affect PCL crystallization at the A/W interface have been absent.

In this chapter, results for the crystallization of poly(ε-caprolactone)-b-poly(tert-butyl acrylate) (PCL-b-PtBA) diblock copolymers at the A/W interface are investigated. The particular block copolymers were selected because both blocks were amphiphilic, and the

PCL block was crystallizable. A previous study showed that PCL homopolymer formed a liquid-expanded (LE) monolayer (highly compressible) and had a collapse pressure of $\Pi_{C,PCL}$ ~ 11 mN•m^{-1} at the A/W interface;[16-17] whereas, PtBA homopolymer formed a condensed (LC) monolayer (less compressible) at the A/W interface with a monolayer collapse pressure, $\Pi_{C,PtBA}$, ~ 24 mN•m^{-1}. Furthermore, PCL/PtBA blends were miscible in the monolayer regime and formed homogenous mixed monolayers below the collapse pressure of the PCL monolayer.[18] In this study, the thermodynamics and morphologies of the PCL-b-PtBA block copolymer monolayers are compared with the reported behavior of PCL/PtBA blends.

4.3. Materials and Methods

. The PCL-b-PtBA block copolymers were prepared by *atom transfer radical polymerization* (ATRP) as described in Chapter 3.1. The PCL monomer number fraction, f_{PCL}, was given by $f_{PCL} = n_{PCL}/(m_{PtBA} + n_{PCL})$, where n_{PCL} and m_{PtBA} were the number average degrees of polymerization for the PCL and PtBA blocks, respectively, determined by ^{1}H NMR. These values along with the number average molar mass (M_n) and polydispersity index (M_w/M_n) of the polymers deduced from gel permeation chromatography are summarized in Table 4.1. Experimental details for Π-A isotherm (Chapter 3.7.1), BAM (Chapter 3.7.3), optical microscopy (OM) and atomic force microscope (AFM) (Chapter 3.9.2) were covered in Chapter 3.

Table 4.1. Compositions and molar mass characteristics of PCL-b-PtBA

n:m	$f_{PCL} = \frac{n_{PCL}}{n_{PCL} + m_{PtBA}}$	**M_n (GPC) kg•mol^{-1}**	**M_w/M_n**
75:0	1	7.5	1.17
75:9	0.90	7.8	1.05
75:15	0.83	12	1.13
75:50	0.60	11.9	1.13
75:67	0.52	19.0	1.11
75:184	0.29	23.7	1.25
75:535	0.12	39.5	1.20

4.4. Results

4.4.1. Π-<A> Isotherms for PCL-b-PtBA Copolymers

Surface pressure (Π)-average area per monomer (Π-<A>) isotherm cycles for the PCL-b-PtBA copolymers were shown in Figure 4.1. Isotherms for compression and expansion corresponded to Figure 4.1 a and b respectively. For clarity, the isotherms for f_{PCL} = 0.52 were not shown. As clearly seen in Figure 4.1 a, the compression isotherms could be divided into two regimes separated by a common cross-over point. The two regimes were highlighted in two boxes in different colors. In the first regime (Π = 0 to 10.5 mN•m^{-1}), which corresponded to the monolayer regime, Π increased slowly with the decrease of <A> in a manner that was consistent with a comprisable monolayer. Meanwhile, the slopes of the curves increased as the PtBA block length increased, a result suggesting that the compressibility of the Langmuir film decreased with PtBA block length. According to a previous study,[18] the PtBA monolayer had a greater rigidity than the PCL monolayer; therefore, decreased compressibility of the Langmuir film correlated with decreasing f_{PCL} of the PCL-b-PtBA copolymers. The cross over point between the two regimes corresponded to Π ~ 10.5 mN•m^{-1} and <A> ~ 25 Å^2•mononer^{-1}. This transition point corresponded to the on-set of nucleation for the PCL crystals. The crossover Π was also the first collapse pressure for the PCL-b-PtBA copolymers ($\Pi_{C1,\ PCL\text{-}b\text{-}PtBA}$) and was similar to the dynamic collapse pressure of a pure PCL monolayer ($\Pi_{C,\ PCL}$) at the A/W interface.[16-17] The similarity between $\Pi_{C,\ PCL}$ and $\Pi_{C1,\ PCL\text{-}b\text{-}PtBA}$ was consistent with nucleation of PCL crystals for the PCL component of PCL-b-PtBA. In the second regime, PtBA blocks remained in a monolayer state. Consequently, Π increased further with compression of the Langmuir film. For the PCL rich block copolymers, f_{PCL} = 0.9 and 0.83, the compression isotherms exhibited a plateau after $\Pi_{C,PCL}$. Similar plateaus were also observed for the pure PCL homopolymer Π–A isotherms and were attributed to crystal growth, at which time, the crystal growth rate was equal to or faster than the barrier compression rate, whereby Π remained similar or lower than $\Pi_{C,PCL}$ respectively.[16-17] The lengths of the plateau decreased and Π in the crystal growth regime increased as the PtBA block length increased. This trend corresponds to the arrow in Figure 4.1 a. The decreased plateau length was attributed to a reduction of crystallizable material in the film as the PtBA block length increased. Stated another way, less PCL meant the monolayer became more like PtBA or less compressible. The compression finally led to the collapse of PtBA monolayer and the second collapse pressure, $\Pi_{C2,\ PCL\text{-}b\text{-}PtBA,}$ gradually approached ~ 24 $mN{\bullet}m^{-1}$ or $\Pi_{C,\ PtBA}$.[21-22]

The plateau in the expansion isotherm was the stage where PCL chains melted and respread (dissolved) on the A/W interface. In Figure 4.1 b, the plateau pressure depended upon PtBA block length: the plateau pressure for expansion increased and the plateau shortened dramatically as the PtBA block length increased. Higher pressures suggested that smaller crystals were formed during compression and these chains melted and respread more easily (at a higher Π). For PtBA-rich block copolymers, f = 0.12 and 0.29, the plateau was absent and only a slight kink in the isotherm was present.

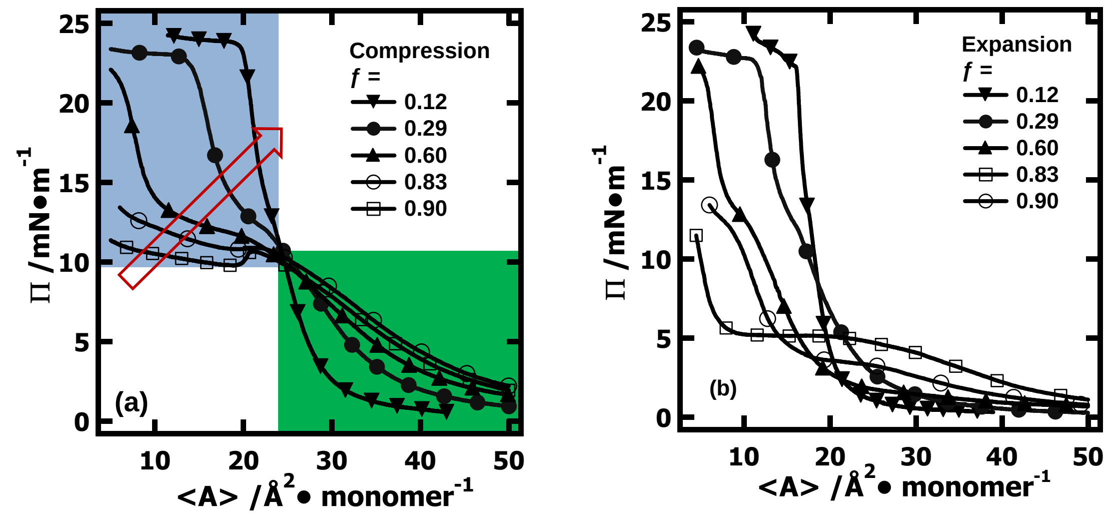

Figure 4.1. Π-<A> (a) compression and (b) expansion isotherms for PCL-b-PtBA copolymers at the A/W interface. The isotherms were obtained at T = 22.5 °C and a compression/expansion rate of 10 cm^2•min^{-1}. The symbols in this figure correspond to *f* = 0.12 (▼), 0.29 (●), 0.60 (▲), 0.83 (○), 0.90 (□).The arrow on (a) indicates that Π for the crystallization plateau increased as PtBA block length increased.

4.4.2. Compressibility of the PCL-b-PtBA Monolayers

For Langmuir monolayers, static dilational elasticities (ε_s) yield quantitative measures of monolayer surface compressibility (κ_s):

$$\varepsilon_s = {\kappa_s}^{-1} = -A\left(\frac{\partial \Pi}{\partial A}\right)_T \tag{4-1}$$

In Eq.4-1, ε_s and κ_s were the 2D analogs of the bulk modulus and bulk isothermal compressibility, respectively.[23] If one views the A/W interface as a 2D solvent for amphiphilic polymers, the surface concentration can be divided into dilute, semi-dilute and concentrated regimes. In the semi-dilute regime, scaling theory predicts Π scales with surface concentration and is molar mass independent.[24] Furthermore, Esker et al.[23] noted that at the start of the semi-dilute regime, $\varepsilon_s \cong z\Pi$ where Z is the scaling exponent. For a good solvent where chains have solvent swollen 2D conformations, z = 3.[25-26] In contrast predictions for theta solvent conditions where chains have unperturbed 2D chain conformations z ranged from = 8 to 101 for different numerical methods to infinity for a mean field model.[27-29] Through this analysis scheme, Li et al.[18] showed that the A/W interface was a good solvent for PCL and nearly a theta solvent for PtBA. In Figure 4.2 a, ε_s for the block copolymers were plotted as a function of Π. For clarity, the curves for f_{PCL} = 0.83 and 0.60 were not included. Two maxima $\varepsilon_{s,max}$ were observed. One was the $\varepsilon_{s,max}$ for the monolayer regime, while the other was the maximum for the second regime. Between the two $\varepsilon_{s,max}$, a local minimum existed. This minimum was attributed to collapse of the PCL block. With the established solvent scaling argument, in the inset of Figure 4.2 a, the initial slopes at low Π in the monolayer regime were compared to a solid line with a slope of 2.86 (good solvent) and a dashed line with a slope of 8 (theta solvent). As observed, the slopes fell between these two lines and the solvent quality shifted toward theta solvent scaling as the PtBA block length increased.

For ε_s versus <A> in Figure 4.2 b, two maximum static elasticities ($\varepsilon_{s,max}$) were also observed in two distinct regions: $\varepsilon_{s,max,1}$ for <A> > 30 Å^2•monomer^{-1} ($\Pi < \Pi_{C,PCL}$) and $\varepsilon_{s,max,2}$ for <A> < 30 Å^2•monomer^{-1} ($\Pi_{C,PCL} < \Pi_{C,PtBA}$). As a summary, all the $\varepsilon_{s,max}$ plus the corresponding <A($\varepsilon_{s,max}$)> for the two regimes are tabulated in Table 4.2. Focusing on the Langmuir monolayer regime, <A> > 30 Å^2•monomer^{-1} ($\Pi < \Pi_{C,PCL}$), there was a progressive increase in $\varepsilon_{s,max,1}$ and decrease in <A($\varepsilon_{s,max,1}$)> as PtBA block length increased. The increase in $\varepsilon_{s,max,1}$ was coupled with a change from good-solvent scaling behavior, to poorer (approaching theta) solvent scaling behavior as the PtBA block length increased. The enhancement of $\varepsilon_{s,max,1}$ with decreasing f_{PCL} was consistent with adding rigid, nonswollen material to the monolayer film. Hence the principal effect, rising modulus, was similar to the case of adding compatible fillers to a soft polymer. After collapse of the PCL monolayer, the crystalline or multilayer PCL domains effectively plasticized the PtBA that remained at the A/W interface and led to progressively smaller $\varepsilon_{s,max,2}$ at smaller <A($\varepsilon_{s,max,2}$)> as shown in Figure 4.2 b and Table 4.2. This thermodynamic analysis of the rigidity for PCL-b-PtBA copolymer monolayers was similar to the results for PCL/PtBA blend monolayers,[18] an indication that the compressibility of the film was not affected by the connection of the two blocks.

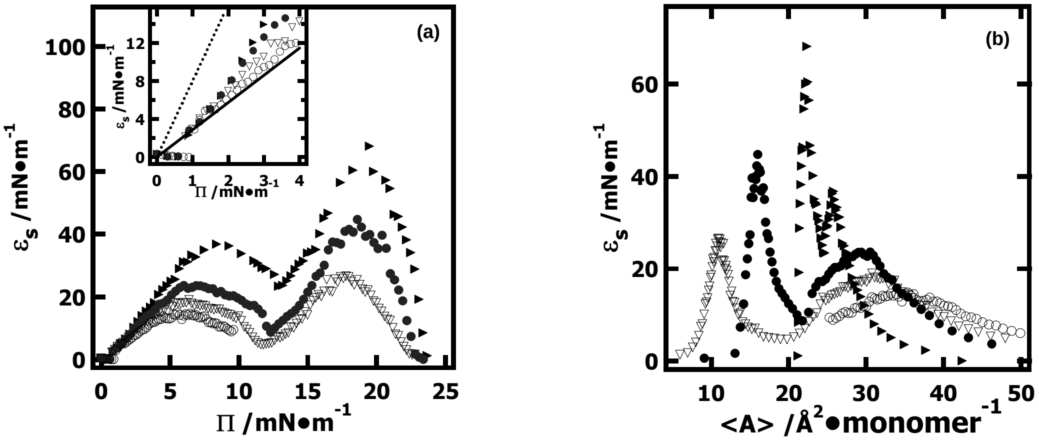

Figure 4.2. (a) ε_s versus Π and (b) ε_s versus <A> for PCL-b-PtBA block copolymers at the A/W interface. ε_s were derived from the isotherms in Figure 4.1. The inset of (a) focused on the behavior at low Π. Theoretical curves, $\varepsilon_s = z\Pi$, for good solvent conditions (z = 2.86, solid line),[26] and the least extreme numerical value for theta solvent conditions (z = 8, dashed line) are included on the inset.[27] The symbols in this figure correspond to *f* = 0.90 (○), 0.52 (∇), 0.29 (●), and 0.12 (►).

Table 4.2. Elasticity maxima for PCL-b-PtBA copolymers at the A/W interface

f	$<A(\varepsilon_{s,max,1})>$ $Å^2$•monomer^{-1}	$\varepsilon_{s,max,1}$ mN•m^{-1}	$<A(\varepsilon_{s,max,2})>$ $Å^2$•monomer^{-1}	$\varepsilon_{s,max,2}$ mN•m^{-1}
1	37.5	13.2	N/O	N/O
0.9	38	13.5	N/O	N/O
0.83	37.0	14	N/O	N/O
0.6	32.0	16	8.0	22.8
0.52	30.8	19.0	11.1	26.3
0.29	29.4	23.6	16.0	44.7
0.12	25.4	36.7	21.0	68.0
0	N/O	N/O	24.6	84.7

N/O = not observed.

4.4.3. Morphological Studies of PCL-b-PtBA Langmuir Films

In a report by Li et al.,[18] the PCL/PtBA blend monolayers formed dendritic crystals due to diffusion limited crystallization and the dendritic morphology were only observed at low PtBA compositions. In the PCL-b-PtBA copolymer monolayers, the presence of PtBA hindered the diffusion of the crystallizable material to the crystal growth front. At the same time, PCL chain mobility was further restricted due to an attachment point with the PtBA block. Therefore, different morphologies were anticipated. Brewster angle microscope (BAM) proved to be less valuable for the study than earlier work with linear PCL homopolymer,[16-17] because the features formed after the collapse of the PCL block were too small to be distinguished by BAM, especially for PtBA rich block copolymers. For PCL rich block copolymers, some vague features in BAM after PCL collapse were observed. Figure 4.3 has a Π-<A> compression/expansion isotherm cycle and representative BAM images for $f = 0.52$. The BAM images were edited by an image processing computer program and the image colors were inverted so that the black background appeared to be gray and the original bright features became black in the edited images of Figure 4.3. At low Π, there were no observable features. This observation was consistent with a homogeneous monolayer for PCL-b-PtBA. After the transition point, some small features were present. Upon expansion of the film, these features disappeared. These observations were consistent with the melting and respreading (dissolution) of PCL at the A/W interface observed for PCL homopolymer.[16-17]

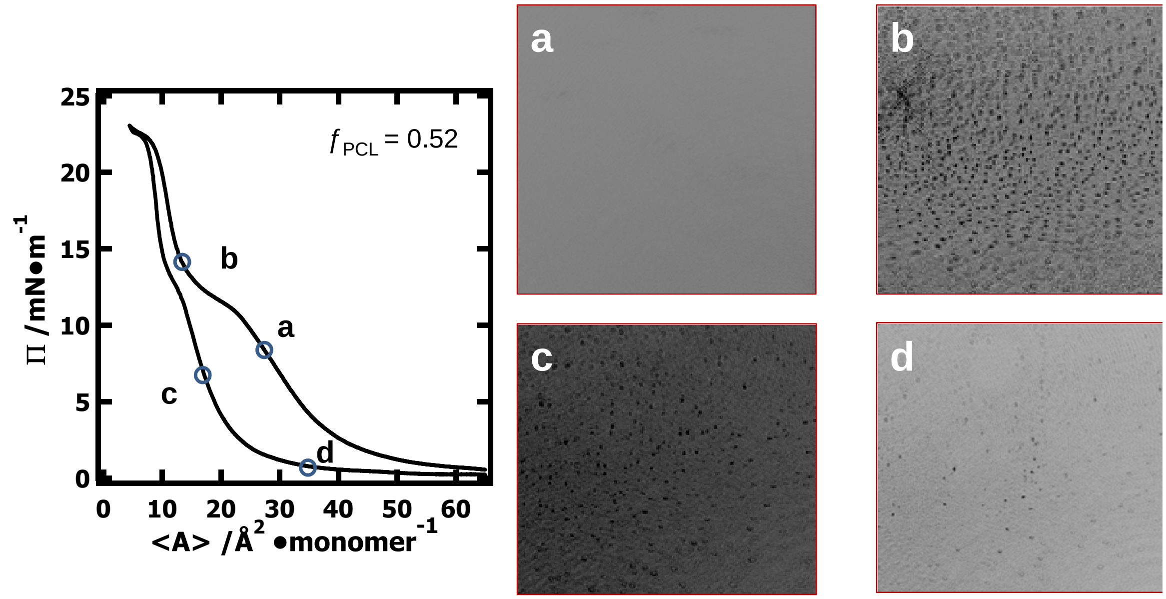

Figure 4.3. (a)-(d) Representative BAM images (1.0 mm × 1.0 mm) for PCL-b-PtBA copolymers at f_{PCL} = 0.52 that corresponded to the Π-<A> compression/expansion isotherm cycle obtained at T = 22.5 °C and a compression/expansion rate of 10 cm^2•min^{-1}. The color of the BAM images was inverted and the contrast was enhanced so that the original bright features appeared black and the black background turned gray.

4.4.4. Morphological Studies of LB-Films of PCL-b-PtBA Copolymers

Detailed morphologies for PCL-b-PtBA crystals grown in the Langmuir films were revealed by optical microscopy (OM) and atomic force microscopy (AFM) studies on LB-films. The LB-films were transferred on the upstroke onto hydrophilic cellulose surfaces regenerated from spincoated trimethysilyl cellulose for optical microscopy (OM) studies and freshly cleaved mica surfaces for AFM imaging. For f_{PCL} = 1, 0.9 and 0.83, the LB-films were transferred at $\Pi \sim 12$ mN•m^{-1}, while the other LB-films were transferred at $\Pi = 17$ mN•m^{-1}. Representative OM images were shown in Figure 4.4. A trend for the morphology change as the PtBA block length increased was clearly observed along the arrow in Figure 4.4. At large f_{PCL}, crystal sizes decreased relatively to the pure PCL starting block.

At f_{PCL} = 0.6 and 0.52, some irregularly shaped crystals were obtained. Finally, for f_{PCL} = 0.29 and 0.12 (PtBA rich block copolymers), the morphological features of the LB- films were smaller than the resolution of OM.

Detailed morphologies of the LB-films were obtained from AFM studies presented in Figure 4.5. The AFM images confirmed the trend observed in Figure 4.4. For f_{PCL} = 0.9 and 0.83 (Figure 4.5 b and c), the crystals were multi-faceted compared to the large crystals of pure PCL in Figure 4.5 a. For f_{PCL} = 0.6 (Figure 4.5 d), the six armed dendrites had one under-developed arm connected to a long stripe. The six axes for the six arms were clearly observed in the expanded image in Figure 4.5. The dendritic six arms had inequivalent sizes that were attributed to the uneven growth of the six arms. For f_{PCL} = 0.52 (Figure 4.5 e), the size of the dendrites diminished further and long stripes became the prevalent features. These structures coexisted with some smaller multi-faceted features, indicating that the polydispersity of the block copolymer may have caused a coexistence of different crystal morphologies. When f_{PCL} = 0.29 (Figure 4.5 f), only long stripes were obtained. For f_{PCL} = 0.12 (Figure 4.5 g), the LB-films had morphologies that resembled “islands and the sea” and in this image, small nanoscale PCL domains protruded from the surface.

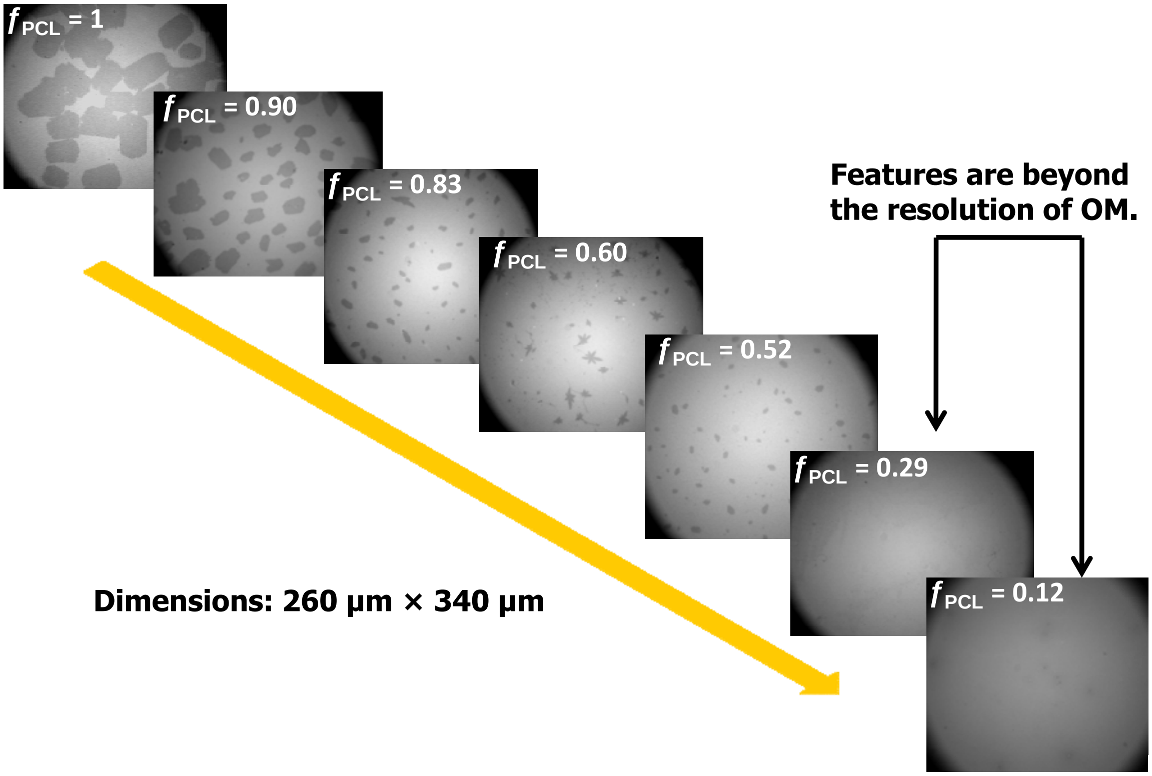

Figure 4.4. OM images for the PCL-b-PtBA LB-films. The arrow highlights decreasing f_{PCL}.

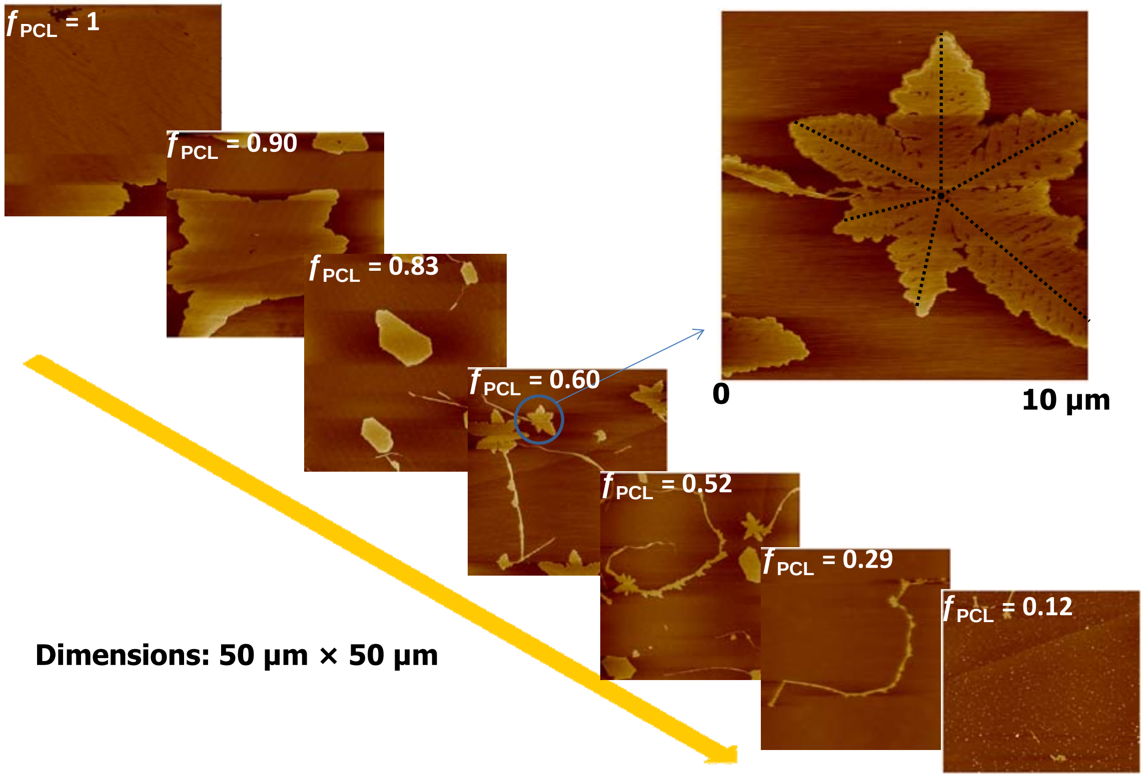

Figure 4.5. AFM height images (*z*-scale 0-30 nm) for PCL-b-PtBA copolymer LB-films. The arrow highlights decreasing f_{PCL}. The larger AFM image (10 μm × 10 μm, *z* scale 0-30 nm) was blown up from the f_{PCL}= 0.60 image. The six dashed lines indicated the six axes for the six arms.

AFM line scan analyses revealed the thickness of the crystals depended on f_{PCL}. As seen in Figure 4.6 a and b, the crystals for a PCL-rich copolymer, $f_{PCL} = 0.9$, had a thickness of ~ 8 nm which was consistent with the reported thickness of PCL homopolymer crystals.[16-17] In contrast, crystals for f_{PCL} = 0.6 were ~ 10 nm thick as seen in Figure 5.6 c and d. This value was ~ 2 nm thicker than the crystals formed by PCL homopolymers and the PCL-rich block copolymers. For f_{PCL} = 0.12, as seen in Figure 4.6e and f, the height of the protruding cylindrical structures varied from 5 to 11 nm.

LB-films were also prepared after the PtBA blocks collapsed ($\Pi > \Pi_{C,PtBA}$) and were subsequently analyzed by AFM. Representative AFM height images and the line scan analyses for f = 0.6, 0.52 and 0.29 are shown in Figure 4.7. As seen in Figure 4.7 a, c, and e, the morphologies were not significantly different from crystals transferred before the collapse of the PtBA block in Figure 4.6. In Figure 4.7 a, f = 0.6, the dendritic morphologies remained after the PtBA block collapsed. However, the line scans in Figure 4.7 b revealed that the edges of the dendrites were significantly thicker than the center of the crystals. Observations made for f_{PCL} = 0.52 and 0.29 were similar. As seen in Figure 4.7 d, line scan showed that the thickness of the edge was twice as thick as the center of the crystal. For f_{PCL} = 0.29, in Fig 4.7 e and f, a small scale bi-continuous striped structure was observed and the thickness of the stripe was ~ 2 nm thicker than the structure obtained before PtBA collapsed.

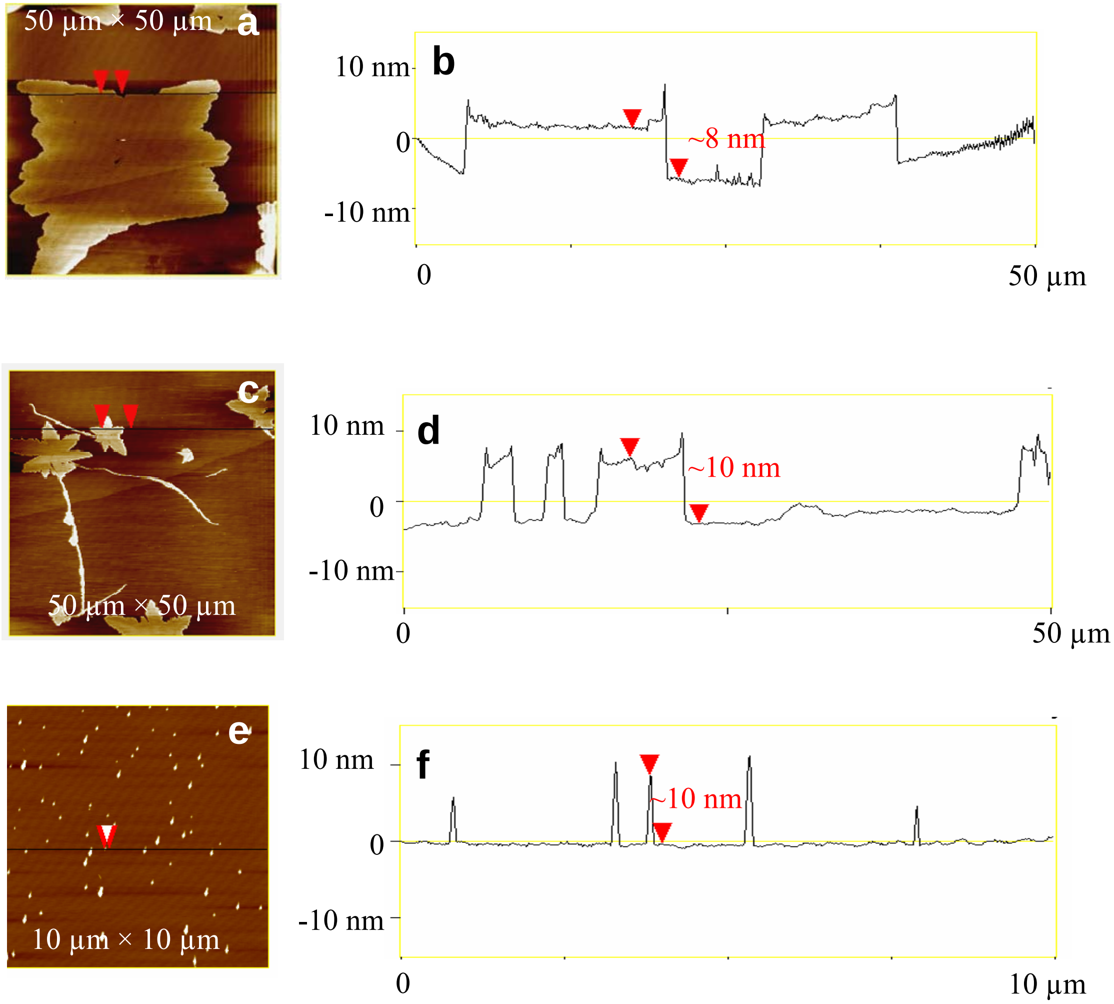

Figure 4.6. Representative AFM height images (*z*-scale = 0-30 nm) and line scans for LB-films: (a) and (b) f_{PCL} = 0.9, (c) and (d) for f_{PCL}= 0.6, and (e) and (f) for f_{PCL} = 0.12.

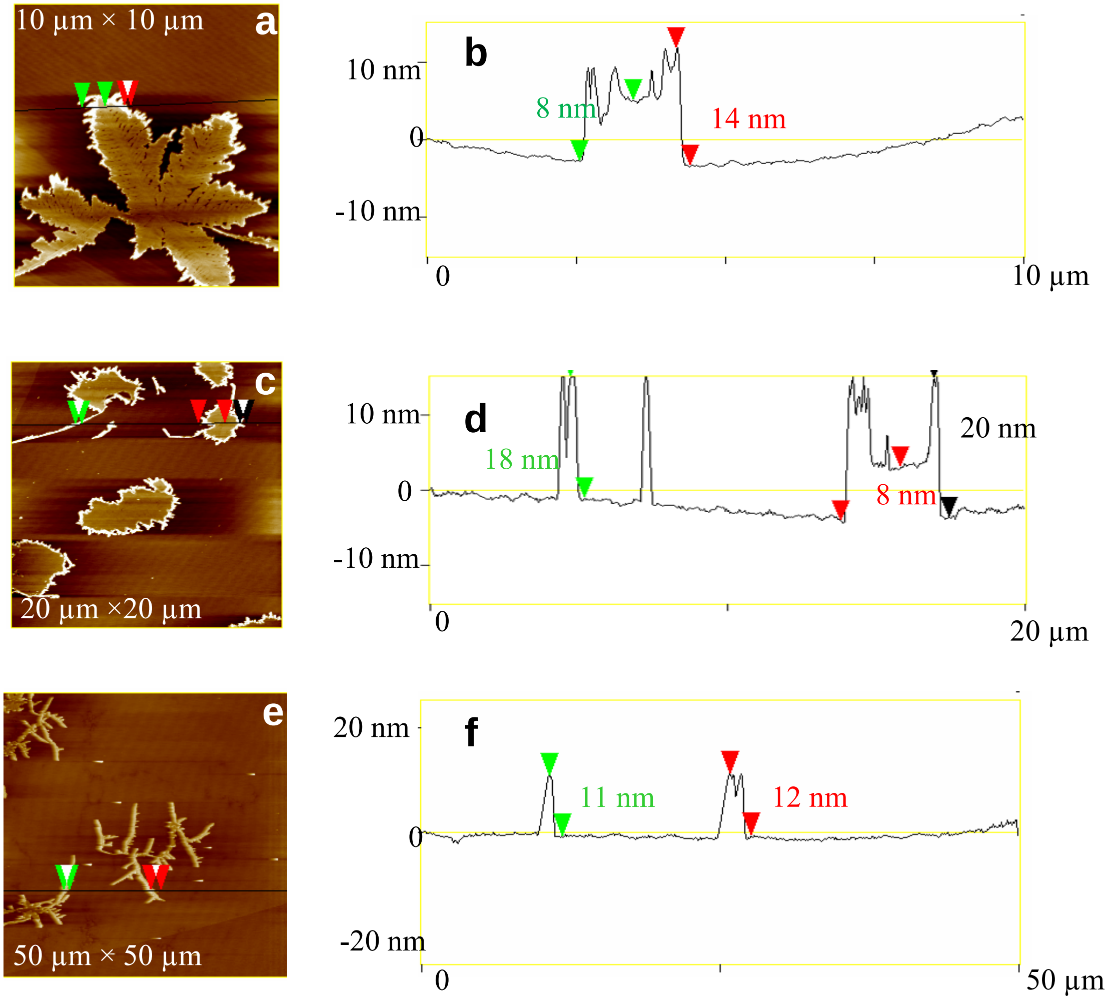

Figure 4.7. AFM height images and line scans for PCL-b-PtBA LB-films transferred after the collapse of the PtBA monolayer: (a) and (b) f_{PCL} = 0.6, $\Pi = 23$ mN•m^{-1}; (c) and (d) f_{PCL} = 0.52, $\Pi = 22$ mN•m^{-1}; (e) and (f) f_{PCL}= 0.29, $\Pi = 23$ mN•m^{-1}.

4.5. Discussion

The morphologies observed for LB-films of the block copolymers discussed above were attributed to hindered diffusion of PCL chains to the crystal growth front. In general, the availability of supersaturated PCL blocks played an essential role in the crystal morphologies; the growth of crystals was mainly controlled by the local diffusion field around the growth fronts and the availability of the crystallizable materials. In the PCL/PtBA blend monolayers, the PCL chains diffused through the amorphous PtBA monolayer phase to reach the crystal growth fronts. Consequently, large diffusion-limited, dendritic crystalline morphologies were observed at low PtBA compositions.[18] In this study, the PCL chains were chemically connected to the PtBA as block copolymers, therefore, the diffusion of PCL chains was further hindered and PCL chains only crystallized with PCL chains in the adjacent area. Moreover, the presence of the amorphous PtBA blocks at the edge of PCL crystals hindered the assembly of the PCL chains onto the crystal growth edges. The direct results were the crystal sizes and morphologies that changed from well-defined single crystals to dendrites with defects, stripes and finally to nano-scale cylindrical domains as f_{PCL} decreased. The conformation of the block copolymers had to arrange in a way that PtBA blocks remained at the PCL crystal edge and maintained a monolayer underneath the crystals when PCL chains folded up to form crystals. This arrangement possibly attributed to the additional ~ 2 nm of thickness observed for intermediate f_{PCL}relative to PCL or PCL-rich copolymer crystals, as noted in the previous AFM results section. However, LB-films of homopolymer revealed monolayer thicknesses of ~ 1 nm.[30] One possible explanation for this discrepancy was that the linking group from the bi-functional initiator between the PtBA and PCL blocks, contributed another ~ 1 nm of thickness to the conformation depicted in Figure 4.8. The conformational prediction of Figure 4.8 was reasonable because the thickness of the center part of the crystals returned to ~ 8 nm after collapse of the PtBA blocks in Figure 4.7 b and d.

A value of 8 nm is the thickness for PCL homopolymers, indicating that the connection groups of the two block may remain at the edge of the crystal during crystallization of the block copolymers. For f_{PCL} = 0.12, the limited amount of PCL for crystallization likely impacted for the height of the crystalline features as some cylinder domains were only ~ 5 nm thick which was significantly thinner than the average thickness of ~10 nm.

The morphological evolution of the crystalline features of the block copolymers could be better understood through analysis of possible 2D polymer chain conformations at the A/W interface. As mentioned previously, the A/W interface was a near theta solvent for PtBA monolayer; whereas, it was a good solvent for PCL monolayer. In 2D, the Flory radius (R_F) of the random coils for a theta solvent is given by assuming an unperturbed 2D random coil conformation:[31]

$$R_F = bN^{0.5} \tag{4-2}$$

while R_F for a good solvent is[28]

$$R_F = bN^{0.75} \tag{4-3}$$

In Eqs. 4-2 and 4-3, b is the length of the repeat unit and N is the degree of polymerization. b is taken as 0.15 nm for the PtBA repeat unit and 0.76 nm for PCL repeat unit. N were obtained from Table 4.2. On the basis of these numbers, R_F for PCL was calculated to be 19 nm and the area occupied by the PCL random coil was equal to R_F^2 = 361 nm^2. This result indicated that PCL chains adopted a highly expanded conformation at the A/W interface. As the PtBA block varied in the PCL-b-PtBA copolymers, calculated values of R_F and R_F^2 for different PtBA blocks were tabulated in Table 4.3. Meanwhile, the cross sectional area (α) for the crystal unit formed by a single PCL block with M_n = 7500 g•mol^{-1} was calculated according to Eq. 4-5.

$$\alpha = \frac{7500}{N_a d_{PCL} h} \tag{4-5}$$

where N_a is the Avogadro's number; d_{PCL} is the density for a PCL crystal (1.05 g•cm^{-3}) and h is the thickness of the PCL crystals (~ 8 nm from AFM). α is calculated to be ~1.5 nm^2 for the PCL block. The ratios of the PtBA random coil area to α were also tabulated in Table 4.3. As seen in the Table 4.3 and Figure 4.5, for small f_{PCL}, the dense PtBA layer inhibited the diffusion of PCL chains onto the crystal growing edge. As a consequence, the crystal could grow significantly in one-dimension and led to long striped crystals. A tentative rule for the morphology formation was developed based on the ratio (θ) of α to $R_{F,PtBA}^2$ ($\theta = \alpha/R_{F,PtBA}^2$), as an analog to the surfactant number which was the ratio of the hydrophobic tail group cross section area to the effective area of hydrophilic head group. For large θ (θ > 4) smaller crystals were obtained; for intermediate θ (1.3 > θ > 0.36), stripes were the pre-dominant features. At θ = 1.3, dendrites with defects were obtained. Finally, small θ led to the formation of cylindrical structures. Due to the polydispersity of the polymer, distributions of the different morphologies were observed. These analyses were analogues to the effects of surfactant number as discussed in Chapter 2.

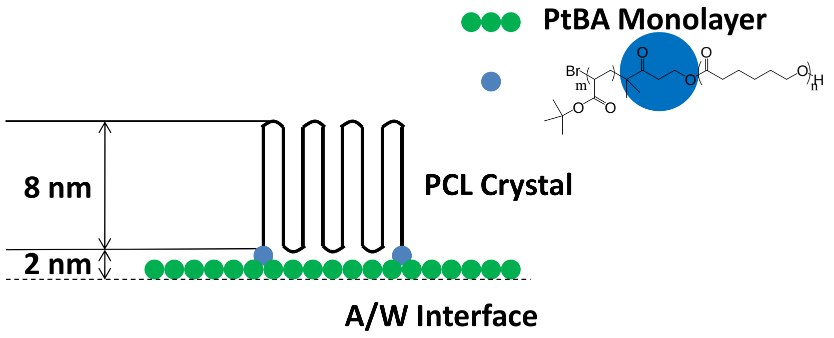

Figure 4.8. A depiction of a possible conformation for PCL-b-PtBA copolymers after the crystallization of PCL block and before collapse of the PtBA monolayer.

Table 4.3. 2D Flory radii for PtBA blocks

f_{PCL}	$(\mathrm{CL})_{75}$-b-$(\mathrm{tBA})_m$ m	$R_{F,PtBA}$ (nm)	$R_{F,PtBA}^2$ (nm^2)	($\theta = \alpha/R_{F,PtBA}^2$)
0.9	9	0.45	0.20	7.7
0.83	15	0.58	0.34	4.5
0.6	50	1.06	1.12	1.3
0.52	67	1.22	1.50	1
0.29	184	2.03	4.14	0.36
0.12	535	3.47	12.03	0.12

4.6. Conclusions

Thermodynamically, Π–A isotherm studies revealed PCL-b-PtBA copolymer monolayers were similar to PCL/PtBA blend monolayers at the A/W interface. Hence, tethering PCL to the PtBA block had little effect on compatibility in the monolayer state. However, the OM and AFM studies for the LB-films transferred after the collapse of PCL block exhibited different morphologies relative to the physical blends and the morphologies were dependent on the block length of the PtBA block. As the block length of PtBA increased, the morphologies of the LB-films became smaller and transitioned to dendrites with defects, stripes and finally nano-scale cylindrical features. The results also showed that the collapse of the PtBA blocks did not affect the crystal morphology which formed before the collapse of PtBA. The collapsed PtBA collected at the edge of the crystalline domains.

This study shows that block copolymers at the A/W interface provide a framework for studying crystallization in restricted 2D environments. As discussed in Chapter 2, theoretical studies predicted striped and spherical domains for micro-phase separation of the block copolymers in 2D. However, it was difficult to prove the concept experimentally due to the difficulty of manipulating molecules in a 2D geometry.[32] In this study, the block copolymers were confined in a psuo-2D system, the A/W interface, and microphase separation was induced by crystallization of one block. Although the mechanism of the phase separation was different from the theoretical predictions, the resulting morphologies exhibited stripes and spherical domains at compositions expected for block copolymers. The study shows that

Langmuir films can be applied to the studies of microphase separation for block copolymers in 2D.

4.7. References

(1) Hamley, I. W. *Prog. Polym. Sci.* **2009**, *34*, 1161.

(2) Albrecht, K.; Mourran, A.; Zhu, X.; Markkula, T.; Groll, J.; Beginn, U.; de Jeu, H. W.; Moeller, M. *Macromolecules* **2008**, *41*, 1728.

(3) Boschetti-de-Fierro, A.; Spindler, L.; Reiter, G.; Olmos, D.; Magonov, S.; Abetz, V. *Macromolecules* **2007**, *40*, 5487.

(4) Busch, P.; Krishnan, S.; Paik, M.; Toombes, E. S. G.; Smilgies, D. M.; Gruner, S. M.; Ober, K. C. *Macromolecules* **2007** *40*, 81.

(5) Liang, G. D.; Xu, J. T.; Fan, Z. Q.; Mai, S. M.; Ryan, J. A. *Macromolecules* **2006**, *39*, 5471.

(6) Fu, J.; Luan, B.; Pan, C.; Li, B.; Han, Y. *Macromolecules* **2005**, *38*, 5118.

(7) Zhang, F.; Chen, Y.; Huang, H.; Hu, Z.; He, T. *Langmuir* **2003**, *19*, 5563.

(8) Verploegen, E.; Zhang, T.; Jung, Y. S.; Ross, C.; Hammond, P. T. *Nano Lett.* **2008**, *8*, 3434.

(9) Olsen, D. B.; Alcazar, D.; Krikorian, V.; Toney, M. F.; Thomas, E. L.; Segalman, A. R. *Macromolecules* **2008**, *41*, 58.

(10) Liang, G. D.; Xu, J. T.; Fan, Z. Q.; Mai, S. M.; Ryan, J. A. *Langmuir* **2007**, *23*, 3673.

(11) Reiter, G.; Castelein, G.; Hoerner, P.; Riess, G.; Sommer, J.-U.; Floudas, G. *Eur. Phys. J. E* **2000**, *2*, 319.

(12) Liang, G. D.; Xu, J. T.; Fan, Z. Q.; Mai, S. M.; Ryan, J. M. *Polymer* **2007**, *48*, 7201.

(13) Yang, P.; Han, Y. *Macromol. Rapid Commun.* **2008**, *29*, 1614.

(14) Wei, Y.; Pan, C.; Li, B.; Han, Y. *J. Chem. Phys.* **2007**, *126*, 104902.

(15) Zhang, X.; Berry, C. B.; Yager, G. K.; Kim, S.; Jones, L. R.; Satija, S.; Pickel, L. D.; Douglas, F. J.; Karim, A. *ACS Nano* **2008**, *2*, 2331.

(16) Li, B.; Esker, A. R. *Langmuir* **2007**, *23,* 2546.

(17) Li, B.; Wu, Y.; Liu, M.; Esker, A. R. *Langmuir* **2007**, *22*, 4902.

(18) Li, B.; Marand, H.; Esker, A. R. *J. Polym. Sci. Part B: Polym. Phys.* **2007**, *45*, 3300.

(19) Joncheray, J. T.; Denoncourt, M. K.; Mathieu, C.; Meier, A. R. M.; Schubert, S. U.; Duran, S. R. *Langmuir* **2006**, *22*, 9264.

(20) Joncheray, J. T.; Denoncourt, M. K.; Meier, A. R. M.; Schubert, S. U.; Duran, S. R. *Langmuir* **2007**, *23*, 2423.

(21) Mudgil, P.; Dennis, G. R.; Millar, T. J. *Langmuir* **2006**, *22*, 7672.

(22) Li, S.; Hanley, S.; Khan, I.; Varshney, S. K.; Eisenberg, A.; Lennox, R. B. *Langmuir* **1993**, *9*, 2243.

(23) Esker, A. R.; Zhang, L.-H.; Sauer, B. B.; Lee, W.; Yu, H. *Colloids Surf. A* **2000**, *171*, 131.

(24) Vilanove, R.; Rondelez, F. *Phys. Rev. Lett.* **1980**, *45*, 1502.

(25) Le Guillou, J. C.; Zinn-Justin, J. *Phys. Rev. B* **1980**, *21*, 3976.

(26) Stephen, M.; McCauley, J. *Phys. Lett.* **1973**, *44A*, 89.

(27) Duplantier, B.; Saleur, H. *Phys. Rev. Lett.* **1984**, *59*, 539.

(28) de Gennes, P.-G. *Scaling Concepts in Polymer Physics*; Cornell University: Ithaca, NY, 1979.

(29) Granick, S. *Macromolecules* **1985**, *18*, 1597.

(30) Mengel, C.; Esker, A. R.; Meyer, W. H.; Wegner, G. *Langmuir* **2002**, *18,* 6365.

(31) Flory, P. J. *Principles of Polymer Chemistry*; Cornell Univ. Press, Ithaca, NY,

1971.

(32) Li, J. F.; Fan, J.; Zhang, H. D.; Qiu, F.; Tang, P.; Yanga, Y. L. *Eur. Phys. J. E* **2006**, *20*, 449.

Chapter 5

Morphological Studies of Poly(ε-caprolactone) Stabilized Magnetic Nanoparticles at the Air/Water Interface

5.1. Abstract

Previous studies of linear poly(ε-caprolactone)s (PCLs) showed they formed butterfly shaped lamellar crystals at the air/water (A/W) interface at elevated surface pressure (Π). In this chapter, the crystallization of three synthesized PCL derivatives, PCL with bulky tri-tert-butyl ester endgroups (PCL triesters), PCL with triacid end groups (PCL triacids), and magnetic nanoparticles stabilized by PCL triacid (PCL MNPs), were studied at the A/W interface. For the case of PCL triester, irregularly shaped crystals formed at the A/W interface and this was attributed to the accumulation of bulky tert-butyl ester groups around the crystal growth fronts. In contrast, regular, round-shaped lamellar crystals were obtained for PCL triacids. These morphological differences between PCL triacids and PCL triesters were molar mass dependent and were attributed to differences in dipole density and the submersion of carboxylic acid groups in the subphase. Nonetheless, enhanced uniformity for PCL triacid crystals was not retained once the polymers were tethered to the spherical surface of a PCL MNP. Instead, the PCL MNPs exhibited small irregularly shaped crystals. This nanoscale confinement effect on the surface morphology at the A/W interface was also molar mass dependent. For the smallest molar mass PCL MNPs, two layers of collapsed nanoparticles were observed.

5.2. Introduction

Polymer nanoparticle composites gained increasing attention in industry and academia due to their wide-spread applications and special properties. A resurgence of nanocomposites research over the past decade was fueled by the growing availability of nanoparticles with precisely controlled sizes and shapes.[1] For a broader application of polymer composites, it is necessary to comprehend their structure-property relationships. Attempts have been made to study blends of nanoparticles with homopolymers or block copolymers.[2-10] When the polymers were semi-crystalline, the crystallization of the nanocomposites was particularly intriguing. The attachment of polymer chains to nanoparticles is another mechanism for chain confinement. Some studies have shown nanoscale objects and nano-fillers effect crystallization. For examples, carbon nanotubes induced polymer crystallization and yielded unique nanohybrid Shish-Kebab morphologies.[11-12] Likewise, nanofillers altered the crystallization kinetics and mechanical properties of polymeric matrices.[13-16] However, there is a lack of studies on the effects nanofillers have on the formation of polymeric lamellar crystals.

At the A/W interface, a pseudo two-dimensional (2D) system, poly(ε-caprolactone) (PCL) was shown to from lamellar crystals at elevated surface pressure (Π).[17] PCL was the first and at present only reported homopolymer which has clearly undergone crystallization at the a A/W interface.[17-18] The unique behavior of PCL enabled systematic studies of the transformation from a monolayer to lamellar crystals. Li et al.[19] subsequently reported that mixtures of PCL and poly(*tert*-butyl acrylate) (PtBA) exhibited dendritic crystalline morphologies resembling the morphologies of binary thin film polymer blends that underwent diffusion limited crystallization.[20-21] Studies of PCL crystallization in block copolymers with a water soluble block, poly(ethylene oxide) (PEO), as a diblock copolymer (PCL-b-PEO),[22] and PEO-PCL star copolymer[23] followed. More recently, PCL crystallization in graft copolymer brushes has also been reported.[24] These studies demonstrated that PCL crystallization at the A/W interface shared many common features with PCL crystallization in thin films on solid substrates. In Chapter 4, we reported how confinement by another amphiphilic block poly(t-butyl acrylate) (PtBA) altered PCL crystallization. The act of tethering PCL to PtBA altered PCL crystallization relative to linear PCL homopolymer and PCL/PtBA blends at the A/W interface. Morphological features of PCL-b-PtBA changed from reduced crystal sizes, dendritic, linear and finally nanoscale protruding cylindrical features as the PtBA block length increased.

In this chapter, the effects confinement of PCL to the surface of a nanoscale sphere had on crystallization were studied. PCLs with a single triester (PCL triester) were synthesized through ring opening polymerization of ε-caprolatone monomers from a synthesized triester initiator. The PCL triesters were then deprotected to afford triacids (PCL triacids)The PCL triacids were subsequently used to convert synthesized oleic acid stabilized magnetic nanoparticles (MNPs) with an average diameter of 9 nm into PCL stabilized MNPs (PCL MNPs) as detailed in Chapter 3. Dynamic light scattering (DLS) and transmission electron microscopy (TEM) were used for the size characterization of the MNPs. These polymers and MNPs were then used for the study of how PCL crystallization at the A/W interface was affected by bulky endgroups and confinement to the surface of the MNPs. Surface pressure-area per monomer (Π–A) isotherms were used to elucidate thermodynamic features of the crystallization process and Brewster angle microscopy (BAM) was used to monitor the surface morphology changes during surface pressure-area per monomer (Π–A) isotherm cycles.

5.3. Materials and Methods

Details for the synthesis of PCL triester (Chapter 3.2.3), PCL triacid (Chapter 3.2.4), and PCL MNPs (Chapter 3.3), were covered in Chapter 3. Throughout this chapter, “k” will be used as short notation for kg•mol^{-1} when the number average molar mass (M_n) is used to distinguish between polymers with different molar masses. For this study, three different PCL M_n were used, 3 k, 6 k and 9 k. Experimental details for Π-A isotherm (Chapter 3.7.1), BAM (Chapter 3.7.3), DLS (Chapter 3.10.2), TEM (Chapter 3.9.3) and thermogravimetric analysis, optical microscopy (OM) and atomic force microscopy (AFM) were also covered in Chapter 3.

5.4. Results and Discussion

5.4.1. MNP Characterization. DLS data for MNPs in $CHCl_3$ are provided in Figure 5.1. In Figure 5.1A, the intensity weighted size distribution obtained from a CONTIN analysis at a scattering angle of 90° showed monomodal and narrow size distributions for the particles before and after ligand exchange. No large aggregates were seen after ligand exchange. Correspondingly, the nearly linear relationships of $(\ln(g_2(\tau) - 1))$ as a function of decay time (τ) in Figure 5.1B-E were consistent with narrow size distributions. $g_2(\tau)$ is the intensity autocorrelation function as introduced in Chapter 2. Average decay rates ($\bar{\Gamma}$) deduced from the fits in Figure 5.1B-E were plotted as a function of the square of the scattering wave vector (q^2) in Figure 5.1F. The almost perfectly linear relationships for all particles were consistent with simple diffusive motion. Furthermore, the zero intercepts were consistent with MNPs that had isotropic spherical shapes. Mutual diffusion coefficients (D_m) deduced from the slopes of the lines in Figure 5.1F were converted into hydrodynamic radii (R_h). D_m and R_h values are summarized in Table 5.1. D_m and R_h systematically increased with PCL molar mass. Values for the polydispersity indices (PDI) are also summarized in Table 5.1.

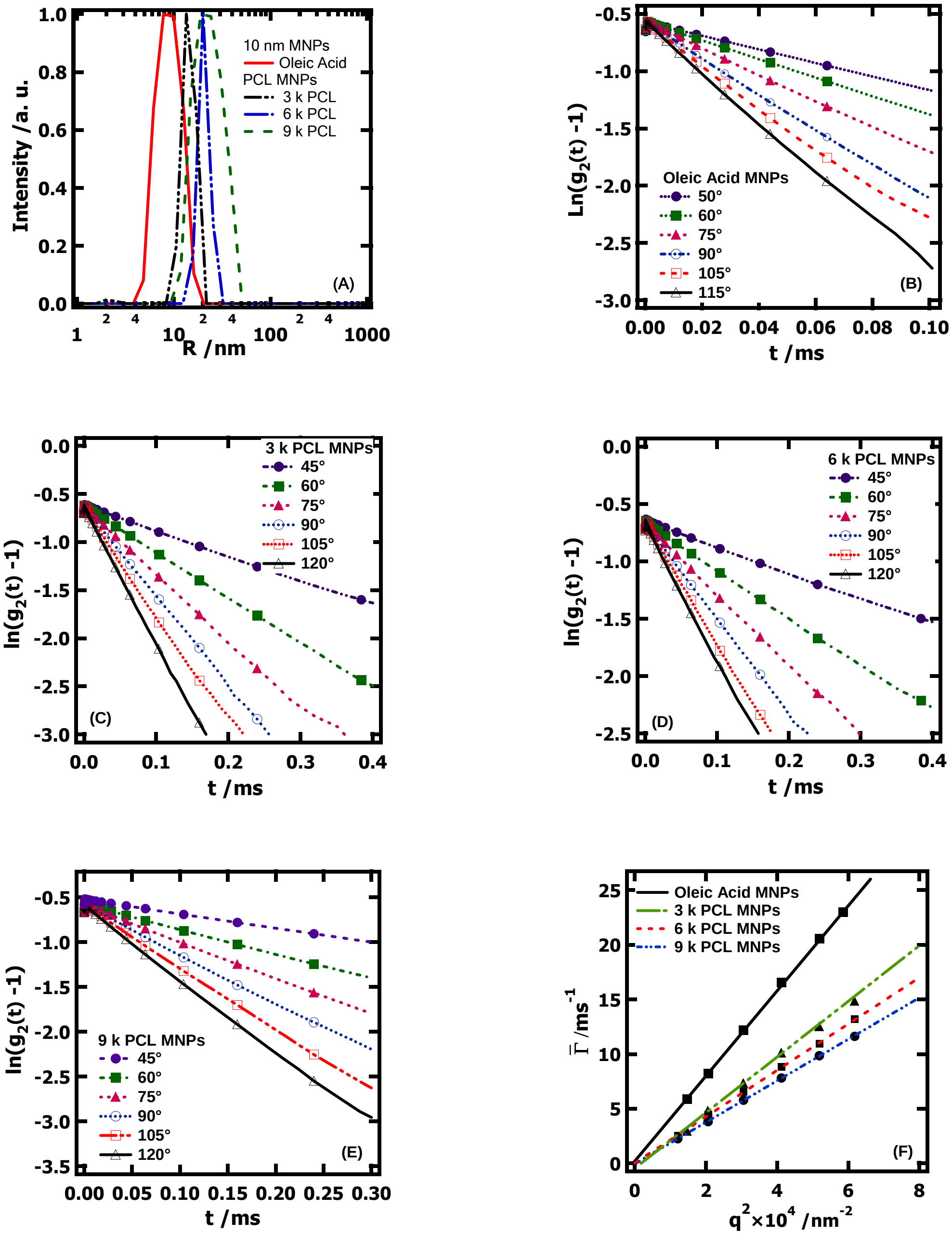

Figure 5.1. DLS results for oleic acid and PCL MNPs in chloroform (~ 0.1 mg•mL^{-1}). (A) Intensity weighted size distributions for MNPs at a scattering angle of 90º. ln(g_2(t)-1) as a function of at different scattering angles for (B) oleic acid MNPs, (C) 3 k PCL MNPs, (D) 6 k PCL MNPs, and (E) 9 k PCL MNPs. (F) $\bar{\Gamma}$ versus q^2 for oleic acid, 3 k PCL, 6 k PCL and 9 k PCL MNPs.

Oleic acid and PCL triacid graft densities on the MNP surfaces were estimated from the TGA data (see Table 5.1). The particle size distributions were narrow. For these estimates, the MNPs were assumed to be spherical with diameters of d = 9 nm (verified by TEM). Under this assumption, surface graft densities were given as ρ_A in units of area per PCL molecule and were deduced from

$$\rho_A = \frac{6M\phi_{Fe_3O_4}}{\rho_{Fe_3O_4} d\phi N_a} \tag{5-1}$$

where $\rho_{Fe_3O_4}$ was the density of Fe_3O_4 (5.17 g•cm^{-3}, CRC Handbook); d (9 nm) was the diameter of the Fe_3O_4 core; M was a number average molar mass of a PCL molecule or oleic acid; N_a was Avogadro's number, and ϕ and $\phi_{Fe_3O_4}$ were the weight fractions of the organic component and Fe_3O_4 from TGA, respectively. Calculated values of ρ_A for oleic acid, 3 k, 6 k and 9 k PCL triacids were ~20, 35, 43, 42 Å^2•molecule^{-1} respectively. For the triacid headgroup, the area of ~ 40 Å^2•molecule^{-1} indicated two of the three carboxylic acids were attached to the surface. The third was likely bound to the linking groups of a neighboring molecule through intra-molecular hydrogen bonding.[25] The results also suggested that the PCL chains were tightly packed at the MNP surface.

Table 5.1. TGA results, ρ_A, D_m, R_h and PDI

Sample	**Fe_3O_4 wt%**	ρ_A **(Å^2•molecule^{-1})**	**D_m ×10^{11} (m^2•s^{-1})**	**R_h (nm)**	**PDI**
Oleic Acid MNPs	75.0 %	20	3.91 ± 0.04	9.6 ± 0.4	0.09
3 k PCL MNPs	35.4 %	35	2.50 ± 0.05	15.0 ± 1.5	0.10
6 k PCL MNPs	24.7 %	43	2.12 ± 0.02	17.7 ± 0.3	0.15
9 k PCL MNPs	17.8 %	42	1.89 ± 0.01	19.9 ± 0.1	0.15

5.4.2. Π-A Isotherm and BAM Studies of PCL Triesters and PCL Triacids

Effects of bulky endgroups on PCL crystallization at the A/W interface were probed through Π-A isotherms and BAM. Figure 5.3 shows representative compression/expansion cycles for 6 k PCL triester (solid line) and 6 k PCL triacid (dashed line) along with BAM images taken at selected A. Both the 6 k PCL triester and 6 k PCL triacid Π-A isotherms exhibited features that were previously reported for linear PCL homopolymers.[17-18] From 70 > A > 25 Å^2•monomer^{-1} for 6 k PCL triester and 6 k PCL triacid, Π increased gently upon compression in a manner that was consistent with a liquid expanded film for both samples. At Π ≈ 10.3 mN•m^{-1} for 6 k PCL triester and Π ≈ 10 mN•m^{-1} for 6 k PCL triacid, a kink in the Π−A isotherm was observed. Li et al.[17-18] attributed this feature to the Π induced nucleation and growth of PCL crystals at the A/W interface. The dependence of Π on A with further compression of the film (smaller A) reflected unhindered crystal growth (plateau regions) and impingement by neighboring crystals (Π increases at the smallest A). Upon expansion of the film, it was observed that both the 6 k PCL triester and triacid exhibited a rapid drop in Π followed by a common "plateau" region around Π ≈ 7 mN•m^{-1}. This feature has been attributed to melting and respreading of PCL (dissolution) at lower Π. It was noted that the relatively flat region of the 6 k PCL expansion curve for the triester was longer than it was for the triacid. For both systems, Π returned to zero at large enough A.

BAM images shown in Figure 5.2 were consistent with PCL crystallization at the A/W interface. For the 6 k PCL triester, crystals could be seen for compression past the kink in the isotherm. These crystals grew anisotropically and exhibited diffusion limited morphologies. Similar features have been observed for PCL blends with poly(t-butyl acrylate) (PtBA).[19] Likewise, the melting and respreading process showed dendritic features like the PCL/PtBA blends and PCL homopolymer films. As seen in Figure 5.2, 6 k PCL triacid crystals were smaller; second, they lacked faceted features, and appeared to be nearly circular relative to 6 k PCL triester crystals at comparable A. The smaller crystal sizes were consistent with the shorter plateau in the expansion isotherms, i.e. less crystal needed to melt and respread and hence a shorter plateau was observed. While not shown, second compression/expansion cycles led to different morphologies for the 6 k PCL triester. This observation was consistent with previous reports for linear PCL,[17-18] where residual nuclei led to heterogeneous nucleation for the second compression step.

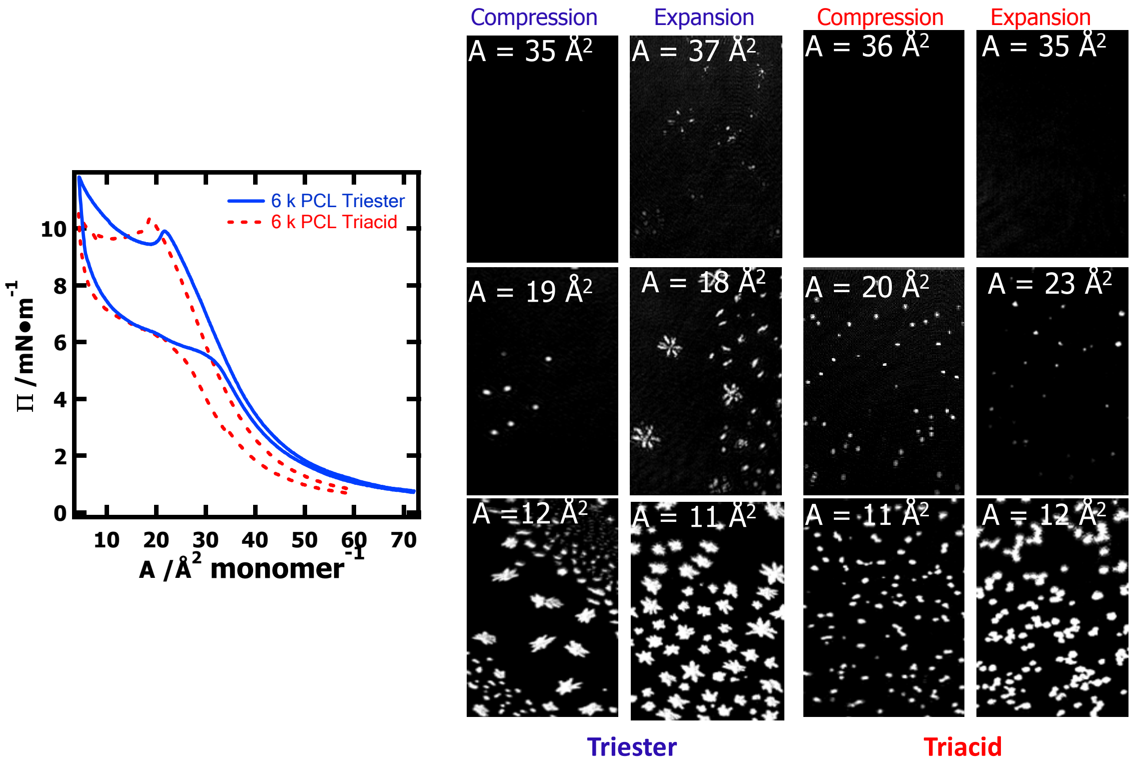

Figure 5.2. Compression/expansion Π-A isotherm cycles at T = 22.5 ºC for 6 k PCL triester and PCL triacid and BAM images at selected A. The BAM images have dimensions of 2 mm × 1 mm.

Representative compression/expansion Π-A isotherm cycles and corresponding BAM images for 9 k PCL and 3 k PCL triesters and triacids are provided in Figures 5.3 and 5.4, respectively. While the 9 k PCL and 3 k PCL isotherms were qualitatively similar to the 6 k PCL isotherms, the 3 k PCL triacid isotherm was markedly different. For the 3 k PCL triacid isotherm, no kink was observed for compression of the film, even up to Π ~ 14 mN•m^{-1}.

Quantitatively, the kinks that appeared in the compression isotherms occurred at higher Π for 9 k PCL triester (Π ~ 11 mN•m^{-1}) and 9 k PCL triacid (Π ~ 12 mN•m^{-1}). In general, kinks of the type observed in the compression isotherms of Figures 5.2 through 5.4 are indicative of the nucleation and growth of three-dimensional (3D) phases (normally monolayer collapse). For PCL, this process led to crystallization. Nucleation of the 3D phase occurred within a metastable state. Once the growth rate for the 3D phase exceeded the compression rate of the film, Π decreased. As previously reported by Li and Esker,[17] PCL homopolymer exhibited a maximum growth rate at intermediate molar masses that corresponded to a minimum in the pressure at the "kink". The fact that 3 k PCL and 9 k PCL samples exhibited higher Π at the kink meant higher Π was needed for crystallization at room temperature. As seen in the BAM images of Figures 5.3 and 5.4 for 3 k and 9 k samples respectively, the crystals that formed under compression were smaller than at comparable A for the 6 k PCL samples (both triacid and triester). Qualitatively, the BAM images in Figures 5.3 and 5.4 revealed similar morphological features as 6 k PCL for the triacids, however, the triester morphologies were less clear because of limited BAM resolution. A more detailed look at the morphology by OM and AFM will be represented in Section 5.4.3. One final feature of Figures 5.3 and 5.4 should be noted. The plateau that corresponded to monolayer melting and respreading occurred at similar Π for most samples (~ 7 mN•m^{-1}), although this transition occurred at a slightly higher Π for 3 k PCL triester (~ 9 mN•m^{-1}). Such a feature indicates easier melting and respreading (dissolution).

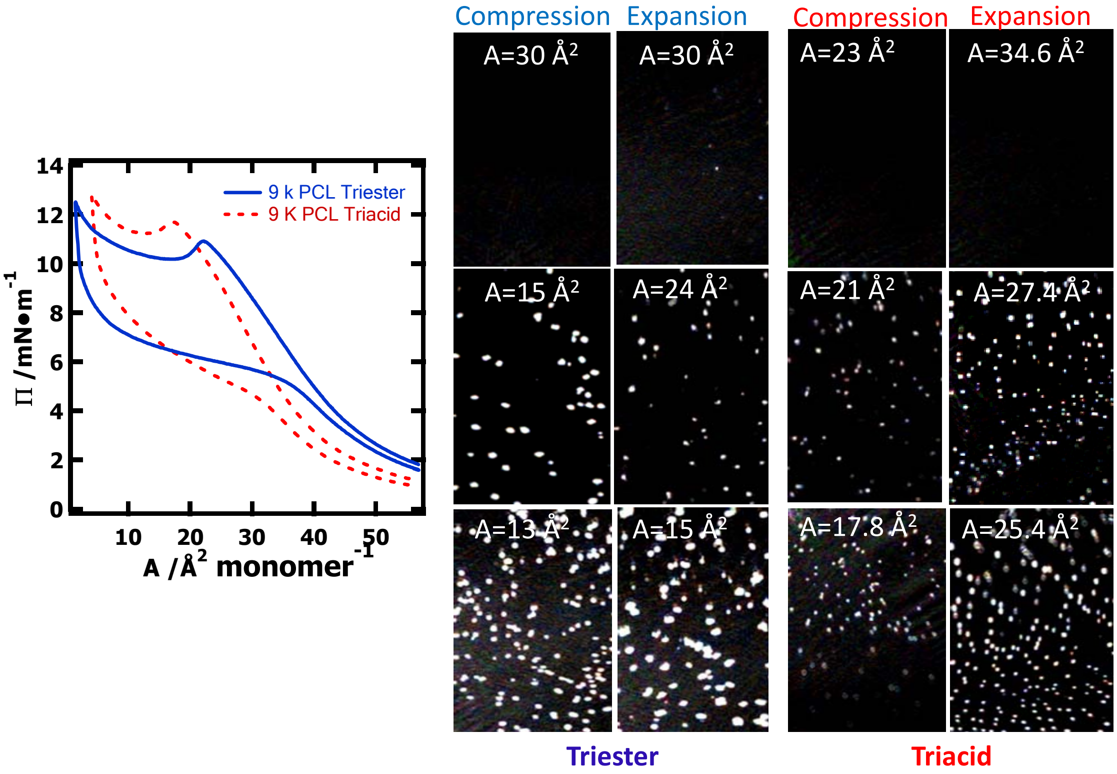

Figure 5.3. Compression/expansion Π-A isotherm cycles at T = 22.5 ºC for 9 k PCL triester and PCL triacid and BAM images at selected A. The BAM images have dimensions of 2 mm × 1 mm.

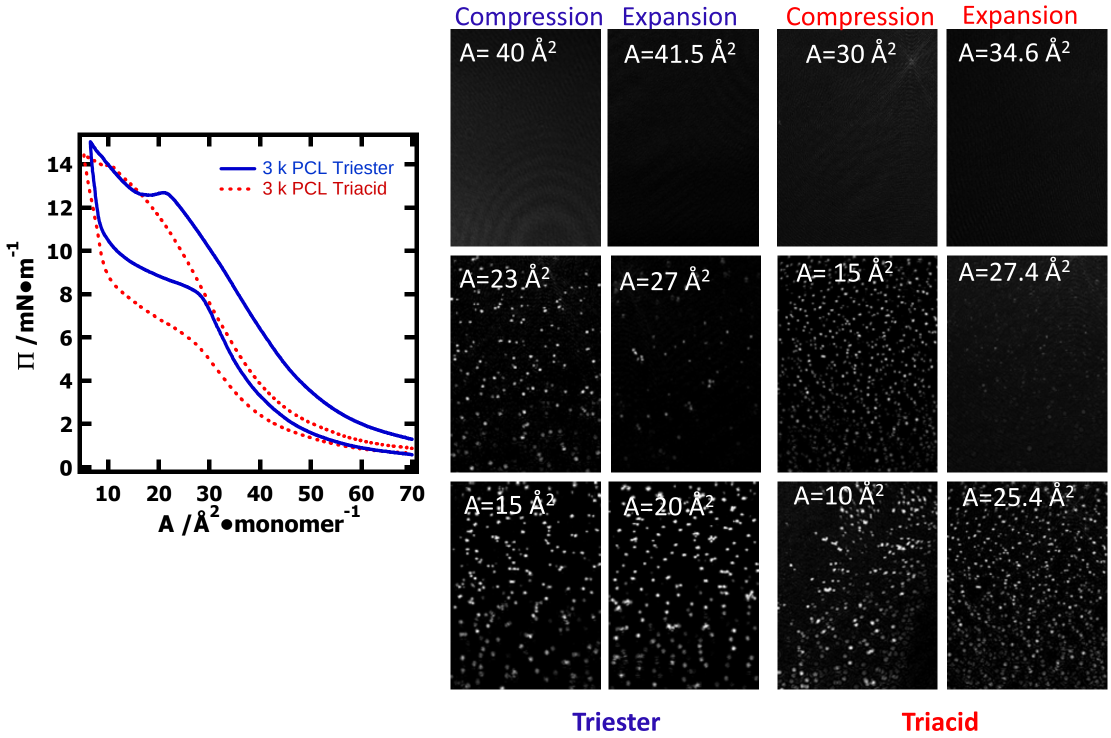

Figure 5.4. Compression/expansion Π-A isotherm cycles at T = 22.5 ºC for 3 k PCL triester and PCL triacid and BAM images at selected A. The BAM images have dimensions of 2 mm × 1 mm.

5.4.3. Optical Microscopy (OM) and Atomic Force Microscopy (AFM) of PCL Triesters and PCL Triacids. Monolayer Langmuir-Blodgett (LB)-films of PCL crystals were transferred onto cellulose coated silicon substrates from the A/W interface on the upstroke. Representative OM images for PCL crystals transferred during compression in the plateau regime (A ~ 10 $Å^2$•molecule^{-1}) are shown in Figure 5.5. As expected from the discussion of the Π-A isotherms and BAM images, the 6 k PCL samples formed larger crystals than the 3 k and 9 k PCL samples. For the 6 k PCL triester crystals, 6 or 7- armed flower-shaped crystals were clearly identified. However, even with the enhanced resolution afforded by OM over BAM, the strongest conclusions that could be drawn for the 3 k and 9 k PCL samples were that they were irregularly-shaped, multifaceted, and that the 3 k PCL crystals were the smallest. For the PCL triacid samples, Figure 5.5 clearly showed elliptical crystal shapes with much smaller crystals for the 3 k PCL triacid than the 6 k and 9 k PCL triacids.

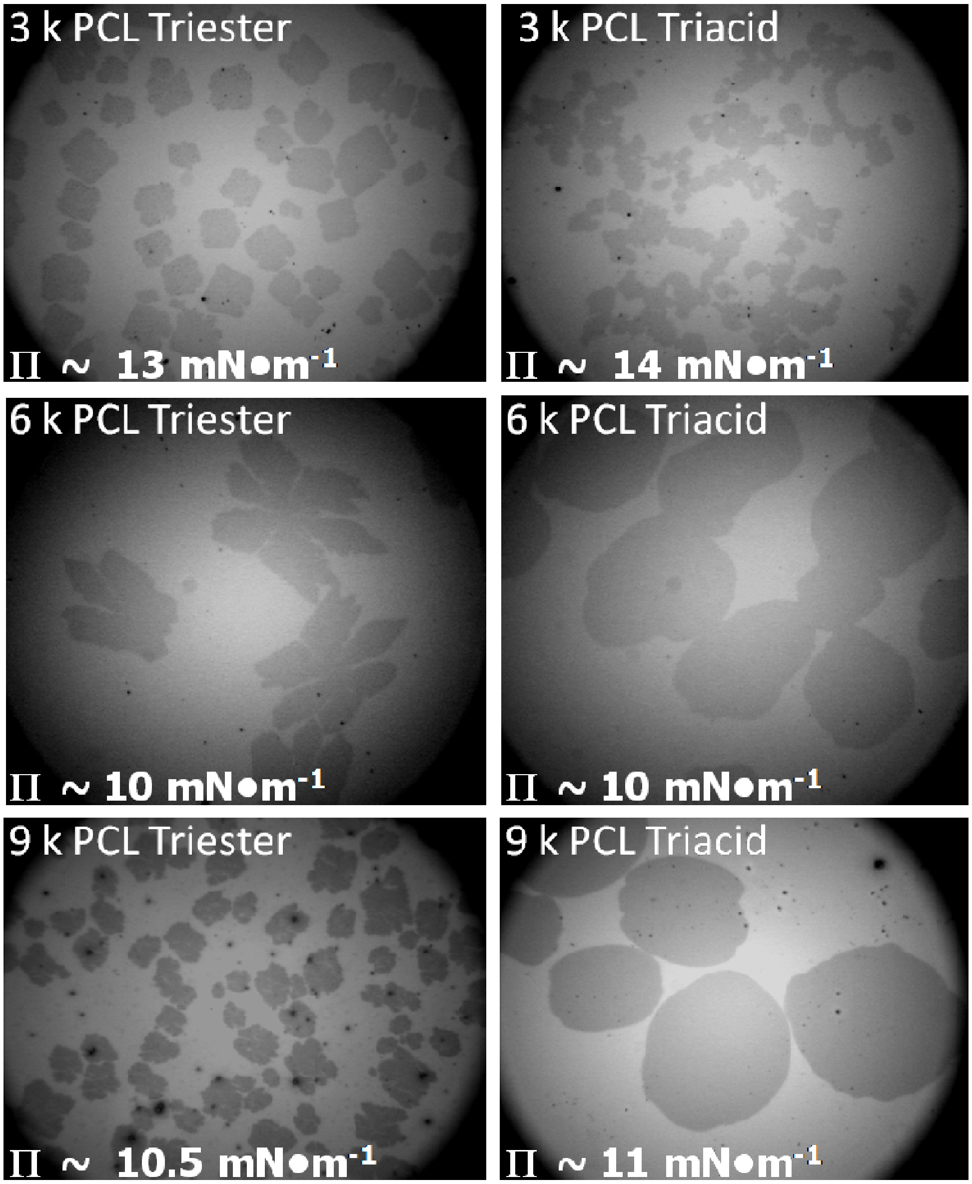

Figure 5.5. OM images (260 μm × 340 μm) of the 3 k, 6 k and 9 k PCL triesters and PCL triacids. All crystals were LB-transferred onto regenerated cellulose surfaces.

Representative AFM images provided in Figures 5.6 and 5.7 for PCL triesters and PCL triacids, respectively, further confirmed the morphological differences. Additionally, line scan analyses showed the air surfaces of the crystals were smooth, and that the crystal thicknesses, d ~ 8 nm, were comparable to previously reported studies for linear PCL at the A/W interface.[17-18] Hence, the only significant effects the headgroup had on the crystals were morphological.

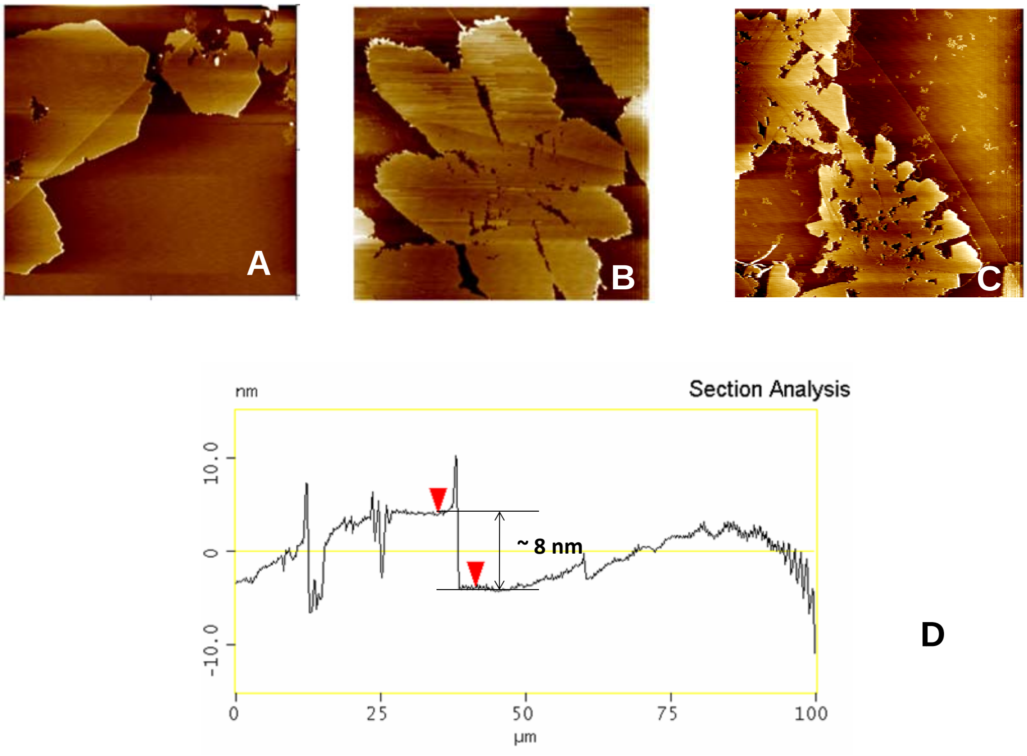

Figure 5.6. Representative AFM height images (100 µm × 100 µm, *z*-scale 0-30 nm) for (A) 9 k (B) 6 k, and (C) 3 k PCL triester and (D) a representative line scan for a 3 k PCL triester crystal.

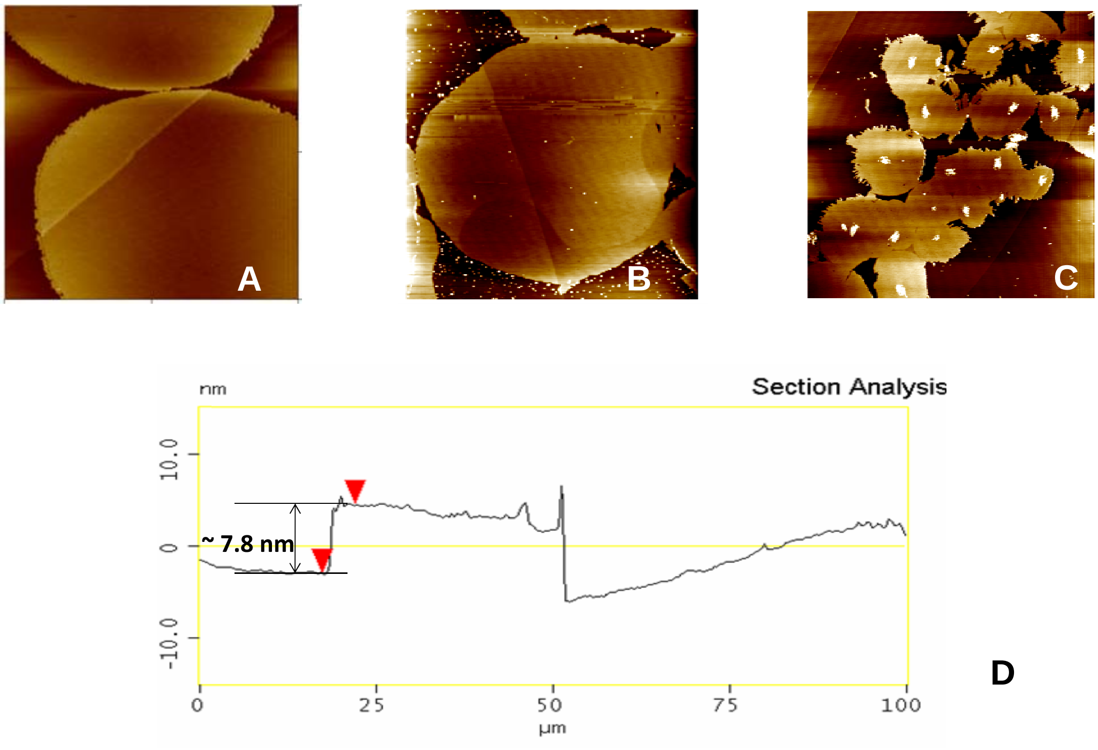

Figure 5.7. Representative AFM height images (100 µm × 100 µm, *z*-scale 0-30 nm) for (A) 9 k (B) 6 k, and (C) 3 k PCL triacid and (D) a representative line scan for 3 k PCL triacid crystal.

Diffusion limited structures observed for PCL triester samples suggested that morphological control was achievable through isobaric crystallization experiments. This was demonstrated for the 6 k PCL triester and key results are provided in Figure 5.8. In these experiments, films were compressed to different Π in the metastable regime (Π close to but below the kink pressure). After the desired Π was reached, Π was held constant. As seen in Figure 5.8, four Π values were selected, Π = 10, 11, 11.5 and 12 mN•m^{-1}. At higher Π, the driving force for crystallization was greater (analogous to greater undercooling in isothermal crystallization experiments for bulk polymer materials). Reprehensive BAM and OM images were taken at A ~ 10 Å^{2}•molecule^{-1}. The OM images were taken from PCL films transferred onto cellulose coated silicon wafers. At low Π, PCL crystals were mostly filled with faceted edges. At high Π, the morphologies were similar to those observed for constant compression rate experiments in Figure 5.6. These morphologies were consistent with a diffusion limited process, where faster crystal growth rates were responsible for the observed morphological features. A plausible explanation for the difference in crystal morphologies between the PCL triesters and PCL triacids centers on an accumulation of bulky ester groups at the interface. Studies with PtBA[19] demonstrated the amphiphilic nature of t-butyl esters. Furthermore, Chapter 4 showed that linear PtBA blocks affected PCL crystal morphologies. In essence, the PCL triester had a trimer of PtBA at its end. As PCL underwent crystallization in the monolayer, t-butyl esters likely remained directly at the A/W.[19] If t-butyl ester groups accumulated at the A/W interface, they could not be incorporated into the PCL crystals and would be a steric hindrance factor for the crystal growth. In a fast crystal growth process, this hindrance would cause diffusion limited growth of PCL crystals, as observed for the 6 k PCL triester. In contrast, the PCL triacid samples had smaller carboxylic acid end groups that were readily solvated in the water phase underneath the crystals. Round morphologies at the A/W interface have been explained in terms of balance between dipole density and line tension.[26-27] The dipole-dipole interactions favored irregular and stripe shaped morphologies, whereas, the line tension favored the formation of round shaped morphologies. For the PCL triacid crystals, the observation of elliptical morphologies suggested that after the removal of the bulky triester groups, the line tension was still stronger than the enhancement of dipolar effects associated with the acid end groups.

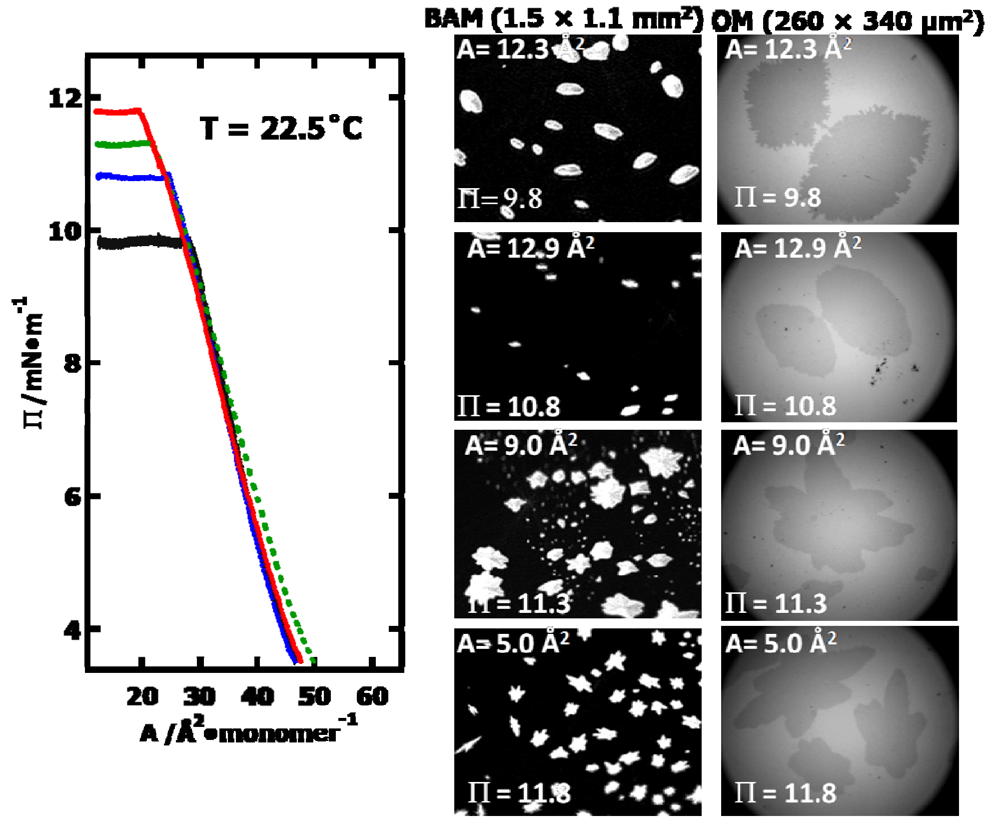

Figure 5.8. Isobaric crystallization experiments at T = 22.5 ˚C for 6 k PCL triester at $\Pi = 9.8$ mN•m^{-1}, 10.8 mN•m^{-1}, 11.3 mN•m^{-1}, 11.8 mN•m^{-1}. BAM images (1.1×1.5 mm^2) and OM images (260×340 μm^2) were taken at A ~ 10 Å^2•monomer^{-1} with exact values indicated on the images.

5.4.4. PCL MNP Π–A Isotherms and BAM. Once the effects of endgroups on PCL crystallization at the A/W interface were established, the effect chain confinement of PCL to the surface of a MNP had on PCL crystallization at the A/W interface was explored. Representative compression/expansion Π–A isotherm cycles for two cycles and BAM images at selected A are provided in Figure 5.9 for 6 k PCL MNPs. In Figure 5.9, A_{PCL} was calculated from the organic fraction of the mass, while Fe_3O_4 was ignored. As a consequence, Fe_3O_4 at the A/W interface occupied space but this was not reflected in the surface concentration. Thus, Π had higher values at all A_{PCL} than 6 k PCL triacid. The fact that PCL chains interacted earlier reflected the fact that some of the surface area at the A/W interface was occupied by impermeable Fe_3O_4 cores. The other important factor associated with the initial compression of the film was Π at the kink was ~12 mN•m^{-1} for 6 k PCL MNP versus ~10 mN•m^{-1} for 6 k PCL triacid (Figure 5.2). As noted for the 3 k PCL and 9 k PCL triester and triacids relative to the 6 k PCL samples, higher Π at the kink meant a sample crystallized less easily. The BAM images in Figure 5.9 from the first compression step revealed two different morphologies for films compressed past the kink. As seen at A =18 Å^2•monomer^{-1} in Figure 5.9, small aggregates appeared, and some but not all of the features grew into larger white domains. Upon expansion of the film, a melting and respreading plateau was observed; however, the resulting hysteresis loop (area between the compression and expansion curves) was much larger. Moreover, the BAM image at A = 59 Å^2•monomer^{-1} still had small observable features. As a consequence, the second compression/expansion Π–A cycle deviated strongly from the first cycle and no growth of aggregates was observed at any A. Moreover, stark qualitative differences between the Π–A isotherms of the 3 k PCL MNPs and 6 k PCL MNPs were observed. As such, features of the 9 k PCL MNPs relative to the 6 k PCL MNPs will be discussed first because they were the most similar. As seen in Figure 5.10, Π was higher at all A_{PCL} for the initial compression of the film up to the kink in the isotherm. As previously explained for the 6 k PCL MNPs, this feature arose from space occupied by the incompressible magnetite cores. Around the kink, deviations from the 6 k PCL MNPs were observed. First Π at the kink was actually higher for the 9 k PCL MNPs than it was for 6 k PCL MNPs. For the comparison between the 6 k PCL triesters and triacids to the 9 k PCL triesters and triacids, the opposite effect was observed. Apparently confinement of the PCL triacid to the surface of the MNP was a bigger impediment for crystallization of the 6 k sample than it was for 9 k sample. Second, the surface morphologies observed by BAM were also different. Large loose raft-like structures were observed for the 9 k PCL MNPs, versus the discrete round domain seen for the 6 k PCL MNPs and no evidence of brighter growing domains was observed. Even though, expansion of the film and the difference between the hysteresis loops of the first and second cycles were similar for 6 k and 9 k PCL MNPs, the 9 k PCL MNPs exhibited no significant differences with respect to morphology between the first and second cycle.

Comparisons between the 3 k and 6 k PCL MNPs were more interesting. As seen in Figure 5.11, the $\Pi\mathrm{-A}$ isotherms for the 3 k PCL MNPs were completely different from the 6 k and 9 k PCL MNPs. The initial compression $\Pi\mathrm{-A}$ isotherm lacked a kink up to $\Pi > 14$ mN•m^{-1}. Moreover, the first expansion isotherm lacked a melting and respreading (dissolution) transition. This observation suggested the 3 k PCL MNPs did not crystallize at the A/W interface or underwent very limited crystallization, such as nucleation without growth. As seen in Figure 5.11, the BAM images were similar to the BAM images for the 6 k PCL MNPs (Figure 5.9) without the formation of the larger bright white domains. As seen in Figure 5.11, the domains that formed never completely disappeared upon expansion of the film. As a consequence, the second compression/expansion $\Pi\mathrm{-A}$ isotherm cycle was very different from the first, whereas the BAM images were quite similar for both cycles.

As discussed in Chapter 4, the static elastic modulus $\varepsilon_s = \kappa^{-1} = -A(\frac{\partial\Pi}{\partial A})_T$ is defined as a 2D modulus. ε_s as a function of Π and monomer area (A) for 3 k, 6 k, 9 k PCL triester , PCL triacid, and PCL MNPs are plotted in Figure 5.12. The dependence of ε_s on Π and A for the PCL triheads was identical to previously reported results for linear PCL.[17] For PCL MNPs, the nanoparticles had no effect on the magnitude of ε_s. This observation meant that the Fe_3O_4 cores could be regarded as non-interacting objects at the A/W interface that decreased accessible surface area but otherwise had no effect on the interactions of PCL with water.

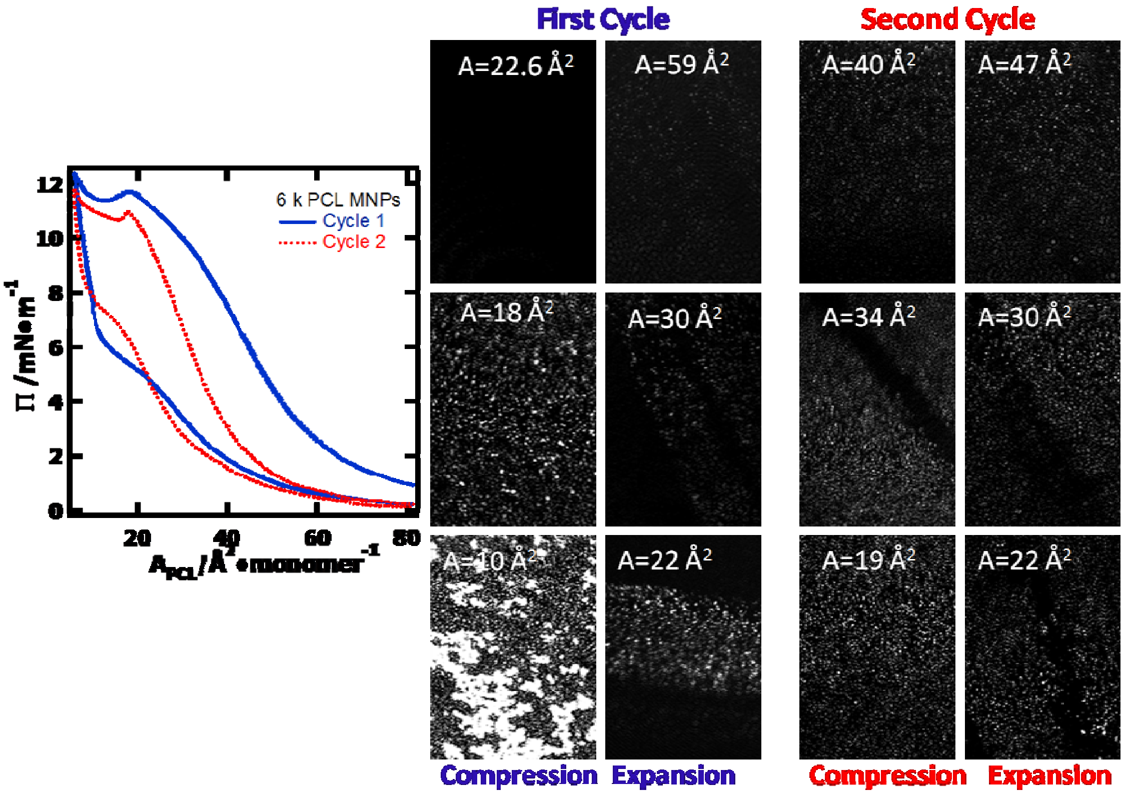

Figure 5.9. Compression/expansion Π-A isotherm cycles at T = 22.5 ºC for 6 k PCL MNPs and BAM images at selected A. The BAM images have dimensions of 2 mm × 1 mm.

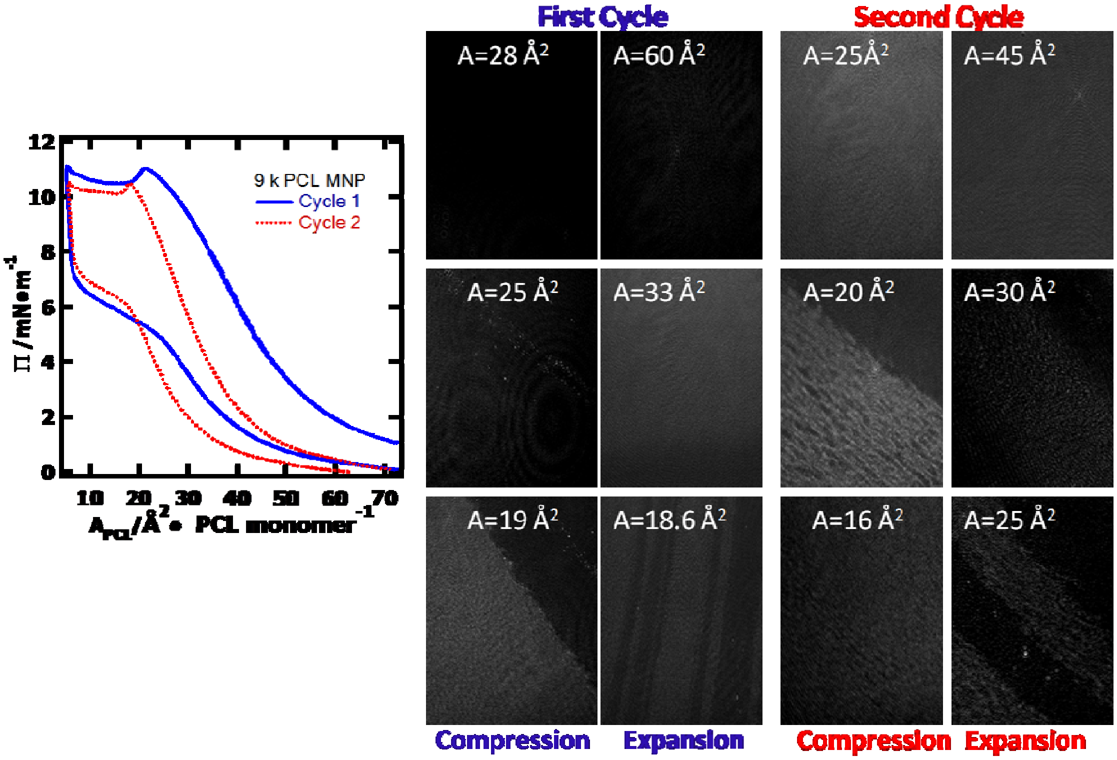

Figure 5.10. Compression/expansion Π-A isotherm cycles at T = 22.5 ºC for 9 k PCL MNPs and BAM images at selected A. The BAM images have dimensions of 2 mm × 1 mm.

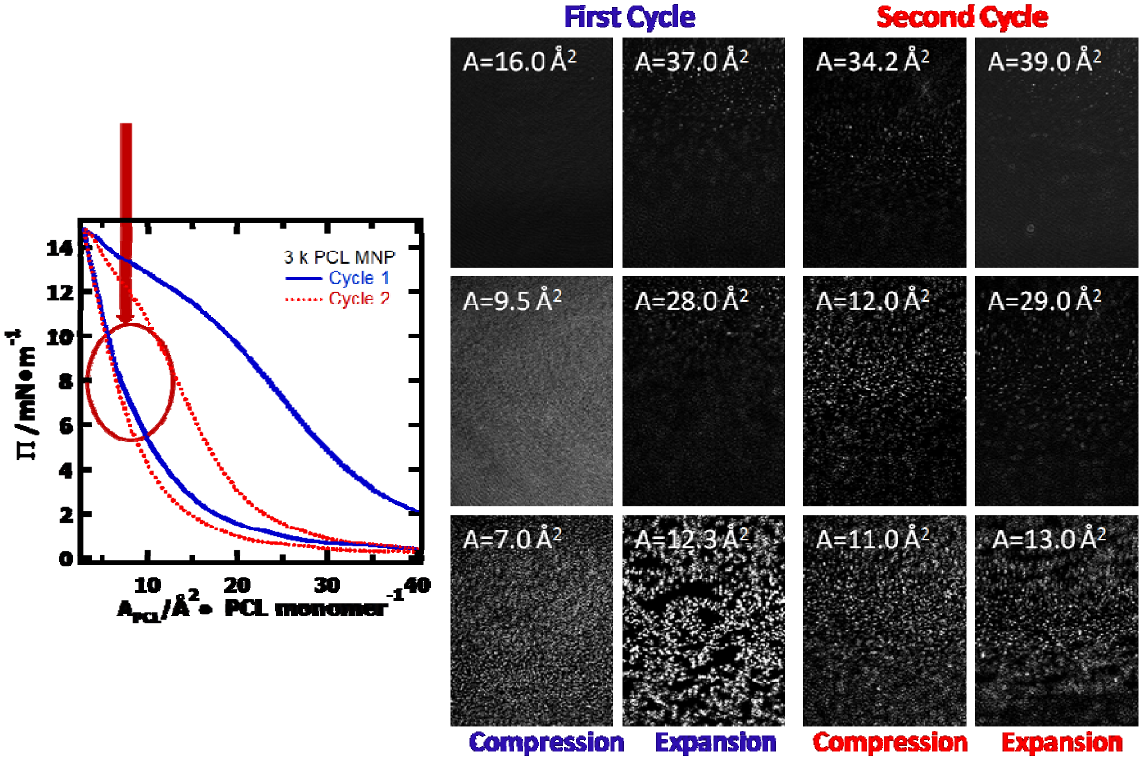

Figure 5.11. Compression/expansion Π-A isotherm cycles at T = 22.5 ºC for 3 k PCL MNPs and BAM images at selected A. The BAM images have dimensions of 2 mm × 1 mm. The red arrow and cycle highlight the missing melting and respreading transition that has been observed for other PCL derivatives.

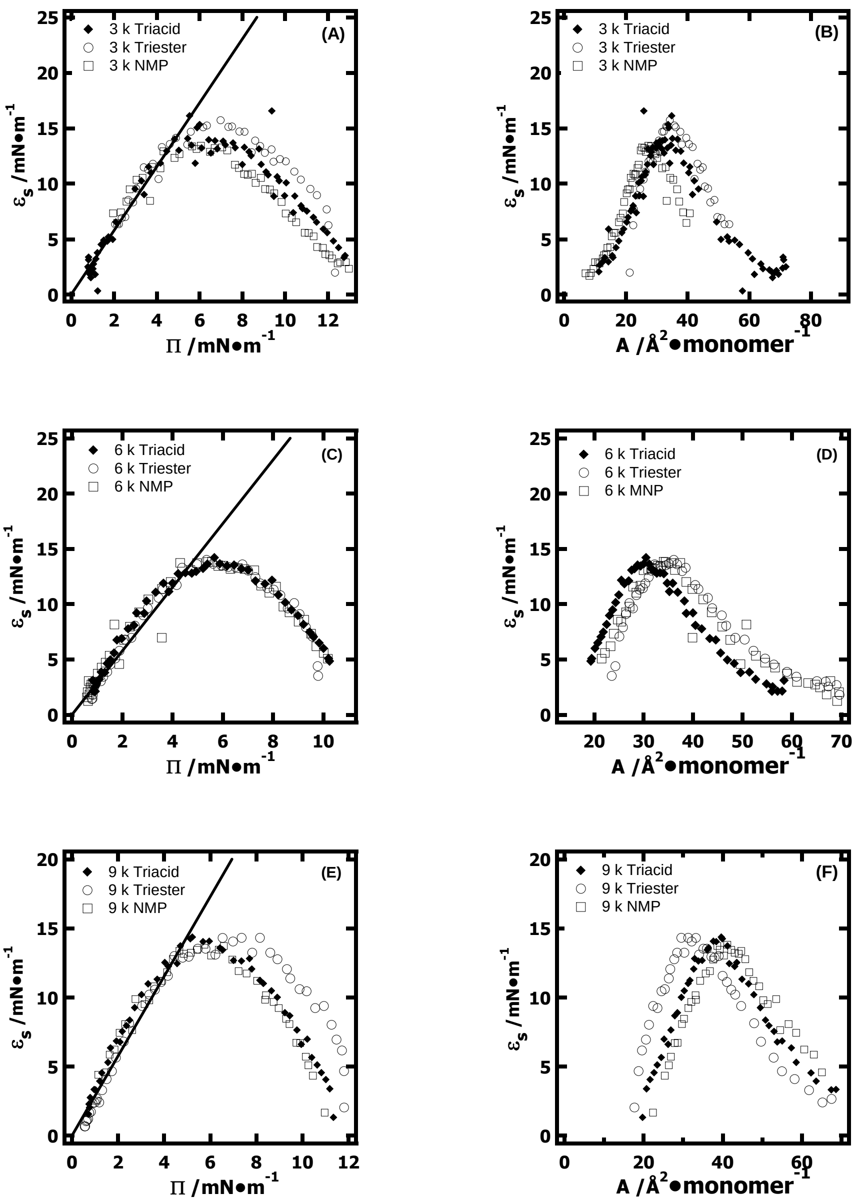

Figure 5.12. ε_s versus Π curves and ε_s versus A for PCL triesters, PCL triacids, and PCL MNPs. (A) and (B) are for the 3 k series. (C) and (D) are for the 6 k series, and (E) and (F) are for the 9 k series. The lines are theoretical curves, $\varepsilon_s = z\Pi$, for good solvent conditions ($z = 2.86$, solid line).[28] The symbols in this figure correspond to (◆) PCL triacids, (○) PCL triesters, and (□) PCL MNPs.

5.4.5. OM, AFM and TEM for PCL MNPs. LB-films of PCL MNPs were transferred onto cellulose coated silicon substrates from the A/W interface on the upstroke. Representative OM images for PCL crystals transferred during compression at the designated surface pressures are shown in Figure 5.13. Compared to the OM images for PCL triacids prior to attachment to a nanoparticle surface (Figure 5.5), PCL MNPs had much smaller feature sizes in Figure 5.13. Evidently, confinement to the MNP surface markedly affected the morphologies of the PCL triacids.

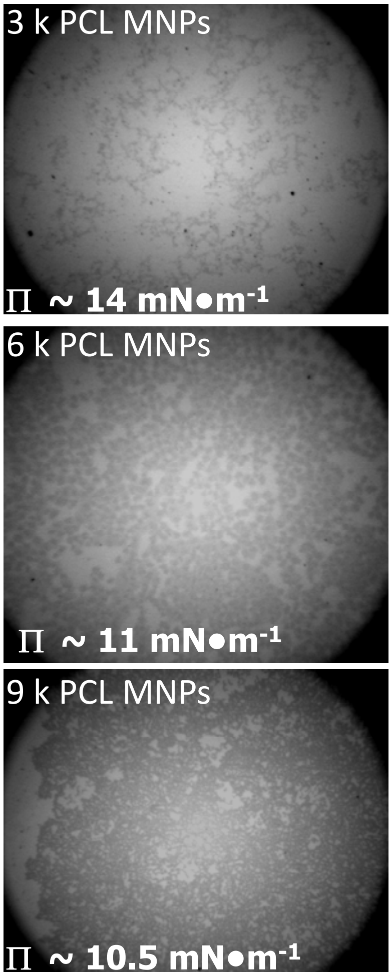

Figure 5.13. OM images (260 μm × 340 μm) of the 3 k, 6 k and 9 k PCL MNPs. All crystals were LB-transferred onto regenerated cellulose surfaces.

As OM images only yielded slight improvements in resolution over BAM, AFM and TEM were employed for further morphological characterization of the films. AFM images for 6 k PCL MNPs are provided in Figure 5.14. Whereas crystals for 6 k PCL triacid and 6 k PCL triester practically filled a 100 µm ×100 µm image (Figures 5.6B and 5.7B), domains transferred from the A/W interface for the 6 k PCL MNPs were ~10 µm × 10 µm. As seen in Figure 5.14, the domains were heterogeneous and the surfaces of the features were much rougher than the surfaces of 6 k PCL triester and triacid crystals (see the line scan analysis of Figure 5.7D). While the overall thicknesses (~ 8 nm) of these domains were comparable to the 6 k PCL triester and triacid (~ 8 nm), these thicknesses were also comparable to the size of the magnetite core (~ 9 nm diameter as seen in the TEM image of Figure 5.15). This factor contributed to the roughness of the surfaces and the brighter parts of the AFM height images. The limited tan, ~ 8 nm thick, sections of the AFM image around the bright spots were likely small crystalline PCL domains.

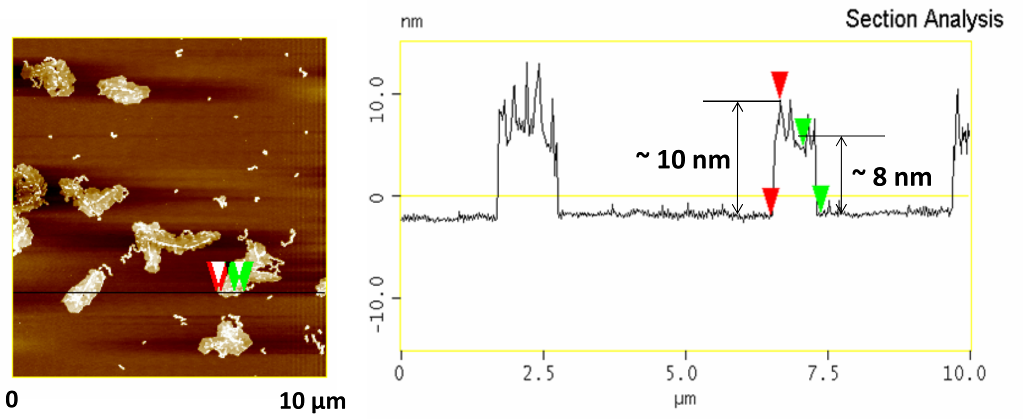

Figure 5.14. (Left) An AFM height image (10 µm × 10 µm, *z* scale 0-30 nm) of a 6 k PCL MNP and (right) a line scan analysis.

The conclusions drawn for the 6 k PCL MNP AFM images in Figure 5.14 were strongly influenced by similar images for 9 k PCL MNPs in Figure 5.15. As seen in Figure

5.15, crystalline PCL domains (~ 8 nm thick) were more obvious around the clustered MNPs, and the surfaces of the crystals were smoother. TEM also revealed MNP aggregates that were similar to the AFM images. In contrast to the 6 k and 9 k PCL MNPs, the features of the AFM images in Figure 5.16 for the 3 k PCL MNPs transferred from the A/W interface were very different. The clusters of MNPs were thicker (~ 20 nm), a thickness that was consistent with a bilayer of MNPs rather than crystalline structures. Limited crystallization (tan features) around the MNPs may have occurred; however, features of the Π−A isotherm like no kink and the absence of a melting and respreading transition, along with the thickness of the transferred structures strongly suggested that 3 k PCL MNPs underwent collapse into multilayers (bilayers) at the A/W interface.

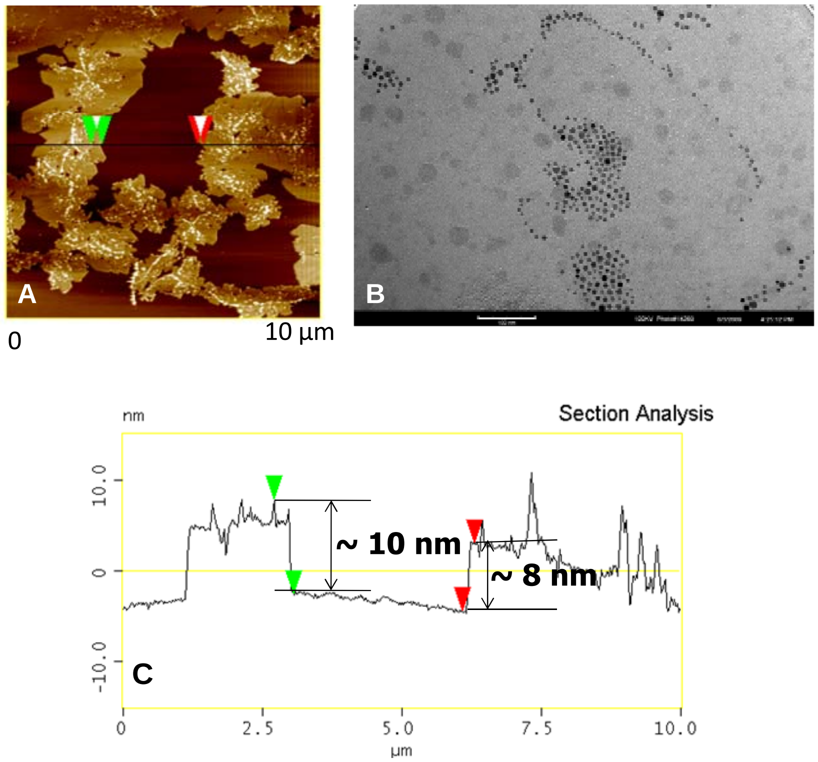

Figure 5.15. (A) AFM height image (10 µm × 10 µm, *z* scale 0-30 nm) of 9 k PCL MNP LB-films. (B) TEM image of a 9 k PCL MNP LB-film on a carbon coated TEM grid. The scale bar corresponds to 100 nm. (C) Line scan from the 9 k MNP height image of (A).

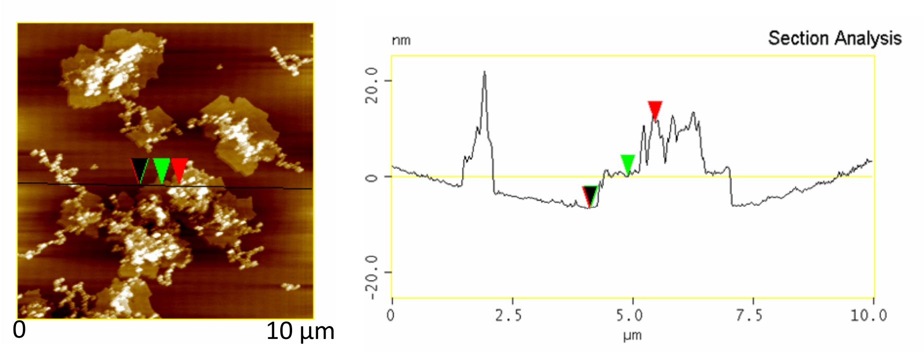

Figure 5.16. (left) AFM height image (10 µm × 10 µm, *z* scale 0-30 nm) of 3 k PCL MNPs and (right) a line scan analysis.

5.5. Conclusions

Dendritic endgroups on PCL dramatically influenced its crystallization at the A/W interface. Bulky amphiphilic t-butyl groups of PCL triesters accumulated at the A/W interface and led to diffusion controlled crystal morphologies. In contrast, conversion of the hydrophobic PCL triesters into hydrophilic triacids led to elliptically shaped crystals. Those structures were attributed to the interplay between altered dipole densities that accompanied submersion of the acid moieties in the subphase and line tension. Polymer molar mass strongly influenced the rate of crystallization. The 6 k PCL sample exhibited the fastest growth rate for the triester and triacid series. A similar feature, a maximum growth rate at intermediate molar mass, was also reported for the rate of crystallization of linear PCL at the A/W interface.[17] In contrast, PCL triacid tethered to MNP surfaces revealed suppressed crystallization. While crystals formed for the 9 k PCL MNPs, they were smaller than 9 k PCL triacid and crystallization for the 6 k and 3k PCL MNPs was almost completely suppressed at the A/W interface. As such, this study clearly demonstrated how confinement of polymer chains to the surface of a filler could hinder crystallization.

5.6. References

(1) Balazs, A. C.; Emrick, T.; Russell, T. P. *Science* **2006**, *314*, 1107.

(2) Abul Kashem, M. M.; Perlich, J.; Schulz, L.; Roth, S. V.; Petry, W.; Müller-Buschbaum, P. *Macromolecules* **2007**, *40*, 5075.

(3) Lauter-Pasyuk, V.; Lauter, H. J.; Gordeev, G. P.; Müller-Buschbaum, P.; Toperverg, B. P.; Petry, W.; Jernenkov, M.; Petrenko, A.; Aksenov, V. *Physica B* **2004**, *350*, e939.

(4) Lin, Y.; Böker, A.; He, J.; Sill, K.; Xiang, H.; Abetz, C.; Li, X.; Wang, J.; Emrick, T.; Lung, S.; Wang, Q.; Balazs, A.; Russell, T. P. *Nature* **2005**, *434*, 55.

(5) Lopes, W. A.; Jaeger, H. M. *Nature* **2001**, *414*, 735.

(6) Lauter-Pasyuk, V.; Lauter, H. J.; Gordeev, G. P.; Müller-Buschbaum, P.; Toperverg, B. P.; Jernenkov, M.; Petry, W. *Langmuir* **2003**, *19*, 7783.

(7) Huh, J.; Ginzburg, V. V.; Balazs, A. C. *Macromolecules* **2000**, *33*, 8085.

(8) Thompson, R. B.; Ginzburg, V. V.; Matson, M. W.; Balazs, A. C. *Macromolecules* **2000**, *35*, 1060.

(9) Thompson, R. B.; Ginzburg, V. V.; Matson, M. W.; Balazs, A. C. *Science* **2001**, *292*, 2469.

(10) Abul Kashem, M. M.; Perlich, J.; Diethert, A.; Wang, W.; Memesa, M.; Gutmann, J. S.; Majkova, E.; Capek, C.; Roth, S. V.; Petry, W.; Müller-Buschbaum, P. *Macromolecules* **2009**, *42*, 6202.

(11) Li, L.; Li, B.; Hood, M. A.; Li, C. Y. *Polymer* **2009**, *50*, 953.

(12) Li, C. Y.; Li, L.; Cai, W.; Kodjie, S. L.; Tenneti, K. K. *Adv. Mater.* **2005**, *17*, 1198.

(13) Luduena, L. N.; Vazquez, A.; Alvarez, V. A. *J. Appl. Polym. Sci.* **2008**, *109*, 3148.

(14) Xu, G.; Du, L.; Wang, H.; Xia, R.; Meng, X.; Zhu, Q. *Polym. Int.* **2008**, *57*,

1052.

(15) Mitchell, C. A.; Krishnamoorti, R. *Polymer* **2005**, *46*, 8796.

(16) Chen, B.; Evans, J. R. G. *Macromolecules* **2006**, *39*, 747.

(17) Li, B.; Esker, A. R. *Langmuir* **2007**, *23*, 2546.

(18) Li, B.; Wu, Y.; Liu, M.; Esker, A. R. *Langmuir* **2007**, *22*, 4902.

(19) Li, B.; Marand, H.; Esker, A. R. *J. Polym. Sci. Part B: Polym. Phys.* **2007**, *45*, 3300.

(20) Mareau, V. H.; Prud'homme, R. E. *Macromolecules* **2002**, *35*, 5338.

(21) Mareau, V. H.; Prud'homme, R. E. *Macromolecules* **2003**, *36*, 675.

(22) Joncheray, J. T.; Denoncourt, M. K.; Mathieu, C.; Meier, A. R. M.; Schubert, S. U.; Duran, S. R. *Langmuir* **2006**, *22*, 9264.

(23) Joncheray, J. T.; Denoncourt, M. K.; Meier, A. R. M.; Schubert, S. U.; Duran, S. R. *Langmuir* **2007**, *23*, 2423.

(24) Yu-Su, S. Y.; Sheiko, S. S.; Lee, H.; Jakubowski, W.; Nese, A.; Matyjaszewski, K.; Anokhin, D.; Ivanov, D. *Macromolecules* **2009**, *42*, 9008.

(25) Williams, A. A.; Day, B. S.; Kite, B. L.; McPherson, M. K.; Slebodnick, C.; Morris, J. R.; Gandour, R. D. *Chem. Commun.* **2005**, 5053.

(26) Gaub, H. E.; Moy, V. T.; McConnell, H. M. *J. Phys. Chem.* **1985**, *90*, 1721.

(27) Keller, D. J.; McConnell, H. M.; Moy, V. T. *J. Phys. Chem.* **1986**, *90*, 2311.

(28) Stephen, M.; McCauley, J. *Phys. Lett.* **1973**, *44A*, 89.

Chapter 6

Quartz Crystal Microbalance with Dissipation Monitoring (QCM-D) Studies of Nonionic Polymeric Surfactant Adsorption onto Phospholipid Bilayers

6.1. Abstract

Relationships between the structure of nonionic polymeric surfactants and their interactions with phospholipid bilayers were examined by the quartz crystal microbalance with dissipation monitoring (QCM-D). Results revealed the adsorption and desorption kinetics had a strong dependence on the hydrophobic tail group structure. Poly(ethylene glycol) (PEG) surfactants with a single linear alkyl tail can insert and saturate the lipid surface quickly. However, the surfactants had fast desorption rates. PEG lipids that contained dioleoyl and cholesterol tails demonstrated slower adsorption and desorption kinetics. The adsorption of Pluronics and Nonoxynol surfactants, two commercially available PEG surfactants, onto phospholipid bilayers was also studied. Pluronics had no apparent affinity for the phospholipid bilayer, while the Nonoxynol surfactants damaged phospholipid bilayer. The degree of destruction by the Nonoxynol surfactants decreased as PEG molar mass increased.

6.2. Introduction

Nonionic polymeric surfactants have continued to gain attention for applications in biomedical fields. The most extensively studied and used surfactants have been based on poly(ethylene glycol) (PEG). PEG, as an amphiphilic polymer, is soluble in water and a wide range of organic solvents. Its low-toxicity and sheathing ability make PEG an excellent material for drug delivery and biomaterial related applications.[1-5] PEGylations of peptides or hydrophobic drug molecules is an area of growing interest for enhancing therapeutic effects.[6]

The conjugation of a lipid molecule with PEGs, (PEG lipids) increased the blood circulation times of the therapeutic liposomes loaded with anti-cancer drugs.[7-8] In addition to the use of PEGs for the molecular design of drug delivery system, simple PEG surfactants were also explored for biological applications directly. For example, TPGS 1000 (d-α-tocopheryl poly(ethylene glycol 1000 succinate), Tween 80, Spans, and Cremophor EL inhibited the proteins associated with drug resistance.[9] Another good example is Pluronics, also known as Poloxamers. The Pluronics consist of a triblock copolymer with a central hydrophobic block of poly(propylene oxide) (PPO) and two hydrophilic chains of poly(ethylene oxide) (PEO) as the outside blocks. Pluronics inhibited not only drug efflux transporters,[10,11] but also the adsorption of proteins and bacterials.[12-18]

Therefore, understanding the nature of the interactions between polymeric surfactants and cell membranes is deemed important for improving applications and nonionic polymeric surfactants. Due to the complexity of natural cell membranes, interpretations of *in vivo* studies in terms of the surfactant-bilayer interactions on the basis of chemical structure are difficult. Therefore, lipid bilayers are employed as model membranes for *in vitro* studies. The traditional approaches usually incorporated unilamellar lipid vesicles with subjects of interest, and followed the changes in the system by ^{31}P NMR,[19] direct force measurements,[20] fluorescence spectroscopy,[21-22] DSC, SAXs,[23] etc. However, real time measurements are desirable for studies of adsorption kinetics. Recently, the quartz crystal microbalance with dissipation monitoring (QCM-D) technique has become a convenient tool for the study of interactions between phospholipid bilayers and water soluble proteins or polymers.[24-25] The QCM-D technique provides ultra-sensitive measurements of mass changes and insight into viscoelastic properties of the adsorbed layer.

Understanding the effects of tail group structure has on interactions between phospholipid bilayers and nonionic surfactants is the aim of this chapter. Furthermore, it is believed that this information could inform the design of drug delivery systems and other biomedical applications from nonionic surfactants in the future.

6.3. Materials and Methods

Details for molar masses and the structure of the PEG surfactants used in this study are described in Chapter 3.4. Phospholipids and the preparation of phospholipid vesicle solutions for bilayer fusion are provided in Chapter 3.5 and 3.6 respectively. QCM experimental details are covered in Chapter 3.11. Throughout this chapter, “k” is used as short notation for kg•mol^{-1} when the number average molar mass (M_n) is used to distinguish different lengths of the PEG headgroups. The lengths of the PEG headgroups are also expressed in terms of the degree of polymerization for the PEG chains (n_{EO}).

6.4. Results

6.4.1. Formation of Lipid Bilayers. The lipid bilayers used as the model surfaces for the adsorption studies were prepared by lipid vesicle fusion as described in Chapter 2 and Chapter 3. Phospholipid bilayers of 2-di-(9Z-octadecenoyl)-*sn*-glycero-3-phosphocholine (DOPC), and L-α-phosphatidylcholine (Egg PC) were prepared at 20 °C because this temperature is well above their gel-liquid transition temperature. In contrast, 1,2-ditetradecanoyl-*sn*-glycero-3-phosphocholine (DMPC) phospholipid bilayers were formed at 25 °C, because its gel-liquid transition temperature (23 °C) was slightly above room temperature (20 °C). Figure 6.1 shows representative QCM-D data for bilayer formation on SiO_2 by the three phospholipids. In Figure 6.1, scaled frequency change ($\Delta f/n$) where n is the overtone number, (blue curves left-hand axis) and dissipation changes (red curves, right-hand axis) were plotted as a function of time (t). The 25 ± 1 Hz scaled frequency shifts and a low dissipation values were consistent with the formation of a phospholipid bilayer.[26]

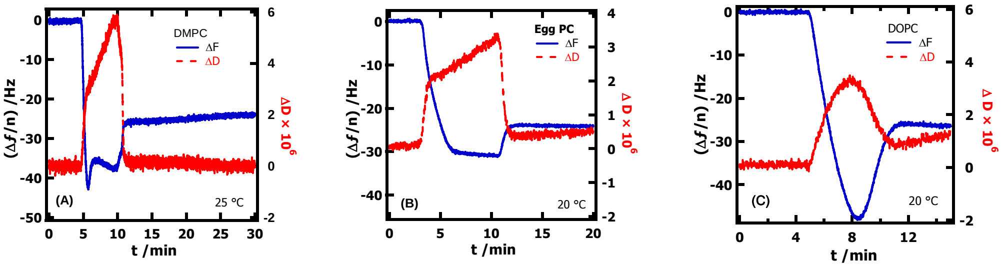

Figure 6.1. (Δf/n) and ΔD versus t for lipid bilayer fusion on SiO_2 sensor surfaces: (A) DMPC, (B) Egg PC, and (C) DOPC.

The small dissipation changes (ΔD) in Figure 6.1 meant a Sauerbrey analysis of the data was appropriate. The packing densities of phospholipids in the bilayer, expressed as a function of (A_{lipid}) area per lipid molecule, were calculated from

$$A_{lipid} = \frac{M \bullet N_a}{\Delta m} = -\frac{n \bullet M \bullet N_a}{\Delta f \bullet C} \qquad (6\text{-}1)$$

where, Δm is the surface mass density of the lipids adsorbed onto the sensor surface, N_a is Avogadro's constant; M is the molar mass of the lipid and C = 17.7 ng•cm^{-2}•Hz^{-1} is a constant that is specific to the QCM crystal. As seen in Figure 6.1, all three phospholipid exhibited similar trends. At short t, the sensor was equilibrated against water (Δf/n) = 0 and (ΔD = 0). After ~ 4 min, phospholipid vesicle solution was introduced into the system and (Δf/n) decreased while ΔD increased as vesicles adsorbed onto the sensor. After t = 8 to 10 min, the vesicles popped and spread onto the sensor. As water was lost in this process, (Δf/n) increased (mass decreased) and ΔD decreased (the film became rigid). The calculation yielded A_{lipid} ~ 60 Å^2•molecule^{-1}. The results showed that the packing densities of these three phospholipids were similar regardless of their structural differences and were consistent with liquid expanded (LE) films.

6.4.2. Adsorption Studies. For bilayer adsorption studies, a baseline was first obtained for the sensor coated by the phospholipid bilayer. The introduction of the surfactant solution can cause three possible responses. First, a negative deviation of the frequency from the baseline is possible. This outcome is consistent with surfactant adsorption onto the lipid bilayer. Second an increase of the frequency from the baseline is possible. Such a result is indicative of the removal of some or all of the bilayer (destruction). As already noted, a bilayer corresponds to $(\Delta f/\mathrm{n}) = 25 \pm 1$ Hz. Hence, if $(\Delta f/\mathrm{n})$ increases by ~ 25 Hz, such a result is consistent with complete removal of the phospholipid bilayer. Lastly, $(\Delta f/\mathrm{n})$ could remain unchanged. For this condition, weak, reversible adsorption occurs. All overtone data exhibited similar trends with different magnitudes. Therefore, the results for the third are presented in this chapter. However, viscoelastic modeling used to determine thicknesses and viscoelastic parameters employed data from all overtones except the first overtone which was excessively noisy. For the remainder of this chapter, results for studies of adsorption onto DOPC bilayers are presented. Control experiments with DMPC and Egg PC as discussed in Section 6.4.2.5 yielded no significant differences. Likewise, no significant differences between adsorption from water versus phosphate buffer saline (PBS) solutions were observed.

6.4.2.1. Pluronic Adsorption onto DOPC Bilayers. The changes of $(\Delta f/\mathrm{n})$ as a function of t for the adsorption of Pluronics onto DOPC lipid bilayers are shown in Figure 6.2. For low concentrations, $C = 0.1$ mg•mL^{-1}, Pluronic solutions exhibited no significant change in $(\Delta f/\mathrm{n})$ with respect to the baseline. This observation was interpreted as weak interactions between Pluronics and the DOPC bilayers. At higher concentrations (5 mg•mL^{-1}), an initial $(\Delta f/\mathrm{n})$ decrease ~ 10 Hz arose from the higher viscosity of the solution. After the solutions were switched back to water (t = ~ 20 min), the bulk effects were removed and $(\Delta f/\mathrm{n})$ quickly returned to a level near the baseline. Pluronic L101 had limited solubility in water. Therefore, only the low concentration solution (0.1 mg•mL^{-1}) was tested. In general, the Pluronics exhibited minor to insignificant interactions with the phospholipid bilayer.

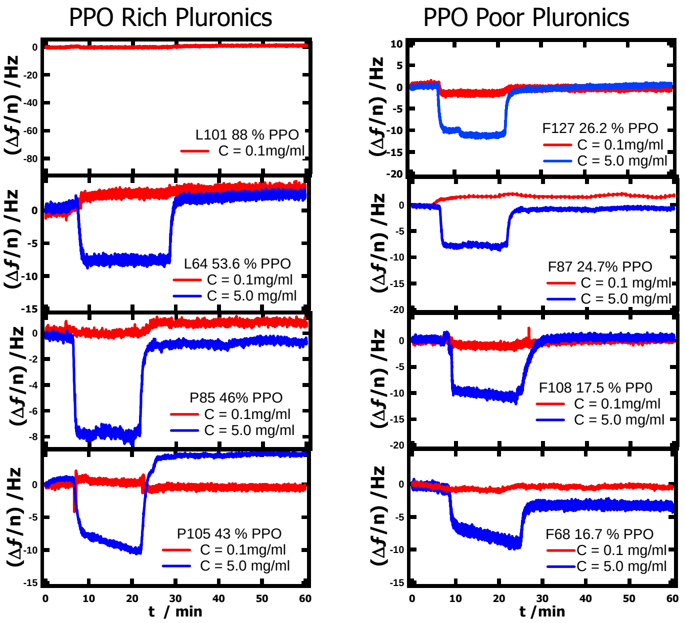

Figure 6.2. (Δf/n) versus t for Pluronic adsorption onto DOPC bilayers.

6.4.2.2. Single Tailed PEG Surfactant Adsorption onto Phospholipid Bilayers. In contrast to Pluronics, monostearate PEG and stearyl PEG ether surfactants adsorbed onto phospholipid bilayers and quickly reached adsorption equilibrium. After the surfaces were rinsed with water, the frequency slowly returned to levels near the baseline over a time range of ~2 hours (Figure 6.3). Effects of concentration are shown in Figure 6.3A. For 2 k monostearate PEG (n_{EO} = 45), (Δf/n) decreased with increasing concentrations. After the surfaces were rinsed, the (Δf/n) curves coincided at (Δf/n) = ~ -20 Hz regardless of the initial concentration. The results suggested that (Δf/n) = ~ -20 Hz was the frequency shift that corresponded to saturated adsorption. The additional initial decrease of (Δf/n) at higher concentrations was probably caused by bulk effects (higher solution viscosity or physical entanglement of the surfactant molecules with adsorbed molecules) at elevated concentrations that disappeared quickly after system was switched from surfactant solution to water. Consequently, the desorption for all the concentrations started at similar (Δf/n). The molar mass dependence for the adsorption of single linear alkyl tailed PEG surfactants is shown in Figure 6.3B. The surfactants had the same hydrophobic moiety, however, they had different PEG lengths. As shown in Figure 6.3B, (Δf/n) increased with the length of the PEG chain. An explanation for this change will be presented in the discussion section. In a control experiment, the hydrophilic 2000 monomethyl PEG ether (MPEG 2 k) showed no affinity for the phospholipid bilayers (Figure 6.3B). Liu at al.[24] also reported the insertion of Brij700 (poly(ethylene glycol) stearyl ether, ($HO\text{-}(CH_2CH_2O)_{100}C_{18}H_{37}$) into Egg PC lipid bilayers. However, no desorption studies for the surfactant were reported. For the one tailed PEG surfactants with small n_{EO} = 10, the surfactants started to show destructive effects on the phospholipid bilayer. As shown in Figure 6.4A and B, both 0.5 k monooleoyl PEG (n_{EO} = 10) and 0.5 k monostearate PEG (n_{EO} = 10) caused (Δf/n) to increase after the solution was switched to water. These results indicated that some of the phospholipid molecules were lost from the bilayer. Single tailed PEG surfactants with smaller n_{EO} had low solubility in water; therefore, they were not tested.

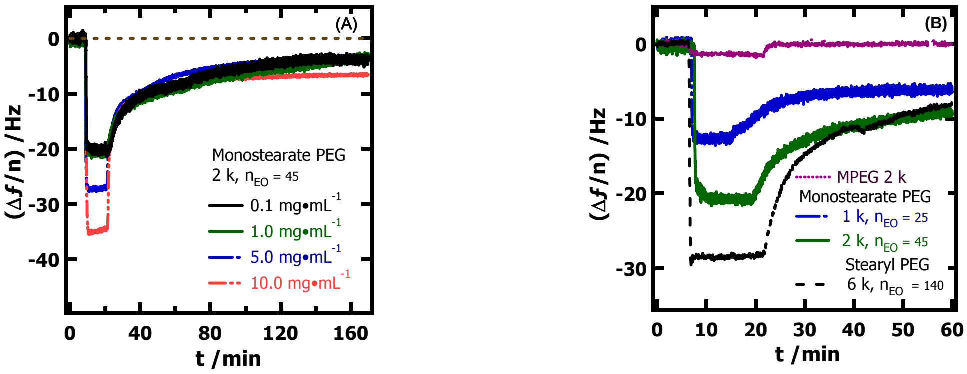

Figure 6.3. (Δf/n) versus t for monostearate PEG and a stearyl PEG ether onto DOPC lipid bilayers. (A) Concentration dependence for 2 k monostearate PEG (n_{EO} = 45). (B) Molar mass dependence for the adsorption of monostearate PEG esters and a stearyl PEG ether. The solution concentration was 0.1 mg•mL^{-1}.

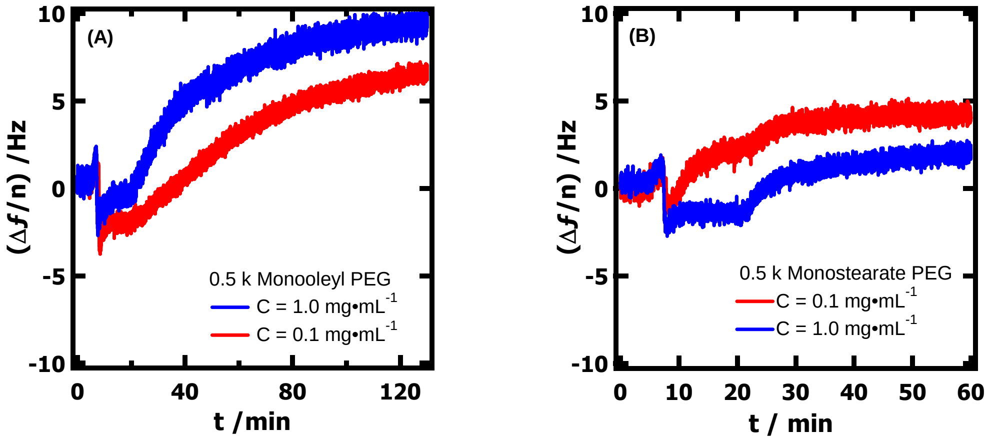

Figure 6.4. (Δ*f*/n) versus t for one tailed PEG surfactant adsorption onto DOPC bilayers at different concentrations: (a) 0.5 k monooleyl PEG (n_{EO} = 10), and (b) 0.5 k PEG monostearate (n_{EO} = 10).

6.4.2.3. Nonoxynol Adsorption onto DOPC Bilayers. Nonoxynols were widely used as spermicides. The ability of Nonoxynols to kill microbes in vitro was initially taken as evidence that it might be effective for the prevention of sexually transmitted diseases (STDs). However, later results[27-29] revealed the surfactants exerted strongly adverse effects on membranes and consequently, the materials have been abolished in most birth control and personal hygiene products. In Figure 6.5, the destructive effects of the Nonoxynols on phospholipid bilayer were investigated. As seen in Figure 6.5, (Δ*f*/n) did not change significantly when the surfactant solutions were introduced to the phospholipid bilayer surface. Once the solution was switched back to water, (Δ*f*/n) increased dramatically. As positive (Δ*f*/n) are indicative of mass loss, Nonoxynols clearly removed phospholipid from the sensor surface. The destructive effects exhibited a dependence on the PEG chain length: for n_{EO} = 10, (Δ*f*/n) increased by ~26 Hz, a result that was consistent with the complete removal of the phospholipid bilayer. In contrast, (Δ*f*/n) for n_{EO} = 15, 18 and 20, were < 26 Hz. Hence, the bilayers were only partially destroyed. Compared to the single tail PEG surfactants (Figure 6.4), the Nonoxynol surfactants exhibited greater destructive effects on phospholipid bilayers. This was possibly due to the highly branched tail group structures which would promote the formation of the mixed micelles that solubilized the phospholipids. It was interesting to note that (Δf/n) did not initially decrease from the baseline when the solution was introduced even for the long PEG chain lengths. Either the highly branched tail group structure hindered the incorporation of the Nonoxynol tail group into the bilayers or the addition of Nonoxynol to the bilayers was offset by a loss of DOPC. The destructive effects of the Nonoxynols were essentially concentration independent as seen in Figure 6.5. These results suggested the problems with Nonoxynols in commercial product arose from membrane destruction. As the cell membranes are the first barriers of defense for cells and their destruction would facilitate the contraction of viruses.

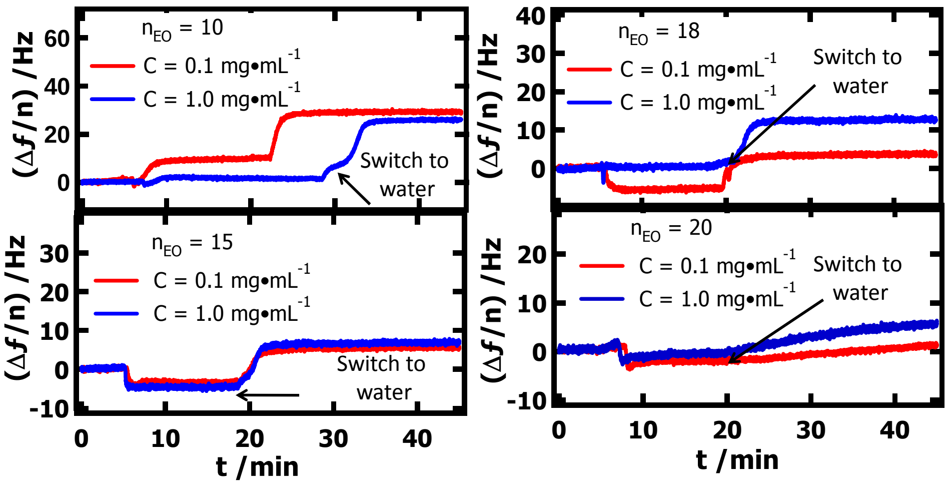

Figure 6.5. (Δf/n) versus t for Nonoxynol (PEG mono-4-nonylphenyl ethers) interactions with DOPC bilayers. A baseline is established by following water over the DOPC lipid bilayer for 5 min followed by the injection of the surfactant solutions. Water then rinsed the surfaces for t > 20 min. Nonoxynol n_{EO} = 7 (not shown) also completely removed the DOPC bilayer.

6.4.2.4. Phospholipid PEG Adsorption onto DOPC Bilayers. Dioleoyl PEG had a hydrophobic tail group structure that was similar to DOPC. Compared to the single tailed PEG surfactants, dioleoyl PEG lipids exhibited significantly slower adsorption and desorption kinetics. In Figure 6.6A, (Δf/n) showed very slow adsorption kinetics for 3 k and 5 k dioleoyl PEGs. Correspondingly, ΔD slowly increased during adsorption (Figure 6.6B). Higher |Δf/n| and ΔD values for 5 k dioleoyl PEG relative to 3 k dioleoyl PEG indicated a thicker hydrated PEG layer formed.

Compared to the dioleoyl PEGs, distearoyl PEGs had two saturated alkyl chains. The interaction of distearoyl PEGs with lipid bilayers was shown in Figure 6.7. As seen in Figure 6.7, an initial decrease in (Δf/n) upon exposure to a distearoyl PEG solution quickly reverted back to the baseline once the solution was switched back to water. This result meant distearoyl PEGs showed no affinity for the phospholipid bilayer. A possible explanation will be provided in the discussion section of this chapter.

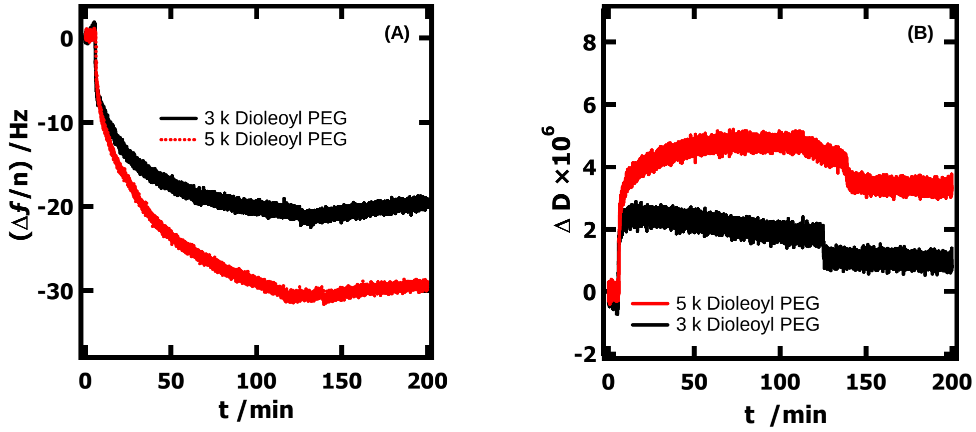

Figure 6.6. Dioleoyl PEG adsorption onto DOPC bilayers: (A) (Δf/n) and (B) ΔD. The concentration C = 1 mg•mL^{-1}.

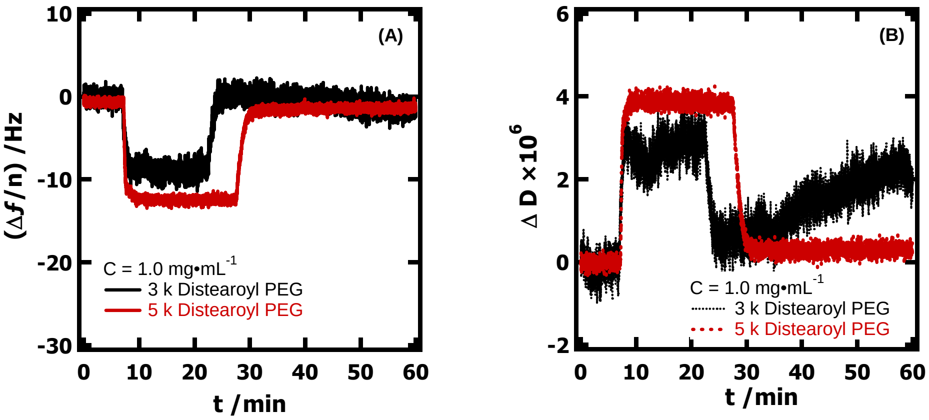

Figure 6.7. Distearoyl PEG interactions with DOPC bilayers: (A) (Δ*f*/n) and (B) ΔD.

6.4.2.5. Cholesterol PEG Adsorption onto DOPC Bilayers. Although cholesterol is classified as a lipid, it has unique biological functions in cell membranes. The cholesterol used in this study has a structure comprised of a short, thermally flexible, hydrocarbon tail and a larger, rigid, hydrophobic, fused ring structure headed with a hydroxyl group. A previous study showed cholesterol increased the bilayer bending and the compression moduli by incorporation into the voids within the phospholipid bilayer.[30] (Δ*f*/n) and ΔD as functions of t for 2.5 k cholesterol PEG (n_{EO} = 57) and 6 k cholesterol PEG (n_{EO} = 140), are shown in Figure 6.8. In contrast to dioleoyl PEG lipids (Figure 6.6), cholesterol PEGs saturated the bilayer surface faster. For 6 k cholesterol PEG, (Δ*f*/n) decreased to a minimum value and then slightly increased before a new equilibrium was reached. Correspondingly, the ΔD exhibited a spike and decreased to a plateau. A possible explanation for these phenomena will be provided in the discussion section.

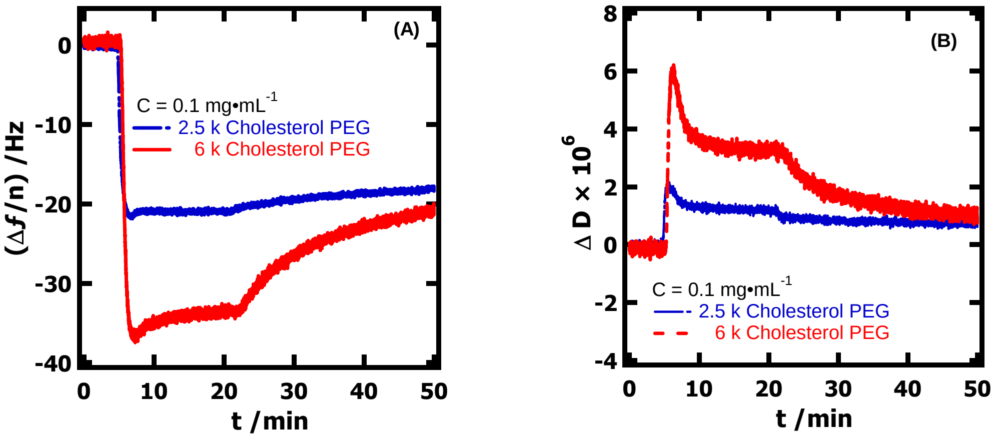

Figure 6.8. Cholesterol PEG adsorption onto DOPC bilayers: (A) (Δ*f*/n) and (B) ΔD.

6.4.2.6. Adsorption of Surfactants onto Different Lipid Surfaces. As mentioned previously, DOPC, Egg PC and DMPC lipid bilayers had similar molecular packing density regardless of the structural differences. The adsorption of PEG surfactants onto DOPC, Egg PC and DMPC was compared in Figure 6.9. The adsorption results of 6 k stearyl PEG and 2.5 k cholesterol PEG onto the three different lipid bilayers were selected as representative examples. As seen in Figure 6.9, almost identical adsorption and desorption was observed and confirmed that that lipid structure difference (at least for these three lipids) had no significant effect on the adsorption/desorption process.

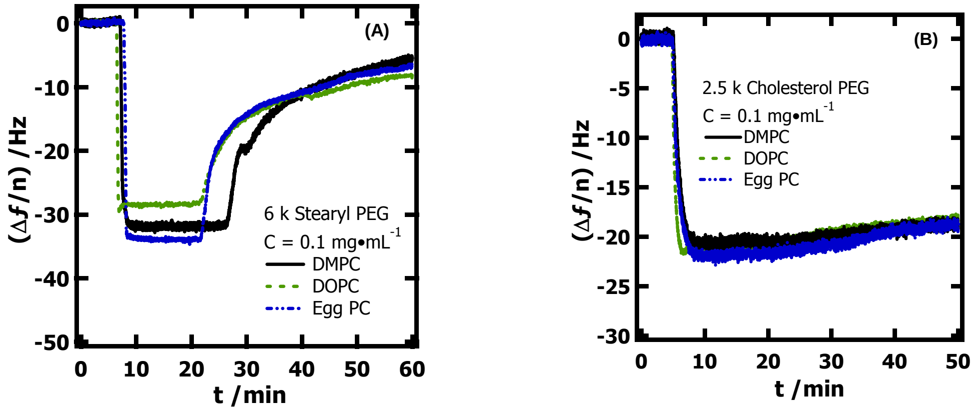

Figure 6.9. (Δ*f*/n) versus t for (a) 6 k stearyl PEG and (b) 2.5 k cholesterol PEG adsorption onto DOPC, DMPC and Egg PC bilayers.

6.5. Discussion

6.5.1. Tail Group Size Effects. The adsorption/desorption of PEG surfactants onto/from the surfaces of phospholipid bilayers showed a dependence on the hydrophobic tail group structures. These two layers of phospholipids are arranged in such a way that the hydrophilic head groups shield the hydrophobic lipid tails from the water. Therefore, the surfactant molecules initially interacted with the hydrated layer upon adsorption. As shown in Figure 6.3B, the PEG homopolymer had no apparent affinity for the lipid headgroup layer. This observation was consistent with theoretical calculations which showed that a large energy penalty existed for PEO chains to cross the lipid bilayer.[31] Therefore, a strong conclusion was drown that the driving force for PEG surfactant adsorption onto the lipid bilayers was the interactions between the surfactant tails and the phospholipid tail groups. As mentioned previously, the lipid bilayers had a packing density of ~ 60 $Å^2$•molecule^{-1}. Hence, the lipid molecules were not tightly packed in bilayers.[32] This specific packing density also imposed a size matching requirement for the hydrophobic tailgroups. The size matching requirement was observed in previous studies of PPO-PEO block copolymer-lipid bilayer interactions. Nejadnik et al.[33] studied the adsorption of Pluronic F-127 (M_n = 12.6 kg•mole^{-1} and PPO mole% = 26.2 %) onto surfaces with different hydrophobicities and found that the interactions between hydrophobes dominated the adsorption. Stated another way, Pluronics only adsorbed onto hydrophobic surfaces through interactions between the PPO hydrophobic blocks and the hydrophobic surfaces. For hydrophilic surfaces, Pluronics had very limited adsorption. Similarly, small angle X-ray scattering (SAXs) and differential scanning calorimetry (DSC) studies also revealed that Pluronics only weakly associated with the lipid membranes.[34] In contrast, the PPO-PEO diblock copolymer showed much stronger incorporation into the hydrophobic layer of the lipid bilayers, especially, when the length of the PPO matched the length of the alkyl chains of the phospholipids.[35] The weak interaction of Pluronics with lipid bilayer was attributed to mismatches of the PPO center block with the hydrophobic alkyl tails of the phospholipid molecules.[34] The *in-situ* adsorption studies presented in this chapter confirmed the interactions of Pluronics with phospholipid bilayers were weak.

The size matching requirement was also applied to the study of Nonoxynols. The average cross-sectional area for the hydrophobic branched tail group of Nonoxynol was obtained from surface pressure-average area per molecule ($\Pi-A$) isotherm studies at the air/water (A/W) interface (Figure 6.10). The Nonoxynols with (n_{EO} = 3, 4, and 5) yielded similar $\Pi-A$ isotherms. The isotherms were characterized by a lift-off area per molecule, the area where Π increased from zero, around $A \sim 70$ Å^2•molecule^{-1}, and the formation of a liquid expanded (LE) monolayer for $70 > A > 20$ Å^2•molecule^{-1}. For $A < 20$ Å^2•molecule^{-1}, collapse of the films began with collapse pressures, $\Pi_C > 35$ mN•m^{-1}. Upon expansion of the film, large hysteresis was observed, a reflection of tail group aggregation upon collapse of the film. An extrapolation of the steepest slope in Figure 6.10 back to the X-axis yielded a limiting cross-sectional area of ~ 60 Å^2•molecule^{-1}. This highly branched tail group structure of the C-9 hydrocarbon chain not only hindered the insertion of the tail group into the membrane, but presumably solubilized the phospholipid of the bilayer that ultimately led to their removal from the surface.

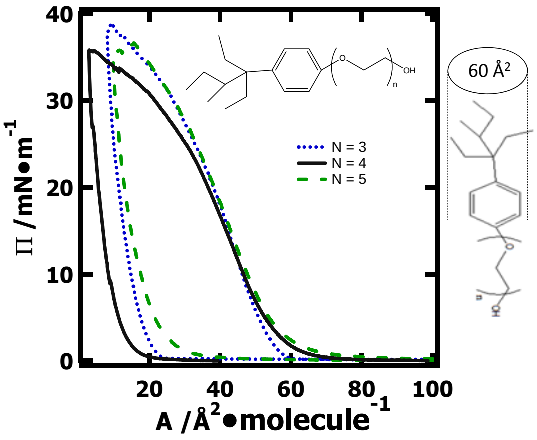

Figure 6.10. Compression/expansion Π–A isotherm cycles at 22.5 ˚C for Nonoxynols with n_{EO} = 3, 4 and 5 at the air/water interface. The compression/expansion rate was 10 mm•min^{-1}. The samples were prepared by flash column chromatography separation of the commercial surfactant and the structures were verified with ^{1}H NMR. The commercial Nonoxynol surfactants were a mixture of different PEG chain lengths and the tailgroups were a mixture of isomers.

The adsorption and desorption kinetics were also related to the size of the tail groups. For a single linear saturated C-18 hydrocarbon tail surfactant, the cross-sectional area for the tail group was ~20 Å^2•molecule^{-1}. In comparison, cholesterol had a cross-sectional area of ~ 40 Å^2 per molecule[36] and the dioleoyl surfactants had an average cross-sectional areas of 60~70 Å^2 which was similar to the calculated molecular area of DOPC in the bilayer. The effects of tail group size on the adsorption and desorption kinetics of surfactants onto phospholipid bilayers were noted. Figure 6.3, 6.6, and 6.8 showed that the time required for saturation of the DOPC bilayer by adsorbing surfactant increased with tail group size. Small tail groups such as PEGs with single or cholesterol tails inserted into and saturated the bilayer surface much faster than dioleoyl PEGs. Upon switching from surfactant solution to water, the surfactants with smaller tail groups desorbed faster. The desorption of the surfactants after the removal of the concentration gradient suggested that the adsorption of the surfactants onto the lipid bilayers was a dynamic competition between adsorption and desorption. Once the concentration gradient was removed, only desorption was observed.

In this study, the adsorption of the PEG surfactant onto DOPC bilayers was treated as a single molecular layer. For a kinetic analysis of monolayer adsorption, the Langmuir equation was used:

$$\frac{d\Gamma}{dt} = k_{ads}C(\Gamma_{max} - \Gamma) - k_{off}\Gamma \tag{6-2}$$

where, Γ is the surface excess, k_{ads} is the adsorption rate constant, k_{off} is the desorption constant, C is the effective concentration of the surfactant, Γ_{max} is the maximum surface excess, and $(\Gamma_{max} - \Gamma)$ was the available binding sites for adsorption. Eq. 6-2 was applied with four assumptions: the adsorbed layer is a monolayer, the adsorption is fully reversible, there are a finite number of (discrete) binding sites, and binding sites are equal. In this study, k_{ads} was related to the activation energy for the incorporation of the surfactants tail groups into the phospholipid bilayers, while k_{off} was related to the energy barrier for the removal of surfactant molecules from the phospholipid bilayer. Additionally, $(\Gamma_{max} - \Gamma)$ served as a measurement of the number of available binding sites for adsorption. Eq. 6-2 also had two important boundary conditions. At the beginning of the adsorption process, or when the desorption was negligible,

$$\frac{d\Gamma}{dt} = k_{ads}C(\Gamma_{max} - \Gamma) \tag{6-3}$$

Integration of Eq. 6-3 yielded:

$$\ln\frac{\Gamma_{max}}{\Gamma_{max}-\Gamma} = k_{ads}Ct \tag{6-4}$$

Eq. 6-4 indicated that at early stages of adsorption, $\ln\frac{\Gamma_{max}}{\Gamma_{max}-\Gamma}$ increased linearly with adsorption time t. The second boundary condition for Eq. 6-2 was for the case where the adsorption term could be treated as zero after the concentration gradient was removed:

$$\frac{d\Gamma}{dt} = -k_{off}\Gamma \tag{6-5}$$

Integration of Eq. 6-5 led to:

$$\ln\frac{\Gamma}{\Gamma_{max}} = -k_{off}t \qquad (6\text{-}6)$$

According to Eq. 6-6, $\ln\frac{\Gamma}{\Gamma_{max}}$ had a linear relationship with time for a desorption process and slopes of $\ln\frac{\Gamma}{\Gamma_{max}}$ versus t yielded k_{off} from the appropriate time regime.

In QCM-D measurements, $(\Delta f/\text{n})$ was directly proportional to the surface excess Γ, therefore Eq. 6-4 and 6-6 were rewritten in terms of $(\Delta f/\text{n})$

$$\ln\frac{(\Delta f_{max}/n)}{(\Delta f_{max}/n)-(\Delta f/n)} = k_{ads}Ct \qquad (6\text{-}7)$$

$$\ln\frac{(\Delta f/\text{n})}{(\Delta f_{max}/n)} = -k_{off}t \qquad (6\text{-}8)$$

where $(\Delta f_{max}/n)$ was the maximum scaled frequency change at the adsorption equilibrium. Plots of $\ln\frac{(\Delta f/\text{n})}{(\Delta f_{max}/n)}$ versus t for the desorption of different surfactants are shown in Figure 6.11 and desorption rate constants obtained from the initial slopes of the desorption curves are tabulated in Table 6.1. In Figure 6.11, the desorption rate attenuated with time. The initial desorption rate constants in Table 6.1 were the constants obtained from the initial 10% changes of $(\Delta f/\text{n})$. As seen in Figure 6.11B, 6 k cholesterol PEG had a faster desorption rate compared to 2.5 k cholesterol PEG. In general, the surfactants that had a longer PEG length desorbed faster for the same tail group. Another conclusion drawn from Figure 6.11 and Table 6.1 was that surfactants with bigger tail groups and comparable PEG length had smaller desorption rate constants. If one compared the desorption of 6 k stearyl PEG and 6 k cholesterol PEG, 6 k stearyl PEG desorbed three times as fast. As dioleoyl PEGs had the largest tail group structures, they had the slowest desorption kinetics. As noted in Chapter 2 for QCM-D measurements, the baseline will drift by ~ 1-5 Hz per hour, therefore, the lowest significant desorption rate constant that could be obtained from QCM-D was 1×10^{-5} s^{-1}. The k_{off} for dioleoyl PEGs less than the detection limit. Therefore, the adsorption of dioleoyl

PEGs was considered irreversible. The decay of k_{off} with time was attributed to the polydispersity of PEG on the surfactants. The faster desorption kinetics in the initial desorption step were likely caused by the desorption of higher molar mass surfactants.

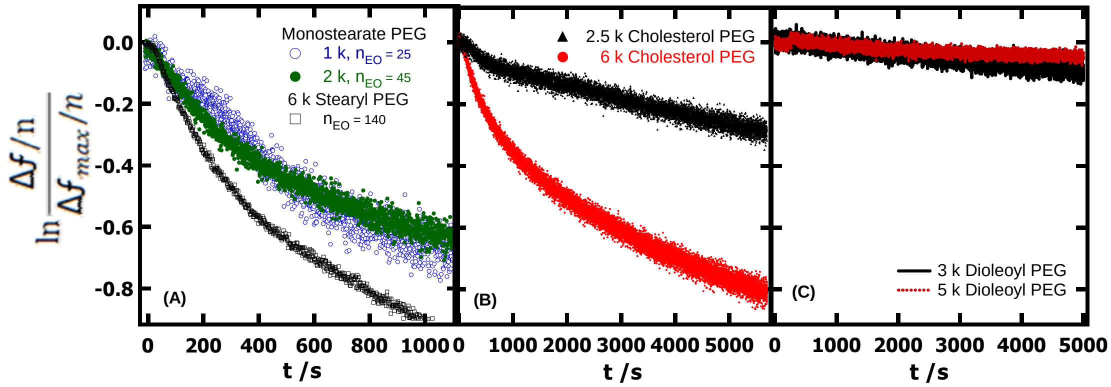

Figure 6.11. Desorption kinetics for: (A) monostearate PEGs and stearyl PEG; (B) cholesterol PEGs and (C) dioleoyl PEGs.

Table 6.1. Initial k_{off} for Various Surfactants from DOPC bilayers

	Monostearate PEG $n_{EO} = 25$	Monostearate PEG $n_{EO} = 45$	Stearyl PEG $n_{EO} = 140$	Cholesterol PEG $n_{EO} = 57$	Cholesterol PEG $n_{EO} = 140$
k_{off} (s^{-1})#	6.9×10^{-4}	6.6×10^{-4}	2.4×10^{-4}	1.3×10^{-4}	7.1×10^{-4}

The fit covered the initial 10% desorbed.

Analysis of the desorption kinetics showed that the size of tail group played a critical role in the desorption kinetics. The relationship between the tail group size and the desorption kinetics aided the analysis of the adsorption kinetics. Plots of $\ln \frac{\Gamma_{max}}{\Gamma_{max}-\Gamma}$ versus t were provided in Figure 6.12. The dashed line denoted 99% surface saturation. The adsorption kinetics studies were done in the experimental conditions of C = 1 mg•mL^{-1} and a solution flow rate of 0.2 mL•min^{-1}. The results also revealed the adsorption kinetics strongly depended upon tail group structure. For tailgroups with smaller cross-sectional areas and simple structures like alky chains, adsorption rates were faster. As monostearate PEGs and stearyl PEGs only differed by the linking group, ester versus ether between the alkyl chains and the PEG, it was not surprising that they both had fast adsorption rates (Figure 6.12A). Nonetheless, slight differences were observed between monostearate PEG and PEG ethers. 6 k stearyl PEG and another linear alkyl ether PEG surfactant, Brij58 ($HO-(CH_2CH_2O)_{20}C_{16}H_{33}$) saturated the surface in ~10 s, whereas, monostearate PEG surfactants took ~20 s for surface saturation. Meanwhile, the deviation of $\ln\frac{\Gamma_{max}}{\Gamma_{max}-\Gamma}$ from the linear relationship with time was observed for monostearate PEGs, suggesting that the desorption of the surfactant or other factors started to affect the overall adsorption rate at certain surface coverage of the monostearate surfactants. From the plots of $\ln\frac{\Gamma_{max}}{\Gamma_{max}-\Gamma}$ versus t, the critical surface coverage, θ_C, at which surfactant desorption caused deviation from Eq. 6-7 could be deduced. For 2 k monostearate PEG, n_{EO} = 45, θ_C was ~85%, and for 1 k monostearate PEG, n_{EO} = 25, θ_C was ~95%. In contrast, stearyl PEG surfactants achieved full surface coverage without a dramatic change in slope. In contrast, cholesterol PEGs exhibited a nearly linear increase in $\ln\left(\frac{\Gamma_{max}}{\Gamma_{max-\Gamma}}\right)$ and saturated the surface in ~ 40 s as seen in Figure 6.12B. In Figure 6.12C, the slowest adsorption kinetics were observed for dioleoyl PEGs. However, the diffusion rate of the molecules was an important factor that needed to be considered for the analysis of the adsorption kinetics. In this study, the baseline was first obtained with pure water. The volume for the QCM-D chamber is ~40 μL. At the initial stage of the adsorption, there existed a concentration gradient due to diffusion of the molecules and the time required for the complete replacement of pure water with the solution in the QCM-D chamber. Consequently, at the beginning of the adsorption process, $\ln\left(\frac{\Gamma_{max}}{\Gamma_{max-\Gamma}}\right)$ increased more slowly than slightly later times where steady state was achieved. Hence the measurement of accurate k_{ads} was problematic for the fast processes in this study.

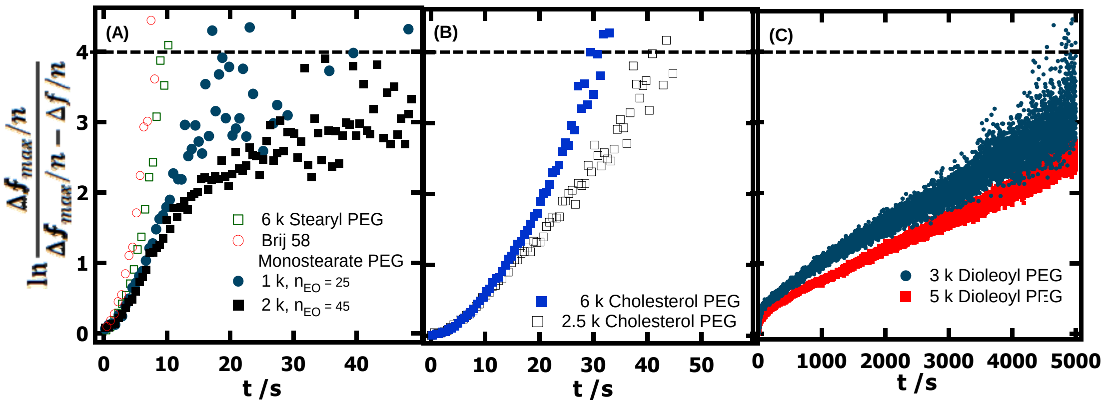

Figure 6.12. Adsorption kinetics for (A) single alkyl tailed PEG surfactants, (B) cholesterol PEGs, and (C) dioleoyl PEGs.

A number of theoretical[37] and experimental[38] studies for grafting polymers with reactive endgroups onto a solid surface have been reported. In all these reported studies, the kinetics of the grafting reactions were very fast. Therefore, the adsorption rates were governed by the diffusion of the polymers onto the solid surface. The adsorption kinetics were divided into two regimes. For the first regime, chains quickly adsorbed onto the surface and adopted mushroom conformations. After the formation of the mushroom layer, there was an abrupt slowdown in the adsorption rate in the second regime, the adsorption kinetics were then controlled by the diffusion of polymer chains through the already tethered chains and the tethering process kinetics were proportional to log(t).[38] Unlike traditional studies, the adsorption in this study was driven by the weak interaction between hydrophobic groups, and the grafting sites were mobile within the fluid-like phospholipid bilayer. As seen in Figure 6.12, PEG surfactants with similar molar mass underwent different incorporation into the lipid bilayers. As the mushroom like conformations for PEGs of similar molar mass would have been the same, the initial “grafting step” must have controlled adsorption and was correlated with the size of the hydrophobic tail.

6.5.2. ΔD versus (Δ*f*/n) Analyses of PEG Surfactant Adsorption onto DOPC Bilayers.

The conformation of the adsorbed surfactants on the phospholipid bilayer surface is an interesting question. As noted in Figure 6.3A, an increase of the concentration caused an increase of the initial |Δ*f*/n|. However, the removal of the concentration gradient caused all the desorption curves to start at the same point. This observation implied that part of (Δ*f*/n) at higher concentration was either from higher bulk viscosity effects or loosely bound surfactant molecules. Inferences about conformations of the adsorbed macromolecules were gleaned from plots of ΔD versus (Δ*f*/n), which eliminated time as an explicit parameter. The dissipation value, ΔD, was related to the packing density, chain conformations and hydration status of the adsorbed film, whereas, (Δ*f*/n) was directly associated with the adsorbed mass (both polymer and water). Therefore, plots of ΔD versus (Δ*f*/n) allows changes in the viscoelastic properties of the adsorbed film to be considered in terms of adsorbed mass increments. This approach was especially useful for comparison of surfactants with similar structure that underwent rapid adsorption. In Figure 6.13A, ΔD versus (Δ*f*/n) was plotted for 6 k stearyl PEG as a representative example. At the initial state, a non-linear increment of ΔD with (Δ*f*/n) was observed for all four concentrations. For the higher concentrations of 5 mg•mL^{-1} and 10 mg•mL^{-1}, an additional increase of ΔD was observed after (Δ*f*/n) initially saturated and increased linearly with a larger slope. On the basis of this observation, the adsorption process was divided into two separate stages. The first stage was attributed to the adsorption of the surfactants onto the lipid bilayer. For this stage, the surface excess was independent of concentration for the concentration range studied. For the second stage, ΔD increased with almost no mass increase. Physical entanglement of the free polymers in the solution with the adsorbed surfactant molecules may have occurred. In the second stage, ΔD increased linearly with |Δ*f*/n| with a much larger slope, an indication that the additional layer formed in this stage had different viscoelastic properties compared to the first layer. A sloppy layer was anticipated for the second layer. The physically entangled layer was removed quickly upon removal of the concentration gradient. As a result, all the desorption curves started from a similar (Δf/n) regardless of the starting concentration differences, as shown in Figure 6.3A.

Plots of ΔD versus (Δf/n) for the adsorption of single tailed PEGs, cholesterol PEGs, and dioleoyl PEGs are shown in Figure 6.13B, C and D respectively. For monostearate PEGs and 6 k stearyl PEG, the slope of the curve decayed with the increasing |Δf/n|. At the beginning of the curve, the ΔD increased nearly linearly with |Δf/n|. However, the linear relationship deviated with increasing |Δf/n| indicating that the adsorbed PEG chains gradually adopted a densely packed conformation as adsorbed mass increased. The slope of the curves continued to decrease until ΔD reached its maximum value. After the maximum value, ΔD started to decrease at the same |Δf/n|, a phenomenon that was more clearly observed with longer PEG chains. As seen in Figure 6.13B, ΔD values significantly decreased at high |Δf/n| for 6 k stearyl PEG, whereas, monostearate PEG n_{EO} = 25 and monostearate PEG n_{EO} = 40 show no decrease in ΔD at the highest |Δf/n|. In Figure 6.13C, ΔD decreased for both 2.5 k cholesterol PEG and 6 k cholesterol PEG, and the change in ΔD for the 6 k film was three times greater than the 2.5 k film. As noted for 6 k cholesterol PEG, |Δf/n| also slightly decreased after the maximum value. ΔD versus |Δf/n| plots for dioleoyl PEGs had distinctively different slopes indicating different kinetics for the incorporation of the bulky tail groups into the lipid bilayers. After saturation, ΔD decreases were also observed for dioleoyl PEGs.

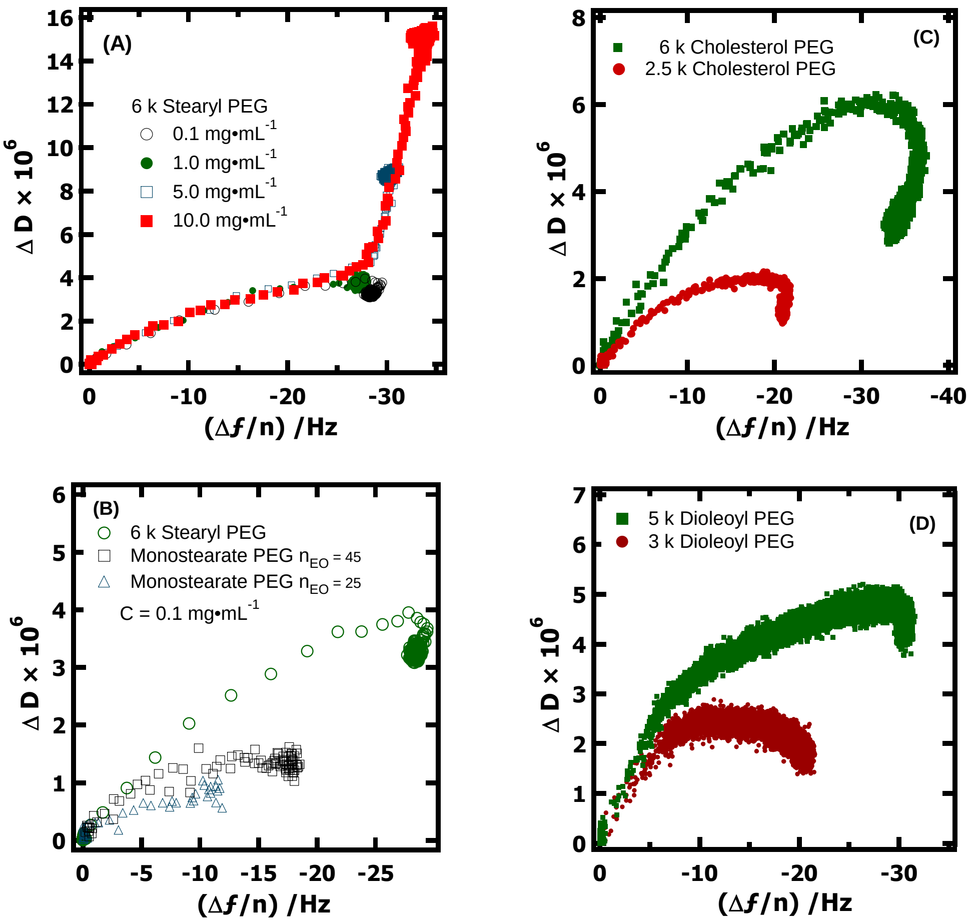

Figure 6.13. ΔD versus (Δ*f*/n) for surfactant PEG adsorption onto DOPC bilayers. (A) The concentration dependence for stearyl PEG 6 k, (B) different single alkyl tailed PEG surfactants, (C) 2.5 k and 6 k cholesterol PEG, and (D) 3 k and 5 k dioleoyl PEG, C = 1.0 mg•mL^{-1}.

Two possible explanations for the decrease of ΔD at large |Δ*f*/n| were considered. First, dehydration of the PEG layer may have occurred. Second, the distribution of PEG chain lengths for tethered PEGs may have changed. For the first argument, the QCM-D instrument senses the total mass of the hydrated adsorbed layer. If the water coupled to the film changed with the increment of the adsorbed mass, the frequency and the dissipation would have also changed. The over-crowded PEGs may change the water coupling status and induce the partial dehydration of the PEG layer. Consequently, ΔD and (Δf/n) would have also decreased accordingly after the maximum value. The second explanation was based on the previous desorption kinetics study. The surfactant with longer PEG chains desorbed faster. The faster desorption would have favored replacement of the larger molar mass surfactants with smaller ones. As a result, ΔD and |Δf/n| would have decreased. In this argument, high molar mass surfactants would demonstrate this effect more clearly compared to small molar mass surfactants, as observed in Figure 6.13. At present, proof for the true cause of the ΔD decrease remains elusive and would require techniques such as surface plasmon resonance (SPR) or Fourier transform infrared spectroscopy (FTIR) to understand the role of coupled water.

6.5.3. Conformations of the Adsorbed PEG Chains. In addition to the adsorption and desorption kinetics, the thickness, shear modulus (elasticity), and shear viscosities of the adsorbed films were modeled with the Q-Tool software which utilized a Kelvin-Voigt model. Here, it was assumed that ΔD decreases after adsorption saturated were caused by a tighter packed surfactant layer and that the phospholipid bilayer could be treated as an extension of the silica coated quartz crystal. Modeling results in Table 6.2 correspond to the equilibrium (Δf/n) and ΔD.

As discussed in Chapter 2, the conformation and thickness of the absorbed polymer chains with one end tethered to a planar surface were dictated by the grafting density and the length of the adsorbed chains. Mushroom and brush conformations were two possibilities. For the mushroom conformation, the thickness (L) in a good solvent is equal to the Flory radius (R_F):[39]

$$L = R_F = \alpha N^{0.6} \tag{6-9}$$

where α is the effective monomer length for the ethylene oxide repeat unit, N is the degree of polymerization (obtained from M_n), and α is taken as 0.35 nm for PEG. In a brush conformation, the chain conformation is stretched and the film thickness is calculated from[39]

$$L = \alpha N \sigma^{1/3} \tag{6-10}$$

where σ is the surface coverage. The direct comparison of R_F with the thickness deduced from viscoelastic modeling was used to judge whether the chains adopted mushroom or brush conformations. The calculated Flory radii for all surfactants are tabulated in Table 6.3. As seen in Table 6.3, the thicknesses of all the PEG layers had comparable values with R_F for all the surfactants. These results suggested that PEG chains tethered to the lipid bilayer surface adopted a closely packed random coil mushroom conformation. The addition of more surfactant molecules would have induced strong steric repulsions from the adjacent PEG chains, with only small gains in favorable van der Waals interactions between the surfactant tailgroups and the phospholipid tailgroups. Therefore, further adsorption stopped.

Table 6.2. Data Modeling Results for the Thickness of the PEG Layers

Surfactants	**R_F [a] (nm)**	**Thickness[b] (nm)**
Monostearate PEG n_{EO} = 25	2.4	2.4 ± 0.0
Monostearate PEG n_{EO} = 45	3.4	3.6 ± 0.1
Stearyl PEG n_{EO} = 140	6.7	6.2 ± 1.0
2.5 k Cholesterol PEG	4.0	3.5 ± 0.2
6 k Cholesterol PEG	6.7	6.6 ± 0.1
3 k Dioleoyl PEG	4.4	3.9 ± 0.2
5 k Dioleoyl PEG	5.9	6.7 ± 0.2

[a] R_F were calculated according to Eq. 6-3. The size of the EO repeat unit was taken as 0.35 nm. One standard deviation error bars were calculated from three separate measurements.

[b] Data modeling parameters: density of the adsorbed layer = 1027 kg•m^{-3} and the viscosity of water = 0.001 Pa•s at 20 ˚C.

6.5.4. DSC Studies of Distearoyl PEGs. The final question was why the distearoyl PEGs did not interact with DOPC bilayers. DSC results for 3 k distearoyl PEG, 5 k distearoyl PEG and 5 k dioleoyl PEG, are provided in Figure 6.14A. As seen in Figure 6.14, the three PEG surfactants all had the characteristic endothermic and exothermic peaks associated the melting and crystallization of PEG. The differences were an extra exothermic peak for the distearoyl PEGs. This peak was assigned to the crystallization of the crystalline distearoyl tail groups at ~ 42 ˚C. This temperature was above room temperature. The crystallization of the tail group for dioleoyl PEG 5 k was not observed because of cis-unsaturation in the tail structure. Dynamic light scattering (DLS) was also performed and the results are shown in Figure 6.14B for 5 k distearoyl PEG. The DLS results revealed time dependent aggregation. In fact, the precipitation of distearoyl PEGs was observed at long enough times. In the aggregate, the crystalline tail groups were wrapped by PEG chains. Therefore, the interaction with the bilayer became similar to the case of non-interacting PEGs interactions with lipid bilayers (Figure 6.3B).

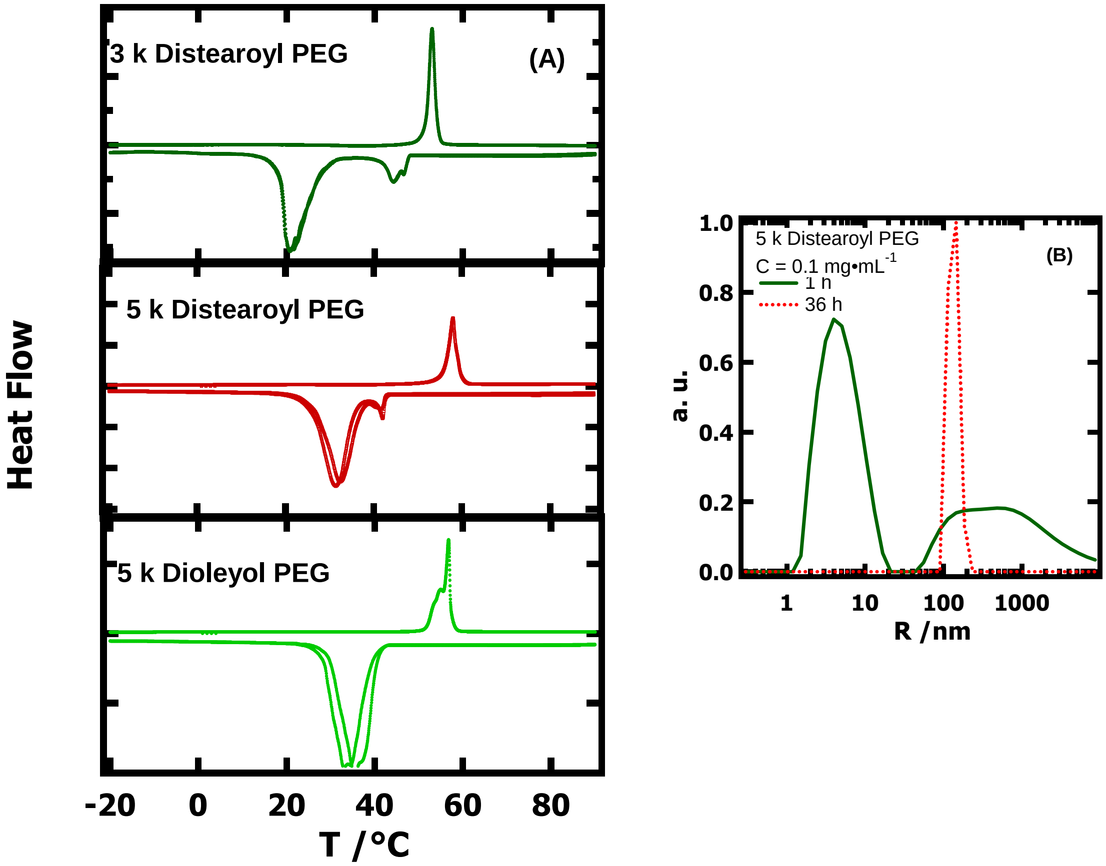

Figure 6.14. (A) The second and third heat flow-temperature DSC heating-cooling cycles for distearoyl PEGs and dioleoyl PEG 5 k. The heating rate was 5 ˚C•min^{-1} and the cooling rate was 20 ˚C•min^{-1}. (B) Time dependence of the size of the 5 k distearoyl PEG vesicles in water, at a scattering angle of 90˚.The surfactant was heated to dissolve the 5 k distearoyl PEG and DLS was performed at 25 ˚C.

6.6. Conclusions

The adsorption of nonionic surfactants onto phospholipid bilayers was dependent upon the structure of the surfactant, but not the phospholipid used (DOPC, Egg PC, or DMPC). Pluronic polymeric surfactants displayed no significant lasting interactions with the hydrophilic phospholipid bilayer surface. Nonoxynols, with highly branched tail group structures, did not insert into the bilayer; but, did damage the membrane. The degree of destruction increased as the molar mass decreased. The PEG surfactants which had a single hydrocarbon tail, cholesterol, dioleoyl tail groups, demonstrated size and structure dependent adsorption and desorption kinetics. The smaller and simpler the tail group structure, the faster the adsorption and desorption. Interestingly, distearoyl PEGs had a very limited affinity for the phospholipid surface, an effect that was attributed to aggregation in water. These results showed that the adsorption and desorption kinetics of the surfactants could be tailored by the choice of proper tail group and the length of the PEG chain. These insights will be useful for designing controlled drug release systems.

6.7. References

(1) Harris, L. G., J.; Carmichael, A.; Riffle, J.; Harburn, J.; St. Pierre, T.; Saunders, M. *Chem. Mater.* **2003**, *15*, 1367.

(2) Holmberg, K. T., F.; Malmsten, M.; Brink, C. *Colloids Surf., A:* **1997**, *123*, 3168.

(3) Kingshott, P. W., J.; Bagge-Ravn, D.; Gadegaard, N.; Gram, L. *Langmuir* **2003**, *19*, 6912.

(4) Li, C. Y., D.; Yang, D.; Milas, L.; Hunter, N.; Kim, E.; Wallace, S. *Anticancer Drugs* **1996**, *7*, 642.

(5) Mai-ngam, K. *Colloids and Surfaces B: Biointerfaces* **2006**, *49*, 117.

(6) Veronese, F. M. *Biomaterials* **2001**, *22*, 417.

(7) Lasic, D.; Marin, F. J.; Gabizon, A.; Huang, S. K.; Papahadjopoulos, D. *Biochim.Biophys. Acta* **1991**, *1070*, 187.

(8) Papahadjopoulos, D.; Allen, T.; Gabizon, A.; Mayhew, e.; Matthay, K.; Huang, S.; Lee, K.; Woodle, M.; Lasic, D.; Redemann, C.; Martin, F. *Proc. Natl. Acad. Sci. USA* **1991**, *88*, 11460.

(9) Collnot, E. M.; Baldes, C.; Wempe, M. F.; Hyatt, J.; Navarro, L.; Edgar, K. J.; Schaefer, U. F.; Lehr, C. M. *J. Control. Release* **2006**, *111*, 35.

(10) Batrakova, E. V.; Kabanov, A. V. *J. Control. Release* **2008**, *130*, 98.

(11) Sriadibhatla, S.; Yang, Z.; Gebhart, C.; Alakhov, V. Y.; Kabanov, A. *Molecular Therapy* **2006**, *13*, 804.

(12) Amiji, M.; Park, K. *Biomaterials* **1992**, *13*, 682.

(13) Bridgett, M. J.; Davies, M. C.; Denyer, S. P. *Biomaterials* **1992**, *13*, 411.

(14) Freij-Larsson, C.; Nylander, T.; Jannasch, P.; Wesslen, B. *Biomaterials* **1996**, *17*, 2199.

(15) Marsh, L. H.; Coke, M.; Dettmar, P. W.; Ewen, R. J.; Havler, M.; Nevell, T. G.; Smart, J. D.; Smith, J. R.; Tmimins, B.; Tsibouklis, J.; Alexander, C. *J. Biomed. Mater. Res., Part A* **2002**, *61*, 641.

(16) Nejadnik, M. R.; van der Mei, H. C.; Norde, W.; Busscher, H. J. *Biomaterials* **2008**, *29*, 4117.

(17) Norde, W.; Gage, D. *Langmuir* **2004**, *20*, 4162.

(18) Schroen, C. G. P. H.; Cohen Stuart, M. A.; van der Padt, A.; van der Voort, K.; van't Riet, K. *Langmuir* **1995**, *11*, 3068.

(19) Holland, J. W.; Cullis, P. R.; Madden, T. D. *Biochemistry* **1996**, *35*, 2610.

(20) Kuhl, T.; Guo, Y.; Alderfer, J. L.; Berman, A. D.; Leckband, D.; Israelachvili, J.; Hui, S. W. *Langmuir* **1996**, *12*, 3003.

(21) Wu, J. R.; Lentz, B. R. *Biochemistry* **1991**, *30*, 6780.

(22) Yoshida, A.; Hashizaki, K.; Yamauchi, H.; Sakai, H.; Yokoyama, S.; Abe, M. *Langmuir* **1999** *15*, 2333.

(23) Firestone, M. A.; Wolf, A. C.; Seifert, S. *Biomacromolecules* **2003**, *4*, 1539.

(24) Liu, G.; Fu, L.; Zhang, G. *J. Phys. Chem. B* **2009**, *113*, 3365.

(25) Rossetti, F. F.; Reviakine, I.; Csúcs, Y.; Assi, F.; Vőrős, J.; Textor, M. *Biophys. J.* **2004**, *87*, 1711.

(26) Richter, R. P.; Brisson, A. R. *Biophys. J.* **2005**, *88*, 3422.

(27) Wilkinsona, D.; Tholandib, M.; Ramjeec, G.; Rutherfordd, G. W. *The Lancet Infectious Diseases* **2002**, *2*, 613.

(28) Phillips, D. M.; Sudola, K. M.; Taylorb, C. L.; Guicharda, L.; Elsenc, R.; Maguirea, R. A. *Contraception* **2004**, *70*, 107.

(29) Fichorova, R. N.; Tucker, L. D.; Anderson, D. J. *The Journal of Infectious Diseases* **2001**, *184*, 418.

(30) Zhang, G.; Wu, C. *Macromol. Rapid Commun.* **2009**, *30*, 328.

(31) Pal, S.; Milano, G.; Roccatano, D. *J. Phys. Chem. B* **2006**, *110*, 26170.

(32) Singer, S. J.; Nicolson, G. L. *Science* **1972**, *175*, 720.

(33) Nejadnik, M. R.; Olsson, A. L. J.; Sharma, P. K.; van der Mei, H. C.; Norde, W.; Busscher, H. J. *Langmuir* **2009**, *25*, 6245.

(34) Firestone, M. A.; Wolf, A. C.; Seifert, S. *Biomacromolecules* **2003**, *4*, 1539.

(35) Firestone, M. A.; Seifert, S. *Biomacromolecules* **2005**, *6*, 2678.

(36) Dynarowicz-Łątka, P.; Hąc-Wydro, K. *Colloids Surf. B* **2004**, *37*, 21.

(37) Hasegawa, R.; Doi, M. *Macromolecules* **1997**, *30*, 5490

(38) Huang, H.; Rankin, S. E.; Penn, L. S.; Quirk, R. P.; Cheong, T. H. *Langmuir* **2004**, *20*, 5770.

(39) de Gennes, P. G. *Macromolecules* **1980**, *13*, 1069.

Chapter 7

Conclusions and Suggestions for Future Work

7.1. Overall Conclusions

7.1.1. Effects of Nanoscale Confinements on Poly(ε-caprolatone) (PCL) Crystallization at the Air/Water (A/W) Interface. In this thesis, two-dimensional (2D) nanoscale confinement effects on PCL crystallization were probed through studies of poly(ε-caprolatone)-b-poly(t-butyl acrylate) (PCL-b-PtBA) copolymers and PCL magnetic nanoparticles (PCL MNPs) at the A/W interface. The act of tethering PCL chains to another amphiphilic amorphous polymer, bulky head groups, or a nanoparticle surface significantly altered the size and shape of the PCL crystals through a reduction of PCL chain mobility.

The studies for PCL-b-PtBA copolymer monolayers at the A/W interface revealed a dependence of the morphologies on the PtBA block length. Although surface pressure-area per molecule ($\Pi-A$) isotherm studies showed similar thermodynamic behavior for PCL-b-PtBA block copolymer monolayers and PCL/PtBA blend monolayers, the connection between the two polymers of the block copolymers significantly altered the PCL crystal morphologies relative to the blends. In the monolayer, the PCL block still underwent nucleation and crystal growth during isothermal compression; however, the limitation on diffusion imposed by the connected amorphous PtBA block inhibited the growth of the crystals. Consequently, the morphologies observed for LB-films exhibited a transition from pure PCL to crystals with reduced sizes, six armed dendrites with defects, stripes and finally to nanoscale cylindrical features as the PtBA block length increased. The collapse of the PtBA blocks resulted in thickening along the edges of the crystals as collapsed PtBA collected. However, the crystals were otherwise unchanged.

Confinement effects that arose from the bulky dendritic endgroups on PCL crystallization were also studied. The bulky amphiphilic t-butyl esters of PCL triesters accumulated at the A/W interface and led to smaller multi-faceted lamellar crystals for 9 k and 3 k PCL triesters. A different, diffusion controlled crystal morphology was observed for 6 k PCL triesters because they had a faster crystal growth rate. In contrast, conversion of the hydrophobic PCL triesters to hydrophilic triacids led to large elliptically shaped crystals. The morphology discrepancy of PCLs with two different headgroups was attributed to altered dipole densities that accompanied submersion of the acid moieties in the subphase and the diminished steric hindrance for the growth of the crystal by the removal of the bulky triester group from the interfacial region.

The confinement of PCL triacids on MNP surfaces suppressed crystallization dramatically. While crystals formed for the 9 k PCL MNPs, they were much smaller than 9 k PCL triacid. The crystallization for the 6 k and 3k PCL MNPs were further suppressed. As such, the studies clearly demonstrated how confinement of PCL chains altered the morphologies of the crystals.

7.1.2. Effects of Tail Groups on Poly(ethylene glycol) (PEG) Surfactant Adsorption onto Phospholipid Bilayers. The adsorption of PEG surfactants onto phospholipid bilayers was studied in Chapter 6. The study revealed the degree of polymerization for the PEG and the tail group structure of the surfactant strongly influenced the adsorption and desorption. Smaller and simpler tail group structures adsorbed more quickly onto phospholipid bilayers. Compared to the fast adsorption kinetics of the surfactants, the desorption kinetics of the surfactants from the lipid bilayer surface were slower. The structure of the surfactant tail group had similar size and structure dependent impacts on the desorption kinetics. Pluronic polymeric surfactants displayed no apparent insertion into the bilayer due to a size mismatch. In contrast, Nonoxynols damaged the lipid bilayers. The degree of the destruction increased with the decreasing PEG molar mass. Distearoyl PEGs had very limited affinity for the phospholipid surface, an effect attributed to aggregation in aqueous solution. Finally, studies with three different phospholipid bilayers, one with two short alkyl chains, one with one cis-unsaturated and one saturated alkyl chain and one with two cis-unsaturated alkyl chains, revealed tail group structure of the phospholipids had little effect on PEG surfactant adsorption. This observation was associated with the loose membrane packing (~ 60 Å^2•molecule^{-1}) and fluidic character of the membrane.

7.2. Suggestions for Future Work

7.2.1. Crystallization of PCL/Oleic Acid MNP Blends at the A/W Interface. As seen in Chapter 5, the confinement of PCL chains to a nanoscale spherical surface suppressed crystallization and only small, scattered PCL lamellar crystals were obtained. Furthermore, the phase separation of the polymer/nanoparticle mixtures was of interest because it offered a new route to pattern and order functional nanoparticles in a lower dimension. Nanoparticles were shown to assemble at the block copolymer phase boundary and achieved a periodic ordered structure.[1-2] One question that remained unclear and interesting was how the crystalline morphology would change in PCL/oleic acid MNP blends. The 9 nm MNPs were passivated by oleic acid. Studies of the PCL/MNP physical blends at the A/W interface could aid the understanding of crystallization in the presence of colloidal aggregates (nanofillers). Some relevant experimental details and preliminary results are provided below.

10 k PCL (weight average molar mass, $M_w = 10$ kg•mol^{-1}, PDI = 1.25 from Polymer Source) was blended with 9 nm oleic acid MNPs in 25 wt%, 50 wt% and 75 wt% mixture. The mixed solutions in chloroform were spread onto the A/W interface and two consecutive compression/expansion (Π−A) isotherm cycles were performed at the compression/expansion rate of 10 cm^2•min^{-1}. The isotherms were plotted as area per repeat unit (monomer) as shown in Figure 7.1. For this calculation, only the amount of PCL spread on the surface was

considered for the calculation of A_{PCL}. The Π-A isotherm cycles for different blends had a similar shape but different lift-off area ($A_{lift\text{-}off}$ = A where Π becomes > 0), an indication that the oleic acid MNPs had no surface activity and only acted as true fillers in the PCL monolayer (they occupied space but were otherwise non-interacting). At the smallest A_{PCL}, Π rose rapidly because of direct contact between oleic acid MNP aggregates and the impingement of PCL lamellar crystals. Langmuir-Blodgett (LB) films of the monolayers at the A/W interface were transferred onto regenerated cellulose surfaces for optical microscopy (OM), mica for atomic force microscopy (AFM) imaging, and SiO_2 coated transmission electron microscopy (TEM) grids for TEM imaging.

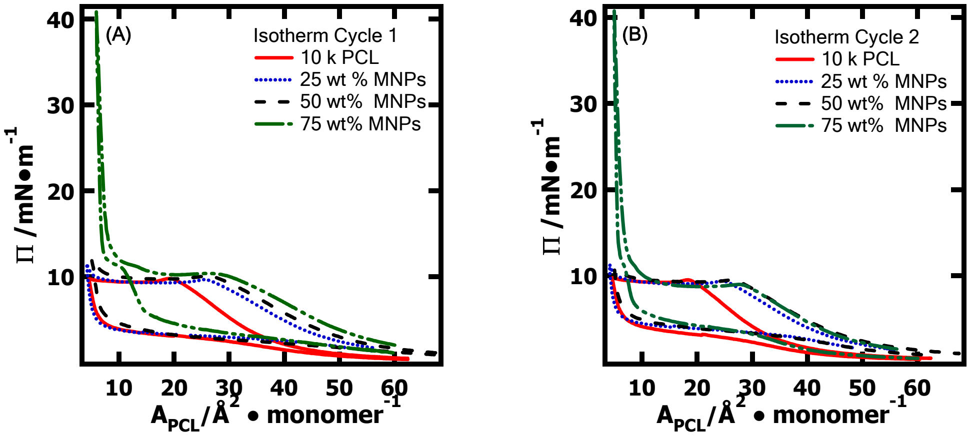

Figure 7.1. Compression/expansion Π-A isotherm cycles for 10 k PCL linear homopolymer and the PCL/oleic acid MNP blends. (A) First cycle and (B) second cycle. The isotherm cycles were performed at 22.5 ˚C with a compression and expansion rate of 10 cm^2•min^{-1}.

As seen in the OM images of Figure 7.2A, the PCL homopolymer crystals had regular shapes. The addition of the MNPs altered the shapes of the crystals. For the 25 wt% MNP blend, LB-films exhibited more rounded crystals than PCL without MNPs and MNP clusters were observed around some of the crystals (Figure 7.2B). For higher wt% MNP (Figure 7.2C and D), the MNP clusters distributed within and outside the PCL crystals.

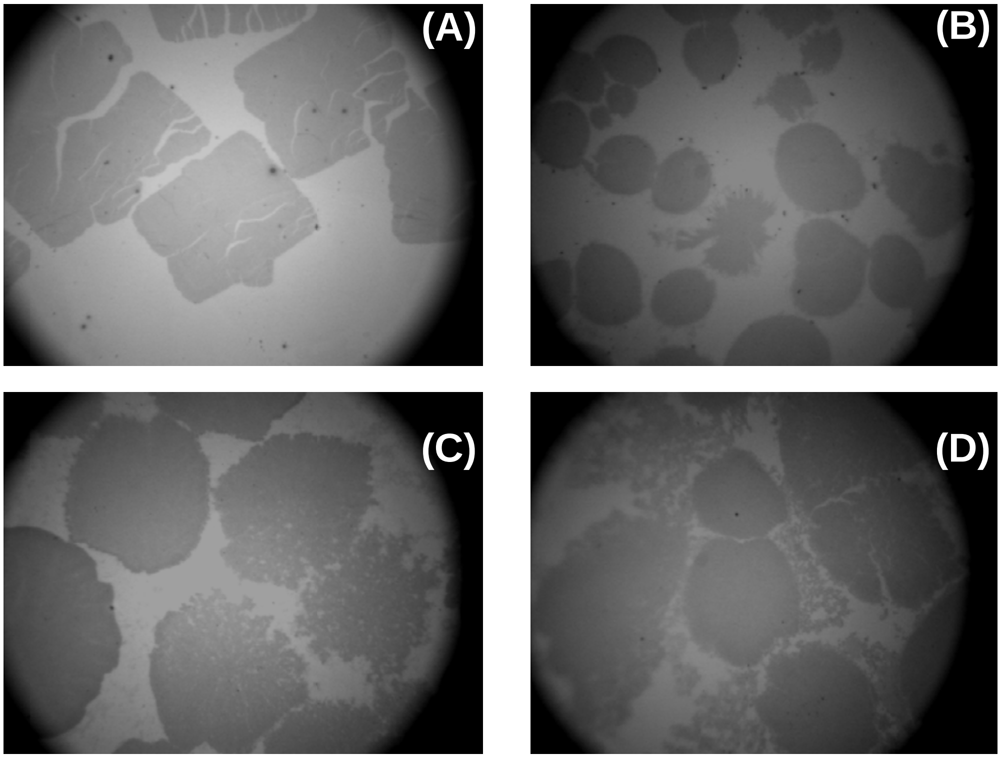

Figure 7.2. OM images (260 μm × 340 μm) for LB-films of PCL/oleic acid MNP blends: (A) 10 k PCL crystals (A_{PCL} = 15 $Å^2$ • monomer^{-1}), (B) a 25 wt% of oleic acid MNP blend with 10 k PCL (A_{PCL} = 20 $Å^2$ • monomer^{-1}), (C) a 50 wt% of oleic acid MNP blend with 10 k PCL (A_{PCL} = 15 $Å^2$ • monomer^{-1}), (D) a 75 wt% oleic acid MNP blend with 10 k PCL(A_{PCL} = 10 $Å^2$ • monomer^{-1}).

In Figure 7.3, TEM images of the LB-films revealed the aggregation status of MNPs in the blend. As seen in Figure 7.3A and B for LB-films with 25 wt% and 50 wt% MNP, the clusters were well separated and the density of the clusters increased as the wt% MNP increased. The empty area that was free of the clusters in Figure 7.3B was the area between crystals. A conclusion that was drawn, the MNP clusters were confined within the PCL crystals. For the 75 wt% MNP in Figure 7.3C, the MNP clusters became the dominate feature and an interconnected necklace morphology for the MNP clusters was observed.

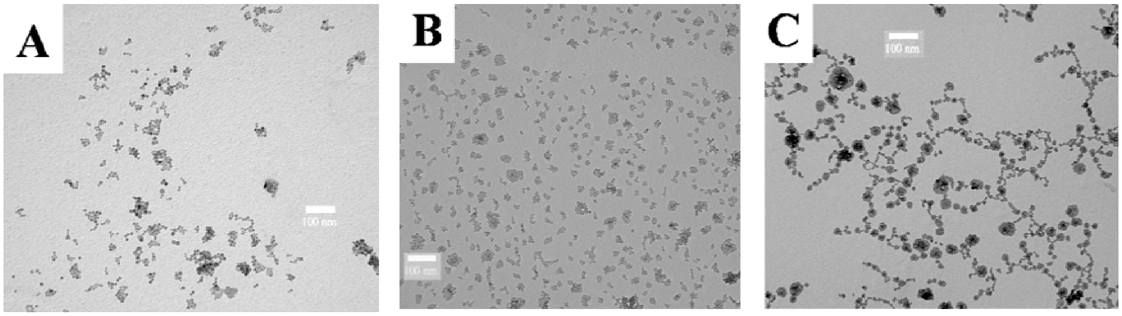

Figure 7.3. TEM images for LB-films of physical blends of 10 k PCL and oleic acid MNPs: (A) 25 wt% MNP; (B) 50 wt% MNP and (C) 75 wt% MNP films were transferred after compression past the transition for PCL crystallization. The scale bar corresponds to 100 nm.

Detailed morphologies and topographies of the blends were obtained from AFM studies on LB-films. Representative AFM results are provided in Figures 7.4 and 7.5. The PCL homopolymer formed large crystals with a smooth surface as seen in Figure 7.4A. This observation was consistent with previously reported results.[3-4] In Figure 7.4B, the hydrophobic MNPs at the A/W interface formed clusters and the aggregated clusters had the inter-connected dendritic features. A round shaped PCL crystal was observed in the AFM image for 25 wt% MNP blend (Figure 7.4C). At a higher magnification (Figure 7.4D) for the 25 wt% MNP blend, the MNP clusters were distributed within the crystal in a low density. Whereas, in Figure 7.4E and F, multi-faceted crystals were obtained for the 50 wt% blend and the density of the clusters within the PCL crystal increased. One conclusion was that within a wt% MNPs window, the MNP clusters dispersed inside the PCL crystals. As the wt% MNP increased and the MNPs become the major component (Figure 7.5), the interconnected MNP clusters prevented the formation of large PCL lamellae. Voids and MNPs were clearly present between the small PCL crystalline domains. The line scans in Figure 7.5B revealed that the bright features in the AFM height image (Figure 7.5A) had a height of ~10 nm which was comparable to the diameter of the MNPs measured by TEM. In contrast, the larger tan features had a thickness of ~ 8 nm, which was consistent with the thickness of the PCL homopolymer crystals. The results suggested that the bright features were the laterally networked MNP aggregates.

Li et al.[4] reported the blend morphologies for medium molar mass polystyrene (PS) and PCL at the A/W interface. The hydrophobic PS collapsed at the A/W interface and formed interconnected micron scaled beads and macrophase separation of PS and PCL phase was observed.[4] The blend monolayers of MNPs and PCL had similar features compared to PS/PCL blends. The PCL chains crystallized in the presence of the nanoparticle aggregates. In the blend system where MNPs were the minor component, the clusters were dispersed within the PCL phase. At a higher density of the MNPs, the dipole-dipole interactions of the MNP clusters induced the formation of necklace shaped aggregates. These results suggested that the nanoparticle ligand, oleic acid, was possibly compatible with PCL homopolymer at the A/W interface. Therefore, a complete study of this system would require an investigation into blends of oleic acid/PCL at the A/W interface. The study of the oleic acid/PCL mixed monolayer would facilitate better understanding of the liquid-liquid phase separation of PCL homopolymer with small molar mass liquids and the results would help explain observations for the physical blends of the oleic acid MNPs with PCL at the A/W interface.

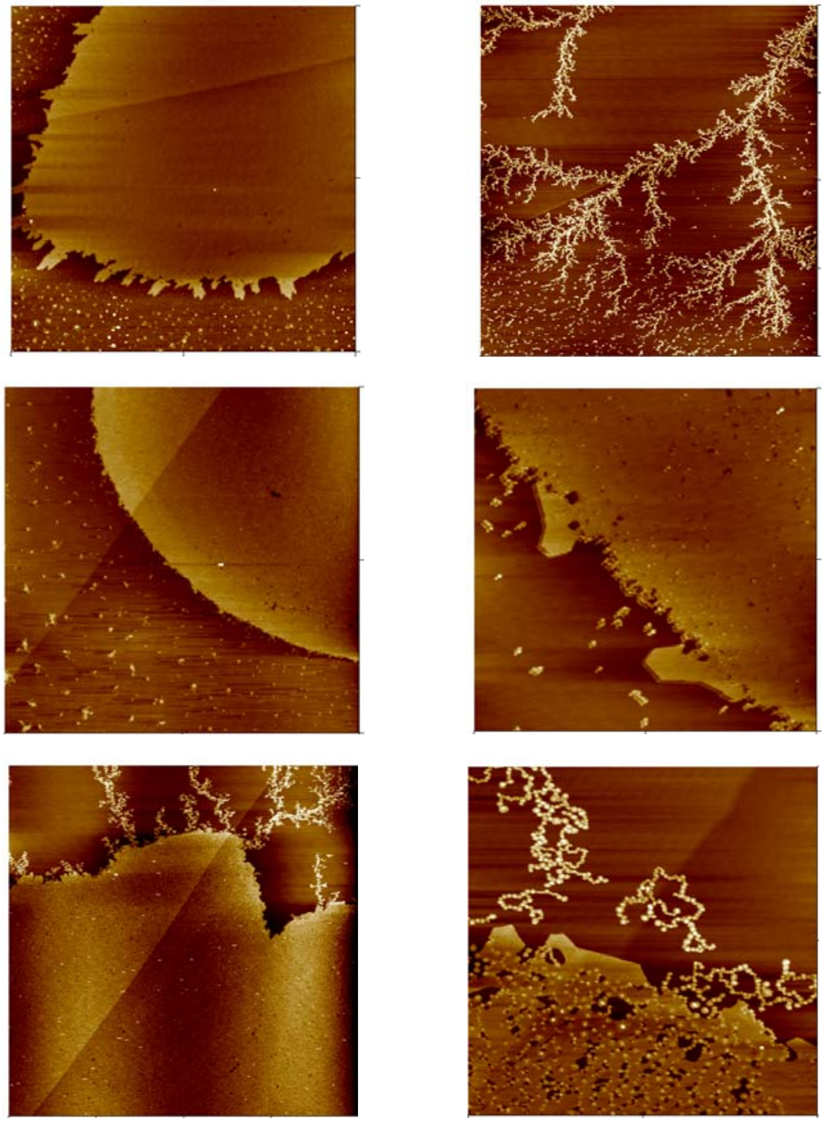

Figure 7.4. AFM height images (z scale 0-30 nm) for PCL/oleic acid MNP blend LB-films: (A) linear 10 k PCL, (B) oleic acid MNPs, (C) a 25 wt% MNP blend, (D) a 25 wt% MNP blend at greater magnification, (E) a 50 wt% MNP blend, and (F) a 50 wt% MNP blend at greater magnification.

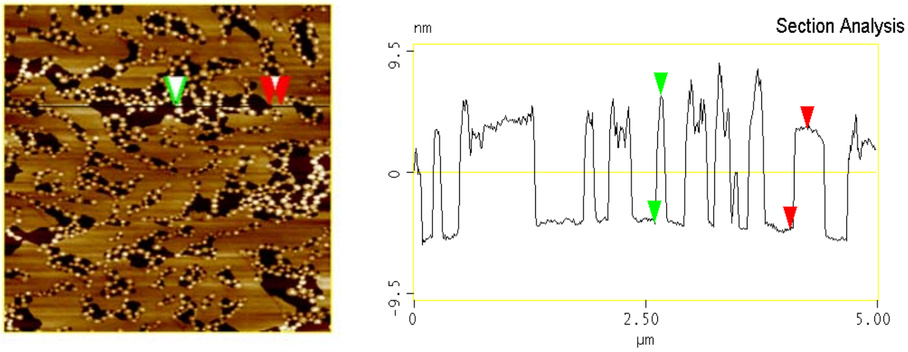

Figure 7.5. AFM height image (5 µm × 5 µm, *z*-scale = 20 nm) and a line scan analysis for a LB-film of a 75 wt% MNP blend with PCL.

7.2.2. Studies of the Morphologies for PCL-b-PS Copolymers at the A/W Interface. Results in Chapter 4 showed PtBA exerted a confinement effect on PCL crystallization for PCL-b-PtBA. The confinement effects from a hydrophilic poly(ethylene glycol) block which dissolved and submerged into the aqueous phase has also been reported.[5-6] However, numerous opportunities for studies of confinement effects exerted by hydrophobic blocks on PCL crystallization at the A/W interface remain to be exploited. Therefore, another proposed area of interest would be studies of PCL crystallization of poly(ε-caprolatone)-b-polystyrene (PCL-b-PS) copolymers at the A/W interface. The PCL-b-PS was prepared by atom transfer radical polymerization (ATRP) from a PCL macro-initiator as described in Chapter 3. Preliminary results were compared with those reported for PCL crystallization in PCL/PS blends at the A/W interface.[4] The molecular compositions and molar masses of the block copolymers for the preliminary study were provided in Table 7.1.

Table 7.1. GPC characterization of PCL-b-PS copolymers

Sample	**M_n (GPC)** [a] **kg•mol^{-1}**	**PDI**
PCL-Br Macroinitiator	8.0	1.18
PCL(8 k)-b-PS(1 k)	8.9	1.04
PCL(10 k)-b-PS(10 k) [b]	20	1.13
PCL(10 k)-b-PS(100 k)	120	1.20

[a] GPC = gel permeation chromatography, [b] The sample was purchased from Polymer Source.

Preliminary results for PCL-b-PS copolymers revealed the Π-A isotherms depended on the PS block length. For PCL(8 k)-b-PS(1 k) (k = kg•mol^{-1}), the Π-A isotherm cycles and BAM images in Figure 7.6 differed between the first and subsequent cycles. In the first isotherm cycle, a slow rise of Π as A_{PCL} decreased was accompanied by featureless BAM images and suggested a homogenous monolayer existed at low Π. As the monomer area continued to decrease, bright features appeared and grew into large round objects in BAM images on the plateau of the Π-A isotherm in Figure 7.6. Nonetheless, the Π-A isotherm did not exhibit the classical "kink" seen in PCL homopolymer films that signaled the onset of crystallization. Moreover, the first hysteresis loop had a much larger area than other PCL systems and the "melting and respreading" plateau was also absent. Even though the round features disappeared during expansion as seen in the BAM images of Figure 7.4, these BAM results suggested that the PCL block still underwent crystallization by a nucleation and growth mechanism. The second and third isotherm cycles resumed the characteristic Π-A isotherms for pure PCL. In the BAM images for the second isotherm cycle, only small crystals were observed, suggesting that residual small crystals from the first cycle served as heterogeneous nucleation centers for the second compression isotherms. As a result, crystals in the second and third cycles were reduced in size. As noted in the first compression isotherm, the slope of the rising surface pressure was higher than the slopes in the second and third compression isotherms. This suggested that the liquid like PS oligomer was acting like a rigid compatible filler in the PCL monolayer and increased the rigidity of the PCL monolayer. During the first compression step, the crystallization of the PCL block induced microphase separation and the PS block was squeezed onto the top of the PCL lamellae. This conformational rearrangement also eliminated the steric hindrance for the growth of PCL crystals; therefore, large crystals formed. This microphase separation was irreversible. Consequently, the melting of the crystal in the first expansion step resulted in many small nucleation centers at the A/W interface. As a result, only small crystals were obtained in the second and third cycles and the isotherms looked similar to those of pure PCL.

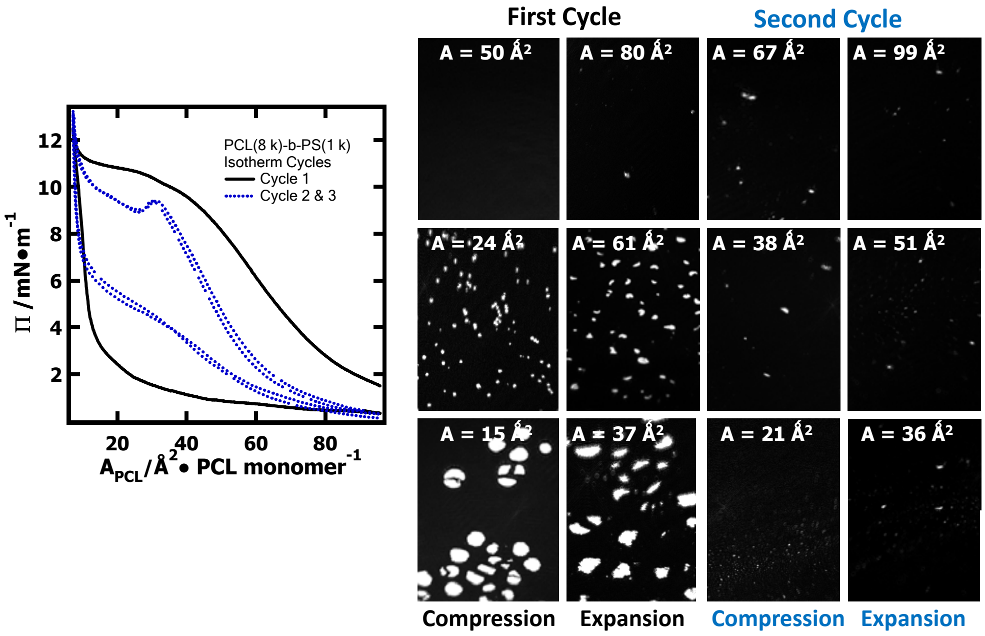

Figure 7.6. Three compression/expansion Π-A isotherm cycles for PCL(8 k)-b-PS(1 k) and BAM images taken at the indicated area. The cropped BAM images had dimensions of 2 mm × 1 mm.

The crystals were LB-transferred onto regenerated cellulose surfaces and mica surfaces for OM and AFM studies. The OM image in Figure 7.7A reconfirmed that the first compression cycle produced large crystals and revealed small textures were present on the lamellae surfaces that were not resolvable in BAM. The crystals formed in the second compression isotherm were much smaller (Figure 7.7B). AFM images provided more detailed topographies for the crystals. As seen in Figure 7.7C, crystals formed during the first compression had long stripes across their surface. The crystals obtained from the second isotherm cycle had smaller sizes and much smoother topographies. Corresponding line scan images, Figure 7.8A and B, showed that the stripes had thicknesses of ~ 2 nm, whereas the large lamella underneath had a thickness of ~ 8 nm which was consistent with the thickness of PCL crystals. As in Figure 7.8C and D, the line scans for the crystals formed during the second compression isotherm had much smoother topographies and the thickness returned to ~ 8 nm, suggesting the PS block had spread-out on the PCL crystal surface. As a result, a smoother surface with a reduced thickness was obtained.

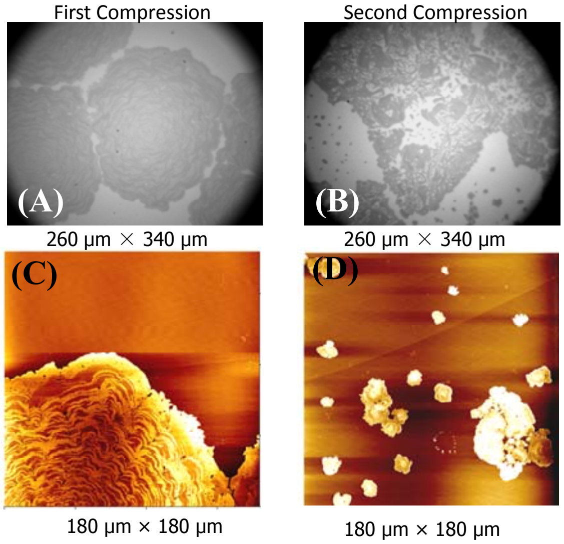

Figure 7.7. OM and AFM images for PCL(8 k)-b-PS(1 k) LB-films transferred from the first and second compression isotherms. OM images for crystal from (A) the first isotherm cycle at Π =11.5 mN•m^{-1} and (B) the second isotherm cycle at Π =10 mN•m^{-1}. AFM images for crystals from the same LB-films as (A) and (B) for the (C) first and (D) second isotherm cycle.

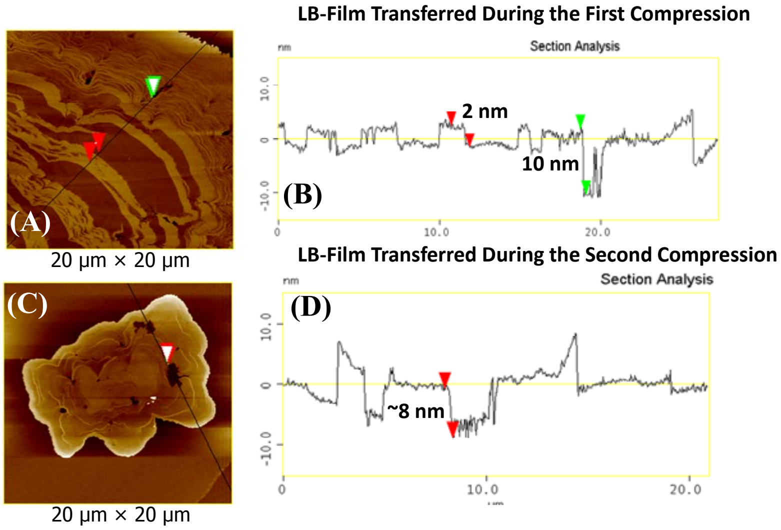

Figure 7.8. AFM height images and the line scans of LB-films of PCL(8k)-b-PS(1k) the crystals obtained during (A) and (B) the first and (C) and (D) the second compression isotherm.

Π-A isotherm cycles and morphologies for LB-films of symmetric PCL(10 k)-b-PS(10 k) are shown in Figure 7.9. The near overlap of the first and second the isotherm cycles indicated that the Π-A isotherm were much more reversible. BAM and OM of LB-films transferred at Π = 11 mN•m^{-1} revealed no significant features as seen in Figure 7.9B for a representative OM image. However, the AFM image in Figure 7.9C showed the LB-films had significantly different morphologies compared to PCL(8 k)-b-PS(1 k). A thin porous layer with a thickness of ~ 2 nm was obtained according to Figure 7.9C and D. The thickness of the LB-film was consistent with the thickness of a polymer bilayer. Therefore, a possible conformational arrangement was that the PS block formed a monolayer on top of the PCL monolayer and this conformational arrangement completely inhibited the crystallization of PCL block. As a consequence, reversible Π-A isotherm cycles were obtained as shown in Figure 7.9A. For PCL(10 k)-b-PS(100 k), the monolayer was no longer stable at the A/W interface and collapsed into the aggregated structures shown in Figure 7.10.

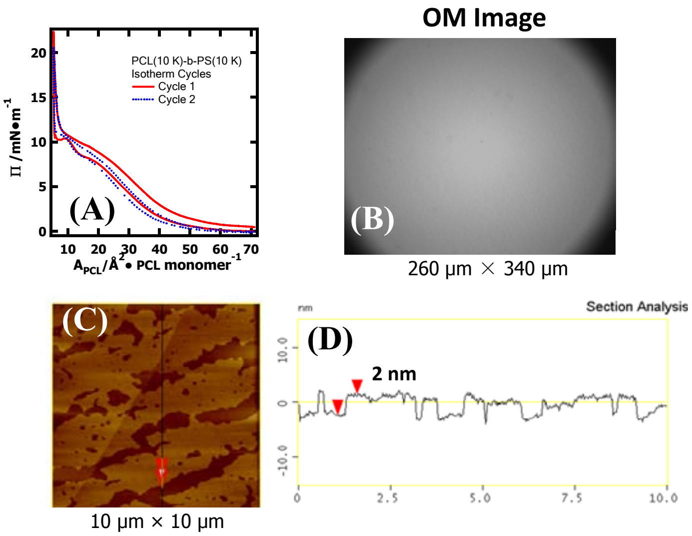

Figure 7.9. Thin films of PCL(10 k)-b-PS(10 k). (A) Compression/expansion Π-A isotherm cycles at 25 ˚C. (B) An OM image of a LB-film transferred onto a regenerated cellulose surface at Π = 11 mN•m^{-1}. (C) An AFM image of the LB-film in (B) with a scan area of 10 µm × 10 µm and z-scale = 20 nm. (D) A line scan analysis of features in (C).

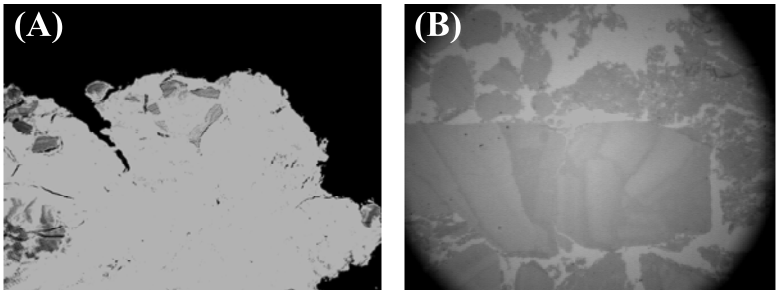

Figure 7.10. (A) BAM (3.6 mm× 4 mm) and (B) OM (260 µm × 340 µm) images of LB-films containing aggregates of PCL(8 k)-b-PS(100 k).

A possible mechanism for the influence of the PS block on the morphologies of the LB-films is schematically depicted in Figure 7.11. At the A/W interface, asymmetric wetting by the block copolymer is expected with the amphiphilic PCL block in contact with the water and the hydrophobic PS block at the PCL/air interface. For a block copolymer with a short polystyrene block, the liquid like PS oligomer may remain at the A/W interface at low Π. Consequently, the first Π-A isotherm cycle for PCL(8 k)-b-PS(1 k) was significantly different from the isotherms for the pure PCL. With the increase of Π, the PS block migrated to the top of the PCL phase and resulted in a microphase separated morphology. The final crystallization of the PCL phase solidified the two phases. The PCL phase formed ~ 8 nm thick crystals, whereas the PS phase formed ~ 2 nm thick amorphous stripes across the surface of the PCL lamellae.

For the symmetric PCL-b-PS block copolymer, the microphase separation resulted in a conformation that completely inhibited the crystallization of the PCL block. Due to the symmetrical block length, the PCL monolayer was "pinned" under the PS monolayer as depicted in Figure 7.11. Therefore, the PCL chains could not diffuse or recruit chains from adjacent areas to crystallize. The AFM results revealed a thickness of ~ 2 nm which corresponded to the thickness of two polymeric monolayers. For the PCL(8 k)-b-PS(100 k) copolymer, the PS block was the major component and the monolayer was no longer stable at the A/W interface. Large aggregates formed instantly once the monolayer was spread onto the A/W interface.

Compared to macrophase separation of the PS/PCL blends at the A/W interface,[4] microphase separation for the PCL-b-PS block copolymer was observed. The glassy amorphous PS monolayer imparted a different type of confinement for the crystallization of the PCL monolayer at the A/W interface. Several suggestions are provided here in order to complete this study systematically. The first is the synthesis of a series of block copolymers that cover the whole range of PS block lengths with consequent Π-A isotherm, BAM, AFM, and OM characterization. The second suggestion is to use AFM equipped with *in situ* heating stage to study the block copolymer LB-films. PCL has a melting point T_m of ~ 60 ˚C and PS has a glass transition temperature T_g of ~ 100 ˚C depending on the molar mass. Therefore, *in situ* AFM monitoring of topographical changes with heating may identify the components of the different phases. The other suggested experiment would involve the use of Fourier transform infrared spectroscopy (FTIR). As noted previously, the symmetric block copolymer will hinder the crystallization of the PCL phase. The packing status of the PCL chains in the LB-films of the symmetric block copolymer can be evaluated by FTIR. A comparison of the FTIR results with spin-coated amorphous PCL films should be instructive.

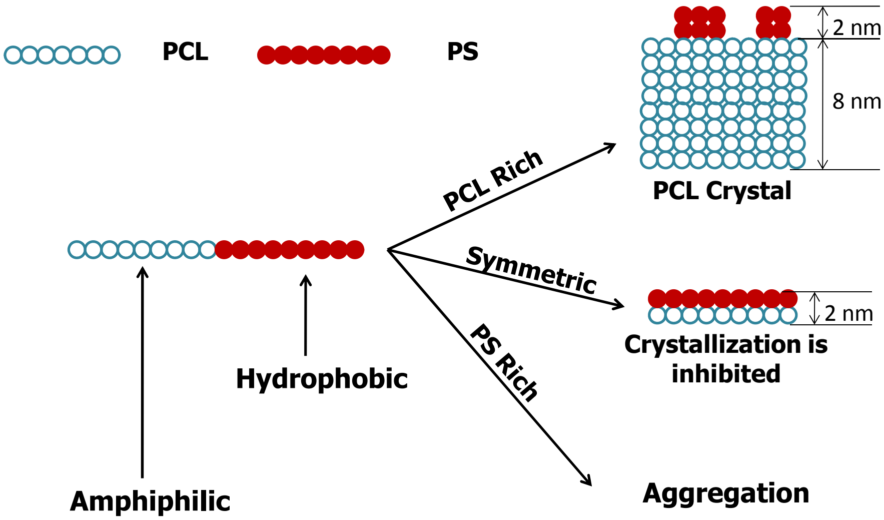

Figure 7.11. Depiction of PS block length dependent confinement effects on the crystallization of PCL at the A/W interface.

7.2.3. Preparation of Cushioned Tethered Phospholipid Bilayers with Poly(ethylene glycol) Surfactants on Metal Oxide Surfaces. Supported phospholipid bilayers are frequently employed as an *in vitro* cell membrane model for fundamental biological research as well as bio-related applications. As mentioned in Chapter 2, phospholipid bilayers were usually prepared by direct vesicle fusion onto smooth hydrophilic solid surfaces such as SiO_2, glass, and mica. However, cell membranes are more than just a bilayer of phospholipid. They were usually regarded as an “alloy” of phospholipids, cholesterol, and membrane proteins. More importantly, asymmetric distributions of lipids and various cell membrane components are present in real cell membranes.[7] The major drawback for the direct fusion method is that the asymmetric lipid distributions for the two leaflets of the bilayers are not possible. Meanwhile, the lipid bilayers formed on a solid substrate lack the fluidity of a true membrane due to direct contact with the solid substrate. Moreover, if transmembrane proteins are introduced to the supported lipid bilayer, mobility of the proteins is reduced and denaturation of their structure can even occur.

Therefore, if tethered asymmetric phospholipid bilayers cushioned by a hydrated polymeric layer could be created, they would be better simulates of a real cell membrane. Several methods for the creation of polymer cushioned phospholipid bilayers have been reported.[8-9] However, the reported methods usually involved expensive materials and were difficult to reproduce. Tamm’s group came up with a method of combining LB-transfer and vesicle fusion to create polymer cushion asymmetric lipid bilayers.[10] However, Tamm’s method utilized expensive silane-PEG-lipid which was limited to silicon surfaces. In Chapter 6, it was demonstrated that the hydrocarbon tail groups with an appropriate size could insert into the phospholipid bilayers with the PEG chains extended into the surrounding water. Meanwhile, some research results in the current group showed that tri-carboxylic acid, phosphoric acid and di-phenol endgroups anchored polymers to various metal oxide surfaces.[11] Experimental results also suggested that the acid end group anchored polymers were removed by a standard cleaning procedure from the metal oxide surfaces. Therefore, if one prepared the polymer cushioned tethered lipid bilayer using surfactants with the acid end groups onto metal oxide surfaces, the expensive sensors were reusable.

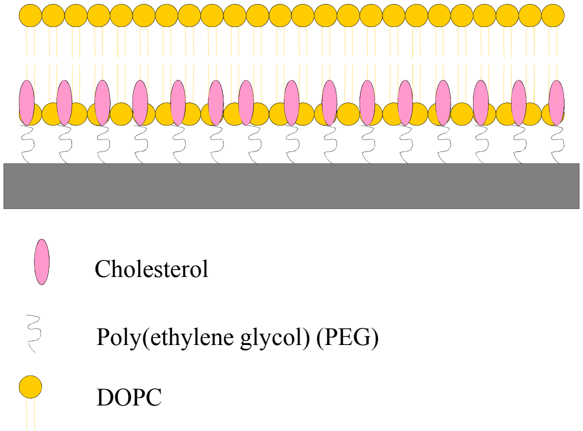

Figure 7.12. Formation of tethered lipid bilayers on metal oxide surfaces by using the cholesterol PEG monolayer as the polymer cushion. The hydrated PEG layer serves as a cushion and the cholesterol end groups insert into the phospholipid bilayer. A monolayer of the cholesterol PEG is formed by the chemisorption of 6 k cholesterol PEG phosphoric acid onto a metal oxide surface in methanol. The bilayer is prepared by LB-transfer of a DOPC layer and subsequent fusion of DOPC liposomes to form another layer.

Inspired by Tamm's method, a method of combining LB-transfer and vesicle fusion for the preparation of cushioned tethered lipid bilayers is proposed here for future work. A monolayer of the cholesterol PEG was first formed on a metal oxide surface by the chemisorption of a phosphoric acid headgroup onto the metal oxide surface. The cholesterol tailgroups inserted into and secured the bilayer, whereas the hydrated PEG layer served as a cushion layer and provided potential space for transmembrane proteins between the bilayer and the solid substrate as depicted in Figure 7.12. As discussed in Chapter 2, the distance between the bilayer and the solid surface can be controlled by the size of the PEG random coils. The goal of this proposed project is the development of a protocol that can use cheap PEG surfactants for tethering phospholipid bilayers onto various metal oxide surfaces with a hydrated PEG layer as the spacer.

7.2.3.1 Preliminary Results. SiO_2, Al_2O_3, Fe_3O_4, ZnO, TiO_2 and hydroxyapatite (denoted as Ha) QCM-D sensors were purchased from Q-Sense AB. Prior to use, the crystals were rinsed thoroughly with ultrapure water and sonicated in an aqueous 2 wt% sodium dodecyl sulfate (SDS) solution for 10 min followed by UV ozone cleaning for 20 min. The ZnO surface was found to be unstable under aqueous conditions. Therefore, some preliminary results for ZnO crystals were ignored. The root-mean-square (RMS) surface roughnesses of the QCM-D sensor surfaces were first checked with AFM and the results are summarized in Figure 7.13.

7.2.3.2 Formation of Cholesterol PEG Monolayers. A layer of cholesterol PEG was first prepared by the chemisorptions of one 6 k cholesterol PEG phosphoric acid layer onto a metal oxide surface in methanol. The self-assembly process was monitored with QCM-D and the results are shown in Figure 7.14. In an exemplary procedure, a baseline was first established with pure methanol and then the 6 k cholesterol PEG phosphoric acid methanol solution ($C = 0.1$ mg•mL^{-1}) was injected until adsorption equilibrium was achieved. Finally, methanol was used to as a rinse for the removal of the loosely bound adsorbates. The QCM-D adsorption results in Figure 7.14 indicated that 6 k cholesterol PEG phosphoric acid adsorbed onto various metal oxide surfaces and the scaled frequency changed by $(\Delta f/n)$ ~ 30 Hz except for the SiO_2 crystal which had an ~ 15 Hz change. Unfortunately, the frequency baseline drifted toward smaller changes. This was possibly caused by the swelling of the O-ring that contacted the sensor. Therefore, future work should use organic solvent resistant O-rings for verification of the preliminary results presented here.

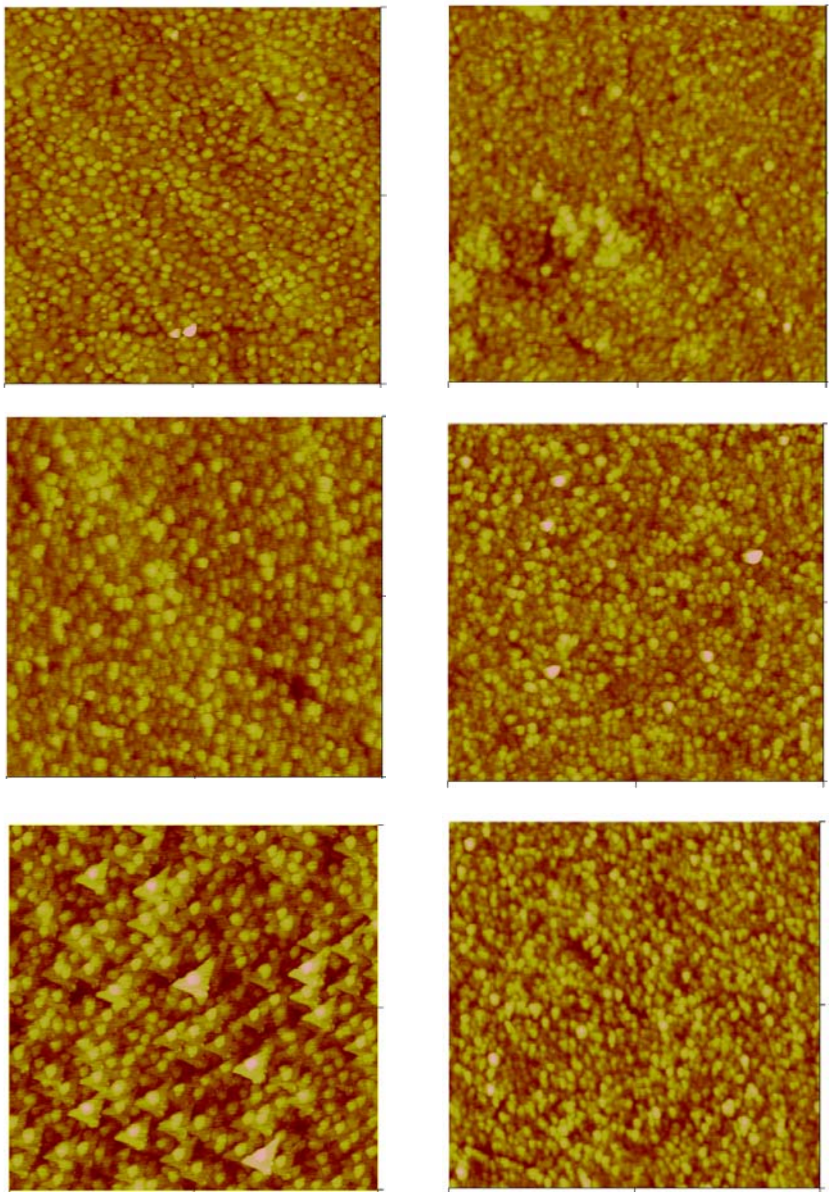

Figure 7.13. Surface roughness characterization for the metal oxide surfaces by AFM (scan area: 2 μm × 2 μm and *z*-scale: 0-30 nm). The RMS surface roughnesses were based on the 2 μm × 2 μm scan areas.

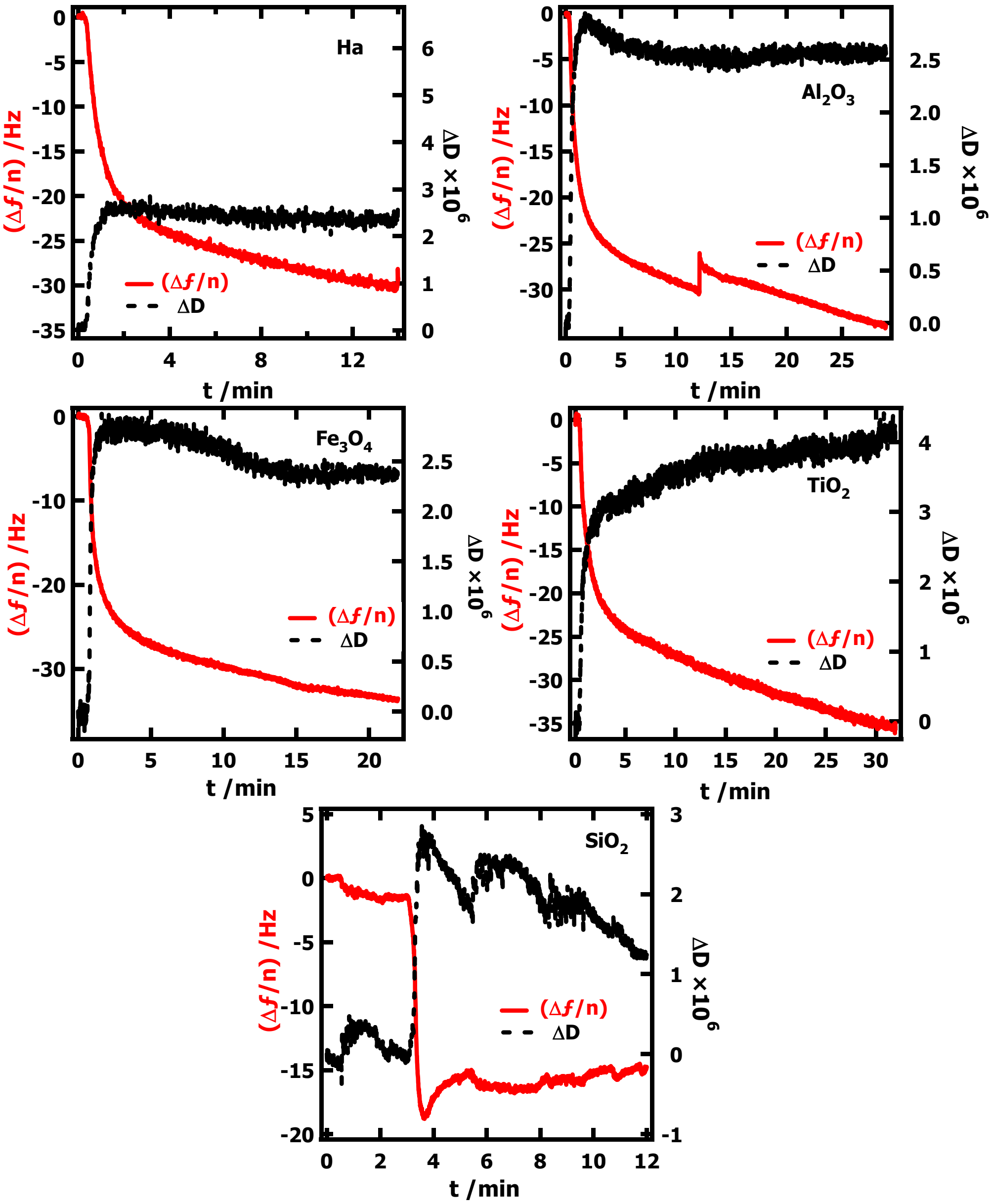

Figure 7.14. QCM-D results for the adsorption of 6 k cholesterol PEG phosphoric acid onto various metal oxide surfaces in methanol. $(\Delta f/n)$ and ΔD correspond to the third overtone (n = 3).

7.2.3.3 Langmuir-Blodgett Transfer and the Formation of Tethered Lipid Bilayers. To add a layer of 1,2-di-(9Z-octadecenoyl)-*sn*-glycero-3-phosphocholine (DOPC) onto the surfactant monolayer, LB-transfer was employed. The phospholipid DOPC monolayer at the

A/W interface was first compressed to a designated $\Pi = 30$ mN•m^{-1}, which was close to the estimated equilibrium surface pressure of a bilayer. Subsequently, one DOPC layer was LB-transferred onto the preformed 6 k cholesterol PEG monolayer by quickly dipping the substrate into the water phase and slowly pulling up at the speed of 1 mm•min^{-1}. A transfer ratio close to unity indicated that the LB-transfer was successful. The QCM-D sensors with the DOPC monolayer on the cholesterol PEG monolayers were then the subjected to DOPC vesicle fusion. In a QCM-D measurement, a baseline was obtained with pure water, followed by the injection of DOPC vesicle solution. Since an intact lipid bilayer corresponded to a 25 ± 1 Hz frequency change and a low dissipation value, the formation of a lipid monolayer was expected to have $(\Delta f/n)$ ~ 12 Hz and a low dissipation value.

In a control experiment, the bare oxide crystals were subjected to the vesicle solutions to observe if any layer formation occurred and the results were shown in Figure 7.15. The adsorption of vesicles onto metal oxide surfaces produced large $(\Delta f/n)$ and ΔD. $(\Delta f/\text{n})$ were normally greater than 40 Hz. This value was consistent with the adsorption of intact vesicles without fusion. After the surface was rinsed, the Fe_3O_4, and Al_2O_3 surfaces showed the same $(\Delta f/\text{n})$ and ΔD they had prior to the rinse. For TiO_2, $(\Delta f/\text{n})$ decreased during the rinse. This observation indicated that the vesicles came off the metal oxide surfaces. For TiO_2 surfaces, reported results showed that phospholipid vesicles fused to form bilayers with the help of Ca^{2+} and a mixture of negatively charged lipids.[12] The frequency shift for the TiO_2 surface in our study was close to frequency change for a bilayer, therefore, the result was possibly caused by the partial fusion of the liposomes. Further studies are required for verification of these findings.

The interactions of liposomes with the 6 k cholesterol PEG monolayer were also investigated as a control experiment as shown in Figure 7.16. Compared to the liposome interactions with the bare metal oxide surfaces, $(\Delta f/n)$ were much smaller. For the SiO_2

surface, $(\Delta f/n)$ ~ 25 Hz and low dissipation values indicated that a cushioned tethered lipid bilayer likely formed by direct fusion of the liposome onto the 6 k cholesterol PEG monolayer on the SiO_2 surface. It has been observed that surfactants with long alky tail groups can cause the rupture of the liposomes and induce the fusion of liposomes.[13] Results on Ha and Al_2O_3 appear to be similar to SiO_2 surface, whereas films on TiO_2 and Fe_3O_4 appeared to be thinner and thicker respectively. Therefore, the lower $(\Delta f/n)$ obtained for the interaction of liposomes with the surfactant monolayer here may be due to the breakage of the liposomes and the formation of lipid multilayers.

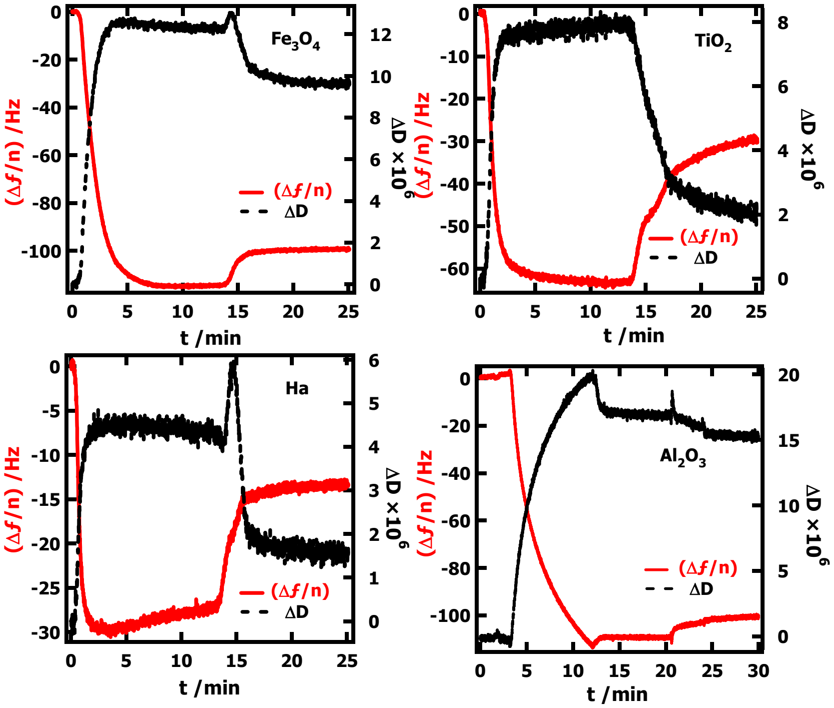

Figure 7.15. QCM-D results for the adsorption of DOPC vesicles onto bare metal oxide surfaces. $(\Delta f/n)$ and ΔD correspond to the third overtone (n = 3).

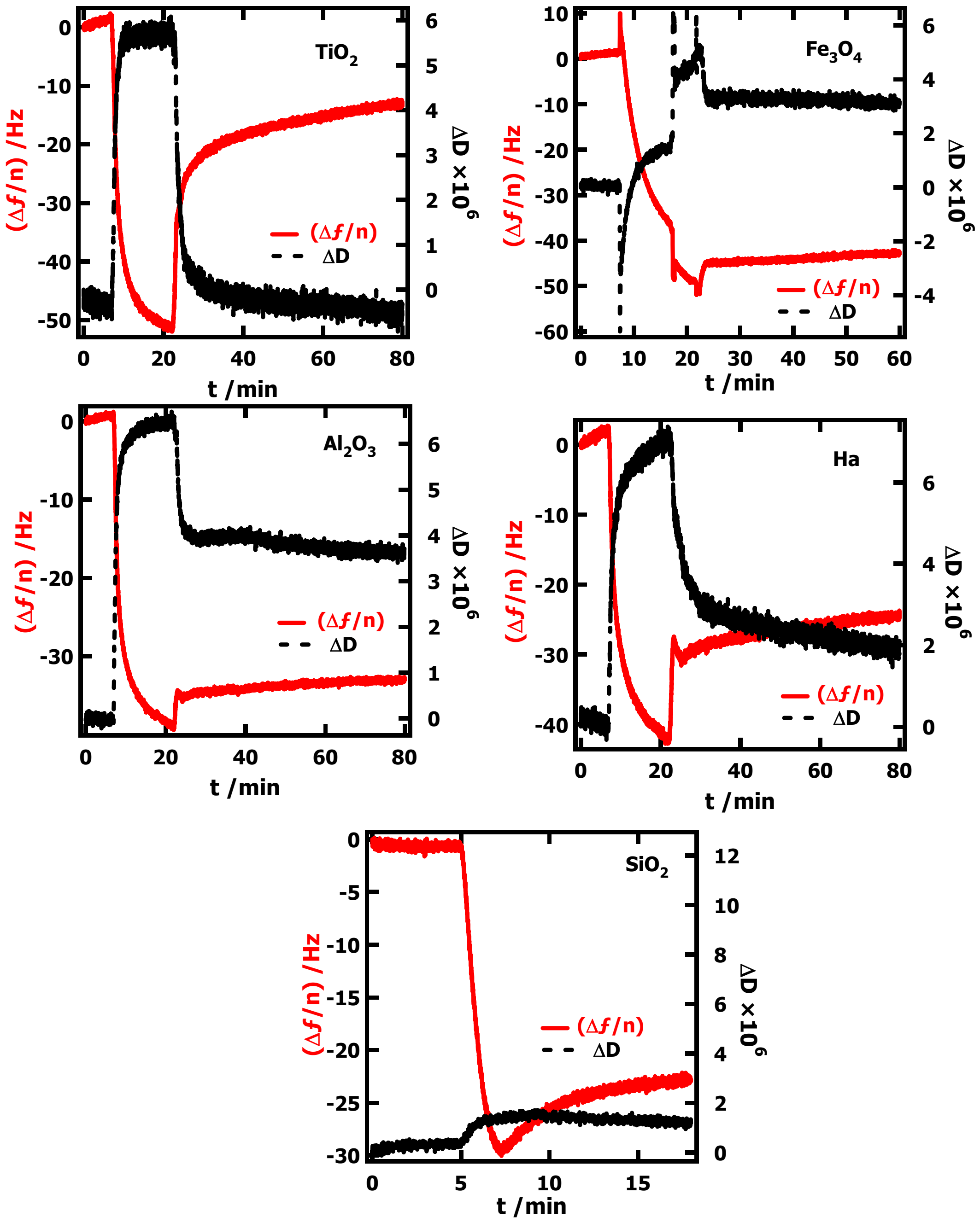

Figure 7.16. QCM-D results for the DOPC liposome adsorption onto self-assembled 6 k cholesterol PEG monolayers on various metal oxide surfaces. $(\Delta f/n)$ and ΔD correspond to the third overtone (n = 3).

Finally, the vesicle fusion results for DOPC lipid vesicles adsorbed onto the supported DOPC monolayer are shown in Figure 7.17. For Fe_3O_4, SiO_2, and TiO_2 surfaces, (Δf/n) of ~ 10 Hz and low (ΔD) were obtained. This result was consistent with the addition of a lipid monolayer onto the preformed monolayer. For Al_2O_3 and Ha surfaces, $|(\Delta f/\mathrm{n})|$ and ΔD are greater than the values expected for a monolayer. The monolayer vesicle fusion results seemed to be related to the roughness of the metal oxide surfaces. As shown in Figure 7.13, Al_2O_3, Fe_3O_4 and Ha surfaces had a higher roughness compared to SiO_2 and TiO_2 surfaces. Consequently, a smooth fusion curve for the formation of a monolayer on SiO_2 and TiO_2 surfaces was reasonable because rough surfaces would hinder vesicle fusion and the spreading of lipid vesicles.

7.2.3.4 Phospholipid/PEG Surfactant Mixed Monolayers for the Preparation of Cushioned Tethered Phospholipid Bilayers. In order to avoid the corrosion of the metal oxide sensor surfaces by the acidic endgroups, the cushioned tethered phospholipid bilayers were also prepared from PEG surfactants without the acid endgroup. In an exemplary procedure, a mixed monolayer of 2.5 k cholesterol PEG /DOPC was first prepared by LB-transfer onto metal oxide surfaces, followed by the formation of the second layer through vesicle fusion. The vesicle fusion results in Figure 7.18 showed that another DOPC lipid monolayer could be formed on the preformed mixed monolayers on SiO_2 and TiO_2 surfaces. By this procedure, a cushioned lipid bilayer was formed on the 2.5 k cholesterol PEG cushion and the PEG chains of the surfactants were physisorbed onto the metal oxide surfaces rather than chemisorbed.

The surface morphologies of the 2.5 k cholesterol PEG /DOPC mixed LB-films were checked with AFM and the results are shown in Figure 7.19. For a blend of DOPC with 1 mol% of 2.5 k cholesterol PEG (Figure 7.19A), a smooth surface was obtained. The SiO_2 surface used for the AFM study had a smooth surface unlike the rough surface of the SiO_2

QCM-D sensor. For the 5 mol% cholesterol 2.5 k blend (Figure 8 B and C), protruding features were observed and the features also demonstrated long range order which was more clearly seen in the tilted view image of Figure 7.19C. The ordered features were possibly attributed to monolayer phase separation of DOPC and the cholesterol tailgroups. During LB-transfer, the shearing factor of the upstroke movement may have induced the long range order of the features.

7.2.3.5. Suggestions for Future Work. The experimental results provided are encouraging preliminary outcomes and show that cholesterol PEGs are a promising candidate for the tethering molecules to phospholipid bilayers and the preparation of polymer cushioned phospholipid bilayers on various metal oxide surfaces. The results also showed how the surface roughness affected the reproducibility of the tethered phospholipid bilayer formation. However, QCM-D measurement could not provide information regarding the integrity of the bilayers. As shown in Figure 7.13, the metal oxide surfaces used had RMS roughnesses of 1.4-2.0 nm. Another question is "Can the formation of the lipid bilayer erase the generic roughness of the studied surfaces and achieve a smooth bilayer surface?" In-situ AFM under aqueous conditions would be a valuable tool for studies of the formation of the lipid bilayer. Results in Chapter 6 also showed that other types of tailgroups could be inserted into the bilayers. Therefore, other suggested experiments include using cheaper industrial PEG surfactants such as monostearate PEGs for the preparation of tethered lipid bilayers. The mobility of the lipid on the as-prepared tethered lipid bilayer can be checked with the fluorescence recovery after photobleaching (FRAP). The long range order of the cholesterol PEG domains within the DOPC monolayer requires additional verification if this approach is successful, this could be an exciting new route to order and pattern functional nanoparticles by using the LB-technique.

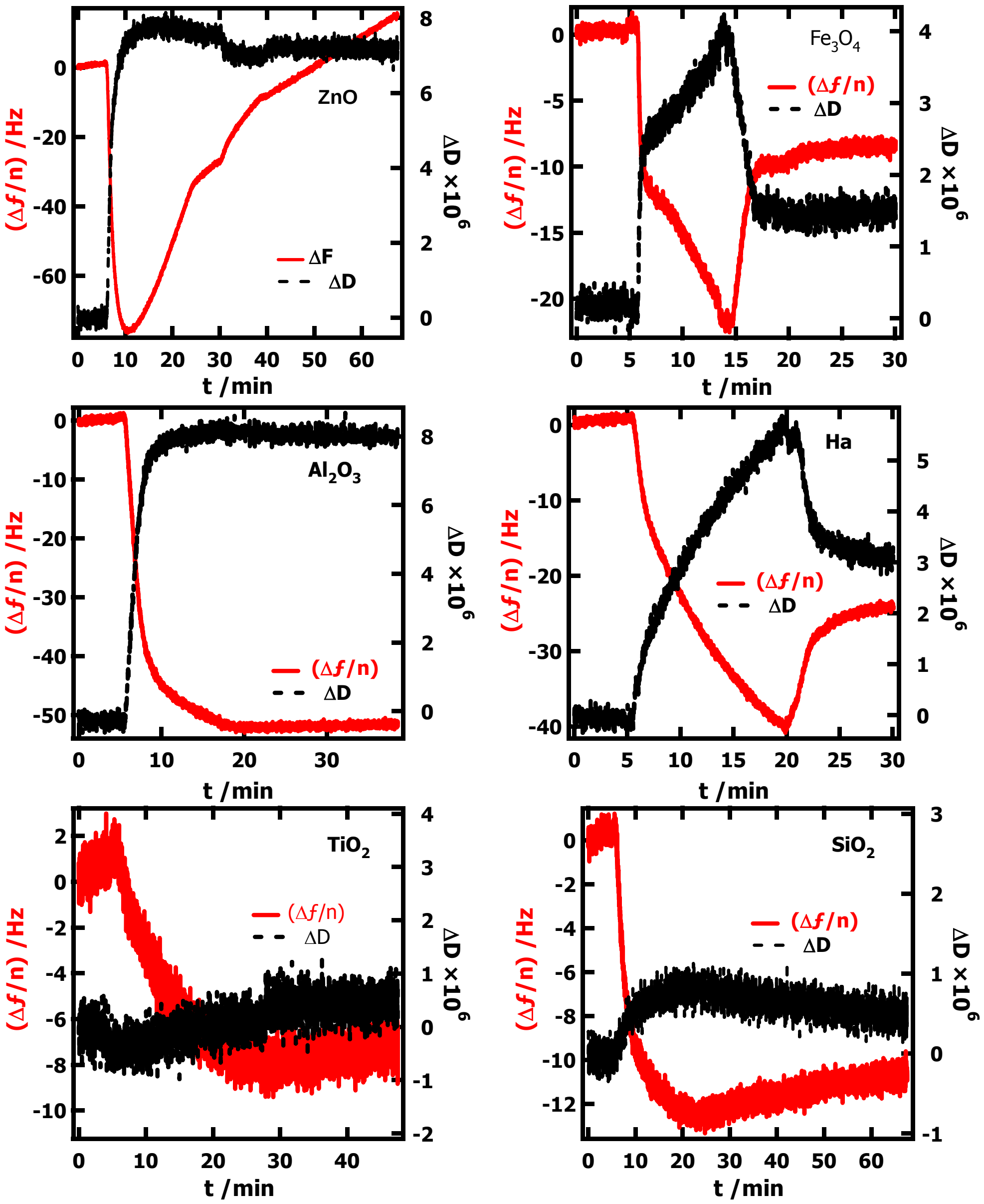

Figure 7.17. QCM-D results for the fusion of DOPC lipid vesicles onto preformed DOPC monolayers on a 6 k cholesterol PEG monolayer for different metal oxide surfaces. $(\Delta f/n)$ and ΔD correspond to the third overtone (n = 3).

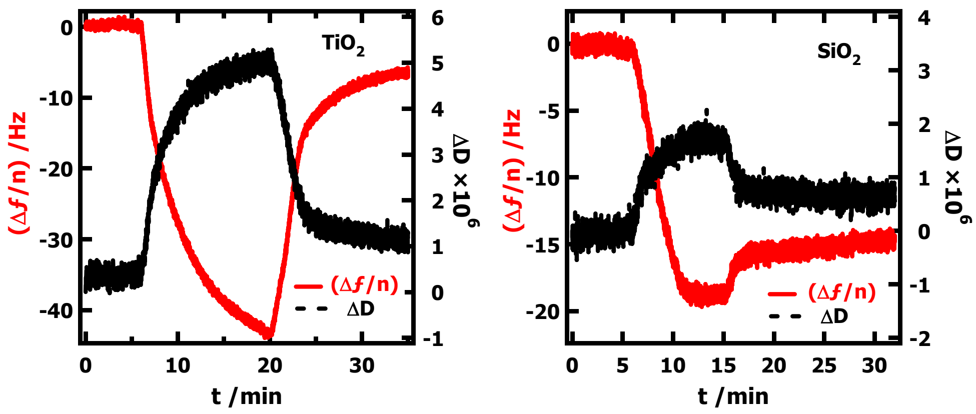

Figure 7.18. QCM-D results for the fusion of DOPC lipid vesicles onto 1 mol% 2.5 k cholesterol PEG /DOPC mixed monolayer on the SiO$_2$ and TiO$_2$ surfaces. $(\Delta f/n)$ and ΔD corresponded to the third overtone (n = 3).

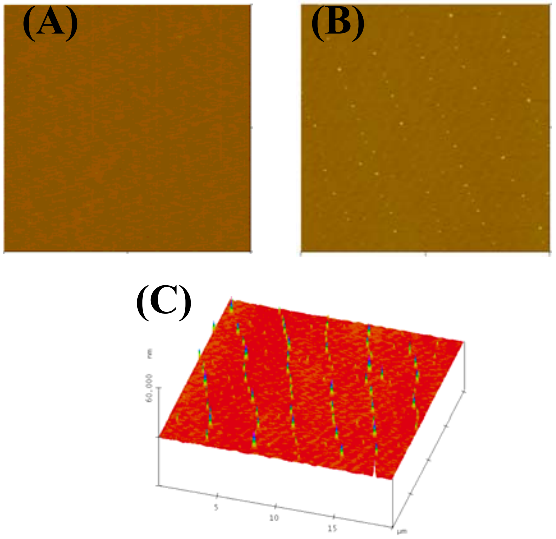

Figure 7.19. AFM height images for 2.5 k cholesterol PEG/DOPC blend LB-films. (A) 1 mol% of 2.5 k cholesterol PEG (scan area: 5 μm × 5 μm and *z* scale: 0-30 nm), (B) 5 mol% of 2.5 k cholesterol PEG (scan area: 20 μm × 20 μm and *z* scale: 0-30 nm), and (C) a tilted view image of (B).

7.2.4. Adsorption of Modified Water Soluble Polysaccharides onto Phospholipid

Bilayers. One important class of biomacromolecules is polysaccharides. Polysaccharides have attracted attention due to their natural abundance, bio-degradable and bio-compatible properties. One of the rising research areas is the application of polysaccharides for drug delivery. This requires an understanding of the interactions of polysaccharide and cell membranes (phospholipid bilayers) and the capability of tuning these interactions through chemical modification of polysaccharides.

Pullulan has also attracted increased attention as a water soluble polysaccharide that is also soluble in certain organic solvents. Therefore, it can be modified with etherification reactions in organic solvents. Results in Chapter 6 provide a useful guideline for modifications that could be made to polysaccharides to enhance their interactions with phospholipid bilayers. Therefore, the future work proposed here is the chemical modification of pullulan with various fatty acids and the subsequent studies of their adsorption onto phospholipid bilayers.

7.2.4.1. Synthesis of Pullulan Phytanate. One example here is the modification of pullulan with phytanic acid (Scheme 7.1). The synthetic details reported here was the work of Zelin Liu in the Esker group at Virginia Tech. In an exemplary procedure, phytanic acid was first synthesized according to a reported method.[14] The carbonyl group in phytanic acid was first activated by reacting with CDI. CDI (0.16 g, 1.38 mmol) and phytanic acid (0.04 g, 0.12 mmol) were dissolved in 10 mL anhydrous DMF. The mixture was stirred for 48 hours at room temperature. 1.0 g of Pullulan (6.2 mmol of glucose) was dissolved in 20 mL DMAc at 80 ˚C and magnetically stirred for ~1h. The activated phytanic acid was added to the reaction flask. The mixture was stirred for 48 hours at 80 ˚C. The cooled mixture was then added into 700 mL ethanol and stirred for 3 hours. The precipitate was vacuum filtered and a solid was collected. The solid was dried in a vacuum oven (25 torr, 60 ˚C) for 24 hours. The phytanyl hydrophobic groups distributed along the backbone after the modification and the density was controlled by varying the reaction conditions.

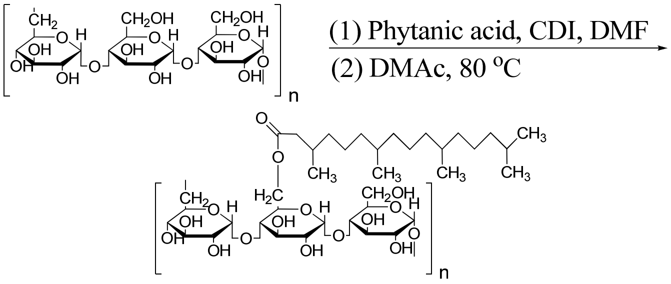

Scheme 7.1. Synthesis of pullulan phytanate (PPh)

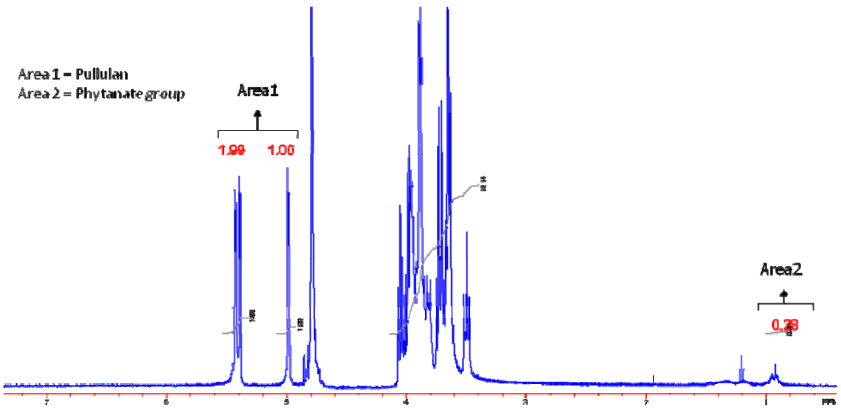

Figure 7.20. ^1H NMR spectrum of pullulan phytanate (PPh) in D_2O.

The degree of substitution (DS) of pullulan phytanate (PPh) was determined by ^1H NMR spectroscopy (JEOL Eclipse 500). A spectrum is provided in Figure 7.20. From Figure 7.20, peaks upfield from 1 PPM (Area 2) come from methyl groups of pullulan phytanate. The literature ^1H NMR spectrum of pullulan in D_2O indicated that peaks at 5 and 5.4 PPM (Area 1) come from the 3 protons at the C1 of the glucose units in pullulan. The DS was calculated from the integration of Area 1 and Area 2. The DS was defined as the number of phytanate groups per anhydroglucose unit. The DS value was determined to be 0.006. The determined value seemed to be valid, as the targeted DS was 0.02.

7.2.4.2. Studies of Pullulan and Pullulan Phytanate Adsorption onto Phospholipid Bilayers. Results for pullulan and pullulan phytanate adsorption onto DOPC bilayers are shown in Figure 7.21. Similar to 2k MPEG, the hydrophilic unmodified Pullulan had a weak affinity for the DOPC bilayer, whereas pullulan phytanate exhibited irreversible adsorption. The interaction between the PPh and the bilayer also appeared to be independent of the concentration; (lower concentration data was not shown). The final $|(\Delta f/n)| \sim 40 \pm 1$ Hz.

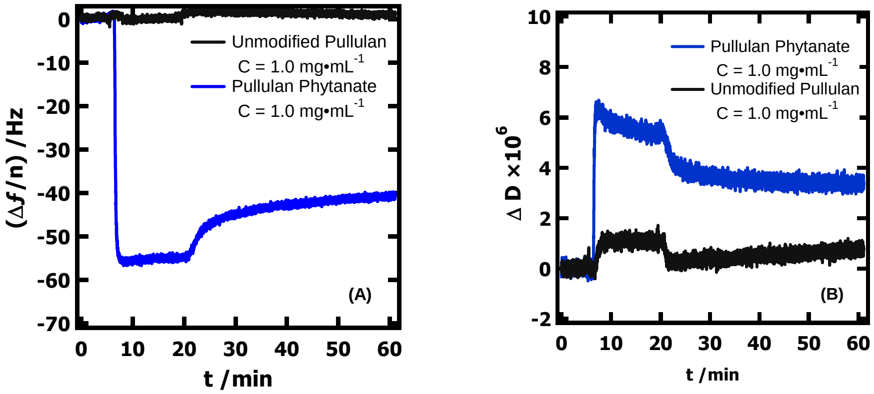

Figure 7.21. Unmodified pullulan and the pullulan phytanate adsorption onto DOPC bilayers. (A) (Δf/n) and (B) ΔD for the third overtone (n = 3).

A suggestion for further study would be the modification of pullulan with other fatty acids, such as oleic acid and stearic acid, and to compare the results for pullulan ester adsorption with studies in Chapter 6. Vitamin E succinic acid is a good candidate and recommended here for study. If one compares the structures of the vitamin E succinic acid and phytanic acid, the two molecules share the same phytanyl group. Vitamin E succinic acid has two fused six member rings with three methyl groups on the benzyl ring. The structural complexity attributed to hydrophilic polymers modified with vitamin E succinic acid should affect adsorption kinetics compared to the surfactants in Chapter 6. In Figure 7.22, an adsorption result shows that Vitamin E (d-α-tocopheryl poly(ethylene glycol) 1000 succinate (TPGS 1000) adsorbed onto DOPC bilayers. The adsorption had a slower saturation rate compared to that of cholesterol PEGs in Chapter 6 due to its greater cross sectional area (~60 Å^2•molecule^{-1}) of the tail group. However, it was still much faster than dioleoyl PEG surfactants.

Figure 7.22. QCM-D results for TPGS 1000 adsorption onto a DOPC lipid bilayer and the structure of TPGS 1000.

7.3. References

(1) Tung, S. H.; Kalarickal, N. C.; Mays, J. W.; Xu, T. *Macromolecules* **2008**, *41*, 6453.

(2) Zhang, Q.; Xu, T.; Butterfield, D.; Misner, M. J.; Ryu, D. Y.; Emrick, T.; Russell, T. P. *Nano Lett.* **2005**, *5*, 357.

(3) Li, B.; Esker, A. R. *Langmuir* **2007**, 2546.

(4) Li, B.; Wu, Y.; Liu, M.; Esker, A. R. *Langmuir* **2007**, *22*, 4902.

(5) Joncheray, J. T.; Denoncourt, M. K.; Mathieu, C.; Meier, A. R. M.; Schubert, S. U.; Duran, S. R. *Langmuir* **2006**, *22*, 9264.

(6) Joncheray, J. T.; Denoncourt, M. K.; Meier, A. R. M.; Schubert, S. U.; Duran, S. R. *Langmuir* **2007**, *23*, 2423.

(7) Kiessling, V.; Wan, C.; Tamm, L. K. *Biochimica et Biophysica Acta* **2009**, *1788*, 64.

(8) Elender, G.; Kühner, M.; Sackmann, E. *Biosensors & Bioelectronics* **1996**, *11*, 565.

(9) Kühner, M.; Tampe, R.; Sackmann, E. *Biophys. J.* **1994**, *67*, 217.

(10) Wagner, M. L.; Tamm, L. K. *Biophys. J.* **2000**, *79*, 1400.

(11) The adsorption of hydrophillic polymers with these acid endgroups onto metal oxide surfaces was confirmed by QCM -D measurements.

(12) Starr, T. E.; Thompson, N. L. *Langmuir* **2000**, *16*, 10301.

(13) Liu, G. F., L.; Zhang, G. *J. Phys. Chem. B* **2009**, *113*, 3365.

(14) Sita, L. R. *J. Org. Chem.* **1993**, *58*, 5285.